Luminosity Tuning at the Large Hadron Collider

Dissertation zur Erlangung des akademischen Titels
Doktor der technischen Wissenschaft

Vorgelegt der Technisch-Naturwissenschaftlichen Fakultät
der Technischen Universität Graz

Durchgeführt am europäischen Kernforschungszentrum
CERN, CH-1211 Genf, und am Institut für Theoretische
Physik der TU-Graz,A-8010 Graz,

von

Walter Wittmer

Für meine Frau Eva und meine
Kinder Maxi und Martin.

Abstract

By measuring and adjusting the β-functions at the interaction point (IP) the luminosity is being optimized. In LEP (Large Electron Positron Collider) this was done with the two closest doublet magnets. This approach is not applicable for the LHC (Large Hadron Collider) and RHIC (Relativistic Heavy Ion Collider) due to the asymmetric lattice. In addition in the LHC both beams share a common beam pipe through the inner triplet magnets (in these region changes of the magnetic field act on both beams). To control and adjust the β-functions without perturbation of other optics functions, quadrupole groups situated on both sides further away from the IP have to be used where the two beams are already separated. The quadrupoles are excited in specific linear combinations, forming the so-called "tuning knobs" for the IP β functions. For a specific correction this knob is scaled by a common multiplier. The different methods which were used to compute such knobs are discussed: (1) matching in MAD, (2) inversion and conditioning of the response matrix by singular value decomposition, and (3) conditioning the response matrix by multidimensional minimization using an adapted Moore Penrose method. For each accelerator, LHC and RHIC, a set of knobs was calculated and the performance compared. In addition the knobs for RHIC were successfully applied to accelerator. Simultaneously this approach allows us theoretically to measure the beam sizes of both colliding beams at the IP, based on the tuneability provided by the knobs. This possibility was investigated. The standard method for LEP to measure the IP β-functions was adapted and advanced to the asymmetric LHC lattice.

Optimierung der Luminositaet des “Large Hadron Colliders” (LHC)

Zusammenfassung

Die Luminositaet wird durch Messen und Variieren der β-Funktion am Wechselwirkungspunkt (WP) optimiert. Im LEP (Large Electron Positron Collider) wurde die Luminositaet mittels der dem WP naechstliegenden zwei Doublet Quadrupole variiert. Dieser Zugang ist fuer LHC (Large Hadron Collider) und RHIC (Relativistic Heavy Ion Collider) durch das asymmetrische Gitter (Anordnung der magnetischen Elemente zur Steuerung, Fokusierung und Korrektur des Teilchenstrahls) nicht anwendbar. Zusaetzlich teilen sich beide kollidierenden Teilchenstrahlen das Magnetfeld in den Triplet Quadrupolen. Um die β-Funktion variieren zu koennen, muessen links und rechts des WP weiter entfernte Quadrupole benutzt werden, da in diesen Bereichen fuer jeden Strahl ein separates Magnetfeld vorhanden ist. Diese Quadrupole werden auf eine bestimmte Weise angeregt und formen den so genannten “tuning knob” fuer die WP β-Funktion. Zur gezielten Anwendung werden diese “tuning knobs” mit einem dimensionslosen Multiplikator skaliert. Die verschiedenen Methoden zur Berechnung werden behandelt: (1) “Matching by MAD”, (2) Inversion und Konditionierung mittels Singulaerwertzerlegung (Singular Value Decomposition, SVD) und (3) Konditionierung der “Response Matrix” durch multidimensionale Minimisierung mittels adaptierter Moore Penrose Methode. Fuer jeden Beschleuniger, LHC und RHIC, wurde ein Paar (horizontale und vertikale Ebene) “tuning knobs” berechnet und die Funktionsweise charakterisiert. Zusaetzlich wurden die “tuning knobs” fuer RHIC am Beschleuniger getestet. Weiters koennen diese theoretisch verwendet werden um die Strahlgroesze der beiden kollidierenden Teilchenstrahlen am WP zu messen. Diese Moeglichkeit wurde neu entwickelt und untersucht. Die standard Methode zur Messung der β-Funktion am WP fuer LEP wurde an das asymmetrische “lattice” von LHC angeglichen und die Methode weiterentwickelt.

Acknowledgment

First of all I would like to thank my wife Eva and two sons, Maxi and Martin, for their love, support and understating during these years of my thesis. The confidence and patience they spent me to face the sometimes difficult time.

I would like to thank my university supervisor Univ. Prof. Dr. Bernhard Schnizer of the Institute fuer Theoretische Physik, TU-Graz, who encouraged me, despite of all circumstances, to start and carry out this thesis, for his help and faith. My CERN supervisor Dr. Frank Zimmermann, of the AB Department, Accelerator and Beam Physics group, for his guidance of this thesis, and the confidence in me and my ideas. With their assistance, patience and many fruitful discussions they made this time a great experience.

I would also like to thank other members, especially Andre Verdier and Daniel Schulte, who always had time to discuss sometimes crazy ideas. This work would not have been possible without the help of the many members of this group.

Contents

Chapter 1

Introduction

1.1 General Description of the Scope of this Work

CERN

CERN, from the French “Conseil Europèen pour la Recherche Nuclaire” is one of the world’s largest scientific research facilities. It is located at the border between France and Switzerland close to the city of Geneva. In English referred to as the European Organization for Nuclear Research, it was founded in 1953. The motivation for establishing this laboratory was to drive the nuclear research to smaller dimensions to win a deeper insight into matter. Starting with the Proton Synchrotron (PS) Complex, demands to increase the energy of the accelerated particle led to expansion of the facility. Figure 1.1 shows a sketch of the now existing or currently being constructed accelerators. The machine built after the PS is the SPS (Super Proton Synchrotron). It provided the energy to discover the weak force particles W^+, W^-, Z^0 earning Carlo Rubbia and Simon Van de Meer the Nobel prize 1984 for their discovery. To push the frontier of energy higher and to obtain more precise data the particle accelerator LEP (Large Electron Positron collider) was built.

LHC

To step one step higher on the energy ladder, currently the LHC (Large Hadron Collider) is constructed. Using two proton beams, it will provide a top center of mass energy of 2×7 TeV (Tera electron Volts = 10^{12} eV) to the high energy physics community. It is currently being installed in the tunnel that earlier hosted the LEP collider. This tunnel and the adaptations are depicted in Fig.1.2. Contrary to LEP the LHC is based on superconducting magnets which are needed to provide the field strengths for guiding and focusing a beam at this energy level. The LHC will collide the two beams in four interaction points (IPs) which host four different experiments with their detectors (ATLAS, CMS, ALICE, LHC-B), and a fifth experiment (TOTEM) installed close to LHC-B.

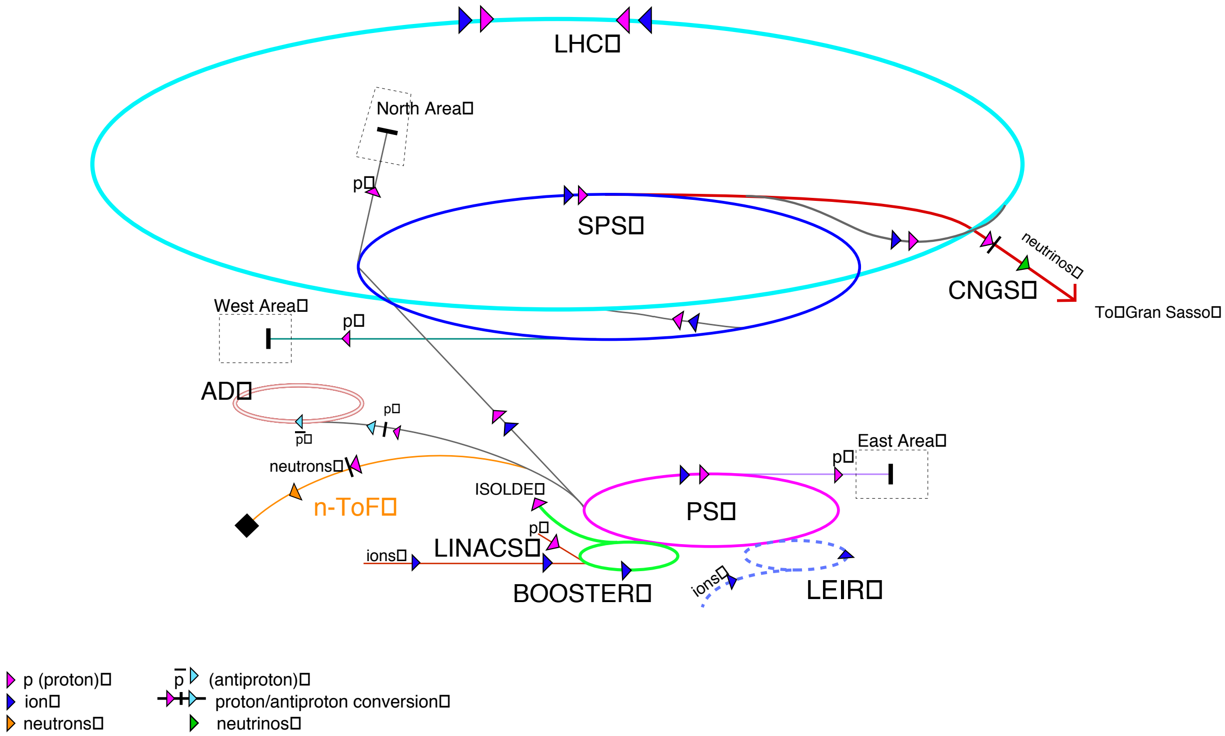

Figure 1.1: The accelerator chain of CERN. Currently the LHC is under construction. Previous accelerators of CERN serve as injectors to the LHC machine (SPS and PS). Further experimental areas for non LHC physics are shown, as the neutrino beam to Gran Sasso (CNGS), and the Antiproton Decelerator (AD), the first stage on the way to antihydrogen.

Luminosity

The increase in energy is one demand that has to be satisfied to probe matter in more detail. The cross-section of events that provide this information is decreasing with energy and thus with the increase in energy the rate of specific events that are looked for is decreasing. To obtain accurate data from the measurements the level of interesting events has to be maximized. Even if the event rate is high enough to measure them but the time needed to collect enough information is too long (for instance 100 years), the experiment will not be practicable. The quantity that is commonly used to characterize an accelerator is the luminosity. It relates the interaction rate to the interaction cross section. The statistics of an experiment is determined by the total number of measured events of interest and therefore the integrated luminosity is the figure of merit for the experiment.

Hence it is of great importance to be able to optimize the luminosity during the operation of an accelerator. This does not always necessarily mean to maximize the luminosity. Not all experiments demand the maximum possible event rate. It is also of interest to be capable to vary the luminosity very accurately around a specific value, and also to decrease it, if necessary, to create the optimum experimental conditions.

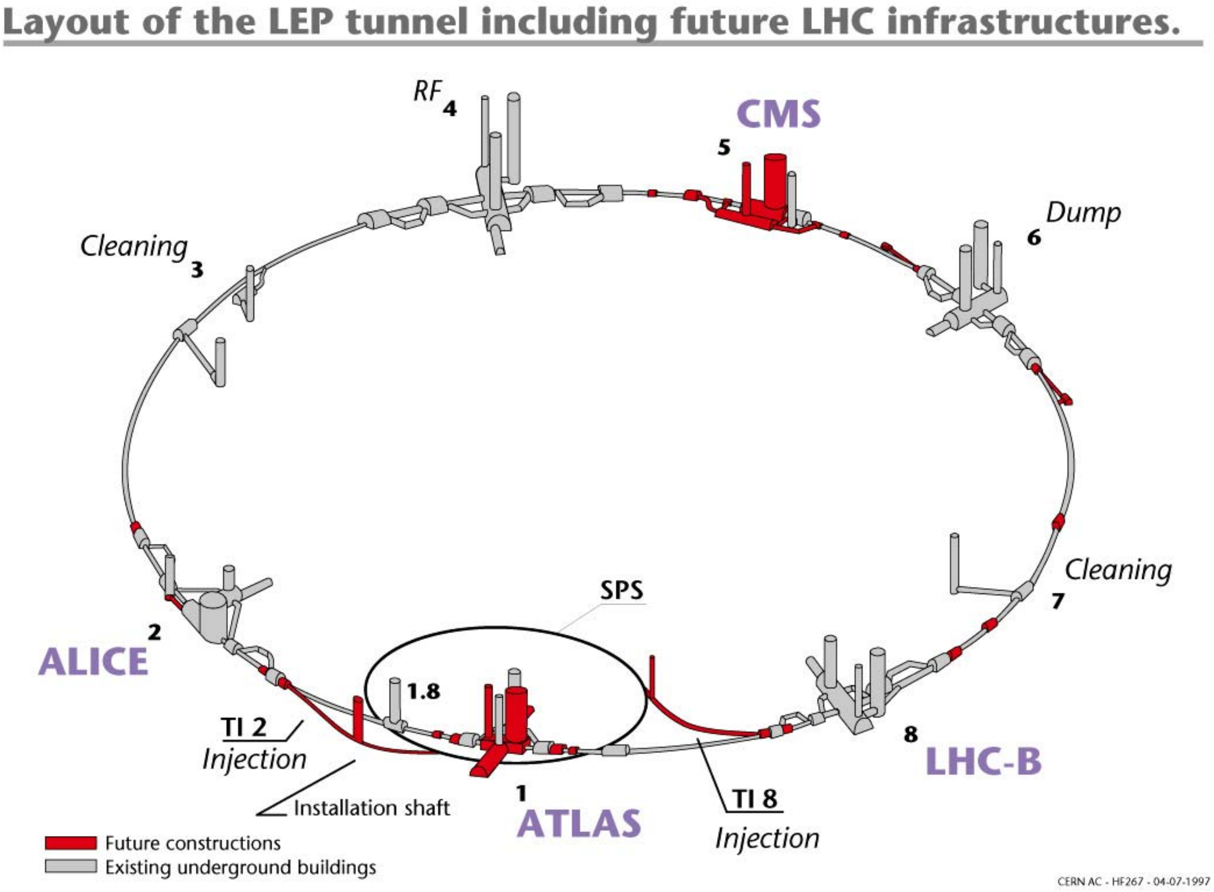

Figure 1.2: Drawing of the LEP tunnel, its installations and the modifications for LHC. The locations of the four main experiments are indicated.

Error Sources for Luminosity Degradation

The luminosity varies with the size of the two beams at the IP. Like an optical system, the “spot size” is a function of the focusing system. This system is composed of magnetic lenses (quadrupoles). The combination of all magnetic elements for guiding, focusing and correcting the beam is referred to as the lattice of the accelerator. Numerical codes are used to design a lattice with specific characteristics.

In the lattice design of an accelerator all elements are treated as ideal. In reality these elements are not perfect. Construction errors and others are the reason that the characteristics of different elements do not comply with their design characteristics. Thus the optics functions of the real machine will differ from the design optic functions. This can introduce an error to the IP beam size and degrade the luminosity. During the operation of an accelerator the field gradient of magnets can change. This will also result in a change of the IP beam size.

Optic Functions

A magnetic lattice is characterized by the optics functions. The β-function, which is the square root of the envelope function of all stable particle trajectories, is related to the square of the beam size by a constant factor. This optics function is determined by the field strengths of the quadrupoles and is used to describe the focusing behavior of the lattice. By changing specific quadrupoles in the interaction region (IR) the β-function at the interaction point (IP), which is referred to as $\beta^{\star}$, is changed. Unfortunately the change of the focusing fields also changes other optics functions which are supposed to be kept constant. It is possible to find a combination of changes in the field strengths for appropriate quadrupoles (tuning quadrupoles) that only creates a change in $\beta^{\star}$ and leaves other functions constant. For this the number of quadrupoles (degrees of freedom) has to be lower or equal to the number of functions which have to be constrained (constraints), plus an additional for the β-function. To confine the changes to a specific area of the lattice, the changes have to be created on the incoming side of the IP to be effective at the IP and then to be canceled on the side of the outgoing beam. This increases the number of quadrupoles needed.

1.2 Specific Description of the Scope and Methods

Method of Optimization

To change the beam size in the interaction point the characteristics of the focal system must be changed. This change has to meet specific conditions. This is due to the fact, that the beam is stored in a ring with more than one experiment, which do not all want to be disturbed by this manipulation. Also the stability of the beam can be negatively affected by such changes.

There are two, in principle, different approaches to compute a solution. One is to use the numerical codes to find an exact solution which creates the desired changes to the beam size. This demands an exact knowledge of the machine condition. In real accelerators this information is only partially available. On top of this the information is measured with an uncertainty. Also the effort to obtain this information can be tremendous. For the second approach the existing solution is perturbed to create the desired changes. The advantage of this method is that the perturbation is calculated for a known condition of the accelerator and no measurements are needed to perform them. The disadvantage is that due to the perturbation and, due to unknown optics errors changes are not necessarily confined to the region of the manipulated IP (interaction region). The changes may propagate around the ring and can affect all other experiments.

$\beta^{\star}$ Tuning Knobs

In this thesis a knob vector refers to as a vector of increments of quadrupole strengths which fulfills the above described conditions. The increments are in constant ratio.

In addition this vector is to be scaled linearly with a dimensionless multiplier. Together this system is named a (linear) "tuning knob". The expression tuning knob is frequently used in a slightly different context. A single quadrupoles which creates a specific change to only one optics function is labeled with the same expression.

Methods of Calculating $\beta^\star$ Tuning Knobs

The standard method of calculating a knob vector is to use a numerical code. Thereby an optimum solution is found by trial and error. For LHC a knob vector for horizontal and vertical β-function has been calculated, characterized and applied successfully to correct a series of randomly distributed errors. The magnitude of expected errors is estimated from measurements of magnets which will be installed in the LHC.

The LHC is still under construction but the functionality of these knobs will be a vital part of the optics control system. For this reason an existing facility with as similar as possible characteristics was chosen to test this correction scheme. This facility is the Relativistic Heavy Ions Collider (RHIC) located at Brookhaven National Laboratory (BNL) on Long Island New York (see Fig.1.3). For the RHIC lattice the standard method of calculating tuning knobs was not successful.

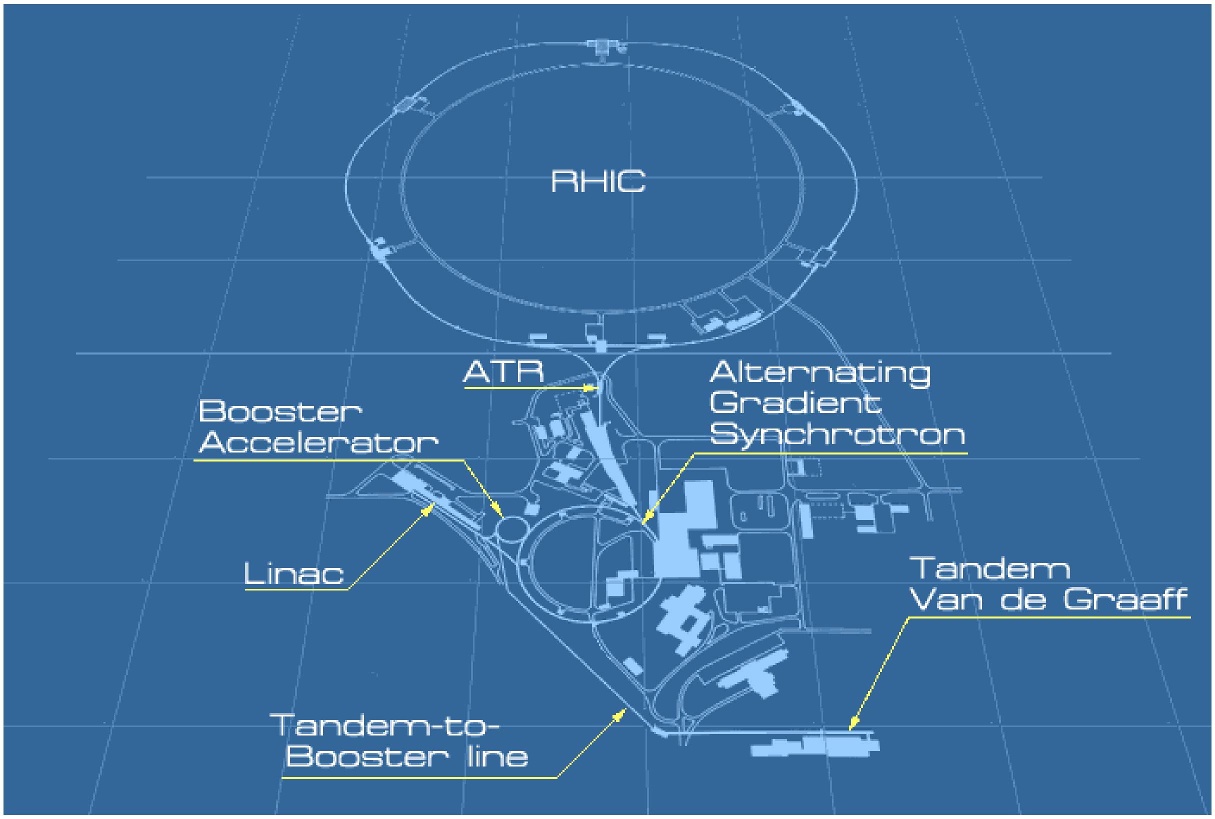

Figure 1.3: Acceleration chain of the installation located at Brookhaven National Laboratory. The Relativistic Heavy Ion Collider is the final stage of this chain. In RHIC gold ions and spin polarized protons are brought into collision.

Hence a new method of obtaining tuning knobs had to be developed. It is based on the response matrix of the insertion quadrupoles. The analysis revealed that part of the problem was the nonlinear response of the constraints to the change of the field strength. An alternative approach for dealing with this problem was adapted, advanced and tested successfully in simulations.

The method of Singular Value Decomposition (SVD) is used to analyze the response matrix for different combinations of degrees of freedom and constraints. This method proved very powerful in optimizing the correction scheme.

Application of Tuning Knobs in RHIC

To prove the applicability of this correction scheme at a real machine the computed tuning knobs were applied to RHIC. In a total of four beam experiments the tuning knobs were used to reduce the IP β-function first in one IP (PHENIX) and then simultaneously in the two IPs of PHENIX and STAR. Thereby the counting rate was increased by $\approx 10\%$ compared to a reduction of the IP β-functions of $\approx 12\%$. The tuning range was limited only by some of the power supplies of the tuning quadrupoles and it is under consideration to replace these by stronger ones.

Measuring the IP β-function

It is very difficult to measure the IP β-function accurately because no measurement instrument can be installed in this area which is occupied by the detector of the experiments. The existing methods either measure the β-function as close as possible to this point and propagate this value by using the lattice model into the IP. Thereby errors are accumulated by the propagation and the measurement. The measurement errors are absolute and result in a big relative uncertainty for the obtained IP β-function value. Other methods calculate the β-function from quanteties measured at the IP and typically involve beam-beam deflections or luminosity signals.

In this thesis an existing method has been investigated and extended to the needs of the LHC lattice. The measurement uncertainty was calculated to be at the percent level. Based on the tuning knobs and the “Vernier Scan“ a new method was developed. The expected uncertainty for this method is estimated to be higher.

Chapter 2

Fundamental Concepts in Accelerator Physics

This chapter introduces the basic concepts and quantities of accelerators physics. This is only a very brief summary and intended as a lexical help for the further chapters and the reader is referred to [1]-[11] for more detailed reviews.

2.1 Accelerator Optics Theory

The purpose of accelerators is to accelerate, store and collide charged particles beams. As a target another particle beam or fixed targets can be employed. To produce particles with high masses two colliding beams are commonly used because all the kinetic energy is converted into center-of-mass energy whereas in fixed target experiments only part of the energy is available. In circular colliders as the LHC these beams have to be kept in storage and collision for several hours. To maintain the particles on their trajectory inside the vacuum chamber both electric and magnetic fields are used. The elements providing these guiding fields are the main constituents of the ring. Dipole fields are used as steering magnets to bend the beam and quadrupoles as magnetic lenses to focus the beam. The particle motion is described by the linear optics theory. During the design of an accelerator the particle path is defined. For the LHC it was determined by the existing LEP tunnel. Then the particle motion is described with respect to this design orbit, which is the orbit of the reference particle with specific initial conditions and energy without any error present. Therefore the coordinate system used has its center on this trajectory. It is often co-moving with an ideal particle propagating around the ring. The transverse plane is defined by a horizontal "$x-$coordinate" and vertical "$y-$coordinate" axis perpendicular to the particle path "$s-$coordinate" (see Fig.2.1, page 8). In the literature the set of variables $x, x', y, y, y', s, \delta_s$ is used to describe the beam optics, where x' and y' denote the slopes of the particles trajectory and δ_s the momentum deviation of a given particle with respect to the reference particle. All "linear" magnets are ideally placed so that the design orbit passes through their center. In real accelerators the design particle follows the so called closed orbit which oscillates around the design orbit. This deviation is caused by field errors. There are

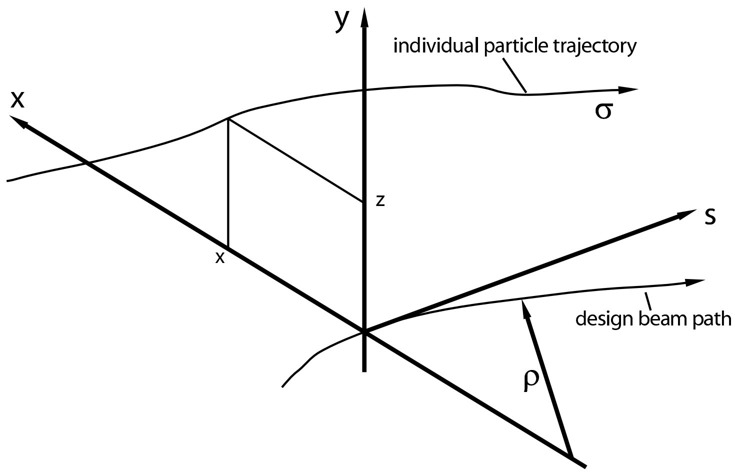

Figure 2.1: Coordinate system of the design orbit.

a variety of sources for these, e.g. misalignment of the magnet center with respect to the design orbit, roll and tilt of the magnetic axis, imperfection in the construction etc. Depending on the strength of these errors, corrections have to be applied. Higher multipole magnets (sextupoles, octupoles, decapoles) can be installed to correct nonlinear imperfections. Examples for the pole faces of higher order multipoles are depicted in Fig.2.2, page 11.There is no exact analytic solution for this problem and perturbation theory is used to estimate the behavior of beams in the presence of nonlinear errors and applied correction. Accelerators are designed using numerical codes e.g. MAD (methodical accelerator design). As the first step a linear optics model is used to design the machine.

2.1.1 Accelerator Magnets

The basic elements of a storage ring are dipole and quadrupole magnets. Dipole magnets bend the trajectory of particles horizontally on a circular path. The horizontal force F (orthogonal to the trajectory of a particle with charge e and momentum $p = \gamma m_0 v$) is provided by the magnetic field B_y of dipoles

$$F = evB_y = \frac{\gamma m_0 v^2}{\rho},$$

which bends the trajectory into an arc of radius ρ:

$$\frac{1}{\rho} = \frac{eB_y}{p}, \quad \frac{1}{\rho}[m^{-1}] = 0.2998\frac{B_0[\mathrm{T}]}{p[\mathrm{GeV/c}]}. \tag{2.1}$$

Quadrupole magnets focus particles on the design trajectory to reduce the needed space inside the vacuum chamber of the accelerator. The magnetic field of a quadrupole is characterized by its gradient

$$g = \frac{\partial B_y}{\partial x} = \frac{\partial B_x}{\partial y}. \tag{2.2}$$

where B_x and B_y are the Cartesian field components in the horizontal and vertical planes. Similar to the bending strength of a dipole magnet, the field gradient of a quadrupole can be related to its optical effect. For this purpose the gradient is normalized to the momentum of the particle so as to define the quadrupole strength:

$$k = \frac{eg}{p}, \quad k[\mathrm{m}^{-2}] = 0.2998\frac{g[\mathrm{T/m}]}{p[\mathrm{GeV/c}]}. \tag{2.3}$$

With l as the length of the quadrupole the effective focal length is calculated by

$$\frac{1}{f} = k \cdot l. \tag{2.4}$$

An important characteristic of quadrupoles is that the horizontal force component only depends on the horizontal position and not on the vertical and vice versa.

$$F_x = evB_y(x,y) = -evgx$$
$$F_y = -evB_x(x,y) = evgy$$

Therefore in machines with only dipole and quadrupole fields the vertical and horizontal particle motion is decoupled.

The focal length of a quadrupole is a function of the particle momentum. Sextupoles are used to correct focusing errors of off momentum particles which suffer from "chromatic" errors. Different to dipoles and quadrupoles, sextupoles (and all higher order multipoles) couple the motion of the transverse planes and generate a nonlinear field:

$$\begin{aligned} B_y &= \frac{1}{2}g'(x^2 - y^2), \\ B_x &= g'x \cdot y. \end{aligned}$$

Similar to dipoles or quadrupoles, a momentum independent sextupole strength is defined as

$$m = \frac{eg'}{p_0}, \quad m[\mathrm{m}^{-3}] = 0.2998\frac{g'[\mathrm{T/m^2}]}{p_0[\mathrm{GeV/c}]}.$$

If the length of an accelerator magnet is much larger than the bore radius the magnetic field has to good approximation only transverse components. The end (fringe) field contribution is small. Using a complex potential function $\tilde{A}$ to describe this field, the latter can be expanded in a power series exploiting its analytic behavior. For superconducting magnets it is convenient to express the potential in cylindrical coordinates as

$$\tilde{A}(z) = \sum_{n=0}^{\infty} \kappa_n z^n = A_s(r,\varphi) + iV(r,\varphi), \quad \kappa_n = \lambda_n + i\mu_n; \tag{2.5}$$

$$A_s(r,\varphi) = \sum_{n=0}^{\infty} (\lambda_n \cos n\varphi - \mu_n \sin n\varphi) r^n),$$

$$V(r,\varphi) = \sum_{n=0}^{\infty} (\mu_n \cos n\varphi + \lambda_n \sin n\varphi) r^n).$$

with λ_n, μ_n being real constants. By taking the gradient of the imaginary part of the scalar potential one obtains the radial and azimuthal field components:

$$\begin{aligned} B_\varphi = -\frac{1}{r}\frac{\partial V}{\partial \varphi} &= -\sum_{n=1}^{\infty} n(\lambda_n \cos n\varphi - \mu_n \sin n\varphi) r^{n-1}, \\ B_r = -\frac{\partial V}{\partial r} &= -\sum_{n=1}^{\infty} n(\mu_n \cos n\varphi + \lambda_n \sin n\varphi) r^{n-1}. \end{aligned}$$

Now the "**normal**" multipole coefficients b_n and the "**skew**" coefficients a_n are introduced

$$b_n = -\frac{n\lambda_n}{B_{main}} r_0^{n-1}, \quad a_n = +\frac{n\mu_n}{B_{main}} r_0^{n-1}.$$

were r_0 is defined as the reference radius for the multipole expansion. The normal differ from the skew fields by a rotation of $\frac{\pi}{2n}$ in the transverse plane. The normal fields for a quadrupole ($n = 2$) are oriented so that the magnetic axes in the transverse plane are parallel to the horizontal and vertical axes. This means that a skew quadrupole couples the horizontal and transverse plane. The main field B_{main} is the field at the reference radius (in the horizontal plane obtained at $r = r_0$, $\varphi = 0$ for normal field and $r = r_0$, $\varphi = \frac{\pi}{2n}$ for a skew field). Replacing λ_n by b_n and μ_n by a_n and considering $B_\varphi + iB_r$ the field can be characterized as

$$\begin{aligned} B_\varphi + iB_r &= B_{main} \sum_{n=1}^{\infty} \left(\frac{r}{r_0}\right)^{n-1} (b_n - ia_n)\, e^{in\varphi}, \\ (|B|)_n &= \left(\sqrt{B_r^2 + B_\varphi^2}\right)_n = B_{main} \left(\frac{r}{r_0}\right)^{n-1} \sqrt{a_n^2 + b_n^2}. \end{aligned} \tag{2.6}$$

For an ideal normal $2n$-pole magnet $b_n = 1$ and all other a_n, $b_n = 0$. Each multipole can be described in this way:

$$\begin{array}{lcll} n & = & 1 & \text{Dipole} \\ n & = & 2 & \text{Quadrupole} \\ n & = & 3 & \text{Sextupole} \\ & \vdots & & \end{array} \tag{2.7}$$

Equation (2.6) shows that the magnitude of the $2n$ polar field **does not** depend on the azimuth φ and scales with the $(n-1)$th power of r and that a_n, b_n are the relative field contributions of the nth multipole to the main field at the reference radius r_0. In a good dipole or quadrupole magnet the unwanted multipole coefficients a_n, b_n are typically a few 10^{-4} or less.

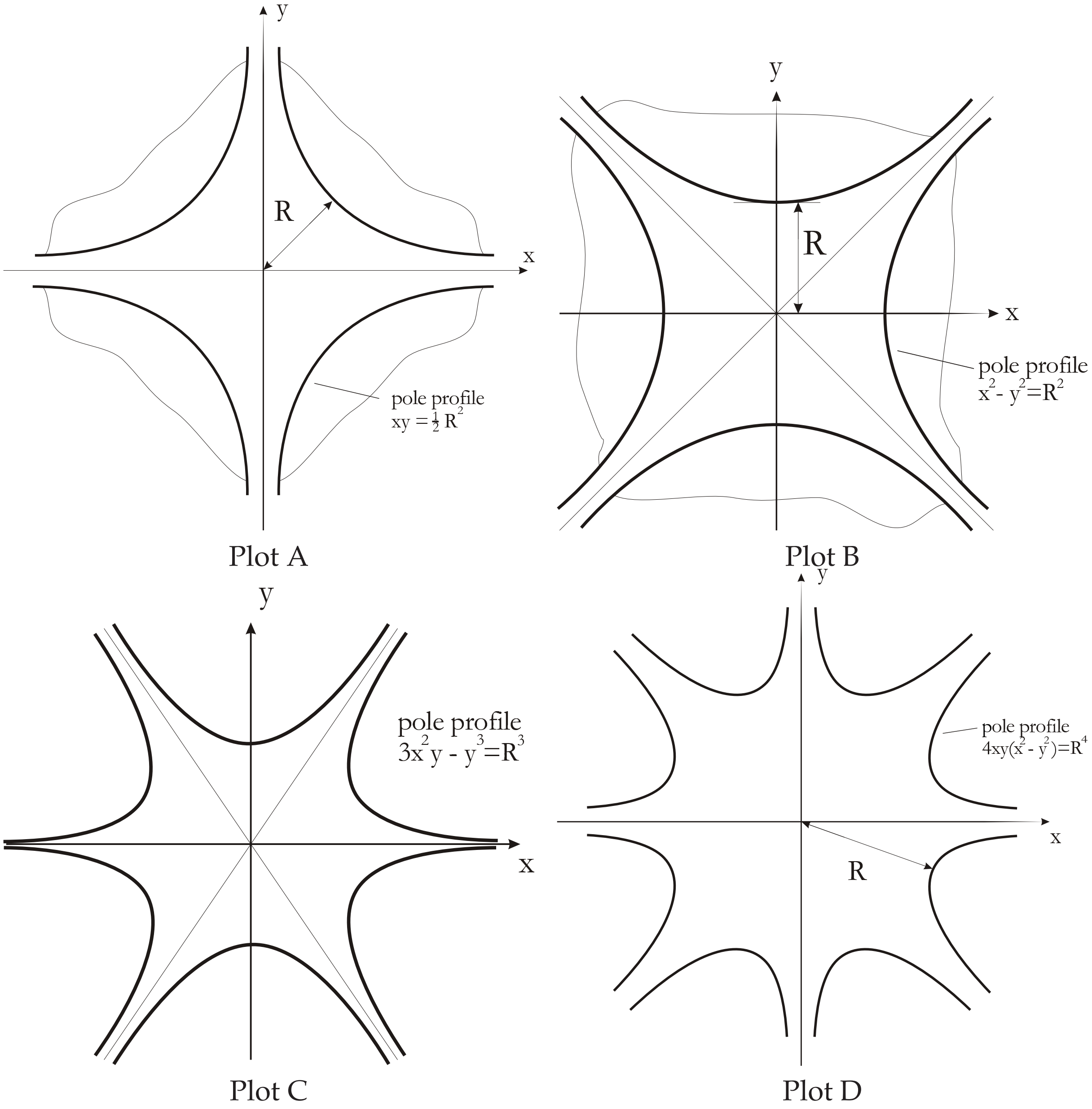

Figure 2.2: Pole shapes for an upright quadrupole magnet (Plot A), a rotated or skew quadrupole magnet (Plot B), an upright sextupole magnet (Plot C) and an upright octupole magnet (Plot D).

Equation (2.5) can be written in Cartesian coordinates

$$A_s(x,y) + iV(x,y) = \sum_{n=0}^{\infty} \kappa_n z^n = \sum_{n=0}^{\infty} (\lambda_n + i\mu_n)(x+iy)^n.$$

By separating real and imaginary part and taking the negative gradient of the latter one obtains the Cartesian components of the magnetic field. We also introduce the normal and skew multipole coefficients and get:

$$\begin{aligned} B_x(x,y) = -\frac{\partial V}{\partial x} = \; & B_{main}\left[-a_1 + \frac{b_2}{r_0}y - \frac{a_2}{r_0}x - \frac{a_3}{r_0^2}(x^2-y^2) + \frac{b_3}{r_0^2}2xy - \right. \\ & \left. \frac{a_4}{r_0^3}(x^3-3xy^2) + \frac{b_4}{r_0^3}(3x^2y-y^3) \pm \ldots \right]. \end{aligned} \tag{2.8}$$

$$\begin{aligned} B_y(x,y) = -\frac{\partial V}{\partial y} = \; & B_{main}\left[b_1 + \frac{a_2}{r_0}y + \frac{b_2}{r_0}x + \frac{b_3}{r_0^2}(x^2-y^2) + \frac{a_3}{r_0^2}2xy + \right. \\ & \left. \frac{b_4}{r_0^3}(x^3-3xy^2) + \frac{a_4}{r_0^3}(3x^2y-y^3) \pm \ldots \right]. \end{aligned} \tag{2.9}$$

Equations (2.8) and (2.9) can also be displayed in the following way:

$$\begin{aligned} B_y + iB_x = -\frac{\partial}{\partial x}(A_s + iV) &= -\sum_{n=1}^{\infty} n(\lambda_n + i\mu_n)(x+iy)^{n-1} \\ &= B_{main}\sum_{n=1}^{\infty}(b_n - ia_n)\left(\frac{x}{r_0} + i\frac{y}{r_0}\right)^{n-1}. \end{aligned}$$

In the LHC the motion of particles is usually described in Cartesian coordinates. Using the Cartesian expansion, the contribution of each individual multipole to the equation of motion is easily seen. If the field of a magnet only consists of normal coefficients b_1 and b_2 there is no coupling between the planes.

2.1.2 Linear beam dynamics

In linear lattice theory, dipoles and quadrupoles are sufficient to design an ideal accelerator. Magnetic elements of higher order fields are used in particle accelerators for nonlinear corrections. Sextupoles are used to correct chromatic effects (second order aberrations of geometrical errors) of particles with small energy difference, octupoles to correct third order aberration of geometrical errors and so on. Because in general the magnitude of the errors decreases with the order, the need of implementing higher order correction decreases. The nonlinear effect on the beam dynamics is considered as perturbation to the motion calculated in linear magnetic field approximation. Therefore here only linear terms are considered for describing the dynamics of particles.

Strong Focusing

If the current density inside the vacuum chamber is zero there are no field gradients that provide restoring forces in both transverse degrees of freedom at the same time. As discussed further above the quadrupole is a focusing element with this characteristics. The focal length of a thin lens quadrupole is given by Eqs.(2.2)-(2.4), page 8. As in geometric optics the change of the path caused by an element can be described in matrix form. For a thin quadrupole the focusing plane is described as

$$\begin{pmatrix} x \\ x' \end{pmatrix}_{out} = \begin{pmatrix} 1 & 0 \\ -\frac{1}{f} & 1 \end{pmatrix} \begin{pmatrix} x \\ x' \end{pmatrix}_{in}$$

and with opposite sign in the focusing term for the defocusing plane. In this notation the drift space between elements is described by

$$\begin{pmatrix} x \\ x' \end{pmatrix}_{out} = \begin{pmatrix} 1 & L \\ 0 & 1 \end{pmatrix} \begin{pmatrix} x \\ x' \end{pmatrix}_{in}$$

with L as the length of the drift space. In geometric optics a focusing and defocusing lens can be combined with a drift space to a compound system such that the net effect of this system is focusing, namely

$$\begin{pmatrix} 1 & 0 \\ -\frac{1}{f} & 1 \end{pmatrix} \begin{pmatrix} 1 & L \\ 0 & 1 \end{pmatrix} \begin{pmatrix} 1 & 0 \\ \frac{1}{f} & 1 \end{pmatrix} = \begin{pmatrix} 1 + \frac{L}{f} & L \\ -\frac{L}{f^2} & 1 - \frac{L}{f} \end{pmatrix}$$

By interchanging the two lenses this still is valid. Thus, a system of alternating thin lens quadrupoles can be built which is focusing in both planes (L has to be small compared to f.) The condition to have focusing in both planes for this system is that $\frac{f^2}{L} > 0$, which is automatically fulfilled. Based on this principle all alternating gradient accelerators are constructed.

Strong Focusing Stability Criterion

As described above the alternating gradient focusing cell is the main feature of a synchrotron. The beam passes through a number of such cells repeatedly. The alignment of all elements which are passed in one turn is called lattice. To be sure that the beam is stable the lattice has to fulfill a stability criterion. As described above the motion of particles through the elements of a lattice is described by their transfer matrices $M_{QD}, M_{QF}, M_B, \ldots$. The transfer matrix M of the entire lattice, usually called one turn matrix, is constructed by the product:

$$M = \ldots M_{QD} M_D M_{QF}$$

When the beam passes through the lattice repeatedly this matrix has to be multiplied by itself for each turn. For the LHC the revolution frequency is $\approx 10kHz$. For a store time of $\approx 28h$ the beam makes $\approx 10^9$ turns.

Any initial condition can be decomposed into the eigenvectors of the one turn matrix. The propagation over n periods is then represented by the n$^{\text{th}}$ product

$$M^n \begin{pmatrix} x \\ x' \end{pmatrix} = a\lambda_1^n V_1 + b\lambda_2^n V_2$$

where a and b are constants, V_1 and V_2 the eigenvectors and λ_1 and λ_2 the corresponding eigenvalues. For stability λ_1^n and λ_2^n must not grow with n. As M is unimodular the eigenvalues are related to each other as $\lambda_1 = 1/\lambda_2$ and can in general be written as

$$\begin{aligned} \lambda_1 &= e^{i\mu}, \\ \lambda_2 &= e^{-i\mu}. \end{aligned}$$

with μ being a complex number. For stability μ must be real. By solving the eigenvalue equation for M and expressing λ in terms of μ we get

$$e^{i\mu} + e^{-i\mu} = 2\cos\mu = \mathrm{Tr}M$$

and for the stability criterion the condition:

$$-1 \leq \frac{1}{2}\mathrm{Tr}M \leq 1. \tag{2.10}$$

Further below, μ will be identified as the phase advance of the transverse oscillation through the lattice represented by M.

In an alternating gradient system a focusing quadrupole with focusing strength f followed by a drift of length L, a defocusing quadrupole and a second drift is treated as a structure and referred to as FODO cell. The stability criterion for this cell is calculated from its transfer matrix

$$M_{FODO} = \begin{pmatrix} 1 & 0 \\ -\frac{1}{f} & 1 \end{pmatrix} \begin{pmatrix} 1 & L \\ 0 & 1 \end{pmatrix} \begin{pmatrix} 1 & 0 \\ \frac{1}{f} & 1 \end{pmatrix} \begin{pmatrix} 1 & L \\ 0 & 1 \end{pmatrix} = \begin{pmatrix} \frac{f^2-fL-L^2}{f^2} & \frac{L(2f+L)}{f} \\ -\frac{L}{f^2} & \frac{f+L}{f} \end{pmatrix}.$$

With Eq.(2.10) the stability criterion for the (thin-lens) FODO cell becomes

$$-1 \leq 1 - \frac{1}{2}\left(\frac{L}{f}\right)^2 \leq 1$$

or simplified

$$\left|\frac{L}{2f}\right| \leq 1.$$

The distance between quadrupoles should not exceed twice their focal length.

Trajectory Equations

The motion of particles in a storage ring is described by Hill's differential equation

$$\frac{d^2u}{ds^2} + k(s)u = 0,$$

where the variable u represents the transverse coordinate x or y. The function $k(s)$ is periodic with the circumference C of the storage ring ($k(s+C) = k(s)$). In a quadrupole field with gradient g, the field strength $k(s)$ is given by

$$k = \frac{eg}{p} \qquad \text{for the horizontal plane}$$

$$k = -\frac{eg}{p} \qquad \text{for the vertical plane}$$

and in a dipole field of bending radius ρ given by Eq.(2.1), and $k(s)$ by

$$k = \frac{1}{\rho^2} \qquad \text{for the horizontal plane}$$

$$k = 0 \qquad \text{for the vertical plane}$$

The equation of motion differs from a simple harmonic oscillator only in that the "spring constant" k is a function of s. In accelerator physics two different methods are used to solve this equation: one is based on matrices for individual elements, the other on a global solution of the differential equation.

Piecewise Method of Solution

Within a single magnetic element of an accelerator the spring constant K normally is a constant by design as shown in Fig.2.3. Therefore the solution for a harmonic oscillator can be used within each element and be put together at the interfaces. There are three

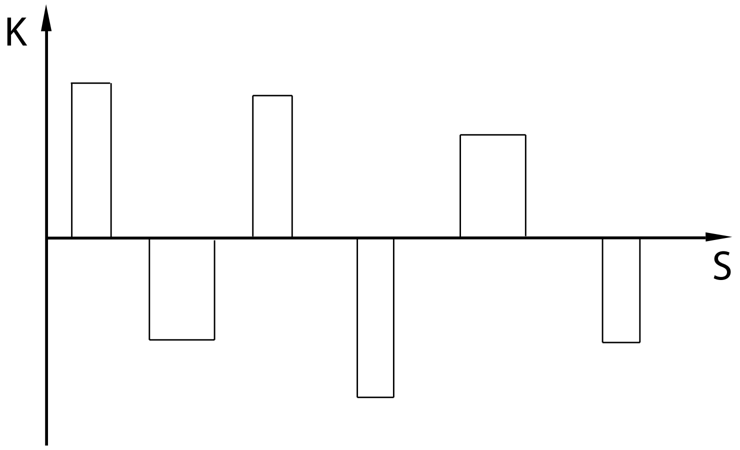

Figure 2.3: The spring constant K varies with the coordinate s but is constant within the individual elements of an accelerator.

cases to be distinguished when describing the particle motion through an element: $k = 0$, $k > 0$ and $k < 0$. The first describes a drift space and the corresponding matrix is the same as discussed before in geometric optics:

$$\begin{pmatrix} x \\ x' \end{pmatrix}_{out} = \begin{pmatrix} 1 & L \\ 0 & 1 \end{pmatrix} \begin{pmatrix} x \\ x' \end{pmatrix}_{in} .$$

For the vertical plane this is valid for a drift or for a dipole with $B_y =$ const. For $k > 0$, the solution of an harmonic oscillator over a distance l in matrix form is:

$$\begin{pmatrix} x \\ x' \end{pmatrix}_{out} = \begin{pmatrix} \cos(\sqrt{k}l) & \frac{1}{\sqrt{k}}\sin(\sqrt{k}l) \\ -\sqrt{k}\sin(\sqrt{k}l) & \cos(\sqrt{k}l) \end{pmatrix} \begin{pmatrix} x \\ x' \end{pmatrix}_{in}$$

and for $k < 0$:

$$\begin{pmatrix} x \\ x' \end{pmatrix}_{out} = \begin{pmatrix} \cosh(\sqrt{|k|}l) & \frac{1}{\sqrt{|k|}}\sinh(\sqrt{|k|}l) \\ -\sqrt{|k|}\sinh(\sqrt{|k|}l) & \cosh(\sqrt{|k|}l) \end{pmatrix} \begin{pmatrix} x \\ x' \end{pmatrix}_{in} .$$

The thin lens solution is derived from these by keeping kl finite as l goes to zero. As described before, the motion of particles through an accelerator is characterized by a matrix which is built by multiplying the matrices of individual quadrupoles and drift spaces in the order in which they are encountered along the particle path.

Closed Form Solution

As noted above, the differential equation describing the particle motion in an accelerator is a special case of Hill's equation,

$$x'' + k(s)x = 0,$$

where the spring constant k is a function of the variable s. For a circular accelerator k is periodic. For this case the general solution of the differential equation is:

$$\begin{aligned} x &= A\omega(s)\cos(\psi(s) + \delta) \\ \psi' &= \frac{1}{\omega(s)}, \end{aligned} \tag{2.11}$$

where A and δ are two constants of integration and $\omega(s)$ is a periodic function with the period of $k(s)$. The phase ψ does not evolve linearly with s. We rewrite Eq.(2.11) as:

$$x = \omega(s)(A_1\cos(\psi) + A_2\sin(\psi)), \tag{2.12}$$

$$x' = \left(A_1\omega' + \frac{A_2 k}{\omega}\right)\cos(\psi) + \left(A_2\omega' - \frac{A_1 k}{\omega}\right)\sin(\psi) \tag{2.13}$$

in order to describe the 1-turn transfer matrix in terms of parameters introduced in this section. Namely, with x_0 and x_0' as initial conditions we can note:

$$\begin{pmatrix} x \\ x' \end{pmatrix}_{s_0+C} = \begin{pmatrix} \cos(\Delta\psi_C) - \frac{\omega\omega'}{k}\sin(\Delta\psi_C) & \frac{\omega^2}{k}\sin(\Delta\psi_C) \\ -\frac{1+(\frac{\omega\omega'}{k})^2}{\frac{\omega^2}{k}}\sin(\Delta\psi_C) & \cos(\Delta\psi_C) + \frac{\omega\omega'}{k}\sin(\Delta\psi_C) \end{pmatrix} \begin{pmatrix} x \\ x' \end{pmatrix}_{s_0} . \tag{2.14}$$

The phase advance of the particle oscillation through one period is given by:

$$\psi(s_0 \to s_0 + C) \equiv \Delta\psi_C = \int_{s_0}^{s_0+C} \frac{k\,ds}{\omega^2(s)}.$$

An important point to mention is, that because of the periodicity of $\omega(s)$, this integral is independent of s_0.

Courant Snyder Parameters

The form of the matrix in Eq.(2.14) is very complicated. To simplify the appearance, in [1] the following new variables are introduced:

$$\beta(s) \equiv \frac{\omega^2(s)}{k}, \tag{2.15}$$

$$\alpha(s) \equiv -\frac{1}{2}\frac{d\beta(s)}{ds} = -\frac{1}{2}\frac{d}{ds}\left(\frac{\omega^2(s)}{k}\right), \tag{2.16}$$

$$\gamma(s) \equiv \frac{1+\alpha^2(s)}{\beta(s)}. \tag{2.17}$$

With these new parameters Eq.(2.14) can be rewritten as:

$$\begin{pmatrix} x \\ x' \end{pmatrix}_{s_0+C} = \begin{pmatrix} \cos(\Delta\psi_C) + \alpha\sin(\Delta\psi_C) & \beta\sin(\Delta\psi_C) \\ -\gamma\sin(\Delta\psi_C) & \cos(\Delta\psi_C) - \alpha\sin(\Delta\psi_C) \end{pmatrix} \begin{pmatrix} x \\ x' \end{pmatrix}_{s_0}$$

with the phase advance:

$$\Delta\psi_C = \int_{s_0}^{s_0+C} \frac{ds}{\beta(s)}.$$

If C represents one turn in a circular machine, the number of oscillations per turn,

$$Q = \frac{1}{2\pi}\oint \frac{ds}{\beta(s)}$$

is called the (betatron) tune of the accelerator. In the literature α, β and γ are referred to as Courant Snyder or Twiss parameters and β as amplitude or beta function. The variables do not only simplify the form of the matrix but also allow rewriting the solution of Hill's equation as

$$x(s) = A\sqrt{\beta(s)}\cos(\psi(s) + \delta). \tag{2.18}$$

Application of Closed form and Piecewise Method of Solution

The two representations of the transfer matrix can be used to calculate the Courant Snyder parameters around an accelerator. The one-turn matrix of the piecewise solution method contains some numerical values a, b, c and d:

$$M_{pw} = \begin{pmatrix} a & b \\ c & d \end{pmatrix}.$$

But as the two different matrices describe the same particle motion they must be equal:

$$\begin{pmatrix} a & b \\ c & d \end{pmatrix} = \begin{pmatrix} \cos(\Delta\psi_C) + \alpha\sin(\Delta\psi_C) & \beta\sin(\Delta\psi_C) \\ -\gamma\sin(\Delta\psi_C) & \cos(\Delta\psi_C) - \alpha\sin(\Delta\psi_C) \end{pmatrix}.$$

Then from the stability criterion we get:

$$\cos(\Delta\psi_C) = \frac{1}{2}(a+d) = \frac{1}{2}\mathrm{Tr}M.$$

This is the point where we see, that the μ in the stability criterion is the phase advance of the amplitude function. Having calculated $\cos(\Delta\psi_C)$ we can determine $\sin(\Delta\psi_C)$ and with this we get for the Courant Snyder parameters:

$$\begin{aligned} \beta &= \frac{b}{\sin(\Delta\psi_C)}, \\ \alpha &= \frac{a-d}{\sin(\Delta\psi_C)}. \end{aligned}$$

The lattice functions are thus determined in one point of the ring. We can now calculate them for every point in the ring. The particle motion from one point to another is described by:

$$\begin{pmatrix} x \\ x' \end{pmatrix}_{s_2} = M(s_1 \to s_2) \begin{pmatrix} x \\ x' \end{pmatrix}_{s_1}.$$

and the transfer matrix $M(s_1 \to s_2)$ can be expressed in terms of the amplitude functions through the use of Eq.(2.12) and Eq.(2.13). Namely, when x and x' are the initial conditions, A_1 and A_2 are given and can be inserted into Eq.(2.12) and Eq.(2.13). We can then rewrite the matrix $M(s_1 \to s_2)$ in terms of the amplitude functions. It is given by

$$M(s_1 \to s_2) = \begin{pmatrix} \left(\frac{\beta_2}{\beta_1}\right)^{\frac{1}{2}} (\cos(\Delta\psi) + \alpha_1 \sin(\Delta\psi)) & (\beta_1\beta_2)^{\frac{1}{2}} \sin(\Delta\psi) \\ -\frac{1+\alpha_1\alpha_2}{(\beta_1\beta_2)^{\frac{1}{2}}} \sin(\Delta\psi) + \frac{\alpha_1-\alpha_2}{(\beta_1\beta_2)^{\frac{1}{2}}} \cos(\Delta\psi) & \left(\frac{\beta_1}{\beta_2}\right)^{\frac{1}{2}} (\cos(\Delta\psi) - \alpha_2 \sin(\Delta\psi)) \end{pmatrix}. \tag{2.19}$$

There is another possibility to calculate the lattice functions around the ring. To see this, we look at Eq.(2.18). It can be shown that A is a constant of motion in an unperturbed linear machine (A can be interpreted as the area of an ellipse in the phase space x, x', divided by π, and is called emittance.). This means it is constant at any point of the ring. Using the relation

$$A^2 = \gamma y^2 + 2\alpha y y' + \beta y'^2$$

we can calculate a 3×3 matrix with which we can calculate all lattice functions in any point of the ring, once they are determined in one point,

$$\begin{pmatrix} \beta \\ \alpha \\ \gamma \end{pmatrix}_{out} = \begin{pmatrix} a^2 & -2ab & b^2 \\ -ac & (bc-ad) & -bd \\ c^2 & -2cd & d^2 \end{pmatrix} \begin{pmatrix} \beta \\ \alpha \\ \gamma \end{pmatrix}_{in}, \tag{2.20}$$

where a, b, c and d are the elements of the transfer matrix between two points calculated by the piecewise method of solution.

Momentum Dispersion

Up to now we only considered particles with the same (design) momentum p_0. Such a particle either travels on the closed orbit, if the initial conditions are $x_0 = 0$ and $x'_0 = 0$, or oscillates about it when either of them are nonzero. If a particle's momentum deviates from the design momentum by $\Delta p = p - p_0$ then even with the initial conditions $x_0 = 0$ and $x'_0 = 0$ it will have a closed orbit different from the design particle, if Δp is not too big. In case of too big momentum deviation there will be no stable solution for this particle and it will be lost. The radial distance $x(s, \frac{\Delta p}{p_0})$ from the design orbit is proportional to $\frac{\Delta p}{p_0}$. The closed dispersion orbit $D(s)$ is defined by:

$$x\left(s, \frac{\Delta p}{p_0}\right) = D(s)\frac{\Delta p}{p_0}.$$

In a strong focusing lattice the focusing quadrupoles bend the trajectory towards the central orbit while the defocusing ones bend it away. The closed dispersion orbit has its maximum deviation from the design orbit therefore in the center of the focusing and its minimum in the center of the defocusing quadrupole as shown in Fig.2.4.

For a particle with $\Delta p = p - p_0 \neq 0$, Hill's equation is non-homogeneous

$$x'' + k(s)x = \frac{1}{\rho(s)}\frac{\Delta p}{p_0}, \tag{2.21}$$

where $\rho(s)$ denotes the s dependent bending radius, and the total deviation of the particle from the reference orbit can be written as:

$$\begin{aligned} x(s) &= x_D(s) + x_\beta(s), \\ x_D(s) &= D(s)\frac{\Delta p}{p_0}. \end{aligned}$$

with $x_D(s)$ as the closed orbit for off-momentum particles and x_β as the betatron oscillation around this closed orbit. $D(s)$ is the periodic dispersion, satisfying the differential equation

$$D'' + k(s)D = \frac{1}{\rho(s)},$$

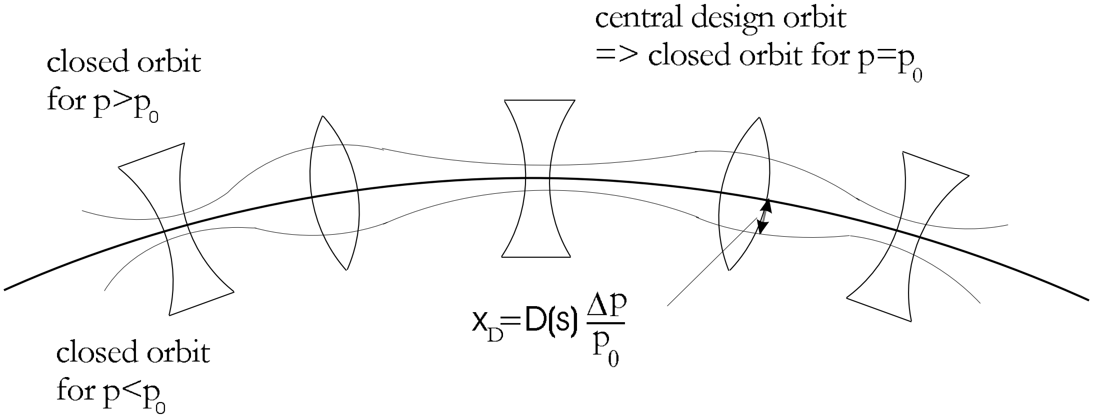

Figure 2.4: Closed orbit for particles with momentum $p \neq p_0$ in a strong focusing circular accelerator.

and is often denoted as $\eta(s)$. This differential equation can be solved for the periodic case with the solution:

$$D(s) \equiv \eta(s) = \frac{\sqrt{\beta(s)}}{2\sin(\pi\mathrm{Q})} \oint \frac{\sqrt{\beta(t)}}{\rho(t)} \cos(|\varphi(s) - \varphi(t)| - \pi\mathrm{Q}) dt.$$

An important fact concerning stability of motion is evident in this result: A finite dispersion orbit exists only if the number of betatron oscillations per revolution Q is different from an integer. If not, the numerator of Eq.(2.22) would become zero and the solution be unstable. The same treatment as for calculating the lattice functions can be applied here. One calculates η and η' in one point in the ring and uses the transfer matrix to calculate the solution at any other point.

A consequence of $\frac{\Delta p}{p_0} > 0$ for a particle is that usually, its path length over one revolution is longer than the reference particle's as shown in Fig.2.5. This behavior is

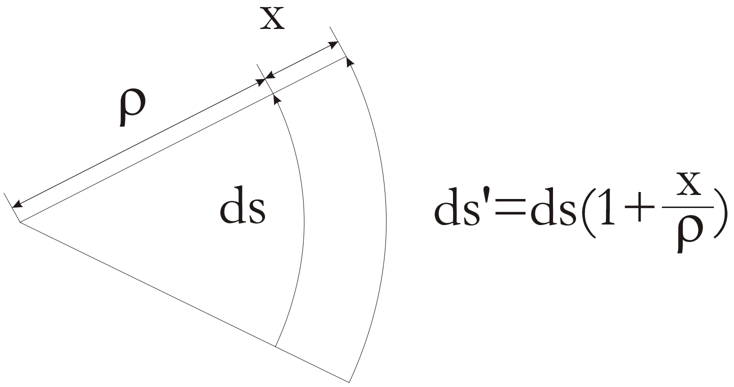

Figure 2.5: Comparison of reference orbit path length ds and particle path length ds'.

expressed by the momentum compaction factor α_C. It relates the relative change in orbit length to the relative momentum deviation:

$$\frac{\Delta C}{C} = \alpha_C \frac{\Delta p}{p_0}$$

and can be computed from the dispersion as

$$\alpha_C = \frac{1}{C}\oint \frac{D(s)}{\rho(s)}ds. \tag{2.22}$$

Field errors

In the presence of dipole field errors there is an additional s dependent Lorentz force which results in a driving term in the equation of motion. Q must again be non integer to have a stable solution. The equation is of the same type as Eq.(2.21). A source of this type of error is the displacement of quadrupoles from the design orbit.

An important optics error is generated by quadrupole field errors. Let $\Delta K(s)$ be a quadrupole gradient error in the ring. It can be shown, that this error leads to a shift in the tune value:

$$\Delta Q = \frac{1}{4\pi}\oint \beta(s)\Delta k(s)ds.$$

This shift is proportional to the magnitude of the gradient error as well as the β-function at the location of the error. Also the β-function is changed by this error. This is often referred as β-beating and described by:

$$\Delta\beta = \frac{\beta(s)}{2\sin(2\pi Q)}\oint \beta(t)\Delta k(t)\cos(2|\varphi(t)-\varphi(s)|-2\pi Q)ds \tag{2.23}$$

Equation(2.23) reveals two important issues. First, gradient errors in the interaction-region (IR) quadrupoles near the collision point are the most dangerous ones because there the β-function has its maximum value. Second, the β-function has a stable solution if Q is different from half integer numbers, else the denominator becomes zero in Eq.(2.23).

This last observation can be extended to higher order multipoles. Sextupoles drive third order resonances, so that tunes at 3rd integers must be avoided and so on. Additionally, in real machines there is coupling between the motion in the two transverse planes. This leads to the following general condition for the unstable tunes:

$$mQ_x + nQ_y = l \qquad m,n,l = 1,2,\ldots \tag{2.24}$$

which creates a resonance diagram as shown in Fig.2.6, page 22. The values of $|m|+|n|$ is referred to as resonance order. The working point (Q_x, Q_y) has to be chosen in a reasonable distance from the low-order resonance lines.

Chromaticity

Particles with $\Delta p \neq 0$ are focused differently in quadrupoles because k is normalized by the momentum. This focusing error

$$\Delta k = \frac{dk}{dp}\Delta p = -\frac{eg}{p_0}\cdot\frac{\Delta p}{p_0} = -k_0\frac{\Delta p}{p_0}$$

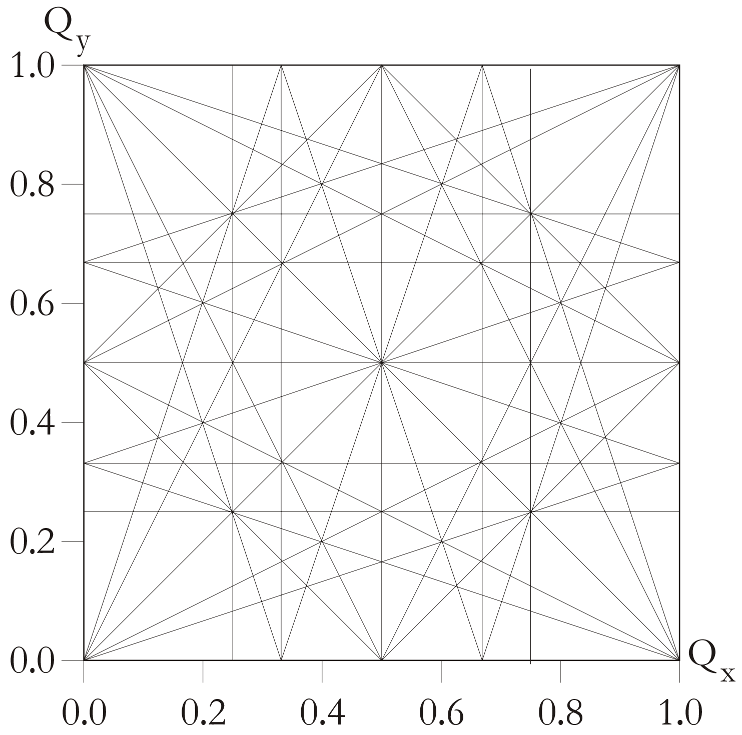

Figure 2.6: Resonance diagram up to fourth order.

results in a tune shift:

$$\Delta Q = \xi \frac{\Delta p}{p_0} \tag{2.25}$$

$$\xi = -\frac{1}{4\pi} \oint \beta(s) k(s) ds \tag{2.26}$$

where ξ is called chromaticity. The major contribution to chromaticity comes from quadrupoles with large k values and where the β-function is large. In large accelerators like the LHC this "natural" chromaticity (from the linear lattice) is large and with the given momentum spread of the beam some part of the beam particles would hit dangerous resonance lines. For this reason it has to be compensated. This is done with sextupoles which are placed in regions of high dispersion. Chromatic correction is necessary (also for the suppression of collective instabilities) but it introduces coupling in the machine, which can be minimized by using a large number of weakly excited sextupole magnets distributed around the ring.

2.2 Luminosity and Beam-Beam Interactions

To optimize the performance of a collider means to optimize the luminosity. A look at Eq.(2.29) shows that this can be done by increasing the number of particles, increasing the collision frequency and decreasing the beam cross sectional area. All these possibilities are limited by different effects. Increasing the bunch intensity will eventually lead to single bunch instabilities and beam beam limitations, multi bunch instabilities are increased by collision frequency boosts, and small beam size increases demands on beam source and focusing system, and it, as well, is limited by beam-beam effects.

2.2.1 Luminosity

In modern high energy accelerators time varying electric fields are used to accelerate. For this reason, non continuous beams are created. The particles are distributed over a sequence of bunches (pulsed particle beams). These bunched beams are brought into collision. If the number of bunches is equal for both beams two bunches each will collide in dedicated places (interaction points, short IPs). Assuming that these two bunches have the same cross section area A and the same number of particles per bunch N, the interaction rate R is related to the interaction cross section σ_{int} as follows

$$R = f\frac{N^2}{A}\sigma_{int} \tag{2.27}$$

where f is the frequency of bunch collisions. The factors in the relation above represent a figure of merit for colliders and are defining the luminosity $\mathcal{L}$.

$$\mathcal{L} = f\frac{N^2}{A}. \qquad [\mathrm{cm}^{-2}\mathrm{s}^{-1}] \tag{2.28}$$

For the calculation above, the particle density was chosen constant over a cylinder as shown in Fig. 2.7. For proton proton colliders as the LHC a truncated round Gaussian distribution in both transverse planes, perpendicular to the direction of motion, is a good assumption. Taking this into account and considering that only the core of the beam contributes to the luminosity it becomes

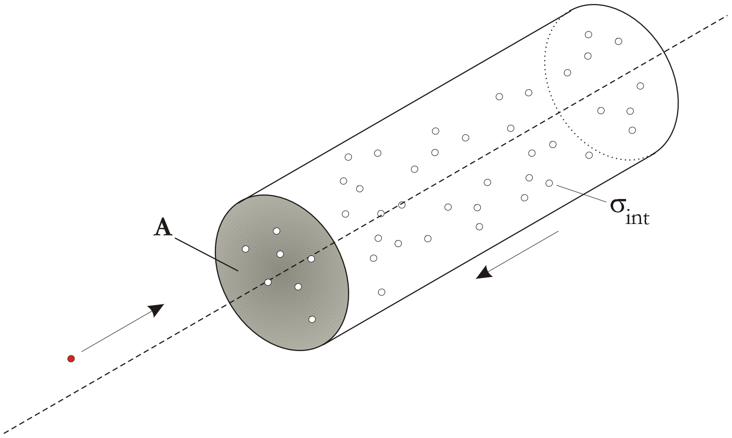

Figure 2.7: Collision of a single test particle from one beam with a particle bunch in the other beam with a constant density and cylinder shape.

$$\mathcal{L} = f\frac{N^2}{4\pi\sigma^2} \tag{2.29}$$

where σ is the RMS beam distribution for the round beam. If the particle number varies for the different bunches, the beams are not round (the dimensions of the transverse axes differ) and are different, the luminosity is calculated by

$$\begin{aligned} \mathfrak{L} &= \frac{N_1 N_2 f_{rev} N_B}{2\pi\sqrt{\sigma_{1x}^2+\sigma_{2x}^2}\sqrt{\sigma_{1y}^2+\sigma_{2y}^2}} && (2.30) \\ f &= f_{rev}\cdot N_B && (2.31) \end{aligned}$$

N_1 and N_2 are the number of particles in the two colliding bunches, N_B the number of bunches per beam and σ_{1x} and σ_{2x} the horizontal beam size for beam 1 and 2 respectively σ_{1y} and σ_{2y} the corresponding vertical beam size, and f_{rev} the revolution frequency.

The discussion up to now treated ideal head-on collisions. For the LHC at least two further implications have to be taken into account. First, the beams collide with a crossing angle. This scheme was chosen because of the number of bunches (2808) and the long common beam path before and after the IPs. Without a crossing angle bunches would collide not only at the IP but also before and after. To avoid this a crossing angle φ is introduced. This yields the factor

$$S = \frac{1}{\sqrt{1+(\frac{\sigma_s}{\sigma_x}\tan\frac{\varphi}{2})^2}} \tag{2.32}$$

in the luminosity equation where σ_s is the longitudinal rms bunch length and φ the (here horizontal) crossing angle. This can be interpreted as a correction of the effective beam size. Due to the crossing angle the "effective beam size" in the crossing plane seen by the opposite bunches is the nominal enlarged by $1/S$.

The second correction comes from an offset. Due to different effects in particular "long range" beam-beam collisions away from the IP the centers of all bunches are distributed around the average orbit. As this is a random distribution it cannot be corrected, only minimized. Because of this most of the bunches collide with a small offset. The correction factor for this is

$$W = e^{-\frac{1}{4\sigma_x^2}(d_2-d_1)^2} \tag{2.33}$$

with d_1 and d_2 being the offset of bunches in the two beams from the orbit. In case both offset and crossing angle are present together, these factors overestimate the luminosity reduction. This is being corrected by defining

$$A = \frac{\sin^2\frac{\varphi}{2}}{\sigma_x^2} + \frac{\cos^2\frac{\varphi}{2}}{\sigma_s^2}, B = \frac{(d_2-d_1)\sin\frac{\varphi}{2}}{2\sigma_x^2} \tag{2.34}$$

and the corrected luminosity can be rewritten as ([9], page 247ff)

$$\mathfrak{L} = \frac{N_1 N_2 f_{rev} N_B}{2\pi\sqrt{\sigma_{1x}^2+\sigma_{2x}^2}\sqrt{\sigma_{1y}^2+\sigma_{2y}^2}} \cdot W \cdot e^{\frac{B^2}{A}} \cdot S. \tag{2.35}$$

This derivation treats the case of crossing angle and beam offset in the horizontal plane. The same factors can be introduced for the vertical plane. In the LHC at the present design there are only crossing angles in one plane at IP1 (vertical) and IP5 (horizontal). With the design values of 2808 bunches per beam, $1.15\,10^{11}$ particles per bunch, $16.7\,\mu$m rms IP beam size for both transverse planes and both beams, 7.7 cm rms bunch length in the longitudinal plane, and 11.245 kHz revolution frequency, the head-on luminosity is $1.2\,10^{34}$cm^{-2}s^{-1}. By introducing a crossing angle of $300\,\mu$rad the reduction factor S is 0.82 and the luminosity $0.984\,10^{34}$cm^{-2}s^{-1}. A detailed derivation can be found in [12].

2.2.2 Beam-beam effects

A particle beam has an electromagnetic potential which acts on other beams and, at low energy, on itself (space charge). The beam-beam force is not linear and is usually limiting the performance of a collider. This is due to the fact that the forces are proportional to the density of the beams, which are needed for high luminosity.

The self force acting on the beam, the space charge, decreases as $1\gamma^2$. Therefore this force is reduced during acceleration and can be neglected in the LHC.

The beam-beam force does not decrease, however can be calculated from the charge distribution. Analytically this is only possible for special distributions. In most of the cases in real colliders numerical methods have to be used to solve the integrals to obtain the potentials. The force acting on the particles is the Lorentz force $\vec{F} = q(\vec{E}+\vec{v}\times\vec{B})$. By taking the gradient of the potential the electrical field can be calculated and the magnetic field component of the Lorenz force follows from $B_{x,y} = -\frac{\beta r}{c}E_{y,x}$. For a round Gaussian beam density distribution of $\rho(x,y) = \rho(x)\cdot\rho(y)$ in the transverse planes an analytical solution can be calculated as

$$F_r(r) = -\frac{Ne^2(1+\beta^2)}{2\pi\epsilon_0}\frac{1}{r}\left[1-e^{\left(-\frac{r^2}{2\sigma^2}\right)}\right].. \tag{2.36}$$

where here β is the Lorentz factor. In Fig.2.8, page 26, the force is plotted as a function of the amplitude. At small amplitudes $(\sigma\lessapprox 1)$ this force is linear and results in a tune change as for a quadrupole, but it is defocusing in both planes (for proton-proton collisions as in the LHC). At higher amplitudes this force is non linear and therefore the tune change becomes a function of the amplitude. From Eq.(2.36) one can see that the beam-beam force includes an infinite number of higher multipoles. This is the reason that it can drive a large number of resonances.

For small amplitudes the beam-beam force acts as a quadrupole. This linear "kick", which is a function of the beam size, can be used to calculate the resulting tune shift. (Opposite to a real quadrupole the beam-beam force is radially symmetric, in case of a radially symmetric charge distribution.) In the linear region the radial kick $\Delta r'$ can be related to a focal length which itself relates to a tune change. The linear beam-beam parameter ξ characterizes this linear force:

$$\xi = \frac{Nr_0\beta_{x,y}}{2\pi\gamma\sigma_{x,y}(\sigma_x+\sigma_y)} \tag{2.37}$$

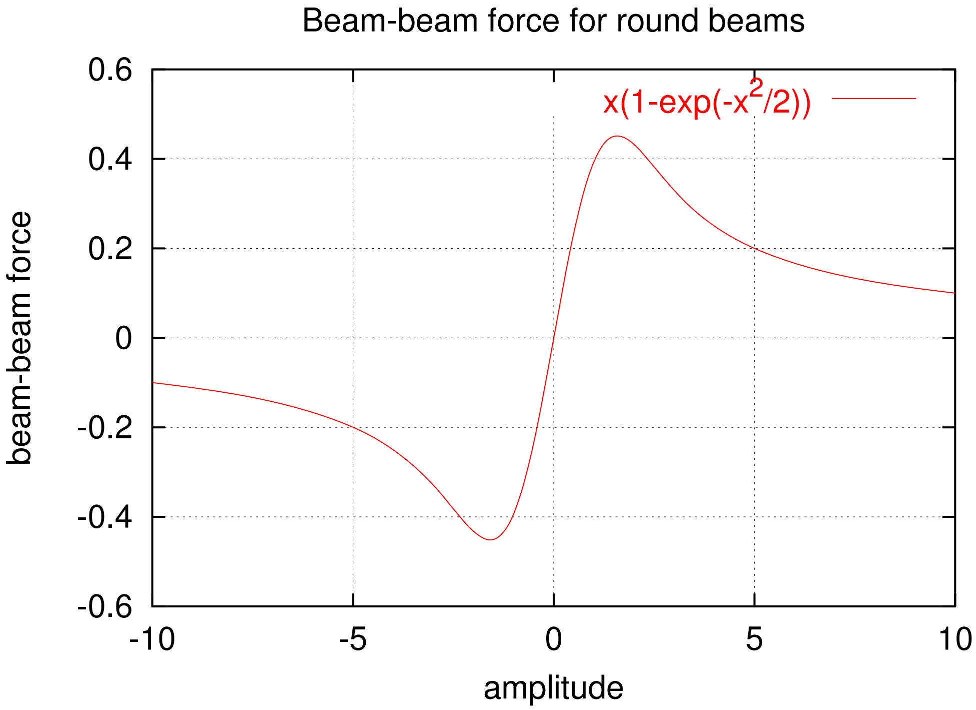

Figure 2.8: Beam-beam force for round beams with arbitrary units for force and units of rms beam size for the amplitude.

with N as the bunch intensity, r_0 the classic particle radius, $\beta_{x,y}$ the beta function at the IP, the relativistic γ and $\sigma_{x,y}$ the rms beam size. If ξ is small and the tune is not too close to linear resonances ξ is equivalent to the linear tune shift ΔQ. For the LHC $\Delta Q \approx \xi = 0.0034$. With $kl = (4\pi\Delta Q)/\beta^\star$ the linear beam-beam force acts as a quadrupole of the integrated strength $kl = 0.086$. The nonlinear beam-beam force results in an amplitude dependent tune shift with the following characteristic: The particles with small amplitudes have the largest tune shift; at very large amplitudes the tune shift eventually becomes zero. To show this behavior the amplitude is mapped into the tune space (Q_x, Q_y), which is called a "tune footprint" as shown in Fig.2.9, page 27. In the case of a single head-on collision the beam-beam parameter ξ is a measure for the tune spread in the beam. The occupied tune space has to fit into the tune diagram such that it does not overlap with dangerous resonances to avoid unstable behavior (not a collective instability), which could result in reduction of the dynamic aperture, bad beam life time, distortion of the beam optics or beam blow up.

In the LHC the two beams travel through the same beam pipe before and after the interaction point (IP), from the combiner to the separation. Because of the short bunch spacing (25 ns) the beams would have 30 parasitic collisions in this region each of which would contribute about the same tune spread as the collision at the main IP. To avoid this the two beams are brought into collision with a crossing angle. The bunches therefore do not collide head-on, but still pass at a certain distance where their long range beam-beam forces act on each other as depicted in Fig.2.10, page 27.

Due to this separation, the effect of a single long range collision is much smaller

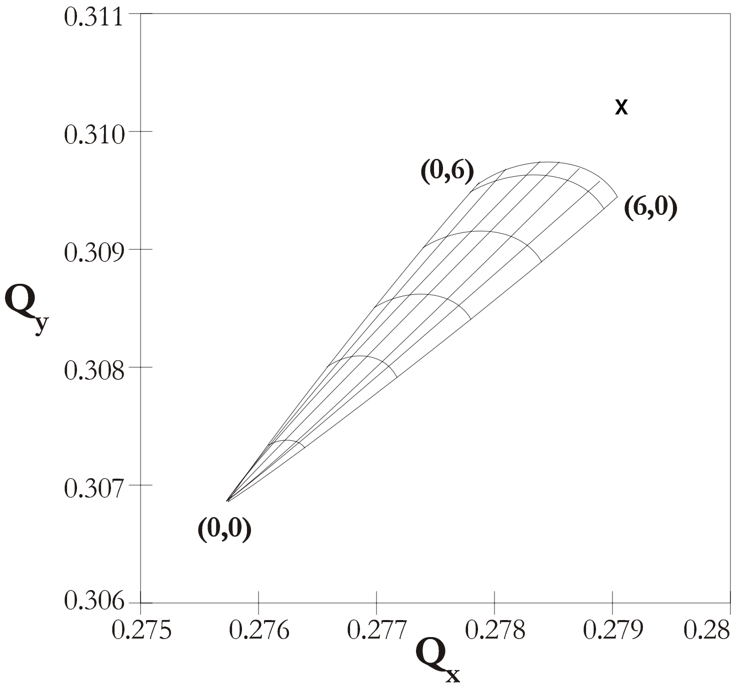

Figure 2.9: Two dimensional tune foot print.

than the head-on collision but the big number (30 per IP with 4 IPs gives 120 long range collisions) makes this a noticeable effect. Mostly particles at large amplitude are effected. The long range force breaks the symmetry between the planes, it introduces a tune shift in the separating plane with opposite sign to the head on tune shift and it changes the closed orbit.

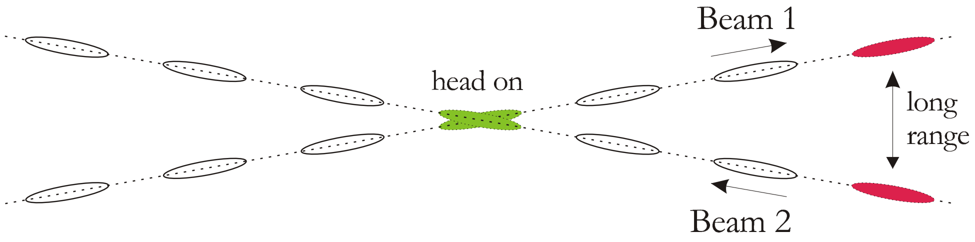

Figure 2.10: Illustration of head-on and long-range interactions in a LHC interaction point in the presence of a crossing angle.

Until now only effects of the beam-beam force on single particle have been discussed. There are also coherent effects. Of these the so-called “dipole oscillation” should be mentioned. It is the result from the coherent kick of the long range force between the two beams. The bunches as a whole can start to oscillate relative to each other. There are two basic modes: The 0-mode where the bunches oscillate in phase and the π-mode where the phase difference is $180°$. Any other coherent bunch-centroid oscillation can be described as a combination of these. The second mode results in a tune shift ΔQ_{coh} which is proportional to ξ [14].

2.3 Simulation Programs

As described earlier the size and complexity of the design of a storage ring does not allow a fully analytical study of the effects of errors. There exists a great variety of codes which do this job. At CERN the principal numerical tool to design the accelerator optics is MAD. As the size and complexity of accelerators grow with time this program has also evolved to comply with increasing demand. Aside of designing, there are other issues to be investigated during the planing of an accelerator. The influence of the long range collisions, as mentioned earlier, is an important issue for the LHC. To be able to estimate their effect the TRAIN program was adapted to be able to deal with the great number of bunches in the LHC. The main function of the TRAIN code is to calculate the new orbit and tunes of all 2800 bunches in either beam in the presence of all long range beam beam kicks.

2.3.1 MAD Methodical Accelerator Design

The program MAD (**M**ethodical **A**ccelerator **D**esign) was first developed at CERN in the early-1980's. Since then it has become the standard optics design tool for designing storage rings and transport lines. The current version is MAD-X. A detailed description of the code and the physical methods implemented can be found in [16] - [17]. A user's reference manual [15] can be found at [18].

The main application is to design a linear optics lattice. This is done based on the theory described earlier. In practice the linear magnetic elements are defined and placed to build the lattice according to certain design rules for the arc and the insertions. A problem is that magnet strength values have to be given to these elements. These values have to create a stable solution in the Twiss matrix. The code is not capable to find the stable solution itself, but this requires some prior analysis or a try-and-error approach by the user. The stable solution then is the starting point from which an optimization can be done by the code.

Matching Algorithm

The MAD code provides three different algorithms for matching. They are all based on the least square minimization algorithm:

- **LMDIF** minimizes the sum of squares of the constraint functions using their numerical derivatives (fast gradient minimization).
- **MIGRAD** minimizes the penalty function using the numerical derivatives of the sum of squares.
- **SIMPLEX** minimizes the penalty function by the simplex method.

A test case was used to compare the speed and solution of the three methods. As a result, LMDIF was chosen as standard method. It proved to be sufficient for the simulations performed in this thesis. A description of the three methods can be found in [28] and [30]. The LMDIF method is the fastest, but it can have problems finding a solution. It uses the Jacobian matrix to determine the the direction of the steepest descent.

2.3.2 TRAIN

The TRAIN [31] code was originally written to simulate the kicks originating from the parasitic beam beam collisions in LEP. The number of bunches in LEP was with a maximum of 16 very small compared to about 3000 in LHC. The parasitic kicks result in a change of the closed orbit of the bunches in both beams. As the kick is a function of the distance of the two bunches, the kick varies with the change of the closed orbit of both beams and the solution has to be calculated in a self consistent way. With this new self-consistent closed orbit many side effects of bunch trains are calculated: vertical offsets and separation, the change of slopes and crossing angles, the dispersion, tunes and chromaticities and the change of luminosity. There are two separate groups of input files. One is generated with MAD and it contains the one-turn linear optics information together with special elements which simulate the long-range beam-beam kick. The other file contains information on the bunch filling scheme and specifies possible variations between the bunches in intensity, distribution et cetera. A detailed study of the self-consistent orbit changes in LHC was performed by H. Grote and W. Herr [32].

Chapter 3

Advanced Linear Optics Theory

In the previous chapter the basic concept of linear lattice optics was briefly introduced to build a conceptual basis. Here the applied methods and advanced theories are described which resulted in a novel approach for the calculations and measurements. First the established methods will be discussed for the matching of $\beta^\star$ tuning knobs with MAD followed by a new approach. With a short discussion on the influence of hysteresis effects on the performance of the tuning knobs at the end.

3.1 Adjusting the IP β-function

The function of a low-β insertion is to deliver the maximum possible luminosity $\mathcal{L}$ (see equation 2.29, page 23) at the interaction point. This is achieved by making the beam cross section as small as possible. The beam cross section σ is a function of β-function, emittance ϵ, dispersion D and energy spread δ as follows:

$$\sigma = \sqrt{\beta\epsilon + (D\delta)^2} \tag{3.1}$$

By changing the β-function at the IP the luminosity can be optimized. This can be either done by rematching the insertion or by using so-called tuning knobs. The first method has the advantage of installing an exact solution; the optimization of the optics introduces no perturbation if the optics model agrees with the actual optics. The problem is, that therefore one needs a model corresponding to the exact condition of the machine. This information is not available or obtainable only with a great effort. The second approach amounts to a perturbation of an existing solution. The magnitude of the perturbation of the different optics functions at the IP and around the machine is a characteristic of the knob and the lattice. It is a priori not possible to say if a solution for a knob exists.

The second term in Eq.(3.1) can be seen as a parasitic contribution for the purpose of optimization. The energy spread and dispersion are effects which should be minimized for the following reasons. In the normal case this term is small enough that it gives no noticeable contribution to the beam cross section. When calculating the knob one has to take care that the perturbation of the dispersion is small enough that for a given energy spread δ, β-function and emittance ϵ the second term stays small as compared to the first one. Fig.3.1 shows the beam cross section as a function of the dispersion with the nominal values for energy spread δ, β-function and emittance ϵ in the LHC. The cross section stays constant up to a certain value beyond which it starts to blow up. This value is about three centimeters for the IP dispersion at IP1 and IP5 at collision. Beside the dispersion the α-function has to be minimized at the IP. It is related to the β-function as follows

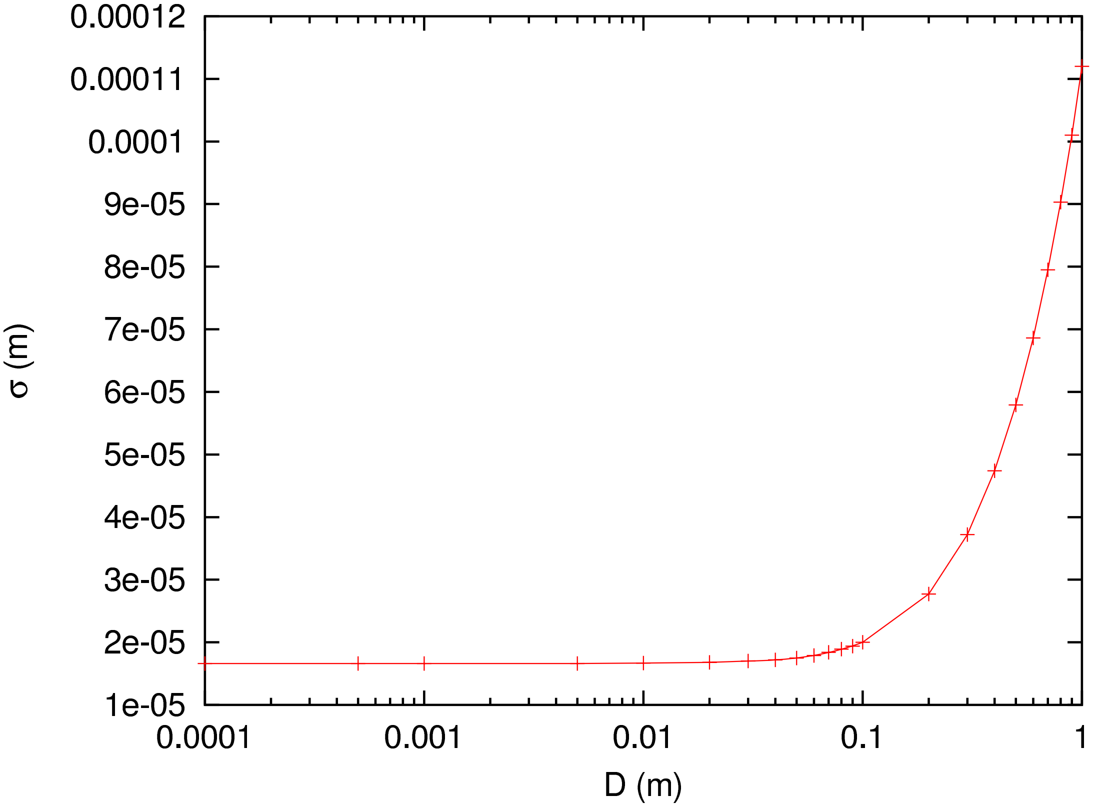

Figure 3.1: Beam size as a function of the IP dispersion with the nominal values for energy spread $\delta = 1.1 \cdot 10^{-4}$, β-function $\beta = 0.5m$ and rms emittance $\epsilon \approx 5.0 \cdot 10^{-10}m$ for LHC at IP1 and IP5 in collision.

$$\alpha(s) = -\frac{1}{2}\frac{d\beta(s)}{ds} \tag{3.2}$$

Namely, the α-function is related to the slope of the β-function. As β is a local minimum at the IP the slope, and therefore α, have to be zero. A change of the α-function can be interpreted as a waist shift of the beam, which increases the cross section at the IP and therefore has to be avoided. Additionally the opposite plane should also not be effected by the β tuning.

These considerations hold locally for one IP. In the LHC, there are four independent IPs. The changes to one of them have to be confined to a local area. Otherwise they would change the conditions elsewhere in the ring. This local area is usually the so called interaction region (IR) which hosts the dispersion suppressor, correction quadrupoles, separation and combiner dipoles and the triplet quadrupoles. The associated magnets are available to change the β-function at the IP. Fig.3.2 depicts the principle how the changes to the lattice functions can be confined to an IP region. Ideally the changes introduced in the IR should be localized in a defined region. The β

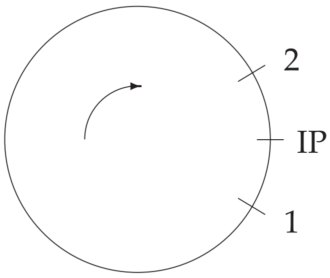

$$M_{12} = M_{IP-2} \cdot M_{1-IP}$$

$$\left.\begin{array}{rcl}\beta_x^\star &=& \beta_x^\star + \Delta\beta_x^\star \\ \beta_y^\star &=& \text{const}\end{array}\right\}\text{at IP}$$

or

$$\left.\begin{array}{rcl}\beta_x^\star &=& \text{const} \\ \beta_y^\star &=& \beta_y^\star + \Delta\beta_y^\star\end{array}\right\}\text{at IP}$$

$$\left.\begin{array}{c}\beta \\ D\end{array}\right\} = \text{const at 1,2}$$

$$\left.\begin{array}{c}\alpha \\ D\end{array}\right\} = \text{const at IP}$$

Figure 3.2: Principle of confining a change of the β-function to a distinct region.

and dispersion-function describe a close curve around the ring. To restrict the change within the two points (1) and (2) the dispersion has to be kept constant at these two points. To confine the changes created within these two points, β-function and its derivative, the α-function, have to be kept constant as well as the boundaries. In terms of the matrix formalism, the matrix describing the change between point (1) and (IP) multiplied with the one describing the changes between the points (IP) and (2) has to give the unity matrix. This is shown in Fig.3.2.

The variation of the tune as a global characteristic of the lattice also has to be minimized. As the tune foot print is tightly fit into the resonance diagram, only very small shifts can be accepted before encountering harmful resonances. Fortunately there are tune correction schemes available in colliders. For the LHC a variation of the main arc quadrupoles creates a tune shift. One problem is, that this also creates a β-beat wave and a second one is that there is only a limited change of quadrupole strength available. Therefore, only a small correction is possible. For the LHC this is approximately $\Delta Q_{x,y} \approx 0.1$.

There are several further issues which have to be considered. A partial list reflects some of these:

- chromaticity
- aperture of the low-β quadrupoles
- strength of the tuning quadrupoles
- tolerances (e.g. power supplies, magnet positions)
- head-on and long range beam-beam interaction

For the correction of the β-function in LEP at the IP the situation was different from the one in LHC. Table 3.1 outlines the major differences for the two colliders. The two most obvious differences are the beam profile (aspect ratio) and the type of particles which are collided.

Table 3.1: Summary of the major differences between LEP and LHC which are important for the considerations in this thesis.

	LEP	LHC
beam profile	flat	round
⇒ lattice	symmetric	asymmetric
⇒ correction	1 plane	2 planes
particles	e^+e^-	p p
⇒ beam pipe	common	mostly separated
⇒ ⇒ errors	equal	unequal

The transverse beam profile in LEP was flat and is round in the LHC. As a result, the design of the lattice functions at the IP for LEP (see Fig.3.3) is symmetric, while it is antisymmetric for LHC (see Fig.3.4). Referring to the matrix formalism discussed earlier it is much easier to find a solution for the symmetric case: if a solution exists that changes the β-function at the IP as a result of quadrupole changes between the points (1) and (IP), this matrix has to be inverted and multiplied to the first to confine the changes to the IR. Practically this means, the quadrupoles left and right of the IP have to be powered symmetrically. For the anti-symmetrical case the powering of the quadrupoles to the left and to the right is not coupled in this way. The solution for the second matrix has to be found separately. This means, that, even if there exists a solution for the first matrix, this must not be the case for the second matrix.

The difference in the beam profile has the following practical implication: the luminosity mainly depends on the vertical beam size. For LEP there only had to be a correction mechanism for the vertical plane and also changes to the horizontal had from this mechanism no major effect and could be neglected. For the round beam profile the situation is more complex: there have to be two orthogonal correction tools, each acting in one plane.

The second difference are the colliding particles, which were electrons (e^-) and positrons (e^+) for LEP (particle and antiparticle) and are protons (particle and particle) in the LHC. For the first case only one guide field is needed for both beams, which means that both beams experience the same field errors and can be corrected simultaneously. For the particle-particle case, two separate guide fields are required. This creates two beams with different error characteristics. These have to be corrected independently.

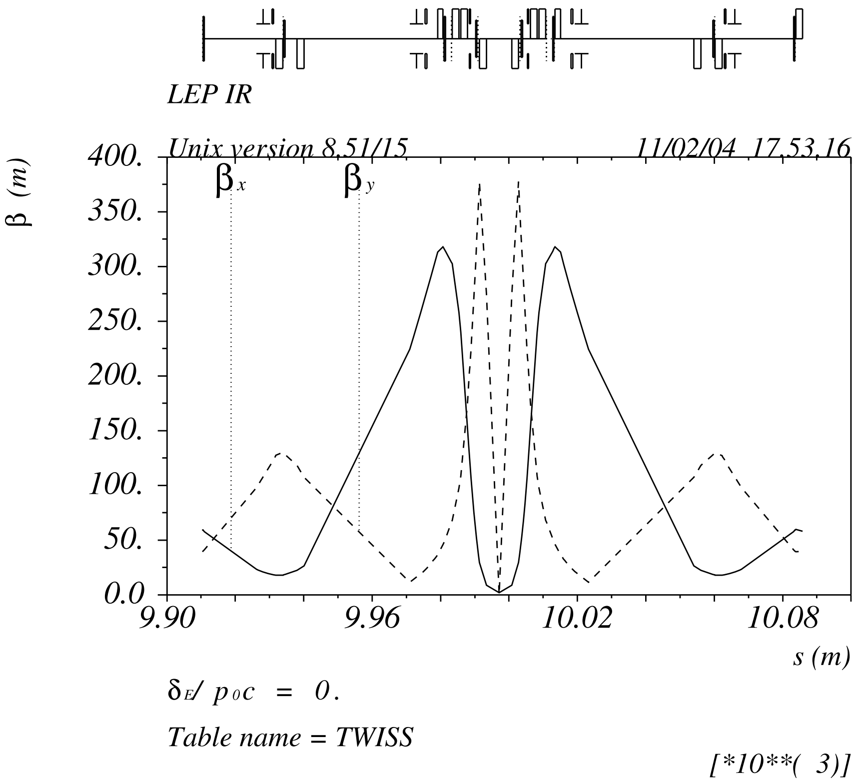

Figure 3.3: Symmetric interaction region in LEP. Plotted are the β-functions in IP2.

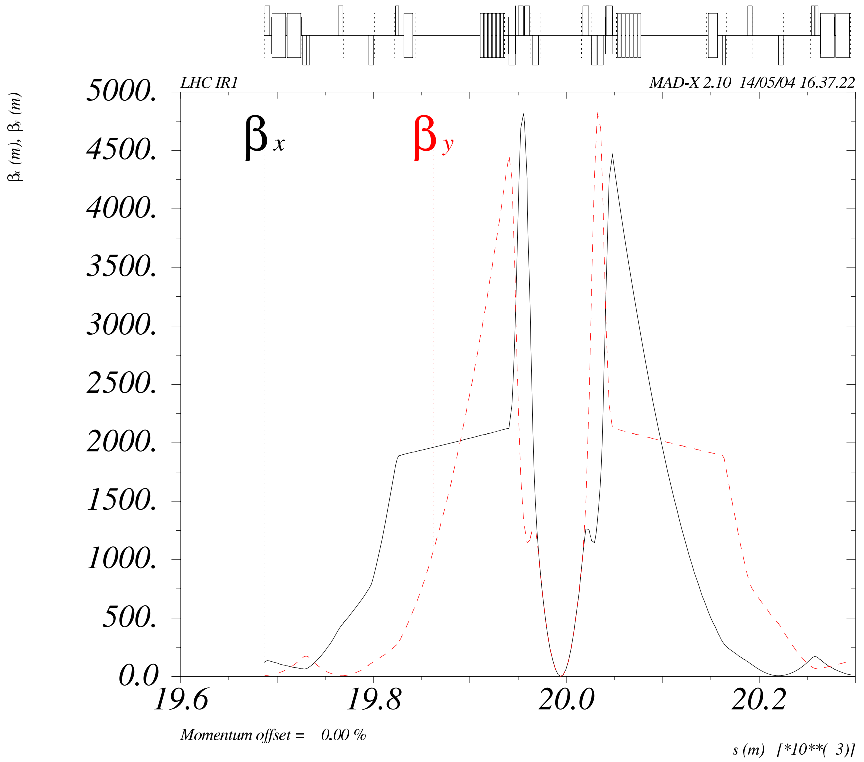

Figure 3.4: Anti-symmetric interaction region in LHC. Plotted are the β-functions in IP1.

For LEP the main correction quadrupoles were the two closest ones to the left and to the right from the IP. For the LHC the same approach is not possible because the two beams share the same quadrupolar guide field in these magnets and a correction for one beam in one plane creates automatically a perturbation in the other plane and in the other beam. Only if the error source happens to be this particular quadrupole a local correction will cancel the error for both beams and both planes.

For this reason a group of quadrupoles located before combination and after separation of the two beams left and right of the IP in the IR was identified as possible correctors. A technical problem can arise from the electrical layout. Not all quadrupoles can be varied independently. If they are powered in series with other magnets they are not available for β tuning.

Adjusting the β-function at the IP Using Tuning Knobs

In accelerator physics the term tuning knob is commonly used for one (or several) magnet(s) which is (are) used to tune one variable. In this thesis a tuning knob is a group of quadrupoles, situated left and right of the IP. In the case of LHC these are situated between the end of the arc and the triplet magnets on either side of the IP (see Fig.3.5). These tuning quadrupoles are powered in series with fixed ratios of excitation strength and form the linear knob vector. To create a specific change of the β-function a common multiplier is used (see Fig.3.6). The vector is normalized such that if the multiplier equals one the vector increases the β-function by one meter.

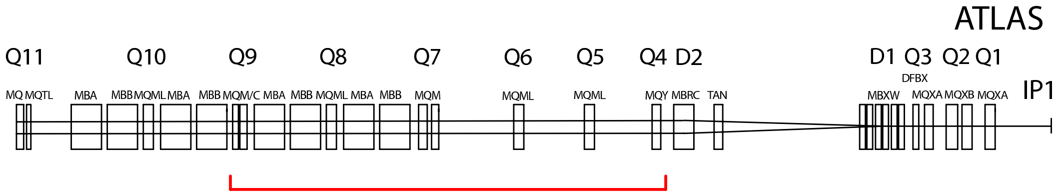

Figure 3.5: Lattice design of one half of the interaction (IR) region of IP1 and IP5. The red line indicates the region were one half of the tuning quads are situated. The second half of the IR is mirrored at the IP.

$$m \cdot \begin{pmatrix} \Delta K_1 \\ \Delta K_2 \\ \Delta K_3 \\ \vdots \\ \Delta K_n \end{pmatrix} \longrightarrow \Delta\beta_{x,y} \qquad \boxed{m = 1 \quad \Longleftrightarrow \quad \Delta\beta_{x,y} = 1m}$$

Figure 3.6: Principle of the composition of the tuning knob. The ΔK values are the fixed increments of change of quadrupole gradient, which are assigned to the different quadrupoles. To create a specific change a common multiplier m is used.

Matching $\beta^\star$ with MAD

As stated earlier MAD has to start with a stable solution for the Twiss matrix. It has to be reached by changing magnet strengths using experience and trial-and-error search. Afterwards MAD can optimize the optics.The matching algorithms, used in MAD, are based on least square minimization. LMDIF (fast gradient minimization) uses the Jacobian matrix to find the steepest decent. The minimum is determined by the starting point which is found by chance. This means that there is no information on whether the found minimum is local or global, or if any other solutions exist in the same parameter space. Recently a so called "genetic" matching algorithm has been added to MAD. It is based on the principle of exciting a given starting point and then moves by random steps in parameter space that are cooled down adiabatically, to find other minima. This is done systematically to determine all possible solutions and to determine the global minima. A problem is that so far it works only for mid size lattices. For LHC the number of parameters are too big, so that the Twiss matrix becomes unstable during the random step.

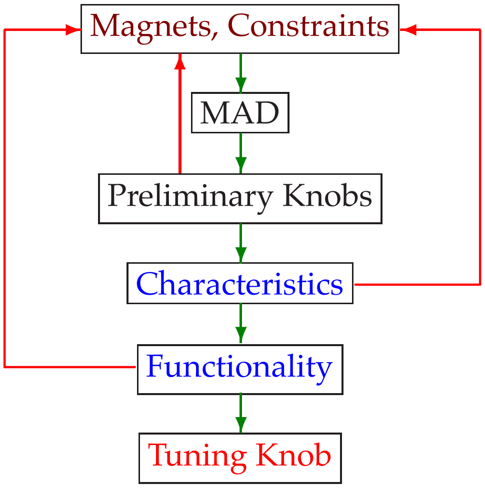

Figure 3.7: Work flow diagram for the procedure to match the tuning knobs with MAD.

A second obstacle is the choice of constraints for the matching. Analytically the number of constraints (variables, which are actively used in the matching process) is limited to be the same as the number of degrees of freedom in order to have a unique solution. The degree of freedom is given by the number of available tuning quadrupoles. In the case of LHC and RHIC the degree of freedom is smaller than the number of constraints for an optimum solution. Also not all tuning quads act on the different constraints in the same way. This is a characteristic of the lattice. One now has to find an optimum combination of applicable tuning quadrupoles and an equal number of constraints, which not only optimizes the chosen constraints, but also other variables, which are not actively used in the matching process. These will be refered to as observables. Which variable will be chosen as constraint or observables has to be analyzed independently for each lattice. A variable is a constraint if it is absolutely necessary to minimize its change and it is possible to do so. This procedure is not straightforward and there are no analytical procedure available, which predicts the result. To find the optimum solution, all possible combinations have to be simulated. Fig.3.7, page 37 shows the flow of this process. To give an idea of the amount of data which has to be processed, the possible sets of constraints and degrees of freedom are compiled in Tab.3.2. The finally used solutions for the two different lattices (RHIC and LHC) illustrate that different combination of constraints generate the best solution depending on the lattice. Also the number of applicable tuning quadrupoles is a characteristic of the lattice.

Table 3.2: List of possible constraints and tuning quadrupoles for the matching procedure with MAD and chosen set for LHC and RHIC.

		Magnets	Constraints
available	LHC	KQ4-KQ13 R+L	$\alpha, \beta, D, D', X, (pX), Y, (pY)$ at IP1 and IP5
	RHIC	K(1-3)A8 K(4-6)A8(I,O) K(4,56)M8, K7A8 K(D,F)AA8, KFBA8	or $\left\{ \begin{array}{c} \alpha, \beta, D, D', X, (pX), Y, (pY) \quad \text{at IP1} \\ \beta, D, X, Y, \quad \text{at I, II} \\ \text{with} \quad (\mathrm{I}) \xrightarrow[k=0,1\ldots]{\Delta\mu=\frac{\pi}{4}(2k+1)} (\mathrm{II}) \end{array} \right.$ and Q, Q'
finally used LHC		KQ4 - KQ9 (KQ13) R+L	α, β, D at IP1 and IP5
finally used RHIC		KQ4-KQ6, L+R K7A8, KFBA8 KDAA8, KFAA8	α, β at IP8 and IP6 Q

3.2 Response matrix

The technique of response matrix analysis is a standard method to measure and correct the closed orbit. LOCO (**L**inear **O**ptics from **C**losed **O**rbit)[19]-[21] is an algorithm for debugging the optics of storage rings. It uses the orbit response measured at the beam position monitors (BPM's) caused by dipole and quadrupole excitations.

The same mechanism is used to simulate the "quadrupole response matrix". In this case, instead of the orbit changes at the BPM's, the changes of the constraints and observables (global and local) as a function of the gradient change at the tuning quadrupoles are recorded. This technique allows us to simulate the behavior of the individual quadrupoles and is a vital tool in the selection process for the composition of the knob vector. By varying ΔK in several steps the change of the investigated variable can be plotted as a function of ΔK as shown in Fig.3.8. By fitting the gradient to a straight line around $\Delta K = 0$ the linear matrix element $\frac{dv}{dK_n}$ is calculated. Repeating this for all quadrupoles and variables (constraints and observables) the response matrix is calculated:

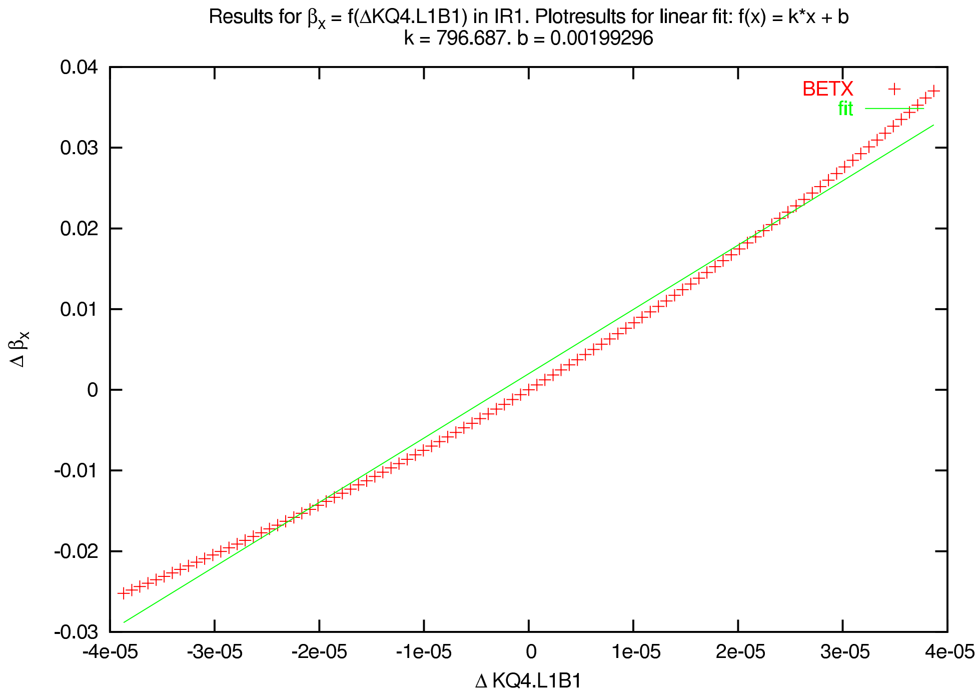

Figure 3.8: Response function for $\Delta\beta_x$ in IP1 in LHC when exciting the fourth quadrupole (KQ4.L1B1) left from the IP.

$$\mathbf{R} = \begin{pmatrix} \frac{\partial\alpha_x}{\partial K_{K1A8}} & \frac{\partial\alpha_x}{\partial K_{K2A8}} & \frac{\partial\alpha_x}{\partial K_{K3A8}} & & & & \frac{\partial\alpha_x}{\partial K_{KDAA8}} \\ \frac{\partial\alpha_y}{\partial K_{K1A8}} & \frac{\partial\alpha_y}{\partial K_{K2A8}} & \frac{\partial\alpha_y}{\partial K_{K3A8}} & \cdots & \cdots & \cdots & \frac{\partial\alpha_y}{\partial K_{KDAA8}} \\ \frac{\partial\beta_x}{\partial K_{K1A8}} & \frac{\partial\beta_x}{\partial K_{K2A8}} & \frac{\partial\beta_x}{\partial K_{K3A8}} & & & & \frac{\partial\beta_x}{\partial K_{KDAA8}} \\ & \vdots & & \ddots & & & \\ & \vdots & & & \ddots & & \\ & \vdots & & & & \ddots & \\ \frac{\partial dQ_2}{\partial K_{K1A8}} & \frac{\partial dQ_2}{\partial K_{K2A8}} & \frac{\partial dQ_2}{\partial K_{K3A8}} & \cdots & \cdots & \cdots & \frac{\partial dQ_2}{\partial K_{KDAA8}} \end{pmatrix} \tag{3.3}$$

The range, for which the calculated matrix is valid, depends on the behavior of the function (see Fig.3.8). If the gradient is not constant the matrix is strictly valid only in an infinitely small range around $\Delta K = 0$. Using it in a finite range will introduce errors in the calculations. To minimize the error, one has to calculate the response matrix, set a small increment and then recalculate again. The amount of data to be handled demands an automated processing and can be rather time consuming depending on the dimension of the matrix.

Calculating Response Matrix Using MAD

To calculate the response matrix with MAD all in principle adaptable quadrupoles were analyzed. This was done by varying the integrated quadrupole strength ΔK

and recording the α-,β-function, dispersion in the IP of interest and at a second point of the ring separated from the IP by phase advance of $\phi = \frac{\pi}{2}$ to minimize the β- and dispersion beat, and the tune change. For the LHC the matrix was calculated once with the dimension 20×20. 400 plots had to be generated and edited. For this reason scripts were written for automation. For the fitting gnuplot is used.

Inverting the Response Matrix

By inverting the response matrix the elements of the knob vector can be directly calculated:

$$\Delta\vec{K} = \mathbf{R}^{-1}\Delta\vec{P} \tag{3.4}$$

$\Delta\vec{P}$ is a vector composed of constraints and observables. This is only possible if the dimension of $\mathbf{R}$ is quadratic and if it is not singular or poorly conditioned (close to singular). If inversion is possible the validity of the solution depends on the behavior of the response functions. A calculated tuning knob might not work in practice if its range of application is too small.

In case of non square matrix and poor condition there exists a mathematical formalism, called **S**ingular **V**alue **D**ecomposition (SVD)[27], which “pseudo inverts” a matrix. The solution is also not mathematically rigorous and has to be analyzed. The formalism is based on a mathematical theorem, that all matrices can be decomposed into a product of three matrices,

$$\begin{pmatrix} & & \\ & \mathbf{R} & \\ & & \end{pmatrix} = \begin{pmatrix} & & \\ & \mathbf{U} & \\ & & \end{pmatrix} \cdot \begin{pmatrix} s_1 & & & \\ & s_2 & & \\ & & \ddots & \\ & & & s_m \end{pmatrix} \cdot \begin{pmatrix} & & \\ & \mathbf{V}^T & \\ & & \end{pmatrix}$$

of which the first and the third are orthonormal and the second is diagonal (only the values on the diagonal are non zero). Due to these special attributes the matrix can be pseudo inverted as follows:

$$\mathbf{R}^{-1} = \mathbf{V}\mathbf{S}^{-1}\mathbf{U}^T$$

The diagonal matrix contains information about the singularity. Codes performing this calculation usually arrange the matrices in a way, that the entry in this matrix is ordered from the largest to the smallest singular value. To invert this matrix the inverses of the diagonal elements are taken. In case of a too small singular value the matrix becomes nearly singular and the inversion would introduce large quadrupole (corrector) changes. To avoid this for small values of s_i, the large quantities $1/s_i$ in the inverse matrix are set to zero. Doing this makes the matrix pseudo invertible but looses some information. The resulting matrix has to be analyzed for its validity.

To characterize different combinations of degrees of freedom and constraints one can make use of the diagonal matrix. The condition of the matrix is characterized by the ratio between the largest and the smallest element. The smaller this ratio is the better the system.

Non Linear Optimization using an Adapted Moore Penrose Method

As stated above, the range of the calculated tuning knob depends on the response function of the tuning quadrupoles. The linearity of the slope of these functions is different for different quadrupoles and constraints. The range of the knobs may be maximized by selecting quadrupoles and constraints with optimum linear response. The change of the constraints can never be exactly zero using a perturbative approach for computing the tuning knobs. Therefore, an allowed range of change is assigned to each constraint. The range of the tuning knob is defined by the limit of the constraint that is reached first. This can be balanced and adjusted by using weight functions for the constraints when computing the knobs. To deal with the nonlinear response of the quadrupoles penalty- (weight-) functions can be introduced to minimize changes of quadrupoles, depending on their nonlinearity. Together with weigh functions for the constraints and quadrupoles, this system is minimized. In the minimization algorithms the error function χ is defined as [28]:

$$\chi^2 = \left(\vec{\hat{c}} - \vec{c}\right)^T \mathbf{W} \left(\vec{\hat{c}} - \vec{c}\right) \tag{3.5}$$

where $\vec{c}$ is the expected constraint vector, $\vec{\hat{c}}$ is the simulated constraint vector and W the weight matrix consisting of the weight factors w_i multiplied with the vector of the allowed constraint's ranges $1/\vec{\sigma}$.

This does not take into account the non linear behavior which can lead to smaller ranges of application. To include this, one has to add a further term to the error function, so that the changes of the quadrupoles are also considered in the minimization process [22]. In addition, to consider the different response (see Eq.3.4) of the quadrupoles also here weight functions have to be added. With

$$\Delta\vec{c} = \vec{\hat{c}} - \vec{c}$$

Eq.(3.5) becomes

$$\chi^2 = (\Delta\vec{c})^T \mathbf{W} (\Delta\vec{c}) .$$

The minimization condition for the change of quadrupoles is added such that the system is dimensionally consistent. To do so the response matrix is included.

$$\chi^2 = \left(\mathbf{R}\Delta\vec{K}\right)^T \mathbf{W}_1 \left(\mathbf{R}\Delta\vec{K}\right) + \left(\Delta\vec{K}\right)^T \mathbf{W}_2 \left(\Delta\vec{K}\right)$$

For minimizing the error function the derivative with respect to $\Delta\vec{K}$ is set to zero.

$$\vec{\nabla}\chi^2 = 2\mathbf{R}^T\mathbf{W}_1\Delta\vec{c}_0 + 2\mathbf{R}^T\mathbf{W}_1\mathbf{R}\Delta\vec{K} + 2\mathbf{W}_2\Delta\vec{K} + 2\mathbf{W}_2\Delta\vec{K}_0 = 0$$

Simplifying the system gives the new condition:

$$\begin{aligned} \mathbf{A}\Delta\vec{K} &= -\mathbf{R}^T\mathbf{W}_1\Delta\vec{c}_0 - \mathbf{W}_2\Delta\vec{K}_0 \\ \mathbf{A} &= \mathbf{R}^T\mathbf{W}_1\mathbf{R} + \mathbf{W}_2 \end{aligned}$$

The minimization of the change of quadrupole strength happens at the cost of the change of the constraints. But due to the nonlinear behavior which is reduced by minimizing quadrupole changes, the overall gain can be that the range of application is extended by minimizing the sum of the weighted change of constraints and quadrupoles in the error function.

3.3 Hysteresis in Superconducting Magnets

One possible problem source is the hysteresis effect of magnets. In the case of LHC with superconducting magnets the hysteresis behavior of each magnet type is measured. This is done to create a calibration curve which relates the current directly to the field. It is common to measure the transfer function (TF), in units of T/m/kA for quadrupoles, to give this relation. Fig.3.9 depicts a typical transfer function for a

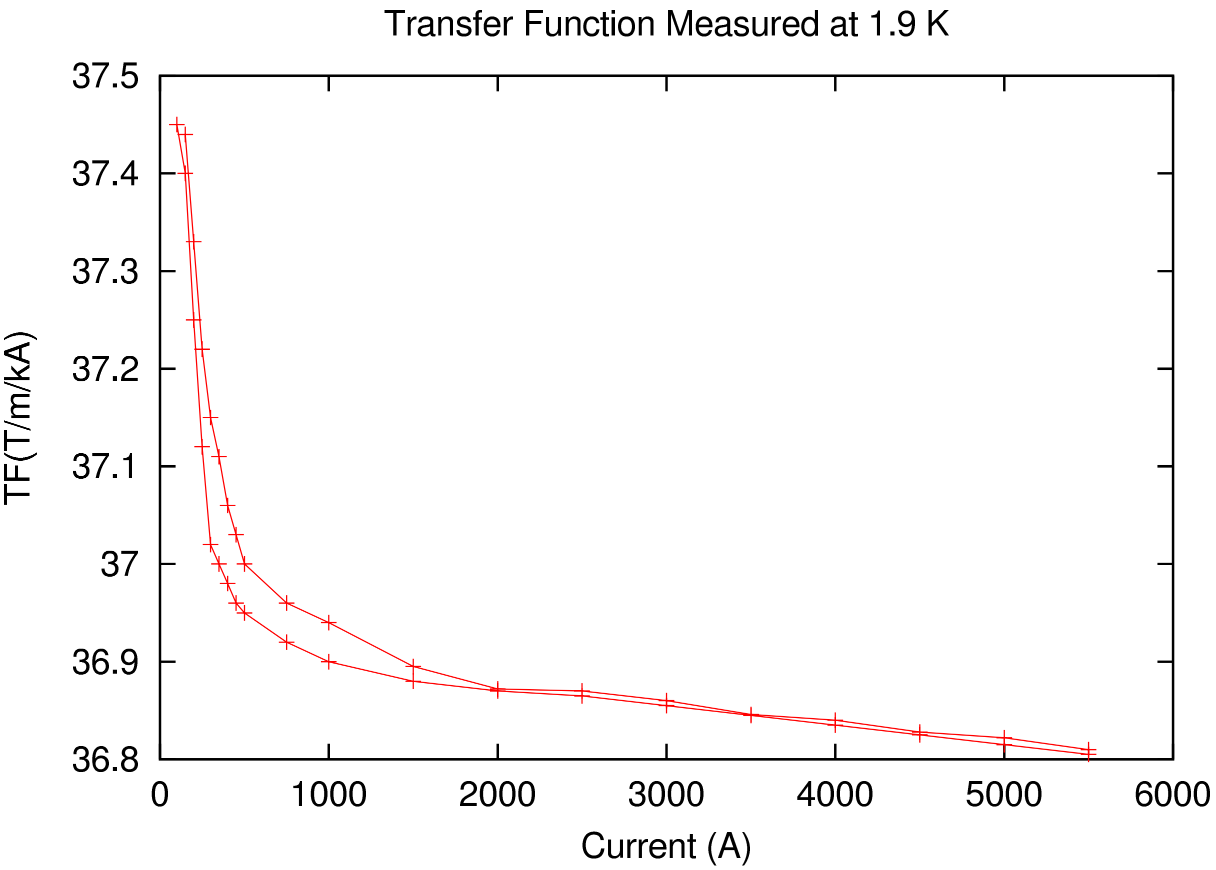

Figure 3.9: Typical transfer function for a super conducting magnet used in the LHC interaction region [23]. The two branches refer to increasing (lower) and decreasing (upper) current, respectively.

quadrupole installed in the LHC interaction region (MQM2). In operation the magnets are powered such that the calibration curve is not left. This means, that during a ramp the current is always increased. If the current is decreased the whole cycle has to be repeated again.

The principle of the correction mechanism using tuning knobs is to ramp a set of magnets repeatedly up and down around their nominal values. This means that the calibration curve will be left during such a procedure. The local hysteresis curve (hysteresis at nominal value) is unknown. It would have to be measured before installing the magnet into the tunnel. As the final nominal values of the different magnets are unknown at this time (the lattice design is still subject to changes and magnet strengths may be changed in operation) it cannot be done.

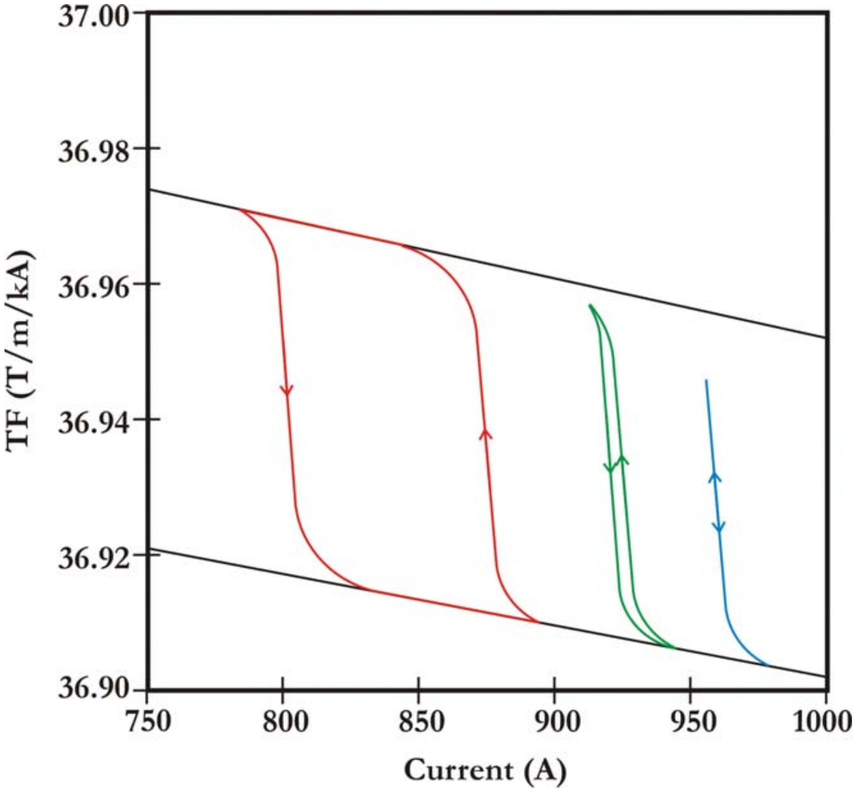

Figure 3.10: Schematic of the expected effect of hysteresis when ramping a magnet up and down around a nominal value. The blue curve shows the case when the change is so small that the conversion from current to field is always unique. The green curve shows a situation when the upper calibration curve is not reached. Due to the hysteresis effect during the up and down ramping different paths are used but the original starting point is reached when returning to the nominal value. The red curve shows the full effect of hysteresis.[24]

From Fig.3.9, page 42 it is clear that the expected effect depends on the nominal value of the ramped magnets. The difference of the lower and upper calibration curve is significant below a specific value. For this example it is approximately 2kA. The main magnets are expected to be powered above this limit. For corrector magnets it is more common, that they are powered at a very low level. These magnets will be cycled for correction reasons not only as part of the procedure described here. One possibility to overcome the hysteresis problem is to run a complete cycle with the magnet when it has to be ramped down. In this case the calibration curve will not be left.

If the magnets are powered above the level were the separation between upper and lower calibration curves starts to be very small and the perturbation of the nominal current smaller than one percent is than Magnet experts at CERN [24] expect that this effect is not significant.

If the nominal value is lower than this level there has to be distinguished between the three cases as shown in Fig.3.10. If the change in current is as shown in the blue curve, the conversion of current to field will be unique. This means that once the local effect is determined and corrected there will be no further ambiguity. If the upper branch is not reached but a certain change is exceeded the field will not be exactly the same during the return to the nominal value but the nominal value itself will be the same. If the upper branch is reached (red curve) the local curve will have to be run through back to the starting point to erase the magnetic memory. The blue, green and red curve in Fig.3.10 are based on expectations and reflect these and are not based on measurements.

In all three cases a correction factor has to be introduced to the field to current conversion so that the field is perturbed in the desired way. In the case of the non unique current to field conversion the operation of the knobs has to defined so that if a change, which decreases the current in a critical magnet, has to be performed, the knob is changed that a cycle is performed for these. But in any case the hysteresis effects for ramping magnets up and down around a nominal value can either be corrected if the changes are small enough or erased if they exceed the limit at which reversing the change in current does no longer correspond to a unique field value.

Chapter 4

Discussion of Analytic Solution with Transfer Matrices

The linear transfer matrix (see Eq.(2.19), Page 18) can be used to describe the change of the lattice functions when propagating from one point to another in a ring or periodic structure as shown in Eq.(2.20), Page 19. In principle one can calculate the individual matrix which propagates the solution of Hill's equation, including its dependence on all magnet strengths, by multiplying the analytical matrices of the elements which constitute the linear structure. The problem is, that even for very small periodic structures this matrix becomes too complex to be handled. Therefore the numerical treatment is chosen.

Yet simplified models of specific areas of a lattice can be used to understand the characteristics of these structures. In this chapter such a model will be built and discussed. This treatment should give an idea of the principle which was used to correct the IP β-function for LEP and why the same approach could not be adapted for LHC. From the treatment it will also become clear why a similar analytical model was not created for the LHC interaction region.

4.1 Example of Analytic Transfer Matrix - A Simple IR Model

A simple example for a low-β insertion is a symmetric drift space with doublet focusing as depicted in Fig.4.1, Page 46. As the system is symmetric it is sufficient to calculate the transfer matrix for one half (outer left quadrupole to IP or IP to outer right quadrupole) of the insertion. In the horizontal plane a negative sign for the K-value corresponds to focusing, a positive sign to defocusing. Equation(2.4), Page(9), relates the focal length f of a quadrupole to the k-value. The integrated focal strength is given by $K = k \cdot l$. For the calculations the thin lens description for the optic elements

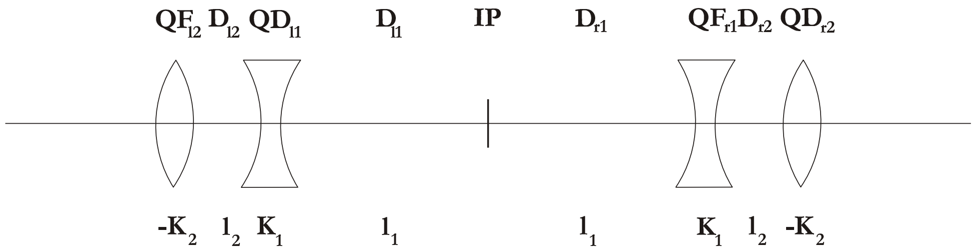

Figure 4.1: View of the horizontal plane of a low-β insertion with symmetric doublet focusing.

is used. The transfer matrix for the right side of the insertion is:

$$
\begin{aligned}
M_{(\mathrm{IP}\rightarrow \mathrm{QD_{r2}})} &= \begin{bmatrix} m_{11} & m_{12} \\ m_{21} & m_{22} \end{bmatrix} \\
&= \begin{bmatrix} 1 & 0 \\ -K_2 & 1 \end{bmatrix} \begin{bmatrix} 1 & l_2 \\ 0 & 1 \end{bmatrix} \begin{bmatrix} 1 & 0 \\ K_1 & 1 \end{bmatrix} \begin{bmatrix} 1 & l_1 \\ 0 & 1 \end{bmatrix} \\
&= \begin{bmatrix} 1 + K_1 l_2 & l_1 + (1 + K_1 l_2) l_2 \\ K_1 - K_2(1 + K_1 l_2) & 1 + K_1 l_1 - K_2(l_1 + (1 + K_1 l_2) l_2) \end{bmatrix} \qquad (4.1)
\end{aligned}
$$

By assuming that trajectories parallel to the beam axis are focused into the IP, an estimate for the quadrupole strengths can be made. This approximation holds, if there is a large first drift space between the IP and the first focusing element. In matrix notation this assumption is formulated as

$$
\begin{pmatrix} x_{r2} \\ 0 \end{pmatrix} = \begin{bmatrix} 1 + K_1 l_2 & l_1 + (1 + K_1 l_2) l_2 \\ K_1 - K_2(1 + K_1 l_2) & 1 + K_1 l_1 - K_2(l_1 + (1 + K_1 l_2) l_2) \end{bmatrix} \cdot \begin{pmatrix} 0 \\ x'_{\mathrm{IP}} \end{pmatrix},
$$

where x_{r2} is the transverse horizontal offset at the outer right quadrupole and x'_{IP} the slope of the trajectory in the IP. It can be rewritten as a system of equations:

$$
\begin{aligned}
(l_1 + (1 + K_1 l_2) l_2) x'_{\mathrm{IP}} &= x_{r2} \\
(1 + K_1 l_1 - K_2(l_1 + (1 + K_1 l_2) l_2)) x'_{\mathrm{IP}} &= 0
\end{aligned}
$$

The second equation can only be true for the general case ($x'_{\mathrm{IP}} \neq 0$) if the expression in the brackets is zero. With the same condition for the vertical plane a system of equations is constructed:

$$
\begin{aligned}
(1 + K_1 l_1 - K_2(l_1 + (1 + K_1 l_2) l_2)) x'_{\mathrm{IP}} &= 0 \\
(1 - K_1 l_1 + K_2(l_1 + (1 - K_1 l_2) l_2)) y'_{\mathrm{IP}} &= 0
\end{aligned}
$$

By solving this system, a condition for the focal strengths can be given:

$$
K_1 = \pm \frac{\sqrt{l_2(l_1 + l_2)}}{l_1 l_2} \qquad (4.2)
$$

$$
K_2 = \pm \frac{1}{\sqrt{l_2(l_1 + l_2)}} \qquad (4.3)
$$

With Eqs.(2.20, Page 19 and 4.1, Page 46) the matrix T propagating the Twiss parameters from the IP to the outer right quadrupole can be calculated.

$$
\begin{aligned}
T &= \begin{bmatrix} m_{11}^2 & -2m_{11}m_{12} & m_{12}^2 \\ -m_{11}m_{21} & (m_{12}m_{21} - m_{11}m_{22}) & -m_{12}m_{22} \\ m_{21}^2 & -2m_{21}m_{22} & m_{22}^2 \end{bmatrix} \\
&= \begin{bmatrix} \left(1 + \frac{\sqrt{l_2(l_1+l_2)}}{l_1}\right)^2 & -\frac{2\left(l_1+\sqrt{l_2(l_1+l_2)}\right)\left(l_1+l_2+\sqrt{l_2(l_1+l_2)}\right)}{l_1} & \left(l_1 + l_2 + \sqrt{l_2(l_1+l_2)}\right)^2 \\ \frac{l_1+l_2\left(-1+\frac{l_2}{\sqrt{l_2(l_1+l_2)}}\right)^2}{l_1^2} & -1 & 0 \\ \frac{\left(l_1+2l_2-2\sqrt{l_2(l_1+l_2)}\right)}{l_1^2(l_1+l_2)} & 0 & 0 \end{bmatrix}
\end{aligned}
\tag{4.4}
$$

For a symmetric lattice in the insertion region the beam waist is zero at the IP. Thus the slope of the β-function in the IP, the α-function, is also zero. With a given value for the β-function at the IP ($\beta^\star$), the lattice functions are determined (see Eqs.(2.17), Page 17):

$$
\begin{pmatrix} \beta \\ \alpha \\ \gamma \end{pmatrix}_{\mathrm{IP}} = \begin{pmatrix} \beta^\star \\ 0 \\ \frac{1}{\beta^\star} \end{pmatrix} \tag{4.5}
$$

Using the T matrix from Eq.(4.4)to propagate these lattice functions from the IP to the outer right quadrupole we get:

$$
\begin{pmatrix} \beta \\ \alpha \\ \gamma \end{pmatrix}_{\mathrm{QF_{r2}}} = \begin{pmatrix} \beta^\star\left(1 + \frac{\sqrt{l_2(l_1+l_2)}}{l_1}\right)^2 + \frac{1}{\beta^\star}\left(l_1 + l_2 + \sqrt{l_2(l_1+l_2)}\right)^2 \\ \beta^\star\frac{l_1+l_2\left(-1+\frac{l_2}{\sqrt{l_2(l_1+l_2)}}\right)}{l_1^2} \\ \beta^\star\frac{\left(l_1+2l_2-2\sqrt{l_2(l_1+l_2)}\right)}{l_1^2(l_1+l_2)} \end{pmatrix} \tag{4.6}
$$

There exists a relation between the Twiss parameters at the two outer quadrupoles due to the symmetry. The β- and γ-functions are equal and the α-functions have the same value with opposite sign. This can be verified by propagating the Twiss vector from Eq.(4.6), with an opposite sign for the second entry, from the outer left quadrupole to the IP. This must give the Twiss vector from Eq.(4.5). Further propagating this vector to the outer right quadrupole gives Eq.(4.6), i.e., the start vector with an opposite sign for the α-function.

Special Cases

Under these conditions one could make the assumption that the T matrix, which propagates the Twiss parameters through the insertion from the left outer to right outer quadrupole has the following form:

$$
T = \begin{bmatrix} 1 & 0 & 0 \\ 0 & -1 & 0 \\ 0 & 0 & 1 \end{bmatrix} \tag{4.7}
$$

By inserting the matrix elements of Eq.(2.19), Page 18 in to Eq.4.4, the general matrix propagating the Twiss parameters from one point to another is built as a function of these parameters. Assuming that Eq.(4.7) is true, these two matrices have to be equal. From this, conditions can be derived for the Twiss parameters. For the symmetric case we have the following condition:

$$\begin{pmatrix}\beta\\ \alpha\\ \gamma\end{pmatrix}_{QF_{l2}} = \begin{pmatrix}\beta\\ -\alpha\\ \gamma\end{pmatrix}_{QF_{r2}} \tag{4.8}$$

This ($\beta_1 = \beta_2 = \beta$, $\alpha_1 = -\alpha_2 = \alpha$) simplifies Eq.(2.19), Page 18 to:

$$\begin{bmatrix}\cos(\Delta\varphi) + \alpha\sin(\Delta\varphi) & \beta\sin(\Delta\varphi)\\ \frac{2\alpha^2\cos(\Delta\varphi)}{\beta} - \frac{(1-\alpha^2)\sin(\Delta\varphi)}{\beta} & \cos(\Delta\varphi) + \alpha\sin(\Delta\varphi)\end{bmatrix} \tag{4.9}$$

By inserting these matrix elements into the top of Eq.(4.4) and setting the matrix elements of this resulting T matrix equal to Eq.(4.7) creates a system of equations which all have to be true and may not exclude each other in order that the solution proposed in Eq.(4.7) is possible. Following this procedure one sees that the equations of $t_{13} = 0$ and $t_{22} = -1$

$$\beta^2\sin^2(\Delta\varphi) = 0 \quad \rightarrow \quad \Delta\varphi = \pi \tag{4.10}$$

$$-(-1+\alpha^2)\cos(2\Delta\varphi) + \alpha(\alpha + (1+\alpha)\sin(2\Delta\varphi)) = -1 \quad \rightarrow \quad \Delta\varphi \neq \pi \tag{4.11}$$

cannot be fulfilled at the same time.

By analyzing Eq.(4.11) one sees, however, that if the sign of the diagonal element of Eq.(4.7) is changed, both conditions are true if $\Delta\varphi = \pi$. This also holds for all other equations for the system. This is a special case for which $\alpha_{QFl2} = \alpha_{QFr2} = 0$.

The general matrix for the propagation with the symmetry condition and the relations for the quadrupole strengths from Eqs.(4.2, 4.3) is an upper triangle matrix with all diagonal elements equal one. From this matrix one can derive the relation for l_1 to l_2:

$$l_1 = \frac{1}{2}(1+\sqrt{5})l_2 \tag{4.12}$$

This would fix all parameters except one drift space. In reality this is not a good solution because it narrows the possibility of matching from the doublet to the arc.

4.2 A Numerical Example - LEP IR2

The final focus of IR2 in LEP, shown in Fig.4.2, corresponds approximately to the model setup in Section 3.1. The major differences to the analytical model is that in the simulation with MAD thick quadrupoles were used. This is important in this case, because the strength of these quadrupoles is very large so that a single thin lens is not a good approximation. Thin lenses were used for the analytical model above because adding additional quadrupoles and drift spaces would have made the example unnecessarily complicated. In simulation it is common to use more than one thin lens to replace a strong thick lens. In LHC one thick lens final focus quadrupole is approximated with four thin lens quadrupoles with drift spaces in between them. The total system corresponds in dimension to the thick lens but the integrated quadrupole strength is not the same. It has to be adapted to give the same results. The effect of this is smaller for the horizontal plane because the β-function is not so large. Tab.4.1 compiles the lattice functions as calculated with MAD. To compare these results with the analytical model the same integrated quadrupole strength values were used and the same values for the Twiss parameters at the IP. Fig.4.3, Page 50 shows the β-functions and the Twiss parameters are displayed in Tab.4.2. Comparing the two plots and tables show that for the horizontal plane the difference is not as big as for the vertical, where the maximum β-function for the thick lens MAD model is 376 meter in the inner quadrupoles compared to the 720 meter from the thin lens analytical model.

Table 4.1: Twiss parameter and integrated quadrupole strength's values for the low β interaction region 2 in LEP taken from the thick lens model simulated with MAD.

Elements	β_x	β_y	α_x	α_y	$K \cdot l$
QF_{l2}	237	106	-15.5	10.3	$\approx$ -0.28
QF_{l1}	29.7	376	-10.8	35.1	$\approx$ 0.32
IP	2.0	0.05	$5.2 \cdot 10^{-03}$	$2.3 \cdot 10^{-02}$	-
QF_{r1}	29.7	367	10.8	-35.1	$\approx$ 0.32
QF_{r2}	237	106	15.5	-10.3	$\approx$ -0.28

Table 4.2: Twiss parameter values for the low β interaction region 2 in LEP calculated with the analytical thin lens model and MATHEMATICA.

Elements	β_x	β_y	α_x	α_y	$K \cdot l$
QF_{l2}	167	108	-19.4	12.5	-0.28
QF_{l1}	20	720	-9.4	110	0.32
IP	2.0	0.05	0	0	-
QF_{r1}	20	720	9.4	-110	0.32
QF_{r2}	167	108	19.4	-12.5	-0.28

4.3 Comparing Tuning Knob Calculated with Exact and Truncated Matrices

In a simplified analytical model one can use the exact matrix. For a real accelerator it is not possible to do that, especially not for a knob composed of several quadrupoles. There are two main reasons for this. First the knob is supposed to be linear. This

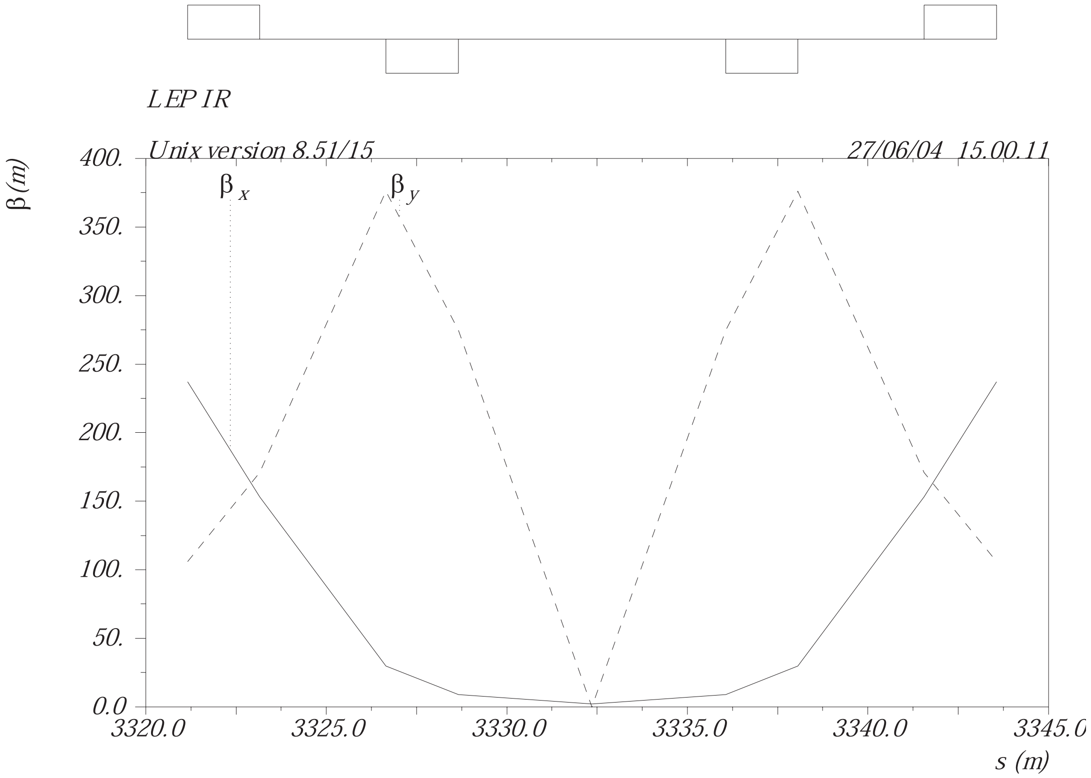

Figure 4.2: Thick lens model of IR2 in LEP only containing the final focus quadrupoles created with MAD.

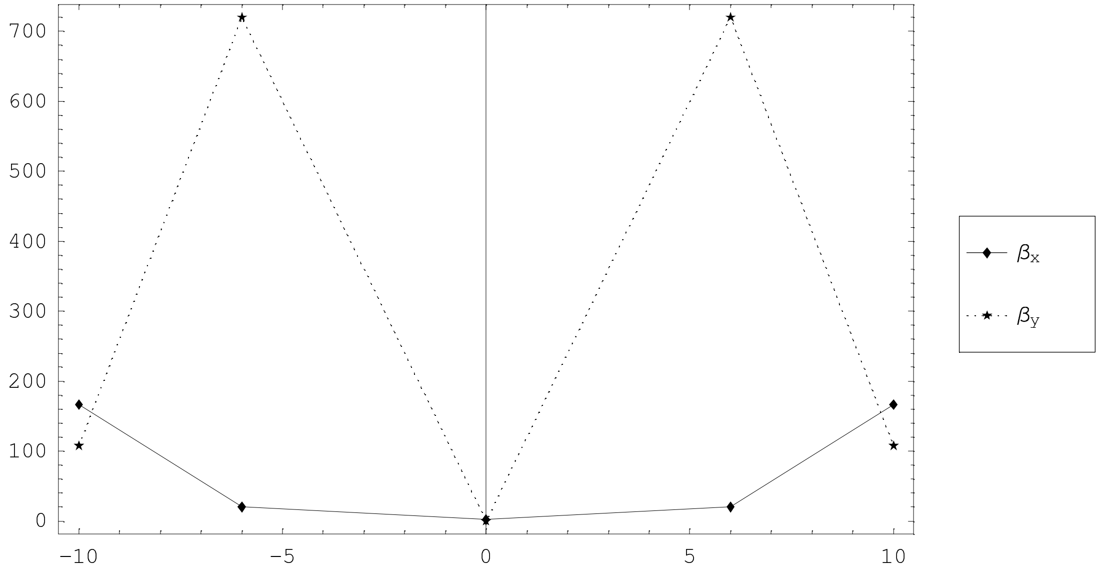

Figure 4.3: Thin lens model of IR2 in LEP only containing the final focus quadrupoles created with analytical thin lens model and MATHEMATICA. The distance in units of meters is assigned to the horizontal axis with the IP located in the origin and the quadrupoles located at 6 and 10 meters left and right from the IP. The vertical axis depicts the β-functions.

means that all nonlinear terms are truncated. Second, though it is in principle possible to create a nonlinear knob, to determine the mixing terms of the different quadrupoles is barely possible.[1] To measure or compute the response matrix including the mixing terms would create an enormous amount of data and would have to be done in a self consistent way because the response is not only depending on the changed magnet but also on the nominal value of all other tuning knobs. In the following the effect of using truncated matrices is analyzed for the analytical thin lens model.

In linear approximation the matrix propagating the Twiss parameters from one point to another containing the nominal settings of the quadrupoles and the strengths changes for the tuning quadrupoles can be written as:

$$T(K+\Delta K) = \underbrace{T(K)}_{\substack{\text{matched}\\\text{matrix}}} + \underbrace{T(\Delta K)}_{\substack{\text{knob}\\\text{perturbation}}} \tag{4.13}$$

The matched matrix corresponds to the nominal solution. The perturbation is obtained by expanding into a Taylor series around the nominal values.

$$\begin{aligned} T(\Delta K) = {} & \underbrace{T(\Delta K_1) + T(\Delta K_2) + \ldots + T(\Delta K_n)}_{\text{first order}} \\ & \underbrace{+T(\Delta K_1^2) + T(\Delta K_2^2) + T(\Delta K_1 \cdot \Delta K_2) + \ldots}_{\text{second order}} \\ & + \mathcal{O}\left[T(\Delta K)\right] \end{aligned} \tag{4.14}$$

For a realistic knob the linear part of this expansion is of interest. The matrix for the nominal solution of the analytical model described in Section 3.1 is:

$$T(K) = \begin{bmatrix} (1+K_1 l_2)^2 & -2(1+K_1 l_2)(l_2 + l_1(1+K_1 l_2)) & (l_2 + l_1(1+K_1 l_2))^2 \\ (1+K_1 l_2)(K_2 + K_1(-1+K_2 l_2)) & 1 + 2(l_2 + l_1(1+K_1 l_2))(K_2 + K_1(-1+K_2 l_2)) & (-l_2 + l_1(1+K_1 l_2))(1 + K_1 l_1 - K_2(l_2 + l_1(1+K_2 l_2))) \\ (K_1 - K_2(1+K_1 l_2))^2 & -2(K_1 - K_2(1+K_1 l_2))(1 + K_1 l_1 + K_2(l_2 + l_1(-1+K_2 l_2))) & (1 + K_1 l_1 - K_2(l_2 + l_1(1+K_2 l_2)))^2 \end{bmatrix} \tag{4.15}$$

---

[1] An attempt of constructing “nonlinear knobs” by iteratively computing linear matrices for small steps has been made by Irwin et. al. and used at the SLC [33].

The two linear matrices for the perturbations ΔK_1 and ΔK_2 are

$$T(\Delta K_1) = \left[\begin{matrix} 2l_2(1+K_1l_2)\Delta K_1 \\ (1-2l_2(K_2+K_1(-1+K_2l_2)))\Delta K_1 \\ 2(-1+K_2l_2)(K_2+K_1(-1+K_2l_2))\Delta K_1 \end{matrix} \right.$$

$$\begin{matrix} -2l_2(l_2+2l_1(1+K_1l_2))\Delta K_1 \\ 2(l_2-K_2l_2^2+l_1(1-2l_2))(K_2+K_1(-1+K_2l_2))\Delta K_1 \\ -2(-1+K_2l_2)(-1+K_2(2l_1+l_2)+2K_2l_1(-1+K_2l_2)))\Delta K_1 \end{matrix} \tag{4.16}$$

$$\left. \begin{matrix} 2l_1l_2(l_2+l_1(1+K_1l_2))\Delta K_1 \\ l_1(2l_2(-1+K_2l_2)l_1(-1+2l_2(K_2+K_1(-1+K_2l_2))))\Delta K_1 \\ 2l_1(-1+K_2l_2)(-1+K_2(l_1+l_2)+K_1l_1(-1+K_2l_2))^2\Delta K_1 \end{matrix} \right]$$

and

$$T(\Delta K_2) = \left[\begin{matrix} 0 \\ (1+K_1l_2)^2\Delta K_2 \\ 2(1+K_1l_2)(K_2+K_1(-1+K_2l_2))\Delta K_2 \end{matrix} \right.$$

$$\begin{matrix} 0 \\ -2(1+K_1l_2)(l_2+l_1(1+K_1l_2))\Delta K_2 \\ (2-4(l_2+l_1(1+K_1l_2))(K_2+K_1(-1+K_2l_2)))\Delta K_2 \end{matrix} \tag{4.17}$$

$$\left. \begin{matrix} 0 \\ (l_2+l_1(1+K_1l_2))^2\Delta K_2 \\ 2(l_2+l_1(1+K_1l_2))(-1+K_2(l_1+l_2)+K_1l_1(-1+K_2l_2))\Delta K_2 \end{matrix} \right]$$

The three second order matrices are

$$T(\Delta K_1^2) = \begin{bmatrix} l_2^2\Delta K_1^2 & -2l_1l_2^2\Delta K_1^2 & l_1^2l_2^2\Delta K_1^2 \\ l_2(-1+K_2l_2)\Delta K_1^2 & -2l_1l_2(l_2+l_1(-1+K_2l_2))\Delta K_1^2 & l_1^2l_2(-1+K_2l_2)\Delta K_1^2 \\ (-1+K_2l_2)^2\Delta K_1^2 & -2l_1(-1+K_2l_2)^2\Delta K_1^2 & l_1^2(-1+K_2l_2)^2\Delta K_1^2 \end{bmatrix}, \tag{4.18}$$

$$T(\Delta K_2^2) = \begin{bmatrix} 0 & 0 & 0 \\ 0 & 0 & 0 \\ (1+K_1l_2)^2\Delta K_2^2 & -2(1+K_1l_2)(l_2+l_1(-1+K_1l_2))\Delta K_1^2 & (l_2+l_1(-1+K_1l_2))^2 \end{bmatrix} \tag{4.19}$$

and

$$T(\Delta K_1\cdot\Delta K_2) = \left[\begin{matrix} 0 \\ 2l_2(1+K_1l_2)\Delta K_1\Delta K_2 \\ (-2+4l_2(K_2+K_1(-1+K_2l_2)))\Delta K_1\Delta K_2 \end{matrix} \right.$$

$$\begin{matrix} 0 \\ -2l_2(l_2+2l_1(1+K_1l_2))\Delta K_1\Delta K_2 \\ 4(l_2-K_2l_2^2+l_1(1-2l_2(K_2+K_1(1+K_2l_2))))\Delta K_1\Delta K_2 \end{matrix} \tag{4.20}$$

$$\left. \begin{matrix} 0 \\ 2l_1l_2(l_2+l_1(1+K_1l_2))\Delta K_1\Delta K_2 \\ 2l_1(2l_2(-1+K_2l_2)+l_1(-1+2l_2(K_2+K_1(-1+K_2l_2))))\Delta K_1\Delta K_2 \end{matrix} \right]$$

This shows, that for a very small model as discussed here, these matrices are already complex. Increasing the number of independent tuning quadrupoles by breaking the symmetry condition for the quadrupole powering creates already four linear matrices and 16 second order matrices.

The effect of truncating the perturbation to linear matrices is shown in Fig.4.4 on page 54. The plots show the effect on the horizontal β-function when changing the integrated quadrupole strengths and keeping the initial Twiss parameter values constant at the outer left quadrupole. This corresponds to a transfer line and not to a storage ring. The ΔK-values are varied from a maximum negative to the same positive value with ten intermediate steps. ΔK_{max} is 0.5% of the nominal value of K for plot A and D, 2.5%for plot B and E and 5% for plot C and F on page 54. The plots on the left side (A,B and C) show the change of the β-function calculated with the exact matrix in comparison to plots D, E and F where the matrix only contains the terms linear in the $\Delta K's$. For small values of the perturbation the difference is negligible as shown in the upper plots. In plots B and E the difference is already clearly visible and the errors of the results from the truncated matrix are 20 percent at maximum. For the last two plots the error is already up to 600 percent.

This shows that truncating the matrix is limiting the applicable range of the tuning knobs. This range is dependent on how many quadrupoles are used. This is due to the fact that the error of each quadrupole excitation due to matrix truncation is amplified by the following excitations. Also the nominal β-function at and phase advance between the tuning quadrupoles influences the magnitude of the created error as shown in Eq.(2.23), Page 21.

To demonstrate the effect of applying a linear tuning knob calculated with the linearly truncated matrix to a system which behaves like a perfect storage ring (exact matrix, perfect magnetic fields) a tuning knob for the insertion model is calculated. Using the linearly truncated matrix the result is a fixed ratio between ΔK_1 and ΔK_2 excitations:

$$\Delta K_2 \approx 0.1096 \Delta K_1 \tag{4.21}$$

For this calculation the numerical values for the integrated quadrupole strengths and drift spaces were chosen the same as in the section of the numerical example above (see Section 3.2). When applying this knob to the linearly truncated matrix the result is as shown in Fig.4.5, Page 55. The numerical values for the horizontal β-function are listed in Tab.4.3 on the same page. Here, the tuning knob is applied ten times changing the nominal quadrupole strength of the inner magnet from minus 25 percent of the nominal value to plus 25 percent with equidistant intermediate steps together with the outer quadrupole powered according to the relation of Eq.(4.21).

This same knob was applied to the exact matrix. The results are presented on page 56 in Tab.4.4 and Fig.4.6. The difference of the IP β-function is depicted in Fig.4.7. The horizontal axis labels the value expected from the calculation with the truncated matrix, the ordinate the difference between the latter and the result obtained with the exact matrix. From this picture it is clear that the applicable range of a linear tuning knob is restricted and that due to the various nonlinearities it is difficult to predict this deviation.

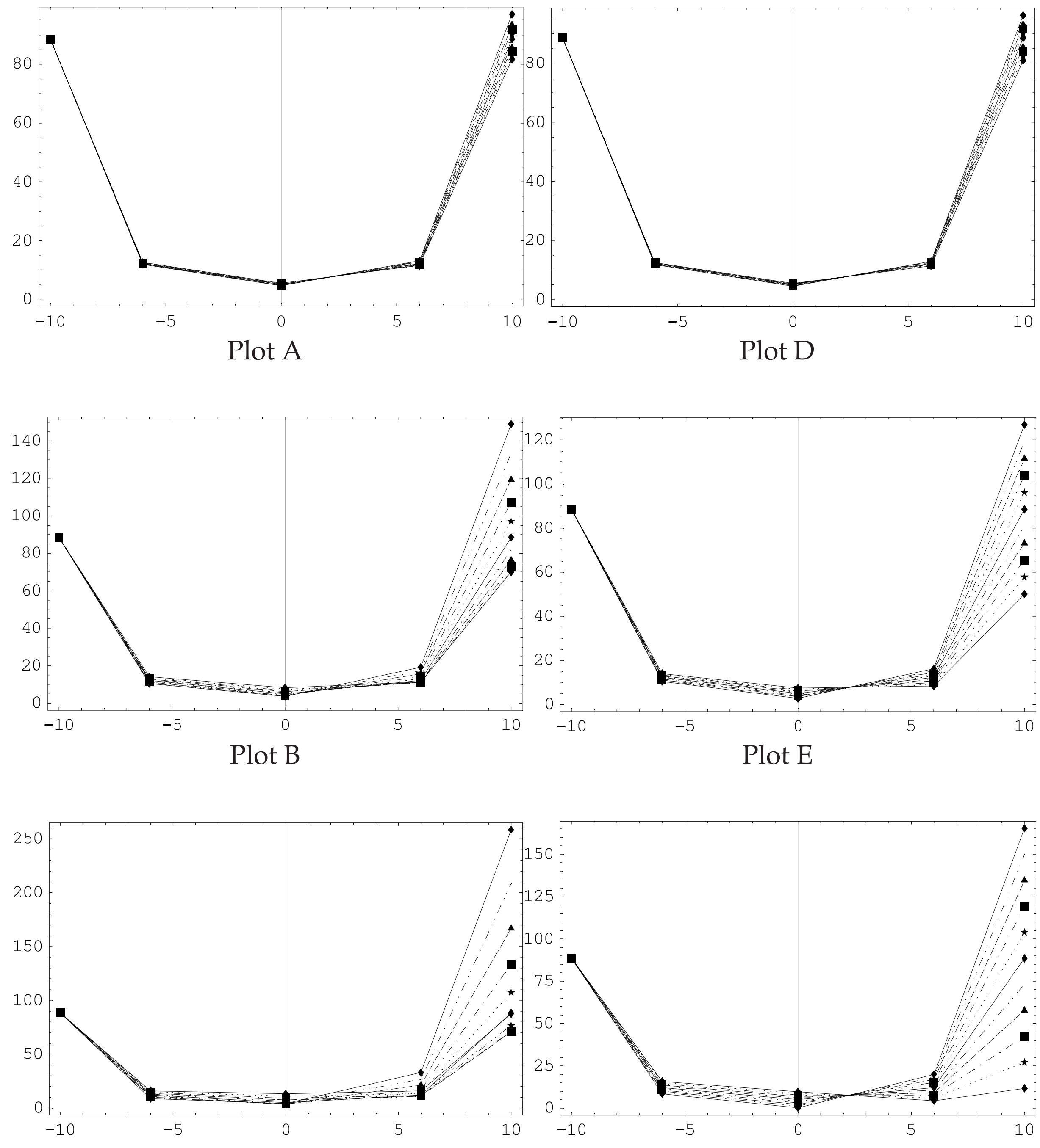

Plot A

Plot D

Plot B

Plot E

Plot C

Plot F

Figure 4.4: Influence of using truncated matrices when describing the β-function change created by quadrupole excitation ($|\Delta K_1| = |\Delta K_2|$). The quadrupoles are excited anti-symmetrically, so that the strengths are increased or decreased simultaneously for both focusing and defocusing quadrupoles. The maximum excitation for the plots in the first row was $\pm 0.5\%$ of the nominal strength value with ten intermediate steps, $\pm 2.5\%$ for the middle row and $\pm 5\%$ for the lower row. The figures on the left side show the β-functions calculated with exact matrices, the ones on the left with truncated matrices. The distance in units of meters is assigned to the horizontal axis with the IP located in the origin and the quadrupoles located at 6 and 10 meters at the left and at the right of the IP. The vertical axis depicts the β-functions.

Table 4.3: Horizontal β-functions values at the quadrupoles at the left and at the right of the IP and at the IP when applying a linear tuning knob which was calculated with linearly truncated matrices. The initial (at the outer quadrupole at the left) β-function is kept constant. The β-function is calculated using the linearly truncated matrix.

m	β_x				
	QF_{l2}	QF_{l1}	IP	QF_{r1}	QF_{r2}
-5	167	24.0	1.50	24.0	167
-4	167	23.2	1.60	23.2	167
-3	167	22.4	1.70	22.4	167
-2	167	21.6	1.80	21.6	167
-1	167	20.8	1.90	20.8	167
0	167	20.0	2.00	20.0	167
1	167	19.2	2.10	19.2	167
2	167	18.4	2.20	18.4	167
3	167	17.6	2.30	17.6	167
4	167	16.8	2.40	16.8	167
5	167	16.0	2.50	16.0	167

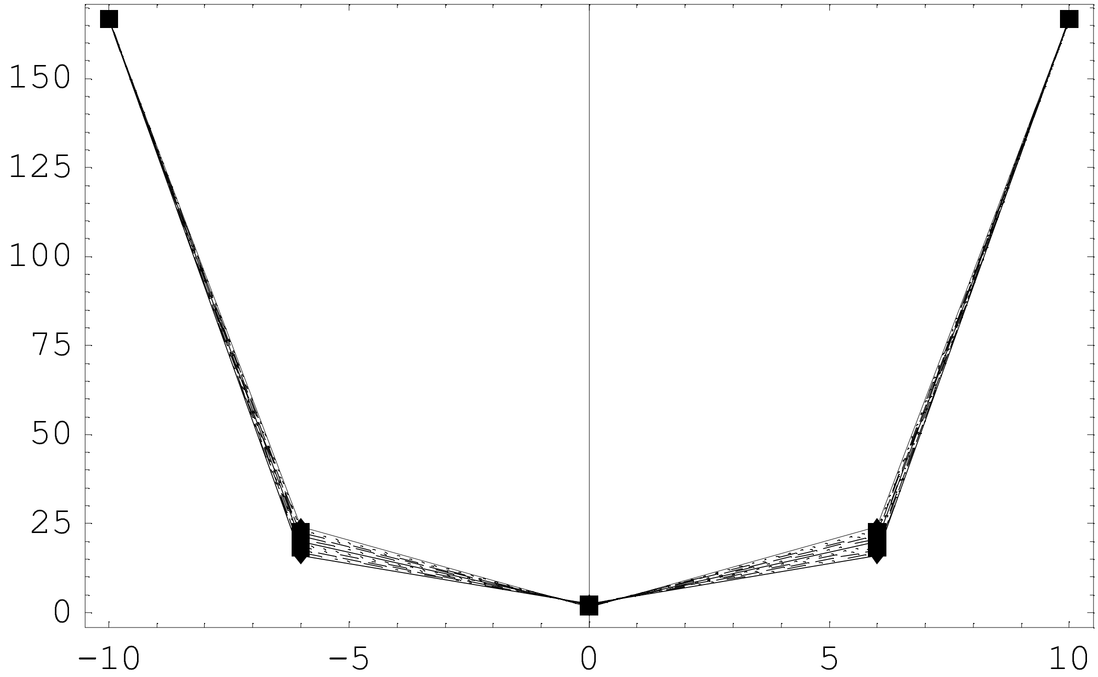

Figure 4.5: Horizontal β-functions when applying a linear tuning knob which was calculated with linearly truncated matrices. The initial (at the outer quadrupole at the left) β-function is kept constant. The β-function is calculated using the linearly truncated matrix. The distance in units of meters is assigned to the horizontal axis with the IP located in the origin and the quadrupoles located at 6 and 10 meters at the left and at the right of the IP. The vertical axis depicts the β-functions.

Table 4.4: Horizontal β-functions values in the quadrupoles at the left and at the right of the IP and at the IP when applying a linear tuning knob which was calculated with linearly truncated matrices. The initial (at the outer quadrupole at the left) β-function is kept constant. The β-function is calculated using the exact matrix.

ΔK	β_x (m)				
	QF_{l2}	QF_{l1}	IP	QF_{r1}	QF_{r2}
-5	167	24.3	1.49	28.8	190
-4	167	23.4	1.57	26.1	182
-3	167	22.5	1.68	24.0	175
-2	167	21.7	1.79	22.3	171
-1	167	20.8	1.90	21.0	168
0	167	20.0	2.00	20.0	167
1	167	19.2	2.10	19.3	168
2	167	18.4	2.18	19.0	171
3	167	17.7	2.26	18.9	176
4	167	16.9	2.32	19.0	184
5	167	16.2	2.38	19.4	194

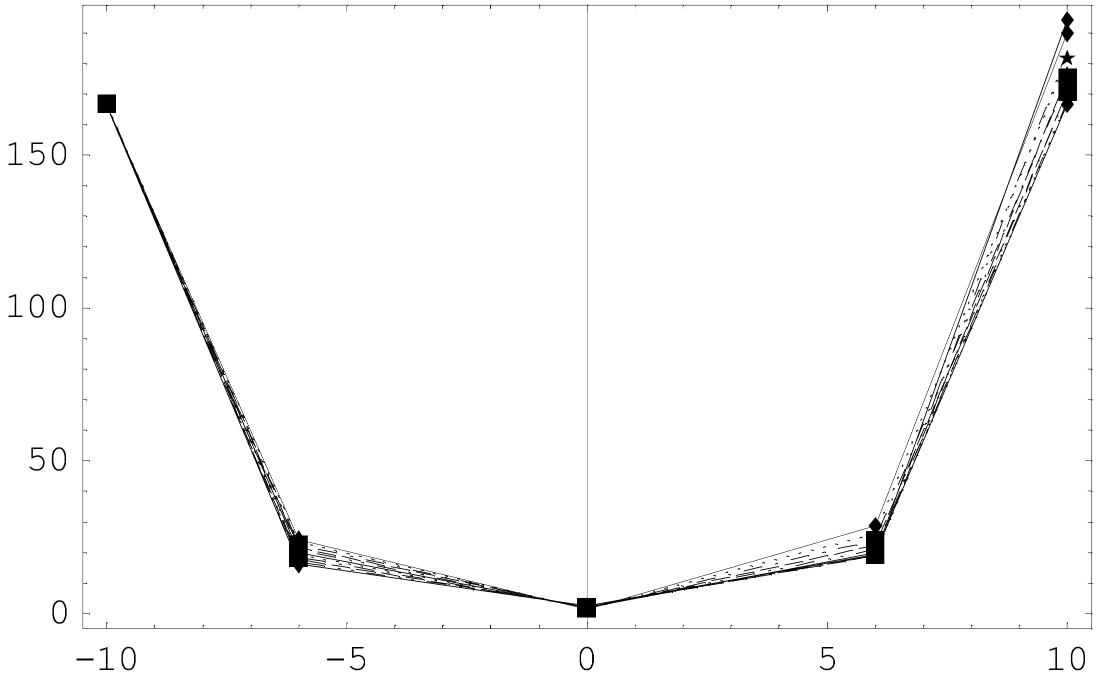

Figure 4.6: Horizontal β-functions values when applying a linear tuning knob which was calculated with linearly truncated matrices. The initial (at the outer quadrupole at the left) β-function is kept constant. The β-function is calculated using the exact matrix. The distance in units of meters is assigned to the horizontal axis with the IP located in the origin and the quadrupoles located at 6 and 10 meters at the left and at the right of the IP. The vertical axis depicts the β-functions.

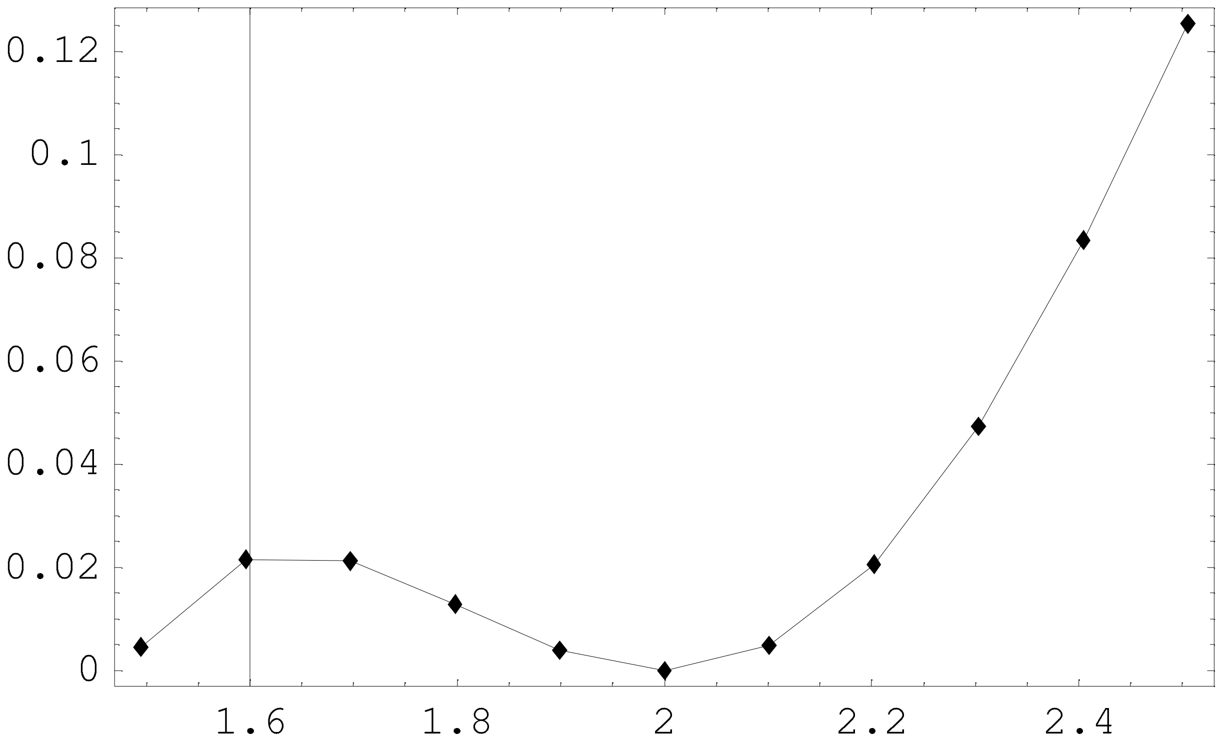

Figure 4.7: Difference of $\beta_x^\star$ when applying a linear tuning knob and calculating the β-function at the IP with the exact matrix and the linearly truncated matrix. This corresponds to applying a calculated linear tuning knob to a real storage ring. The horizontal axis shows $\beta_x^\star$ in units of meter calculated with a linearly truncated matrix. The vertical axis shows the difference to $\beta_x^\star$ in the same units calculated with the exact matrix.

A possible solution to this problem would be to calculate a tuning knob with the exact matrix, find the (nonlinear) relation between the quadrupole excitations, and then truncate it. This would also be applicability for a real machine as for the calculation of such a knob a simulation program like MAD can be used. To investigate this possibility a nonlinear knob was calculated with the analytical model. The result is given by:

$$\begin{aligned}\Delta K_2 = & \frac{-0.00455862 + (0.0503816 + 0.0863889\Delta K_1)\Delta K_1}{(0.57 + \Delta K_1)(0.736667 + \Delta K_1)} \\ & + \frac{0.005599923\sqrt{0.28214 - \Delta K_1}\sqrt{1.58881 + \Delta K_1}\sqrt{1.28807 + \Delta K_1(1.30667 + \Delta K_1)}}{(0.57 + \Delta K_1)(0.736667 + \Delta K_1)}\end{aligned} \tag{4.22}$$

The plot of this function is shown in Fig.4.8. It is strongly nonlinear in this case. Also ΔK_1 is not mapped into ΔK_2 uniquely. The range of application is determined by this behavior. Applying this knob to the exact matrix creates a change of the horizontal β-function as represented in Fig.4.9, Page 59. The values for the horizontal β-function in the quadrupoles and at the IP are collected in Tab.4.5 on the same page.

The application of this knob is rather complex in reality. Truncating this knob, which means to fit a tangent at the origin to the graph shown in Fig.4.8, results in

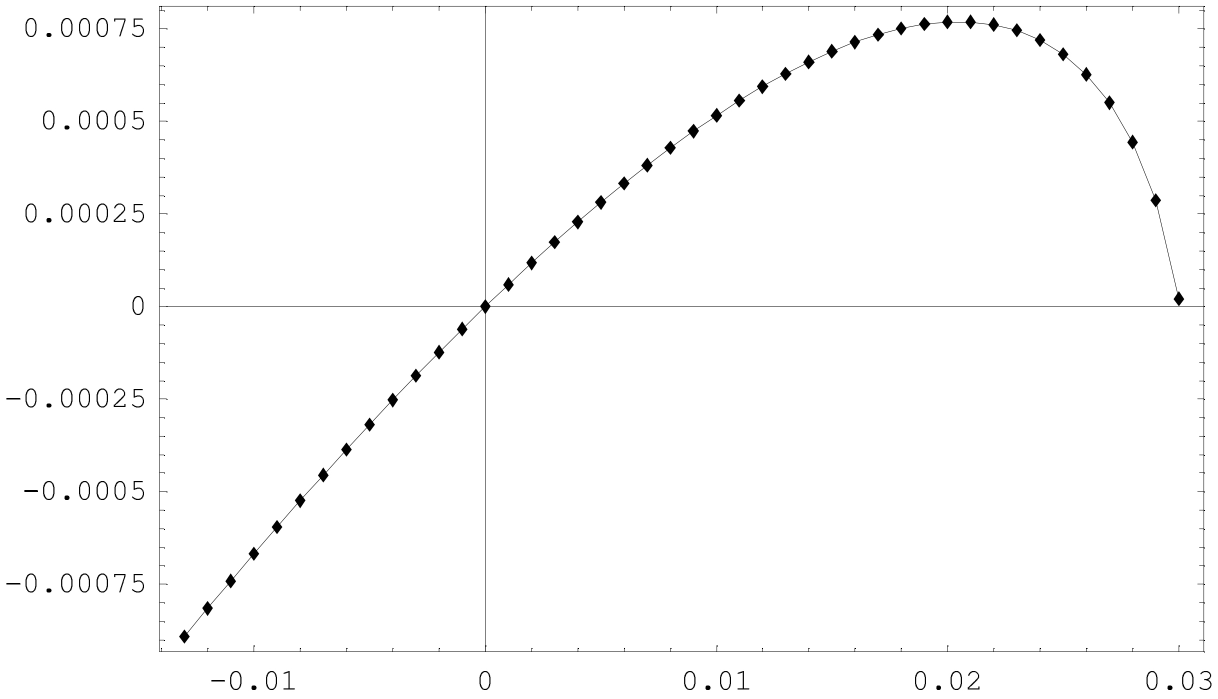

Figure 4.8: Non linear relation of ΔK_1 to ΔK_2 of the exact tuning knob. The horizontal axis depicts ΔK_1. The vertical axis shows $\Delta K_2 = f(\Delta K_1)$.

the following relation between ΔK_1 and ΔK_2:

$$\Delta K_2 \approx 0.1080 \Delta K_1 \tag{4.23}$$

Applying this truncated knob to the exact matrix creates the perturbation of the horizontal β-function depicted in Fig.4.10 with the corresponding numerical values in Tab.4.6.

Comparing these results with those obtained by applying a linearly calculated tuning knob to the exact matrix shows for this model, that the results are similar. As a result from these calculations it is sufficient to calculate the linearly tuning knob. To give a clear statement, which of the two knobs, linearly calculated or exactly calculated and truncated, gives the better result can not be stated from these results and it should be noted that they should be equal because analytical it makes no difference when you truncate. The difference is caused by the numerical treatment, were it matters at what stage the perturbation is done. Further comparison of lattice parameters would have to be performed which is beyond the scope of this chapter.

Of course also the nonlinear knob (see Eq.(4.22)) could be applied directly as shown in Fig.4.9 and Table 4.5. Its performance is, however, sensitive to small optics errors and orthogonality between two such knobs would be poor.

Table 4.5: Horizontal β-functions values in the quadrupoles at the left and at the right of the IP and at the IP when applying an exact tuning knob which was calculated with exact matrices. The initial (at the outer quadrupole at the left) β-function is kept constant. The β-function is calculated using the exact matrix.

ΔK	β_x				
	$\mathrm{QF}_{\mathrm{l2}}$	$\mathrm{QF}_{\mathrm{l1}}$	IP	$\mathrm{QF}_{\mathrm{r1}}$	$\mathrm{QF}_{\mathrm{r2}}$
-5	167	24.8	1.55	24.8	167
-4	167	23.7	1.63	23.7	167
-3	167	22.7	1.72	22.7	167
-2	167	21.7	1.81	21.7	167
-1	167	20.8	1.90	20.8	167
0	167	20.0	2.00	20.0	167
1	167	19.2	2.10	19.2	167
2	167	18.5	2.21	18.5	167
3	167	17.8	2.33	17.8	167
4	167	17.2	2.45	17.2	167
5	167	16.6	2.57	16.6	167

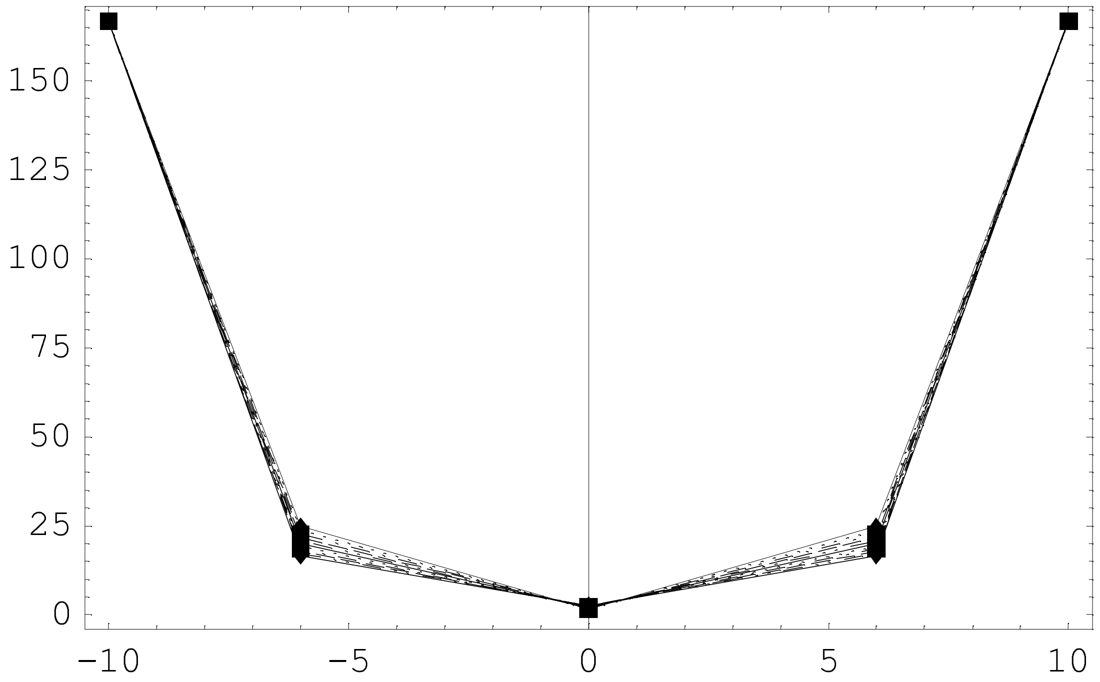

Figure 4.9: Horizontal β-functions values when applying an exact tuning knob which was calculated with exact matrices. The initial (at the outer quadrupole at the left) β-function is kept constant. The distance in units of meters is assigned to the horizontal axis with the IP located in the origin and the quadrupoles located at 6 and 10 meters at the left and at the right of the IP. The vertical axis depicts the β-functions.

Table 4.6: Horizontal β-functions values in the quadrupoles at the left and at the right of the IP and at the IP when applying an exact tuning knob which was calculated with exact matrices and afterwards linearized by truncation. The initial (at the outer quadrupole at the left) β-function is kept constant. The β-function is calculated using the exact matrix.

ΔK	β_x				
	QF_{l2}	QF_{l1}	IP	QF_{r1}	QF_{r2}
-5	167	24.2	1.50	29.2	193
-4	167	23.3	1.57	26.5	184
-3	167	22.5	1.67	24.2	177
-2	167	21.6	1.78	22.5	172
-1	167	2.08	1.89	21.1	168
0	167	20.0	2.00	20.0	167
1	167	19.2	2.10	19.3	167
2	167	18.4	2.19	18.8	170
3	167	17.7	2.27	18.6	174
4	167	16.9	2.34	18.7	181
5	167	16.2	2.40	19.0	190

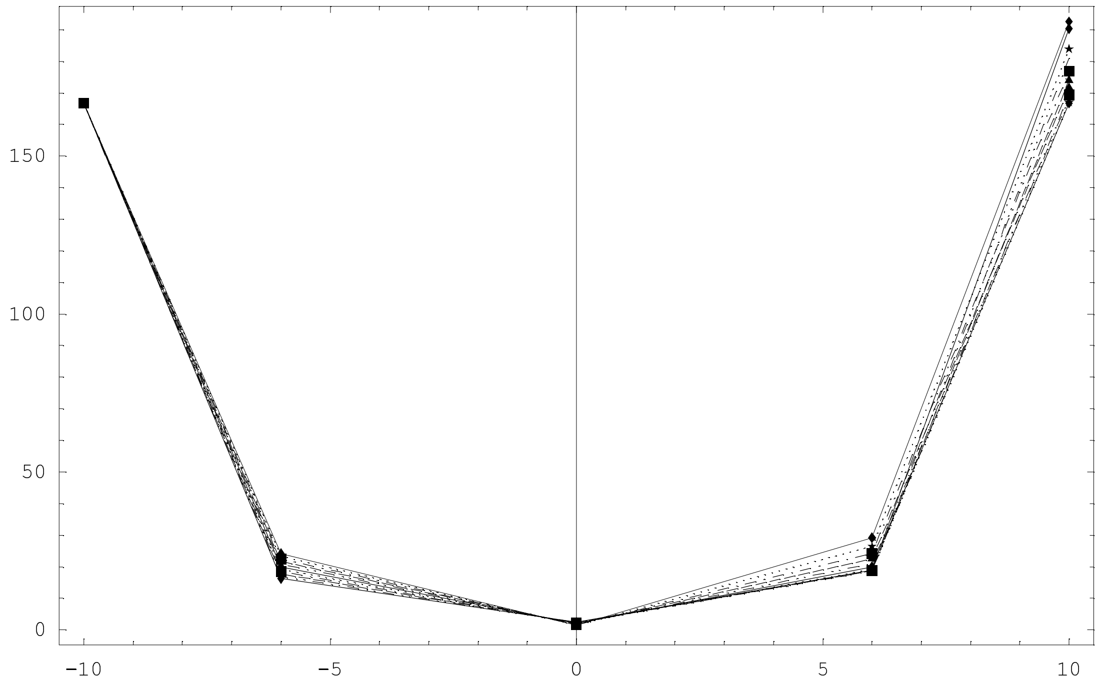

Figure 4.10: Horizontal β-functions values when applying an exact tuning knob which was calculated with exact matrices and afterwards linearized by truncation. The initial (at the outer quadrupole at the left) β-function is kept constant. The β-function is calculated using the exact matrix. The distance in units of meters is assigned to the horizontal axis with the IP located in the origin and the quadrupoles located at 6 and 10 meters at the left and at the right of the IP. The vertical axis depicts the β-functions.

Chapter 5

Measuring the IP β Function

To measure the IP β-function is a difficult task. The primary problem is the fact that no measuring device can be installed in this area because the experimental detectors occupy this space. There a two approaches to deal with this situation. One is to measure the β-function as close as possible to the IP and propagate the results, by numerically computing the transfer function with MAD e.g., into the IP. This requires a very accurate model of the lattice in this region which is not always available, especially if magnetic elements are between the point of the measurement and the IP. The standard method in LEP was to measure the mean β-functions in the two doublet magnets closest to the IP ($Q0_L$ and $Q0_R$) by K modulation.

The second approach is to use a quantity measured at the IP like the luminosity or beam-beam deflection and to deduce the β-functions from this measurement. In RHIC the standard method to minimize the beam offset is to scan one beam across the other and record the luminosity. The minimum offset is given at the peak value of this "Vernier" scan (also called Van der Meer scan). This is done for both planes.

5.1 Method Using Tuning Knobs

If the beam profile for both colliding beams is in a good approximation Gaussian or at least a truncated Gaussian, the "Vernier" scan can be used to measure the so called folded beam size. This is the quadratic sum of the two colliding beams

$$\Sigma_i = \sigma_{i_1}^2 + \sigma_{i_2}^2 \qquad i = x, y, \tag{5.1}$$

were σ_1 and σ_2 denote either the horizontal or the vertical beam size of the first beam (yellow in RHIC e.g.) and the second beam (blue in RHIC e.g.), respectively. If the beam sizes of the two colliding beams are equal, $\sigma_1 = \sigma_2 = \sigma$, then the folded beam size is simply:

$$\Sigma_i = \sqrt{2} \cdot \sigma_i \qquad i = x, y,$$

and the single beam sizes are obtained.

If the beam sizes are unequal, there is no direct method to decompose the folded beam size. However, by applying the tuning knobs to change the beam size and measuring the beam sizes with a Vernier scan the folded beam size can be decomposed into its two components. This is shown in the following section.

Derivation

When the tuning knobs are applied to change the beam size of one beam, the change can be added to the original beam size Eq.(5.1) by Taylor Series expansion. Truncating after the linear term yields

$$\sigma = \sigma_0 + \Delta\sigma = \sqrt{\epsilon\beta} = \sqrt{\epsilon \cdot \beta_0} + \frac{1}{2}\sqrt{\frac{\epsilon}{\beta_0}}\Delta\beta + \mathcal{O}\left[\Delta\beta\right], \tag{5.2}$$

were σ_0 and β_0 are the unperturbed beam size and β-function and ϵ the emittance (phase space area occupied by the beam). This is a valid treatment as the perturbation, created by the knobs, is by definition (applicable range of the tuning knobs) small. Applying a positive and negative change $\Delta\sigma$ Eq.(5.1) becomes

$$\Sigma_A^2 = (\sigma_1 + \Delta\sigma_1)^2 + \sigma_2^2, \tag{5.3}$$
$$\Sigma_B^2 = (\sigma_1 - \Delta\sigma_1)^2 + \sigma_2^2, \tag{5.4}$$

where Σ_A and Σ_B are the folded beam sizes measured by two Vernier scans. By substituting Eq.(5.2) into Eq.(5.3) and Eq.(5.4) the folded beam size is given as a function of the unperturbed β-functions, emittance, and changes of the β-functions introduced by the knobs

$$\Sigma_A^2 = \epsilon_1\beta_1 + \epsilon_1\Delta\beta_1^{(+)} + \frac{1}{4}\frac{\epsilon_1}{\beta_1}\Delta\beta_1^{(+)^2} + \epsilon_2\beta_2, \tag{5.5}$$
$$\Sigma_B^2 = \epsilon_1\beta_1 - \epsilon_1\Delta\beta_1^{(-)} + \frac{1}{4}\frac{\epsilon_1}{\beta_1}\Delta\beta_1^{(-)^2} + \epsilon_2\beta_2, \tag{5.6}$$

were the suffix represents the two different beams. Taking the difference of the two measured folded beam sizes gives:

$$\Sigma_A^2 - \Sigma_B^2 = \epsilon_1\left(\Delta\beta_1^{(+)} + \Delta\beta_1^{(-)}\right) + \frac{1}{4}\frac{\epsilon_1}{\beta_1}\left(\Delta\beta_1^{(+)^2} - \Delta\beta_1^{(-)^2}\right). \tag{5.7}$$

$\Delta\beta_1^{(+)}$ and $\Delta\beta_1^{(-)}$ are the changes of the β-function when applying the knobs once to increase and the other time to decrease the β-function. If the knob is linear these values are the same. Shown by the analysis of the characteristics of the tuning knobs this is true in first approximation

$$\Delta\beta_1^{(+)} = \Delta\beta_1^{(-)} = \Delta\beta_1 \tag{5.8}$$

and then Eq.(5.7) becomes

$$\Sigma_A^2 - \Sigma_B^2 = 2\epsilon_1\Delta\beta_1. \tag{5.9}$$

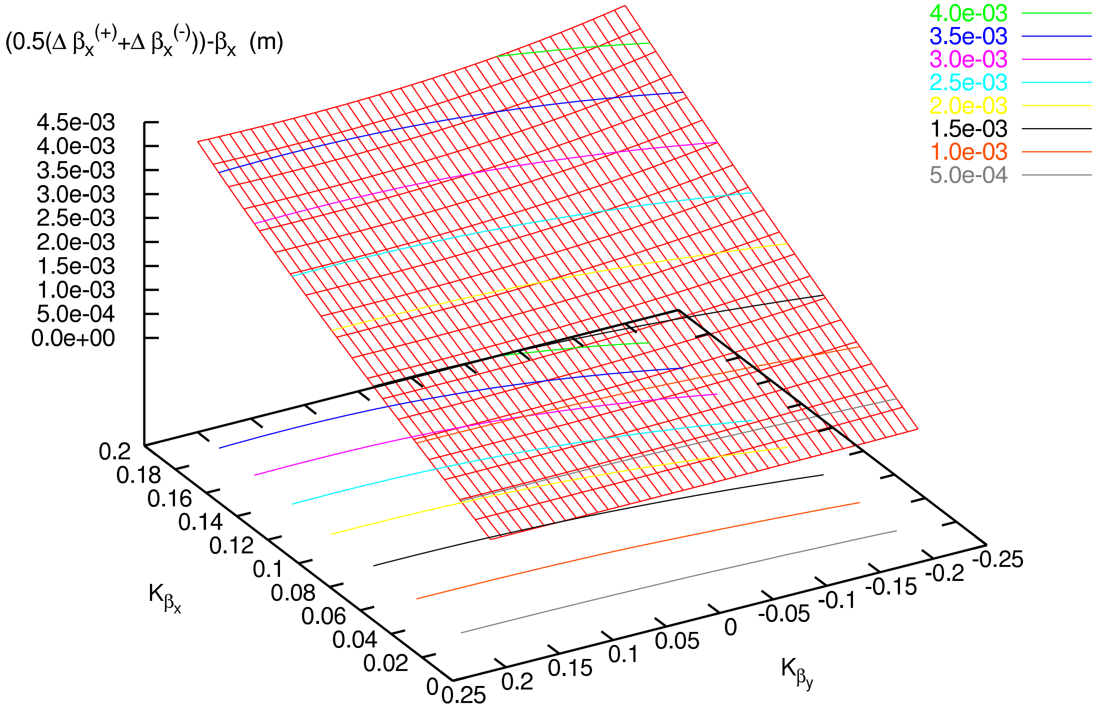

Figure 5.1: Error estimation for the assumption that the knob is linear. The effect of the difference between simulated and assumed change of the β-function for the linear term of Eq.(5.7) was computed for a horizontal tuning knob.

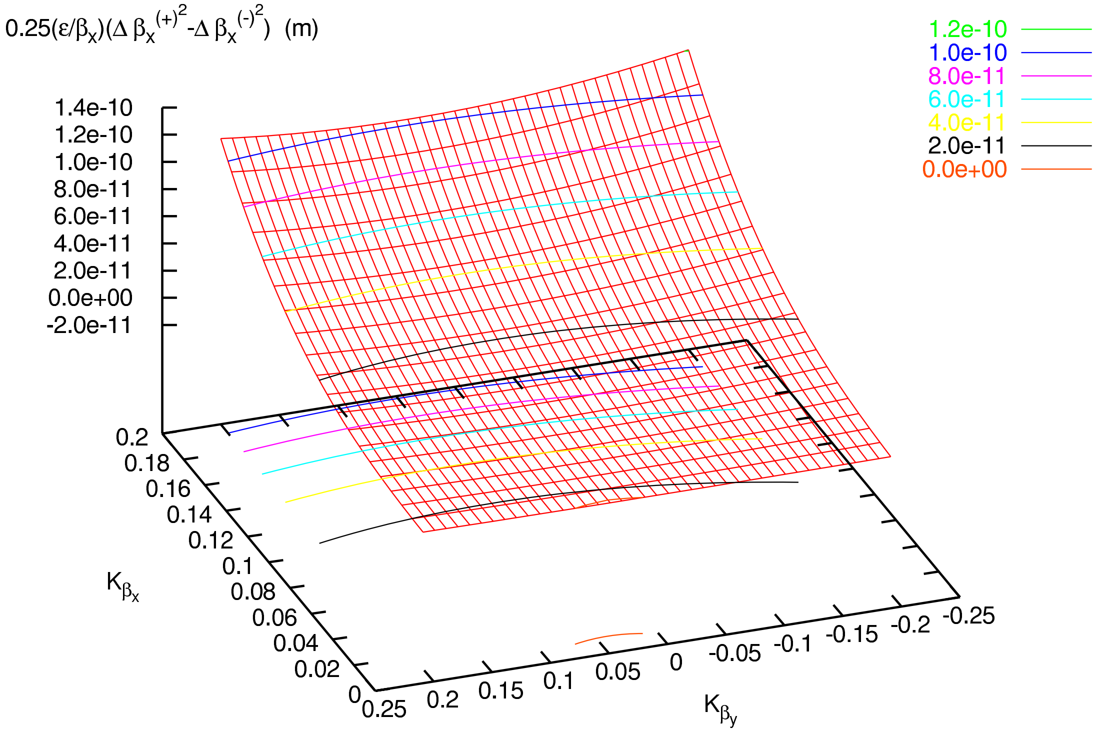

Figure 5.2: Error estimation for the assumption that the knob is linear. The effect of the difference between simulated and assumed change of the β-function for the quadratic term of Eq.(5.7) was computed for a horizontal tuning knob.

Thus assuming the emittance of beam 1 is known the change of the β-function of beam 1 created by the knob can be calculated

$$\Delta\beta_1 = \frac{\Sigma_A^2 - \Sigma_B^2}{2\epsilon_1}. \tag{5.10}$$

The error introduced by the assumption that the knob is linear ($\Delta\beta_1^{(+)} = \Delta\beta_1^{(-)} = \Delta\beta_1$) is shown in Fig.5.1 for the linear term of Eq.(5.7) and in Fig.5.2 for the quadratic term of Eq.(5.7). The effect of the quadratic term is extremely small because it is multiplied by the emittance. This estimation was computed for the RHIC knobs.

When using a third Vernier scan to measure the folded beam size with no tuning knob applied

$$\Sigma_0^2 \quad = \quad \sigma_1^2 + \sigma_2^2 \tag{5.11}$$

the beam size of beam one can be determined as

$$\beta_0 = \frac{1}{8\epsilon}\frac{\left(\Sigma_A^2 - \Sigma_B^2\right)^2}{\Sigma_A^2 + \Sigma_B^2 - 2\Sigma_0^2} \tag{5.12}$$

This procedure can be repeated for the orthogonal plane and the other colliding beam. By doing so, the four individual beam sizes of the two colliding beams can be extracted.

Measurement Error Estimation

The drawback of this method is that the measured, knob induced change of the β-function has a measurement uncertainty of approximately the same order of magnitude. This is caused by the measurement error of the Vernier scan. The error of the emittance measurement is, as compared to the latter error, one order of magnitude smaller. For the RHIC simulation the calculated error, when assuming a measurement error of 5% for each Vernier scan, is $\pm 90\%$. For the same measurement error assumption the calculated uncertainty for $\Delta\beta$ is $\pm 72\%$. The measurement uncertainty for the calculation of β_0 was several orders of magnitude higher. To apply this method in practice with reasonable results an improvement for the measurement error of the Vernier Scan has to be achieved.

5.2 K Modulation Method

The measurement of $\beta^\star$ at interaction or symmetry points is described on page 36f in [34]. There the case of a symmetric IP is discussed. By exciting the pair of triplet quadrupoles closest to the IP with an asymmetric strength change ΔK (the same ΔK for both quadrupoles with an opposite sign) the error of $\beta^\star_{design}$ can be determined:

$$\begin{aligned} \beta^\star &= \beta^\star_{design}(1 + \alpha_{optics}\eta^2) \\ \eta &= \langle\beta_+\rangle - \langle\beta_-\rangle = 4\pi\frac{\Delta Q_+ - \Delta Q_-}{\Delta K} \end{aligned}$$

Here $\beta^{\star}_{design}$ is the nominal IP beta function, $\langle\beta_+\rangle$ and $\langle\beta_-\rangle$ the average β-functions at the exited quadrupoles and α_{optics} is a lattice dependent factor which can be determined with an optics program, e.g. MAD. η is the ratio of introduced tune change to quadrupole excitation multiplied by 4π. The tune change

$$|\Delta Q_+| - |\Delta Q_-| \tag{5.13}$$

is zero to first order when the optics is perfectly symmetric. A further advantage of this method is that due to the phase advance ϕ between the quadrupoles closest to the IP, which is usual 180°, there is no beta beat created outside this region.

The IPs in LHC and RHIC are antisymmetric as described earlier. Therefore the absolute values of the average beta functions at the exited quadrupoles are not equal and the tune shift introduced by antisymmetric excitation will not be zero in the nominal case. But in the case of a round beam the tune shift introduced must be equal for the horizontal and vertical plane. Equation 5.13 can therefore be adapted to

$$(|\Delta Q^{as}_+| - |\Delta Q^{as}_-|)_x - (|\Delta Q^{as}_+| - |\Delta Q^{as}_-|)_y = 0 \tag{5.14}$$

for the antisymmetric excitation. This can also be the case if the optics is distorted. For this reason a second measurement has to be carried out. The excitation of the triplet quadrupoles can also be symmetric. In this case the introduced beta change at the quadrupoles will add up and create a beta beating in the ring. Also the tune change will not cancel but add up, which means that the excitation can be smaller to create a measurable tune change and the created beta beat will be acceptable. The sum of the created tune change has to be zero in the symmetric case:

$$(|\Delta Q^{sym}_+| + |\Delta Q^{sym}_-|)_x + (|\Delta Q^{sym}_+| + |\Delta Q^{sym}_-|)_y = 0 \tag{5.15}$$

Together with Eq.5.14 the problem is determined. When both Eqs.(5.14 and5.15) are satisfied then the α-function is zero at the IP.

Fig.5.3 shows a simulation of this procedure for the horizontal plane and Fig.5.4 for the vertical plane with MAD. The mean β-functions in the two closest triplet quadrupoles, one on the left and one on the right side, are measured. This is done by excitation of the same two quadrupoles in a specific manner. The same increments to the integrated quadrupole strength are applied once symmetrically ($\Delta K_L = \Delta K_R$), once anti-symmetrically ($\Delta K_L = -\Delta K_R$). The plots show the tune change ΔQ as a function of the excitation ΔKl. The suffixes on ΔQ indicate the measured plane and the sign of the excitation in the quadrupoles. The slope of the curve corresponds to a combination of the mean β-functions in the quadrupoles of the form $(\langle\beta\rangle \pm \langle\beta\rangle)_{x,y}$. Plot A and B in Fig5.3 depict the results for horizontal, plot C and D in Fig.5.4 for the vertical plane in IP1. The results are shown in the header of the plots. To compare these with the values for the mean β-functions in MAD the triplet quadrupoles were sliced in 1000 pieces and the average value over all slices computed:

$$\begin{aligned}
\langle\beta\rangle_{x_L} &= 1548.75\\
\langle\beta\rangle_{x_R} &= 1231.44\\
\langle\beta\rangle_{y_L} &= 1241.05\\
\langle\beta\rangle_{y_R} &= 1559.84.
\end{aligned}$$

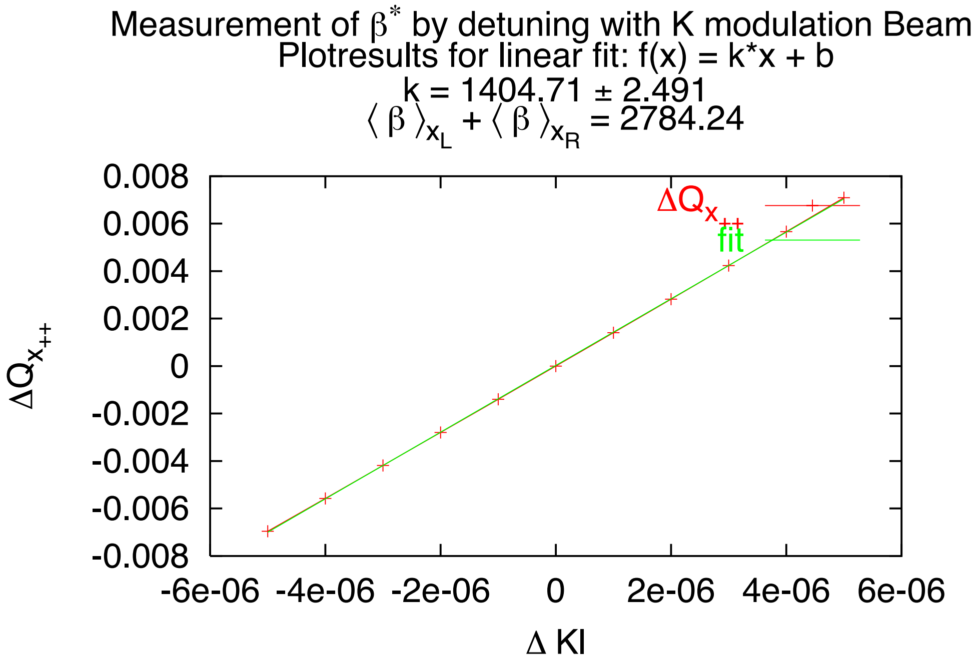

Plot A

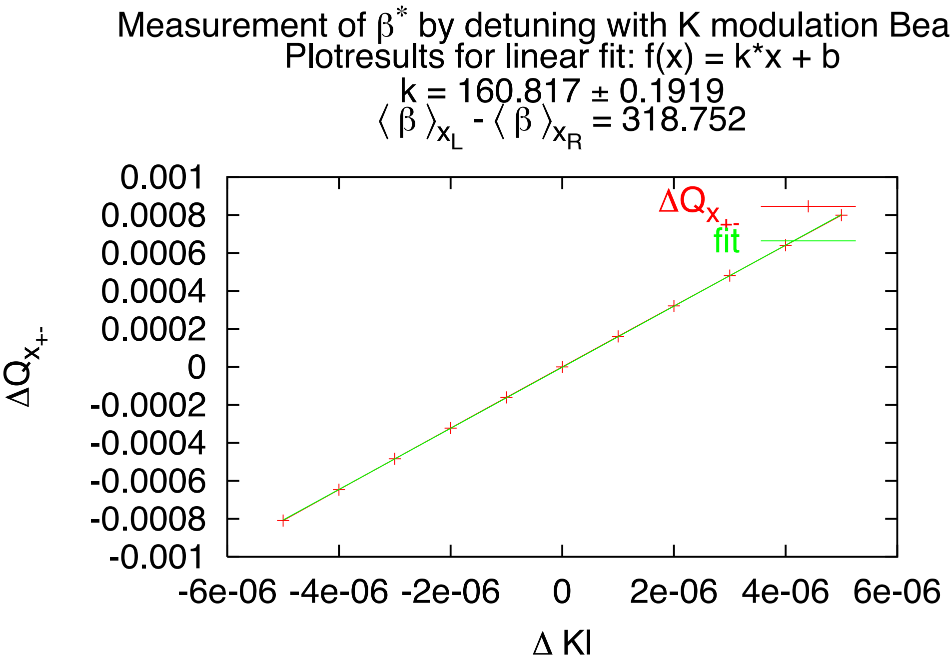

Plot B

Figure 5.3: Simulation of $\beta^\star$ measurement for the horizontal plane with MAD. The results are shown in the header of the plots. To compare these with the values for the mean β-functions in MAD the triplet quadrupoles were sliced in 1000 pieces and the β averaged over these slices: $\langle\beta\rangle_{x_L} = 1548.75 \quad \langle\beta\rangle_{x_R} = 1231.44$.

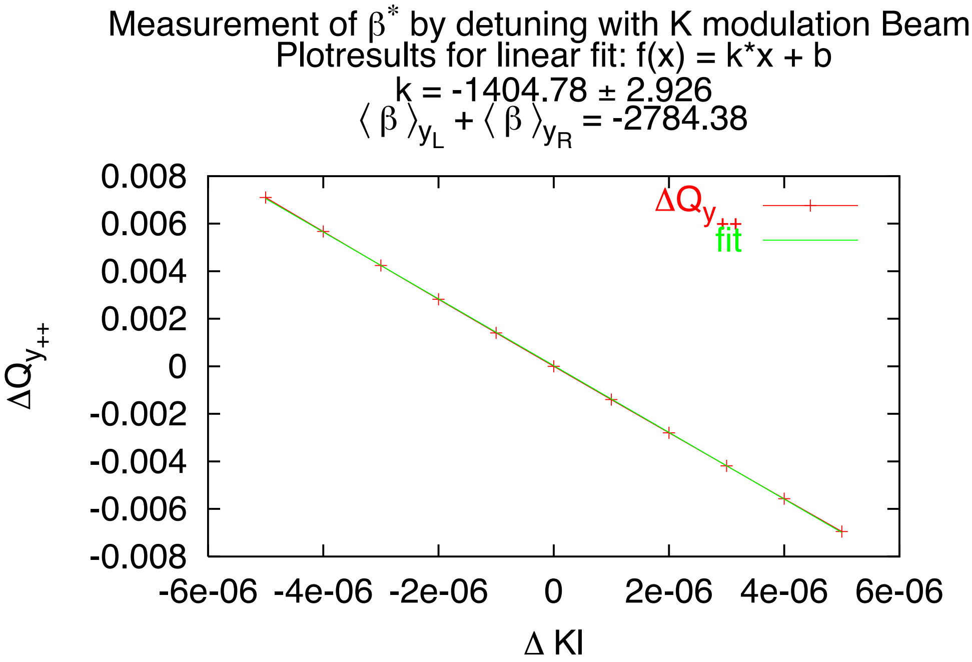

Plot C

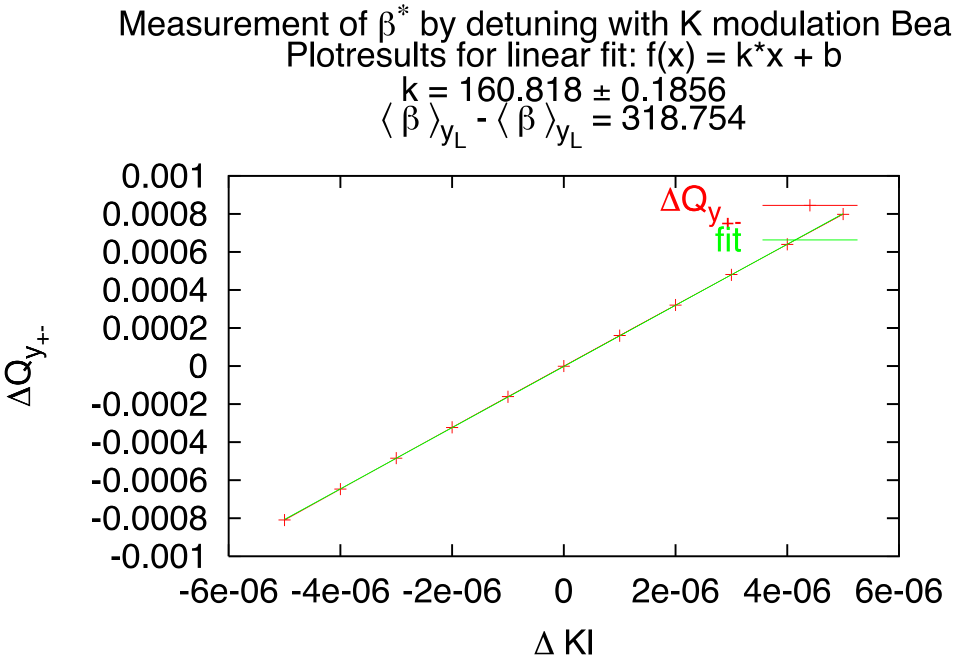

Plot D

Figure 5.4: Simulation of $\beta^\star$ measurement with MAD for the vertical plane. The results are shown in the header of the plots. To compare these with the values for the mean β-functions in MAD the triplet quadrupoles were sliced in 1000 pieces and the β averaged over these slices: $\langle\beta\rangle_{y_L} = 1241.05 \quad \langle\beta\rangle_{y_R} = 1559.84$.

In this previous simulation no errors were present. When changing the IP β-function with the tuning knobs the mean β-functions measured by K modulation in the triplet quadrupoles also changes. This is shown in Fig.5.5. This function can be used to deduce the IP β-functions from the ones measured in the quadrupoles. In this example the beam waist is kept constant in the IP ($\alpha^{\star} = 0$).

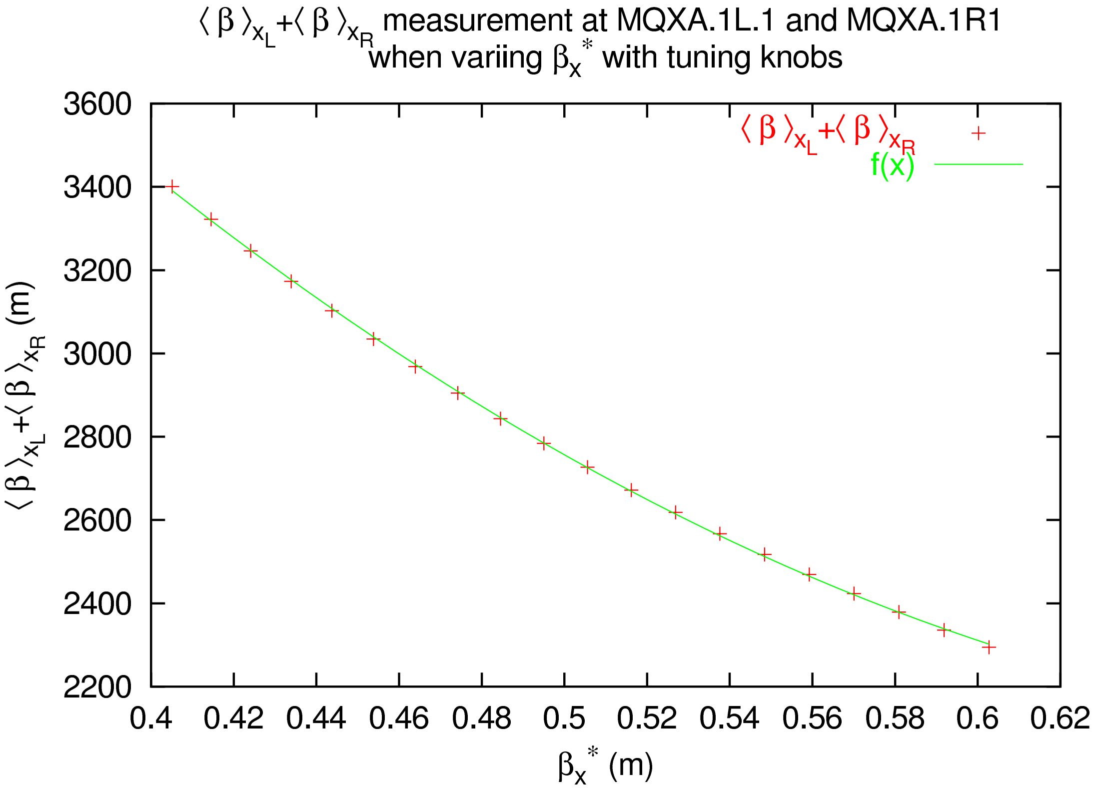

Figure 5.5: Simulated measurement of $\langle\beta\rangle_{x_L} + \langle\beta\rangle_{x_R}$. The IP β-function was changed with the tuning knobs and by symmetric K modulation the sum of the mean β-function in MQXA.1L1 and MQXA.1R1 was calculated.

When introducing random quadrupole gradient errors the situation is more complex. The beam waist will be moved ($\alpha^{\star} \neq 0$) and in addition the β-function will be changed. When measuring in this situation the β-function in the quadrupoles with K modulation using the curve of plot 5.5 to calculate the IP β-function will give a wrong value, because the waist shift is not taken into account. Fig.5.6 shows the simulation results when calculating the β-function in the triplet quadrupoles MQXA.1L1 and MQXA.1R1 on the left and on the right side of IP1 by K modulation. These values are plotted as a function of the IP β-function. In addition the values have been marked in color according to the waist shift. Two important features are evident. The larger the waist shift the bigger the error introduced by disregarding this effect. Second, the offset from the values with no waist shift is not linearly dependent on the magnitude of the latter. The red curve in Fig.5.6 is the curve obtained from plot 5.5. The problem is to find a way to correct the measured values. For this, the waist shift has to be determined. Taking the ratio of the single K modulation measurements $\langle\beta\rangle_{x_L}/\langle\beta\rangle_{x_R}$ and

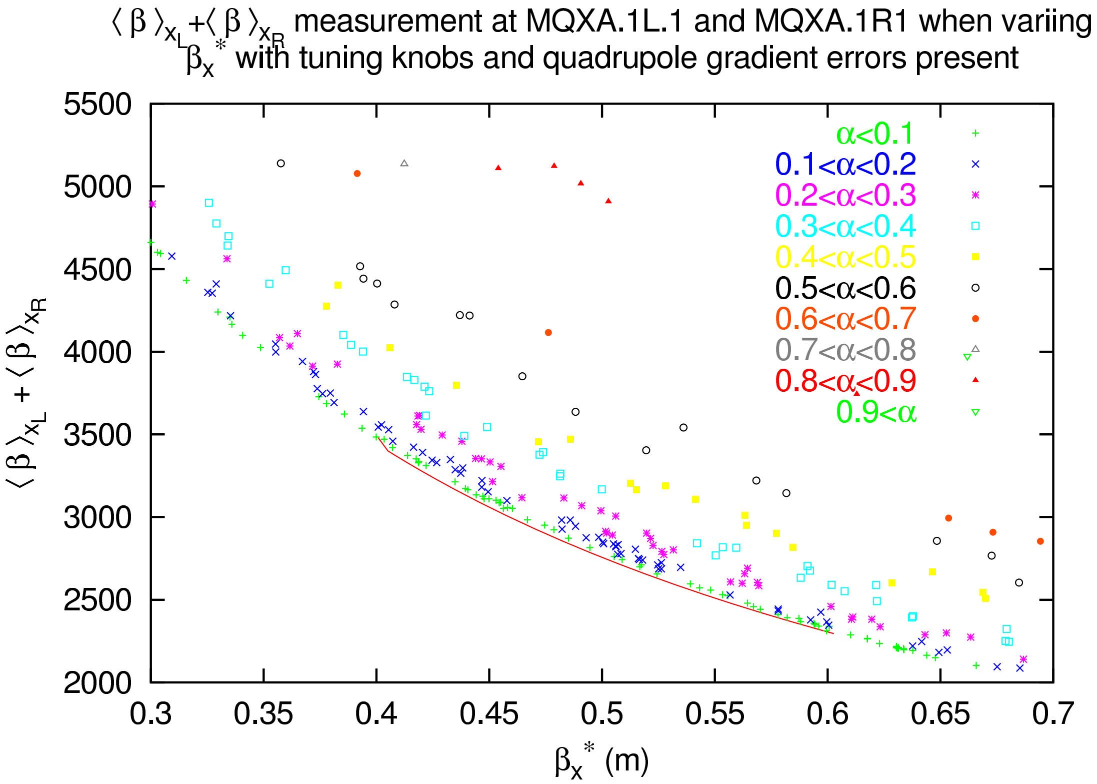

Figure 5.6: Simulated measurement of $\langle\beta\rangle_{x_L} + \langle\beta\rangle_{x_R}$ with random quadrupole gradient errors in the ring.

plotting the α-function at the IP as a function of this ratio a result is obtained as shown in Fig.5.7. There is a strong correlation and nearly linear dependence! For the values with a larger waist shift there is a larger spread around the mean value represented by the green curve. A correction factor using the lattice model and MAD can be calculated to describe the linear dependence of α on $\langle\beta\rangle_{x_L}/\langle\beta\rangle_{x_R}$, using the same approach as in [34]. With the assumption, that there is a simple relation between measured sum of mean β-functions with waist shift, $\alpha^\star$ and measured sum of mean β-functions measured without waist shift and change of $\beta^\star$ with tuning knobs

$$\underbrace{\langle\beta\rangle_{x_L} + \langle\beta\rangle_{x_R}}_{\text{with waist shift}} - \alpha^\star_{MAD} \cdot C = \underbrace{\langle\beta\rangle_{x_L} + \langle\beta\rangle_{x_R}}_{\text{tuning knobs}},$$

the correction factor C can be computed. An attempt of finding such a simple model is shown in Fig.5.8. Using this correction a simulation was carried out where random gradient errors were introduced in the lattice. Then the mean β-function measurement by K modulation was simulated and the results obtained were used to calculate the β-function at the IP. These values were corrected with the factor calculated above. The resulting $\beta^\star$ was then compared to the one computed by MAD. This comparison is presented in Fig.5.9. The correction works fine for β values between 0.4 and 0.6 meters. Outside this boundary the scattering around the diagonal becomes clearly larger. This is due to the fact that the error of the tuning knobs are only small around the nominal $\beta^\star$ of 0.5 meter.

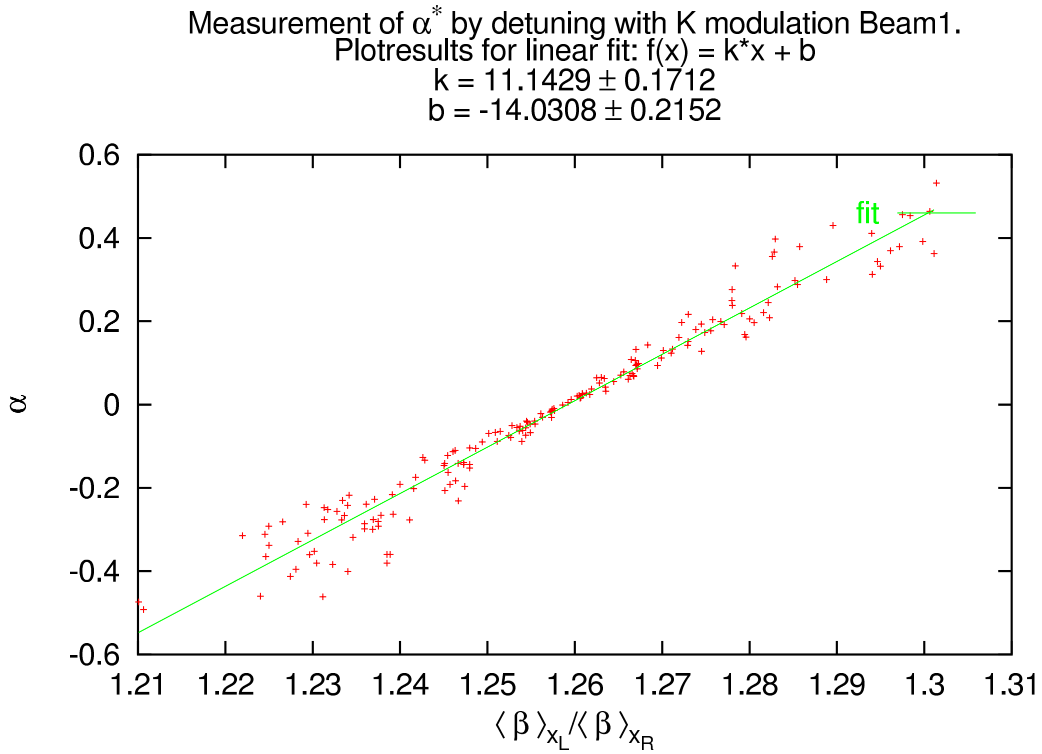

Figure 5.7: Relation between the $\langle\beta\rangle_{x_L}/\langle\beta\rangle_{x_R}$ and the α-function at the IP.

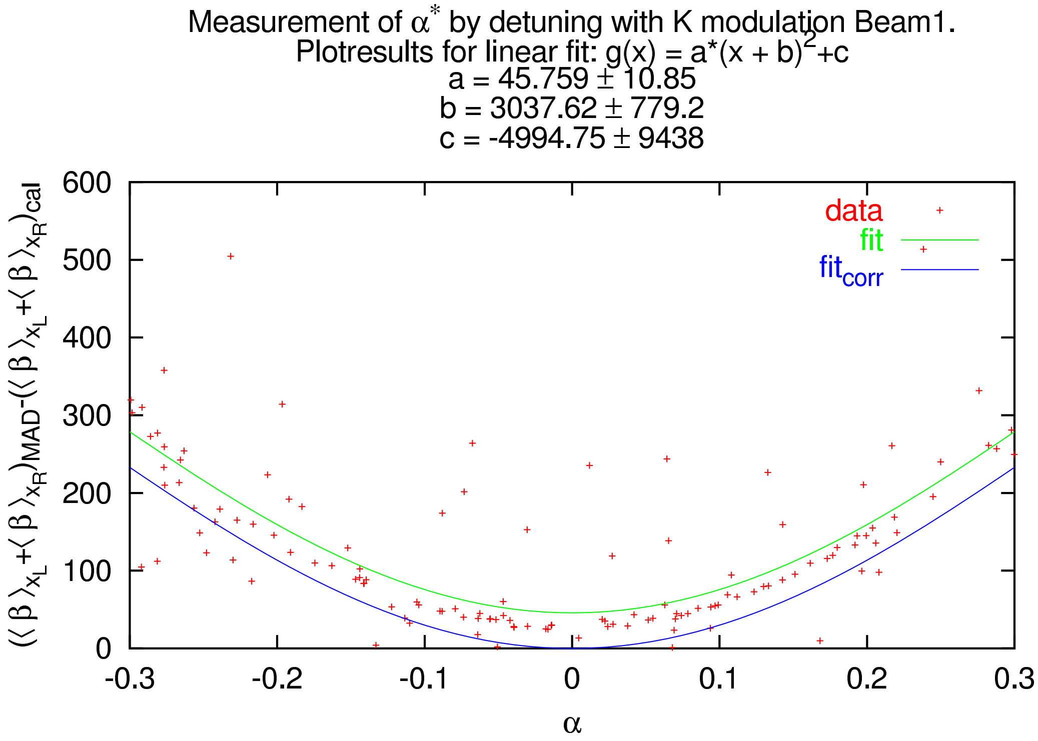

Figure 5.8: Computed correction factor for the α-function. The green curve shows the fit of the data points. There is an offset at $\alpha = 0$. The blue curve shoes a correction of this fit by the offset.

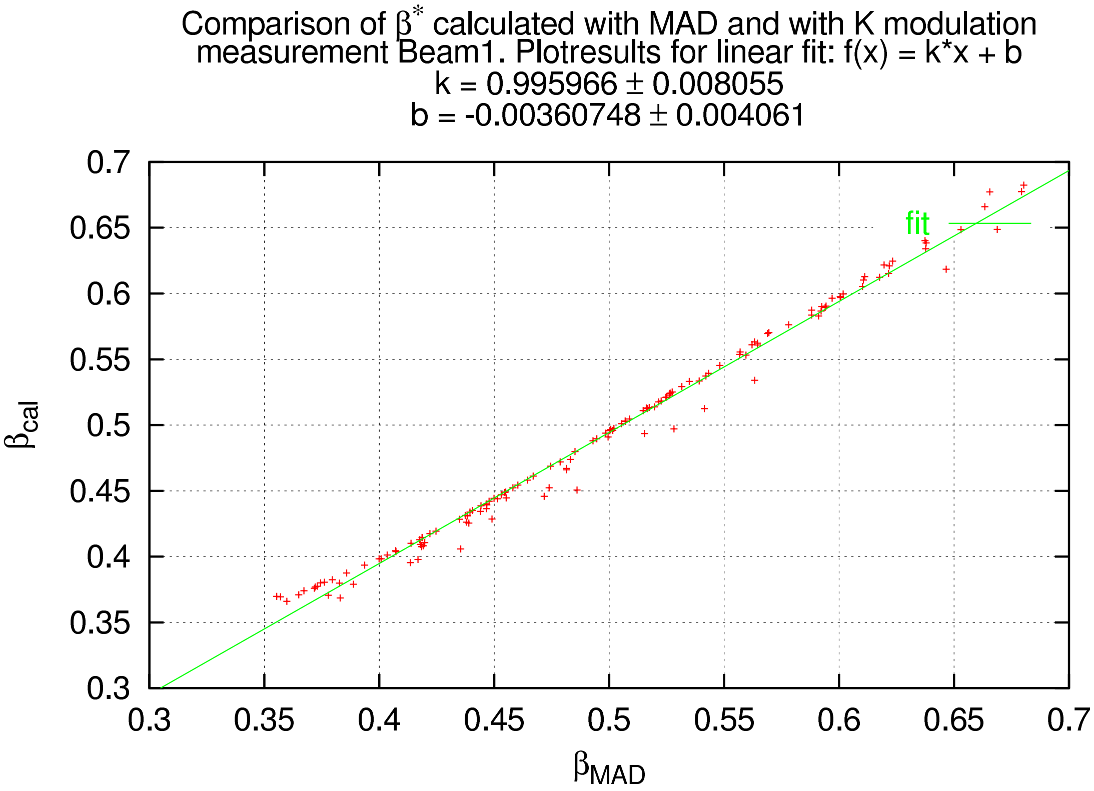

Figure 5.9: Comparison of β-functions obtained by simulated K modulation in the presence of quadrupole gradient errors and using the correction factor calculated as described in the text to correct the error from the waist shift with the “exact” value from MAD.

This method to determine the β-function can be applied when the error of the nominal $\beta^\star$ is small, of the order of $\pm 20\%$. In this case, the accuracy is very good. To measure larger deviations other methods are favorable where the precision needs not be so high.

Chapter 6

$\beta^\star$-Tuning Knobs for LHC

The various methods of obtaining a tuning knob have been described in chapter 3. For LHC the first set of knobs (one knob for each plane) was calculated with the MAD match method using MAD8 and LHC lattice version V6.2. The lattice used had no crossing angle in IP1 and IP5. For this reason there was no dispersion in the vertical plane.

The demands on the knobs are to function within a variation of $\pm 20\%$, to be orthogonal in the horizontal- and vertical- plane, and to create no β-beating outside the manipulated insertion region. The scaling of the $\beta^\star$ with respect to the variable m was to be linear, the change of other constraints to lie within a specified region. They should correct the $\beta^\star$ independently of the source of the error, and be simple for operation.

The performance of the knobs had to be tested. Both knobs, when varied over their nominal range, must meet the conditions of the different criteria described above. If this is the case the second stage of testing is started. Various errors are introduced in the lattice and the knobs are used to correct them. This is done step by step to see to which types of errors the knobs could be applied.

Due to a lattice update to version V6.4, which was only available for MADX (MAD version 10), the validation of the tuning knobs was repeated to verify the impact of the lattice changes. With this new version also the crossing angle was included into the lattice. Including the crossing angle forced a recalculation of the tuning knobs. In Addition this allowed a study of the effect of the tuning knobs on the crossing angle.

The correction algorithm for the closed orbit was rewritten in the new MAD version based on the planed correction scheme for LHC. This new orbit correction module was used to simulate closed orbit distortions based on the expected errors and a correction to realistic level of 0.5mm rms. The applicability of the tuning knobs was tested under these conditions.

A further possible limitation of the use of the tuning knobs is the long-range beam-beam effect. The performance of the tuning knobs in the presence of the other beam was tested with the TRAIN code and the effect on beam separation and luminosity investigated.

6.1 Calculating $\beta^\star$ Tuning Knobs with MAD8 and Lattice Version V6.2

Layout and Design Criteria

The design of the LHC insertion regions for IP1 and IP5 is asymmetric (see Fig.6.1). These two insertions have the identical optical layout. The only difference concerns the crossing angle. In IP1 the crossing angle is in the vertical plane and in IP5 it is in the horizontal plane. The beams pass through the inner triplet magnets (Q1-Q3) at the left and at the right from the IP, also called final focus) in a common beam pipe off center of the magnetic field axis. The offset is chosen so that the beam with the larger beam size is closer to the magnetic axis to reduce the effect of non linear field errors which increase with the distance to the magnetic axis and to use the maximum possible physical aperture. Therefore the magnets of the inner triplet cannot be used to adjust the $\beta^\star$.

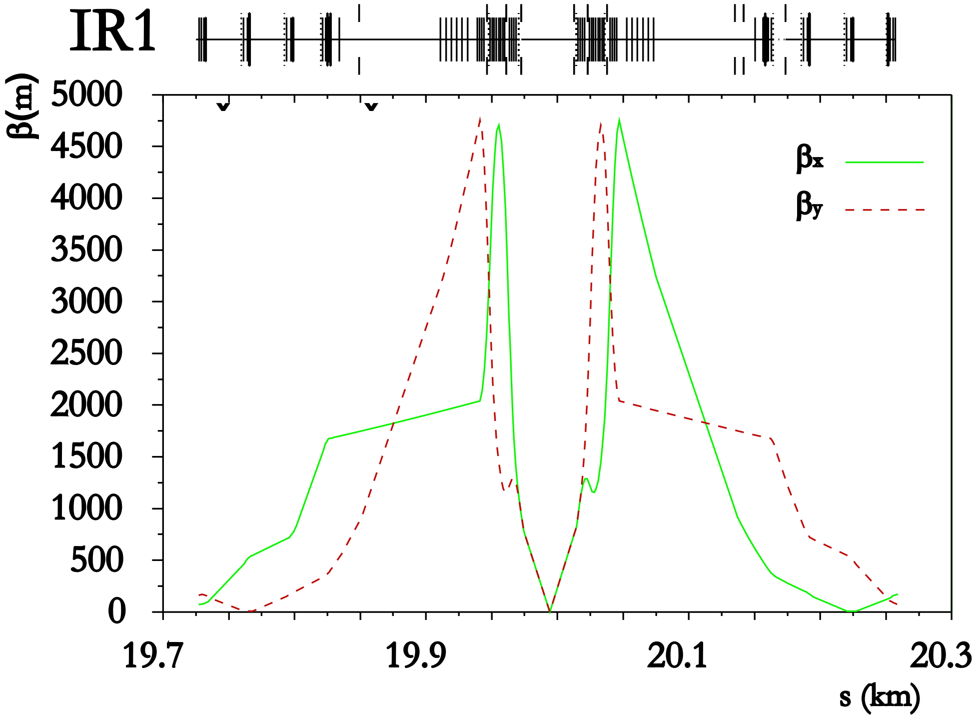

Figure 6.1: β-functions at IR1 between Q7 left and right from IP1 computed with MAD8 and lattice version V6.2.

The closest magnet that can be used is Q4 at the left and at the right from the IP. It is separated from the triplet by the combiner and separation dipoles (dogleg-magnets). These combine/separate the incoming/outgoing beams. There are three further quadrupoles (Q5-Q7) which can be used without any restriction. It has to be noted that Q7 is the last quadrupole of the dispersion suppressor. This means that the dispersion is already close to zero in this magnet. Q4 is part of the system that creates the crossing angle. A change of its integrated magnet strength will thus effect the crossing angle. The magnitude of this effect will be shown in the section that describes the simulation including crossing angle.

Because of the asymmetric β-functions, the different phase advance and the need to correct both planes, there is no pair of quadrupoles that can accomplish the correction for either of the planes without changing the other plane's β-function. This and the fact that the triplet magnets cannot be used is the reason that the LEP correction scheme is not applicable for LHC.

The position of the different tuning quadrupoles and the dipoles separating and combining the two beams are shown in Fig.6.2.

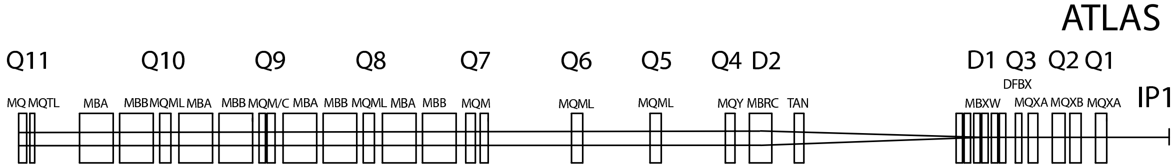

Figure 6.2: Position of the different magnets in LHC IR1 and parts of the dispersion suppressor.

Preserving Asymmetry

An original design goal was to preserve the asymmetry when the corrections are applied. The implication on the tuning knobs from this condition was that these must also be asymmetric. This means that the tuning quadrupoles on the left and on the right side of the IP have to be soft-wired (these values are fixed in relation to each other and therefore each pair only represents one degree of freedom) in the calculations. A first simulation study showed, by creating the expected error scenario, that this condition cannot be fulfilled. To correct an error under this condition the errors in the two planes also have to be related. This can be explained by the fact that the preservation of the asymmetric powering couples the $\beta^\star$ values of the planes to each other. Also the number of degrees of freedom is reduced and thus the number of allowed constraints are reduced. This either affects the characteristics (change of optics functions by the knob) or else the number of tuning quadrupoles has to be doubled. Even if the second approach is taken it might not be possible to find a solution. As this idea has no practical basis it was dropped after the initial study.

First Knob Vectors

The first knob vectors were constructed using Q4 to Q7 at the left and at the right from the IP1 for the horizontal plane. As constraints where chosen $\beta^\star$, $\alpha^\star$ and two β-functions values at two points in the ring outside the insertion which are separated by a phase advance of $\phi = \frac{\pi}{4}$. This was done for both planes. The $\beta^\star$-value of one plane is set to the nominal value, for the LHC at collision equal to 0.5 meters, so as to create no change of the β-function in this plane, while the other is varied to create the desired change. The knob vector was constructed by matching a change to the horizontal $\beta^\star$ value from 0.5 to 0.6 meter. The changes of the integrated strengths of the tuning quadrupoles formed the vector. To create a desired change of different magnitude this vector was scaled by multiplication.

When matching to the target value it is important to check how good the match is. For this particular case the most important criterion is to create no β-wave outside the insertion region. This was checked for each match by taking the difference of the β-function around the whole ring before and after the match. This is shown for the horizontal plane in Fig.6.3. Except in one region the difference is zero. This region at $s = 20$ km is the insertion region where the manipulations are performed. To see the effect of these a zoom of this area is shown in Fig.6.4. The difference of the β-function starts with the first tuning knob to reach the desired change in the IP and then eventually drops to zero at the last tuning quadrupole. The same procedure has to be repeated for the orthogonal plane, in this case the vertical plane. The result is in the optimum case comparable to the one of Fig.6.3. There is no difference in the β-function before and after the match except in the area depicting the insertion of the tuning quadrupoles. A zoom of this insertion is plotted in Fig.6.5. Here the situation must be different compared to the horizontal β-function. The changes of the β-function starts at the incoming side of the insertion with the first tuning quadrupole but, is contrary to before, brought to zero in the last tuning quadrupole of the same side of the IP to maintain a constant $\beta^{\star}$. At the other side of the insertion it fulfills the same condition namely to produce no β-wave propagating around the ring.

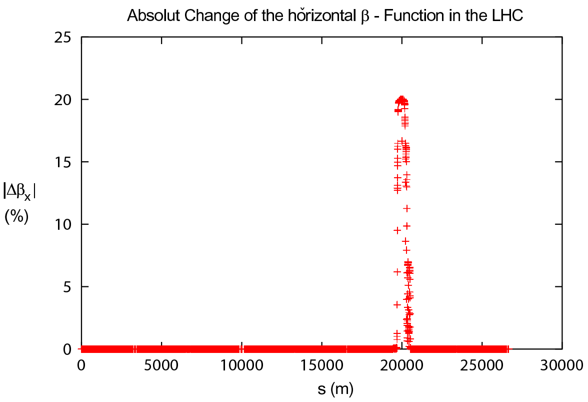

Figure 6.3: Change of the β function in the horizontal plane when the IP1 tuning knob for this plane is applied. The changes occur only in the region between KQ13.L1B1 and KQ13.R1B1.

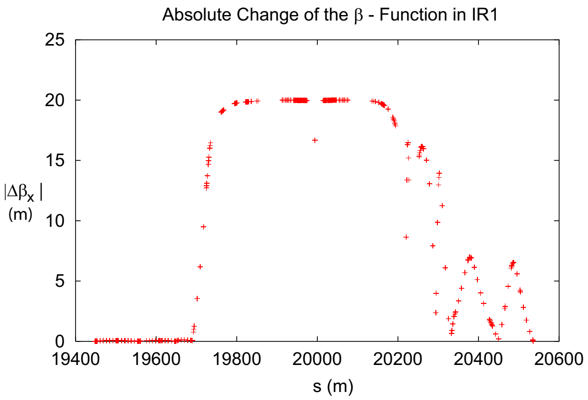

Figure 6.4: Change of the β function between KQ13.L1B1 and KQ13.R1B1 in the horizontal plane when the tuning knob for this plane is applied. In order to have the desired change at the IP the difference in the incoming β function on the left side of the IP creates this change. The outgoing beta function changes create no β beating in the rest of the ring.

It is important to not only observe the behavior of the constraints, but also to monitor what is happening to other optics functions of interest (observables) like the horizontal dispersion in this case. If is not constrained to be zero outside the specific insertion region, a dispersion wave will be created. The task is to check the size and

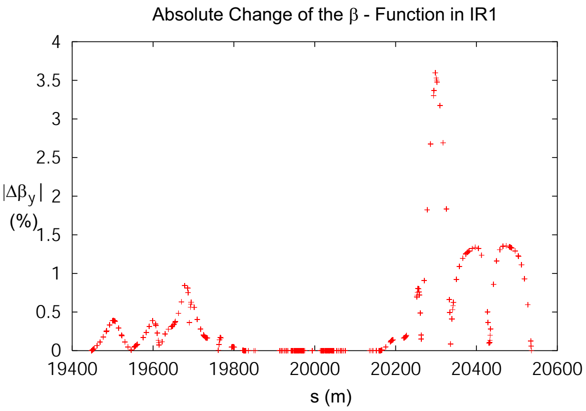

Figure 6.5: Change of the β function between KQ13.L1B1 and KQ13.R1B1 in the vertical plane when the tuning knob for the other plane is applied. This shows the orthogonal behavior of this knob.

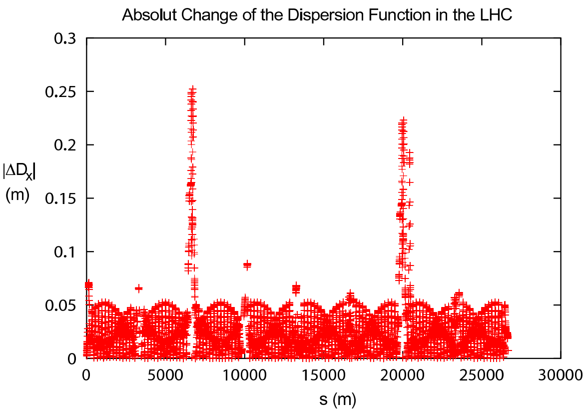

Figure 6.6: Dispersion beat around the ring created by applying the tuning knob for the horizontal plane. The biggest changes of the dispersion are in IR1 and IR5.

magnitude of this wave around the whole ring and to analyze, if in critical areas the growth is not too big. A graph of the dispersion wave created by the match for a horizontal tuning knob is shown in plot 6.6. Nearly everywhere a wave is visible, propagating around the ring with a maximum amplitude of approximately six centimeters, except in two points where two spikes of approximately 25 centimeters are located. These and, as already discussed in theory, other critical areas for dispersion changes have to be investigated closer. A zoom of the two areas where these spikes appear shows that in Fig.6.6 the high dispersion points are the low β IPs at IP1 and IP5. The plots for IR1 (see Fig.6.7) and IR5 (see Fig.6.8) show the same characteristic behavior.

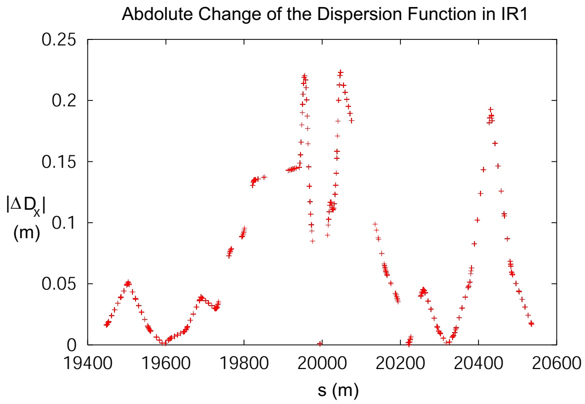

Figure 6.7: Zoom of figure 6.6 showing the region between KQ13.L1B1 and KQ13.R1B1. The change of the dispersion at the IP is smaller than in the rest of the region.

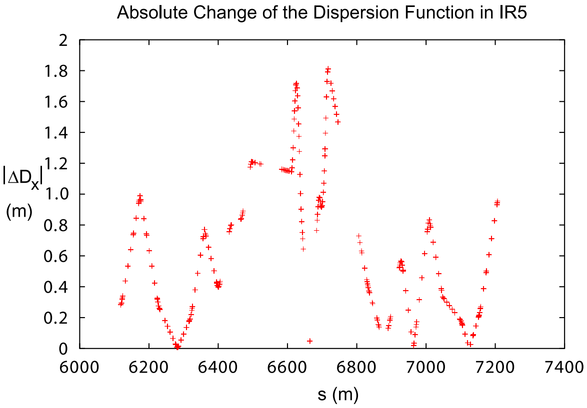

Figure 6.8: Zoom of figure 6.6 showing the region between KQ13.L5B1 and KQ13.R5B1. The change of the dispersion at the IP is smaller than in the rest of the region.

In the IP the dispersion wave is small and acceptable. But in the triplet quadrupoles the maximum is reached. It has to be verified that the dispersion growth in the triplet causes no problems (dynamic aperture, etc.).

The first calculated tuning vector fulfilling the above described conditions (minimum dispersion and no β beat), was characterized by scaling the $\beta^\star$ from 0.45 to 0.55 meter (it was assumed that by using half the desired operating range of the tuning knobs the created changes would be minimized) and observing the behavior of the $\alpha^\star$ and $\beta^\star_y$ values as shown in Plot 6.9 and 6.10. From these plots two important facts can be obtained. From the left figure one clearly sees a problem of this method. While the changes of the α-functions are in a small range when applying the knob between the origin and the target (there the constraints have practically not changed) of the match, in the opposite direction the α_x value increases exponentially. This also holds when the knob is used to increase the change beyond the target of the match. The second problem concerns the orthogonality behavior. The orthogonal β-function is changing depending on the direction in which the knob is "turned".

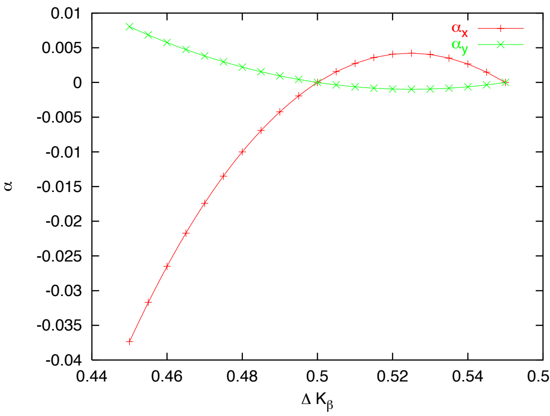

Figure 6.9: Change of the horizontal and vertical α-functions in IP1 when applying the knob to change the horizontal β-function between in IP1 0.45 and 0.55 meter.

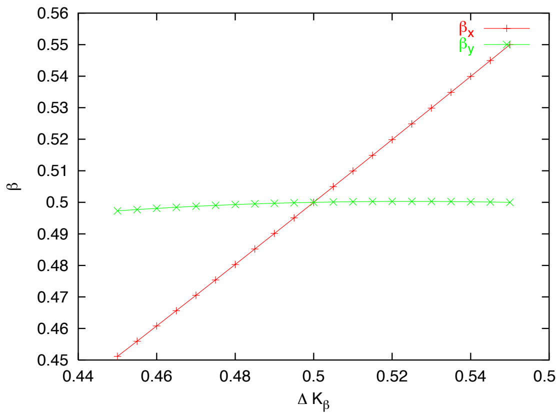

Figure 6.10: Change of the horizontal and vertical β-functions in IP1 when applying the knob to change the horizontal β-function at the same IP between 0.45 and 0.55 meter.

To find an optimized solution concerning these issues, a variety of knobs were calculated with different target values for direction and step width. This analysis brought to the surface a further problem of this approach. The changes of the tuning quadrupoles obtained from the matching cannot be scaled with the step width, neither linearly nor with any other analytic function. Plotting the changes of the tuning quadrupoles as a function of the horizontal β-function revealed that the matched quadrupole strengths seem to jump randomly around a mean value. This meant, that constructing a knob this way was dependent on the step width and an optimization was not possible. The smoothed mean dependence however showed an analytical behavior. Fitting this function was a possible solution. It would not optimize the knob for a specific step width but instead for a chosen range. This seemed a reasonable approach but as this knob is supposed to be linear the mean functions should also be close to linear. As shown in Fig.6.11 this was not the case.

Because of this, the lattice was analyzed to extend the number of tuning quadru-

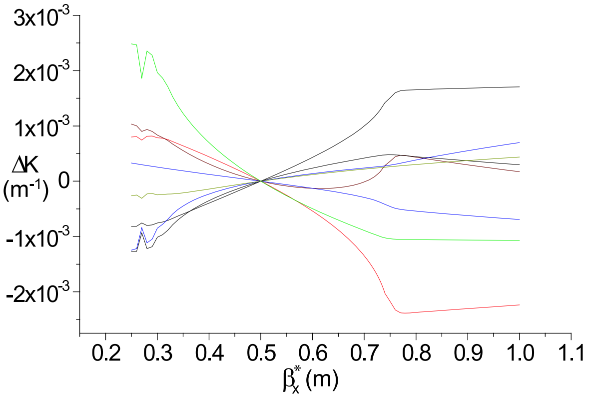

Figure 6.11: The change of the tuning quadrupoles as a function of $\beta^{\star}$, $\Delta K = f(\beta_x^{\star})m^{-1}$, which are obtained by matching. The chosen constraints are $\beta_x^{\star}, \beta_y^{\star}, \alpha_x^{\star},\ \alpha_y^{\star}$ at IP1 and β_x, β_y at the quadrupole slices MQY.A4R8.B1..1 and MQY.A4L8.B1..2, which have a phase advance of $\Delta\phi \approx \frac{\pi}{4}$.

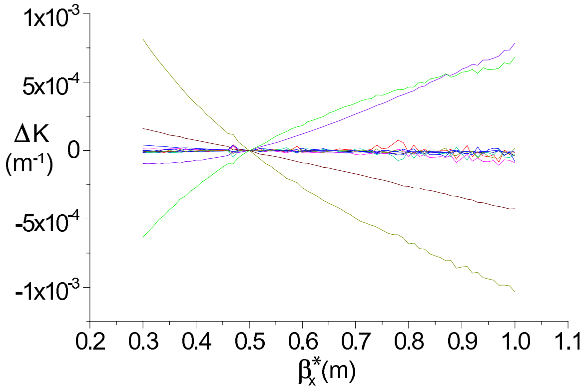

Figure 6.12: The change of the tuning quadrupoles as a function of $\beta^{\star}$, $\Delta K = f(\beta_x^{\star})m^{-1}$, which are obtained by matching. The chosen constraints are $\beta_x^{\star}, \beta_y^{\star}, \alpha_x^{\star},\ \alpha_y^{\star}$ at IP1 and β_x, β_y at the quadrupole slices MQY.A4R8.B1..1 and MQY.A4L8.B1..2, which have a phase advance of $\Delta\phi \approx \frac{\pi}{4}$.

poles on both sides of the IP. There are two further quadrupoles on each side (Q8 and Q9) which are part of the dispersion suppressor. To use these means to create additional dispersion at the IP. By changing K of Q13 with the same relative change as that of Q9 the introduced dispersion can be reduced. This additional dispersion must not be greater than the value at which the dispersion starts to blow up the beam size at the IP. For the LHC the nominal beam size at collision is $16\mu m$. With the nominal energy spread $\delta_e = 1.10 \cdot 10^{-4}$ the dispersion must be smaller than approximately $D \leq 1 \cdot 10^{-2} m$ according to the expression of the spot size at the IP $\sigma = \sqrt{(\beta \cdot \epsilon) + (D \cdot \delta_e)^2}$.

The relation between β and ΔK for the new set of tuning quadrupoles, including Q8 and Q9, are plotted in Fig.6.12. In first approximation the curves are linear. Various combinations of four or more out of this six quadrupoles on each side of the IP with the same set of constraints was used to construct a knob vector. The result of this investigation was that the best knob vector was created by using all six quadrupoles on each side and extending the number of constraints from eight to twelve. Here again a series of knobs was calculated to see which additional constraints would optimize the result. Despite of other expectations the best result was to add the α-function in the two points separated by $\phi = \frac{\pi}{4}$.

It is apparent from Fig. 6.12 that four tuning quadrupoles change more than the other eight which seem to fluctuate around their nominal value. It was tried to only use these four to construct the tuning knob, but this attempt did not lead to reasonable results. The tuned $\beta_x^{\star}$ value does only change about $(+0.02/-0.1)m$ although it should change $(+0.5/-0.25)m$. In addition, $\beta_y^{\star}$, which should be constant, is changed by $\approx -20\%$. Taking the achieved range and scaling the vector to create the desired range implies a far too big change of the constraints, which are to be kept constant. Also a scaling of ΔK would exceed the limits of maximum powering of the quadrupoles.

Final Set

The new tuning knob was constructed by linearly fitting the curves of the match results for the latter set of quadrupoles and constraints and taking the slope at $\beta_x^\star = 0.5$ meter. A corresponding tuning knob was computed for the vertical plane.

For each of these tuning knobs the behavior of the optics function (constraints and observables) was analyzed in a range between $\beta_x^\star = 0.25$ and $\beta_x^\star = 1.0$ meters.

As these tests were successful first correction tests of simulated quadrupole gradient errors were performed. For these tests the IP β-function for the horizontal and vertical plane had to be corrected simultaneously. It quickly turned out, that by applying the knobs for both planes together the changes in the constraints do not add up but are changing partially exponentially.

For this reason the characterization of the knobs was repeated. This was done by probing the two dimensional range of the two tuning knobs. As a result three dimensional plots were created to reveal the effect of the simultaneous application of the pair of tuning knobs. The result for the orthogonality behavior ($\Delta\beta_x^\star = f(\beta_x^\star, \beta_x^\star)$, $\Delta\beta_y^\star = f(\beta_x^\star, \beta_x^\star)$) is shown in Fig.6.13 and Fig.6.14. Two features immediately caught the attention when these plots were analyzed. The first is, that the behavior of $\beta^\star$ is different for the horizontal and vertical plane. This should not be the case for a perfectly antisymmetric lattice. A closer analysis shows the asymmetry is not exactly fulfilled

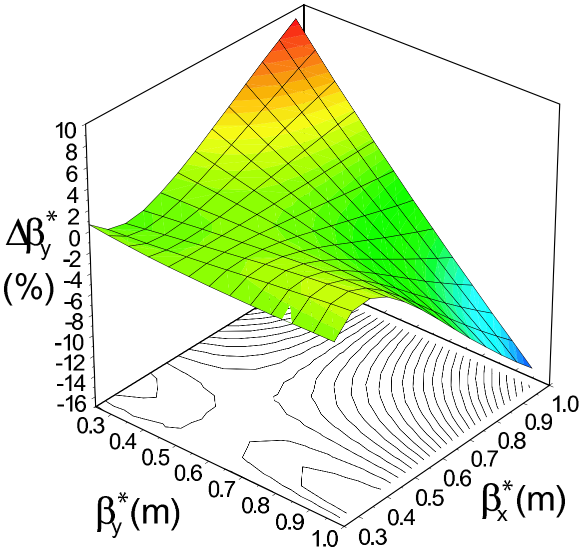

Figure 6.13: Orthogonality behavior of the $\beta_x^\star$ knob. $\Delta\beta_y^\star$ is shown as a function of $\beta_x^\star$ and $\beta_y^\star$ ($\Delta\beta_y^\star = f(\beta_x^\star, \beta_y^\star)$). To only see the change of $\beta_y^\star$ created by the $\beta_x^\star$ knob, $\Delta\beta_y^\star$ is normalized as follows: $\Delta\beta_y^\star = \frac{\beta^\star_{y_{ist}} - \beta^\star_{y_{soll}}}{\beta^\star_{y_{soll}}}$. $\beta^\star_{y_{ist}}$ is the actual value and $\beta^\star_{y_{soll}}$ is the value if only the knob vector for $\beta_y^\star$ is applied. The ranges on the $x-$ and $y-$ axes are $(+100/-50)\%$.

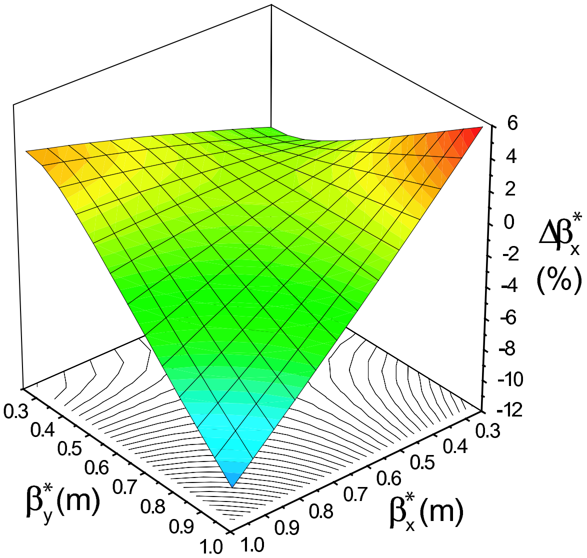

Figure 6.14: Orthogonality behavior of the $\beta_y^\star$ knob. $\Delta\beta_x^\star$ is shown as a function of $\beta_x^\star$ and $\beta_y^\star$ ($\Delta\beta_x^\star = f(\beta_x^\star, \beta_y^\star)$). To only see the change of $\beta_x^\star$ created by the $\beta_y^\star$ knob, $\Delta\beta_x^\star$ is normalized as follows: $\Delta\beta_x^\star = \frac{\beta^\star_{x_{ist}} - \beta^\star_{x_{soll}}}{\beta^\star_{x_{soll}}}$. $\beta^\star_{x_{ist}}$ is the actual value and $\beta^\star_{x_{soll}}$ is the value if only the knob vector for $\beta_x^\star$ is applied. The ranges on the $x-$ and $y-$ axes are $(+100/-50)\%$.

Table 6.1: Relation of the β-functions at IR1 and phase advance $\Delta\mu$ between the tuning quadrupoles and IP1.

NAME	β_x	β_y	$\frac{\beta_x}{\beta_y}$	$\frac{\beta_y}{\beta_x}$	ϕ_x	ϕ_y
KQ9.L1B1	13.3884	163.777		12.2328	0.5370	1.0764
KQ8.L1B1	141.876	10.5264	13.4781		0.3661	0.8894
KQ7.L1B1	76.4196	167.610		2.19329	0.2996	0.7063
KQ6.L1B1	515.796	6.69436	77.0493		0.2708	0.4787
KQ5.L1B1	745.398	180.832	4.12205		0.2623	0.2804
KQ4.L1B1	1648.63	363.751	4.53230		0.2584	0.2637
IP1	0.50000	0.50000	1.0		0	0
KQ4.R1B1	363.751	1648.63		4.53230	0.2637	0.2584
KQ5.R1B1	180.832	745.398		4.12204	0.2804	0.2623
KQ6.R1B1	6.69436	515.796		77.0493	0.4787	0.2708
KQ7.R1B1	167.927	76.2554	2.20217		0.7063	0.2996
KQ8.R1B1	12.2194	133.042		10.8878	0.8654	0.3679
KQ9.R1B1	132.846	37.8208	3.51251		1.0778	0.4723

by the LHC lattice in IR1. This can be seen in the values for the β-functions and the phase advances between the IP and the tuning knob quadrupoles which are different for the two sides, as shown in Table 6.1. The first column shows the name of the tuning quadrupoles, columns two and three the β-functions taken at the center of the quadrupoles and columns four and five the ratios $\frac{\beta_x}{\beta_y}$ and $\frac{\beta_y}{\beta_x}$. Only values greater than one for the ratios are shown to indicate which β exactly is greater than the other. Columns six and seven show the phase advance between the IP and the quadrupole for the horizontal and vertical plane. To compare the right values one has to keep in mind that due to the asymmetric lattice the horizontal values from one side should be equal to the vertical values from the other side and the other way around. For the same variation of $\beta^\star$ by the tuning knobs $\Delta\alpha_x^\star, \Delta\alpha_y^\star, Q_x, Q_y, D_x, Dp_x$ were analyzed. In these cases the knobs were applied simultaneously. The ranges of the horizontal and vertical axes are $(-50/+100)\%$. The results are presented in the figures on the following pages.

For the IP α-functions the main result is that there is very small crosstalk between the knobs and the orthogonal plane. The change of α is to a large extent caused by the knob for the β-function of the same plane. This change is only slightly magnified depending on the change of the knob for the orthogonal plane. This is indicated in plots 6.15 and 6.16.

The variation of the horizontal dispersion $D_x^\star$ and its slope $D_x^{\star'} \equiv Dp_x^\star$ are displayed in Fig.6.17 and Fig.6.18. The bigger part of the change is created by the knob for the horizontal β-function. The slope of the dispersion is stable around the nominal $\beta^\star$ value and changes more rapidly towards larger values of $\beta^\star$.

The tune change for both planes, as indicated in plot 6.19 and 6.20, show the same principal behavior. Each tuning knob creates the bigger part of the tune change in the same plane with some minor cross talk to the orthogonal plane. The created change is

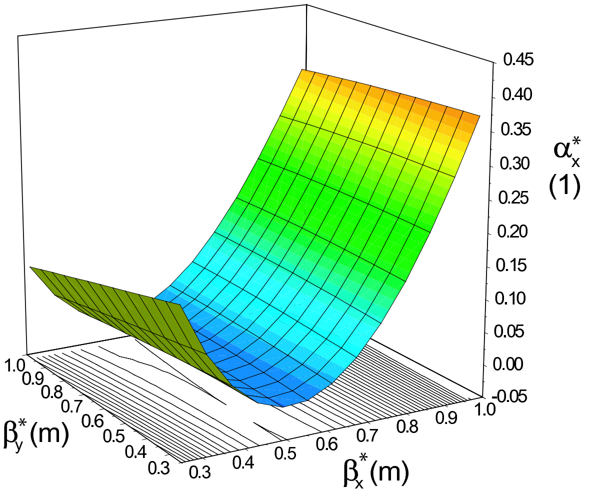

Figure 6.15: Influence of the knob vectors on the horizontal α-function at IP1 $\alpha_x^{\star} = f(\beta_x^{\star}, \beta_y^{\star})$. On the $x-$ and $y-$ axes the values of the β-functions at IP1 for both planes, $\beta_x^{\star}$ and $\beta_y^{\star}$, are shown within a range of $(+100/-50)\%$. On the $z-$ axis $\alpha_x^{\star}$ is shown.

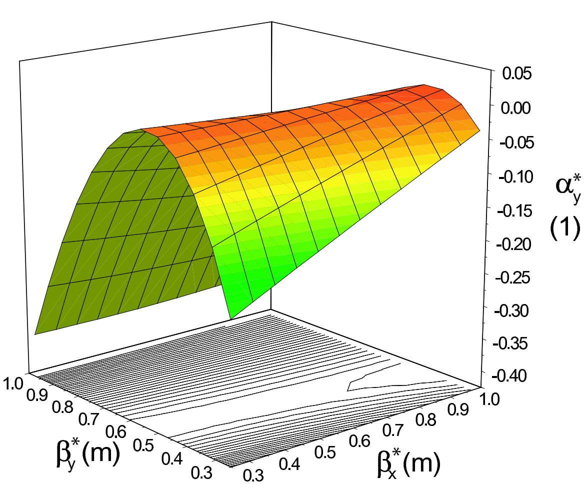

Figure 6.16: Influence of the knob vectors on the vertical α-function at IP1 $\alpha_y^{\star} = f(\beta_x^{\star}, \beta_y^{\star})$. On the $x-$ and $y-$ axes the values of the β-functions at IP1 for both planes, $\beta_x^{\star}$ and $\beta_y^{\star}$, are shown within a range of $(+100/-50)\%$. On the $z-$ axis $\alpha_y^{\star}$ is shown.

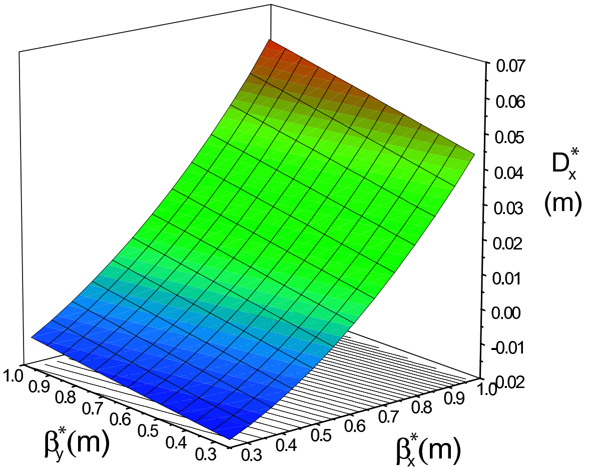

Figure 6.17: Influence of the knob vectors on the dispersion $D_x = f(\beta_x^{\star}, \beta_x^{\star})$ at IP1.On the $x-$ and $y-$ axes the values of the β-functions at IP1 for both planes, $\beta_x^{\star}$ and $\beta_y^{\star}$, are shown within a range of $(+100/-50)\%$. On the $z-$ axis D_x is shown.

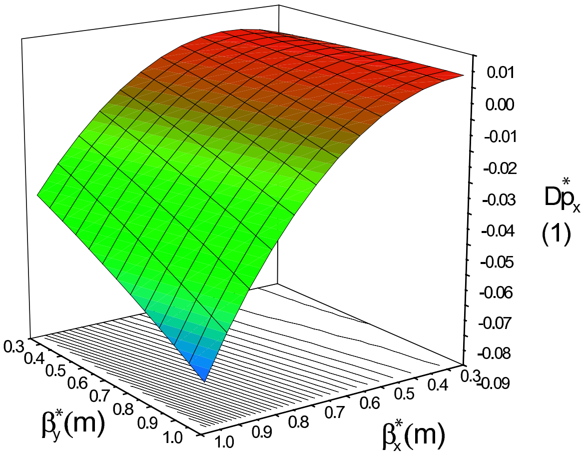

Figure 6.18: Influence of the knob vectors on the slope of the dispersion $Dp_x = f(\beta_x^{\star}, \beta_y^{\star})$ at IP1. On the $x-$ and $y-$ axes the values of the β-functions at IP1 for both planes, $\beta_x^{\star}$ and $\beta_y^{\star}$, are shown within a range of $(+100/-50)\%$. On the $z-$ axis Dp_x is shown.

linear in first approximation. This is desirable because then the created change can be compensated simultaneously with the dedicated standard tune correction scheme. For the LHC there are quadrupole correctors located in each arc for the tune correction.

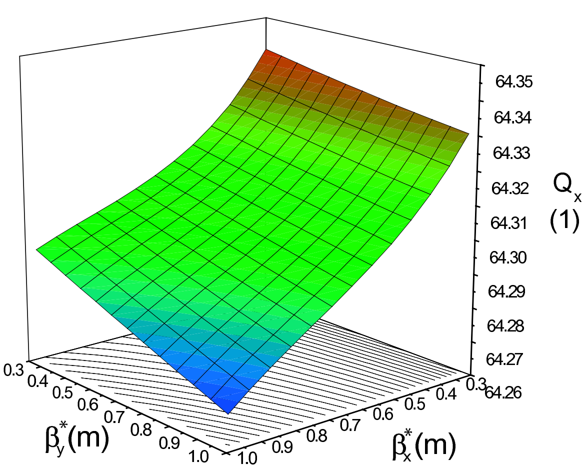

Figure 6.19: Influence of the knob vectors on the horizontal tune $Q_x = f(\beta_x^\star, \beta_y^\star)$. On the $x-$ and $y-$ axes the values of the β-functions at IP1 for both planes, $\beta_x^\star$ and $\beta_y^\star$, are shown within a range of $(+100/-50)\%$. On the $z-$ axis Q_x is shown.

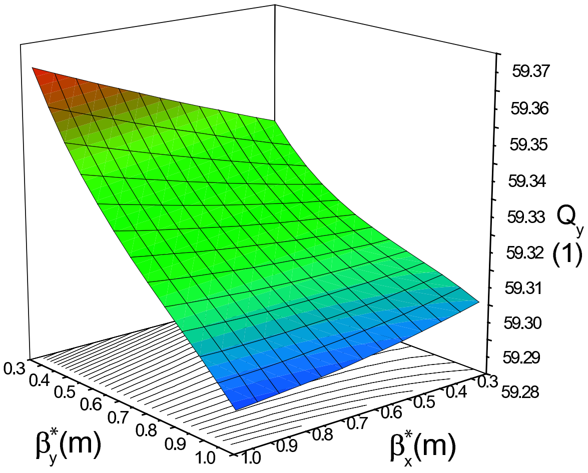

Figure 6.20: Influence of the knob vectors on the vertical tune $Q_y = f(\beta_x^\star, \beta_y^\star)$. On the $x-$ and $y-$ axes the values of the β-functions at IP1 for both planes, $\beta_x^\star$ and $\beta_y^\star$, are shown within a range of $(+100/-50)\%$. On the $z-$ axis Q_y is shown.

The behavior of the constraints, as shown in the these figures, of the tuning knob utilizing Q4-Q9 and Q13 at the left and at the right of the IP is much improved as compared to the previous knob set. After all, with $\pm 20\%$ the interval, over which the knobs shall be used, is much smaller than the range shown and therefore enough safety margin remains.

A summary of these results is given in Table 6.2. The values of the four most outlying points of the "tuning field" (area which is scanned by the tuning knobs) for each analyzed constraint and observable are given. The changes of $\Delta\beta_x^\star$, $\Delta\beta_y^\star$, $\Delta\alpha_x^\star$, $\Delta\alpha_y^\star$, ΔQ_x and ΔQ_y are acceptable for adjustments in operations. The created dispersion reaches the tolerable limit for a change of $(+20/+20)\%$. As this is not a hard limit it is not critical but in operation the dispersion should be closely monitored.

As the results were acceptable and further studies of different combinations of constraints brought no additional improvement, these knobs were used for the error simulations.

6.2 Calculating $\beta^\star$ Tuning Knobs with MADX and Lattice Version V6.4

At this time the LHC lattice was not finalized. Due to different changes and the need to verify the effect of the tuning knobs on the crossing angle a re-computation had to be

Table 6.2: Variation of $\beta_x^\star$, $\beta_y^\star, \alpha_x^\star, \alpha_y^\star, Q_x, Q_y, D_x$, Dp_x at changes of $\pm 20\%$ for both horizontal and vertical IP β-function introduced by the tuning knobs and computed with MAD8 for lattice version V6.2.

VAR	$\beta_x^\star$ $\beta_y^\star$	$+20\%$ $+20\%$	$+20\%$ -20%	-20% $+20\%$	-20% -20%
$\Delta\beta_x^\star/(\%)$		-0.72	0.69	0.41	-0.44
$\Delta\beta_y^\star/(\%)$		-0.47	0.44	0.38	-0.42
$\Delta\alpha_x^\star/(1)$		0.023	0.019	0.017	0.023
$\Delta\alpha_y^\star/(1)$		-0.027	-0.013	-0.016	-0.029
$\Delta \mathrm{Q}_x/(1)$		0.0083	0.0046	-0.0069	-0.0098
$\Delta \mathrm{Q}_y/(1)$		0.0049	-0.0104	0.0071	-0.0052
$\Delta \mathrm{D}_x^\star/(m)$		0.010	0.0069	-0.0060	-0.0084
$\Delta \mathrm{Dp}_y^\star/(1)$		-0.0073	-0.0040	0.0023	0.0031

done. In lattice version V6.2 no crossing angle was included. The new lattice version V6.4 was only available for the new version of MAD. Fig.6.21 exhibits the horizontal and vertical β-functions in IP1 computed with lattice version V6.4 and MADX. The curves should be the same as in Fig.6.1, Page 74.

For this new version parts of the code were completely rewritten and thus most of the existing MAD scripts were obsolete. The first step of the re-computation implied to construct exactly the same set of tuning knobs with MADX lattice version V6.4 and to compare this set with the one previously computed by MAD8 for lattice version V6.2. There were small differences in the knob vectors but the differences in the characteristics were negligible.

When introducing the crossing angle in the lattice, the effect on the constraints was characterized in an analogous manner as in Section 6.1. The results of the previously monitored constraints and observables were roughly the same as the ones without crossing angle. The change of the crossing angle was for a $\pm 20\%$ β change at maximum ten percent. This value was considered to be too high and it was decided to-recompute the knob set considering the crossing angle as a constraint. The orbit shift in the IP introduced by the tuning knobs was also very large and of the order of magnitude of the beam size. A minimization of this effect was also part of the recalculation efforts. The reason for these rather big effects by the set of knobs can be understood from the fact, that Q4 is part of the knob vector. As it is also part of the system creating the crossing angle, a change of the integrated field strength will effect the crossing angle.

As a first result the fixed powering Q13 in relation to Q9 was not imposed anymore. Due to the crossing angle a residual dispersion was introduced at the IP which was so high that the change of dispersion created by Q9 was negligible. Q13 is not considered as a tuning quadrupole from this point. The complete procedure of computing and characterizing tuning knobs was run through. The results for the characterization are indicated in Table 6.3.

By comparing the values of Table 6.3 and Table 6.2, Page 84, it becomes evident that the recalculation was successful. The negative effects on crossing angle and orbit shift

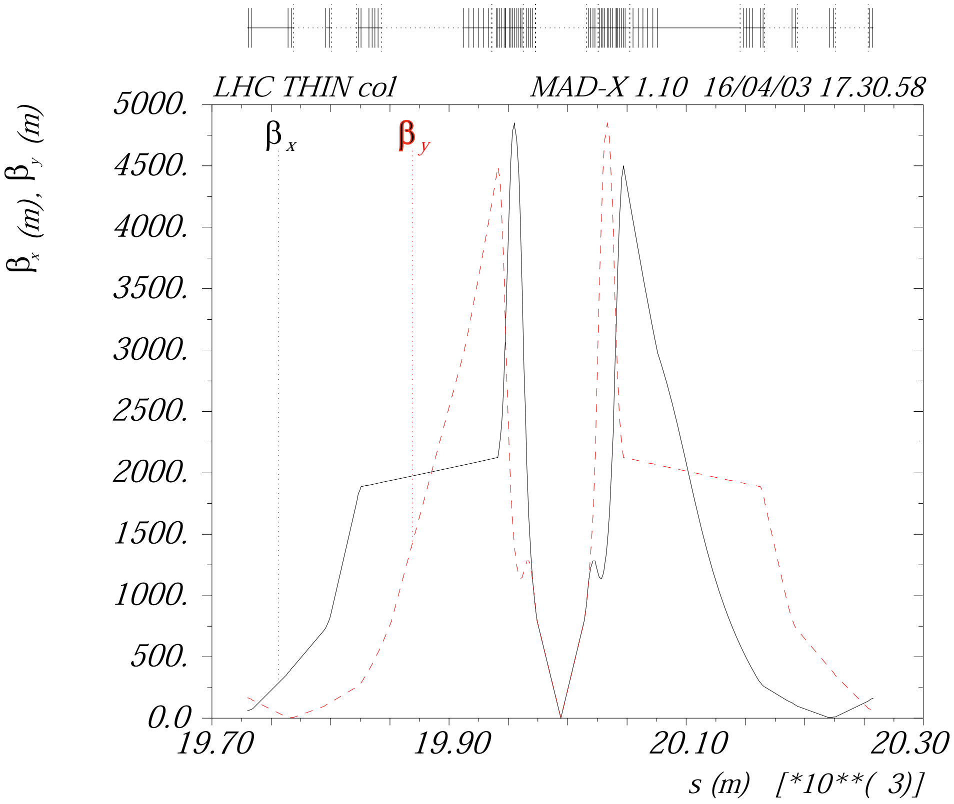

Figure 6.21: β-functions at IR1 between Q7 left and right from IP1 computed with MADX and lattice version V6.4.

Table 6.3: Changes of $\beta_x^\star$, $\beta_y^\star, \alpha_x^\star, \alpha_y^\star, Q_x, Q_y, D_x$, Dp_x for changes of $\pm 20\%$ for both horizontal and vertical IP β-function introduced by the tuning knobs and computed by MADX for lattice version V6.4.

VAR	$\beta_x^\star$	$+20\%$	$+20\%$	-20%	-20%
	$\beta_y^\star$	$+20\%$	-20%	$+20\%$	-20%
$\lvert\Delta\beta_x^\star\rvert/(\%)$		0.8	0.6	0.5	0.6
$\lvert\Delta\beta_y^\star\rvert/(\%)$		0.7	0.5	0.7	0.4
$\Delta\alpha_x^\star$		+2.43E-02	+2.15E-02	+2.21E-02	+3.16E-02
$\Delta\alpha_y^\star$		-3.62E-02	-1.76E-02	-2.36E-02	-3.45E-02
ΔQ_1		-7.30E-03	-8.80E-03	+1.15E-02	+8.70E-03
ΔQ_2		-6.00E-03	+5.20E-03	-4.20E-03	+4.00E-03
$\Delta D_x^\star/(m)$		+4.30E-03	+4.66E-03	-4.18E-03	-4.22E-03
$\Delta D_y^\star/(m)$		+5.73E-04	-2.00E-04	+5.60E-04	-9.38E-06
$\Delta X/(m)$		-8.94E-15	+3.17E-13	-4.64E-14	-1.34E-14
$\Delta Y/(m)$		-3.73E-08	+1.57E-07	-1.55E-07	+3.58E-08
$\Delta pX^\star/rad$		-1.28E-13	+3.43E-13	+5.13E-13	+1.23E-13
$\Delta pY^\star/rad$		+1.00E-09	+2.53E-07	-1.85E-07	+3.00E-09

could be corrected without affecting other constraints and observables in an unwanted manner. The results for crossing angle and orbit from the characterization of the tuning knobs is shown in Fig.6.23 and Fig.6.22. The orbit distortion was reduced by approximately two orders of magnitudes and the one for the crossing angle even more. The residuals are negligible.

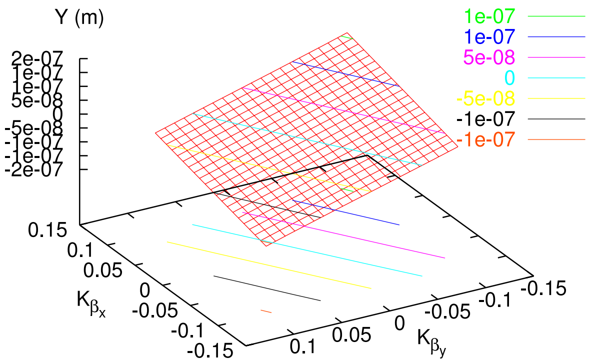

Figure 6.22: Influence of the knob vectors on the vertical orbit $Y = f(\beta^{\star}_x, \beta^{\star}_y)$ at IP1.

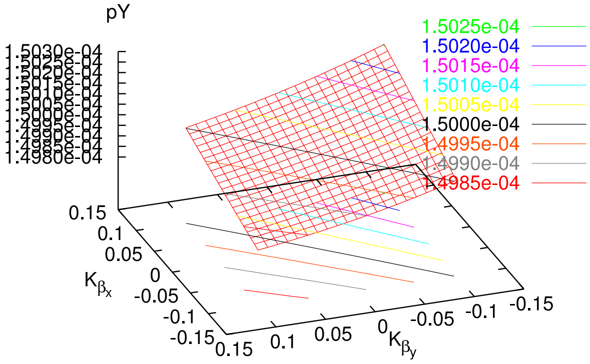

Figure 6.23: Influence of the knob vectors on the change of the crossing angle (vertical plane) $pY = f(\beta^{\star}_x, \beta^{\star}_y)$ at IP1.

For this set of tuning knob vectors, the changes of integrated field strengths necessary to create a nominal change of the β-function of $\pm 20\%$, do not exceed the limits of the maximum field strengths of the tuning quadrupoles. The maximum relative change was introduced in Q8 at the right of the IP with $\approx 6\%$. As the nominal gradient of this quadrupole is about 50% of its maximum field strength the effect of hysteresis is not expected to cause severe problems in operation (see the discussion on hysteresis in Section 3.3).

6.3 Error Tests

Correcting Quadrupole Gradient Error

To test the behavior of the knobs, errors were introduced in the lattice. A preliminary correction was applied, i.e., orbit correction for $b1$ field errors, and $b3, b4, b5, a2, a3$ correction with corrector spool pieces, based on assumed magnetic field measurements. Then the tuning knobs were applied and their effect was observed. To obtain a diversified result demonstrating for which type of error the knobs work, a test program is followed containing a variety of different magnets, fields and error types.

In a first study [25] errors where introduced in the arc dipoles (MB) and arc quadrupoles (MQ). As error field types b1 to b11 were applied. For all cases the $\beta^{\star}$ values at IP1 could be corrected. Details of the results are summarized in [25]. In these studies there was no crossing angle. Simulations were performed with lattice version V6.2 and MAD 8. A summary of this test can be found in Table 6.4.

To test the knobs in the presence of the crossing angle, version V6.4 with MAD X was used. Two test series were performed one with and one without the crossing angle

Table 6.4: Results from the test run with systematic and random errors of the field type b1 to b11 in the arc dipoles MB and arc quadrupoles MQ with lattice version V6.2 and MAD 8.

	mean value	rms	min	max		tk appl min	tk appl max
$\Delta\beta_x$	2.1E-02	1.5E-02	-1.1E-03	-6.9E-02	β_x	5.0E-01	5.0E-01
$\Delta\beta_y$	2.3E-02	1.8E-02	1.2E-03	8.6E-02	β_y	5.0E-01	5.0E-01
ΔD_x	1.4E-02	5.1E-02	-1.5E-04	-3.9E-01	D_x	1.5E-03	-1.6E-02
ΔDp_x	4.0E-02	1.9E-01	3.8E-04	-1.5E+00	Dp_x	-8.9E-03	-3.2E-02
ΔQ_x	7.2E-02	4.6E-02	-3.2E-03	1.8E-01	Q_x	64.313	64.312
ΔQ_y	5.6E-02	3.5E-02	3.0E-04	-1.3E-01	Q_y	59.322	59.317

active. The results of the latter test series were similar to the results shown in Table 6.4 and are therefore not repeated here.

The results with active crossing angle are shown in Table 6.5 for version V6.2. The test series were constructed in the same way as in [25] except that no dipole errors (b1) were applied for technical reasons. Columns two and three in Table 6.5 show the mean and rms value of the changes between the introduction of the errors and the application of the tuning knobs, column four the maximum negative, column five the maximum positive change for sixty different random seeds of field errors and columns seven and eight the resulting maximum positive and negative final values of $\beta_x, \beta_y, D_x, D_y, Q_x, Q_y, X, Y, pX, pY$ over 60 random seeds after the tuning knobs were applied.

Table 6.5: Results from the test run with systematic and random errors of the field type b2 to b11 in the arc quadrupoles MQ with lattice version V6.4 and MAD X.

	mean value	rms	max neg	max pos		tk appl max pos	tk appl max neg
$\Delta\beta_x$	-1.5E-3	1.23E-2	-3.11E-2	1.88E-2	β_x	5.0E-1	5.0E-1
$\Delta\beta_y$	3.6E-3	1.39E-2	-2.08E-2	3.16E-2	β_y	5.0E-1	5.0E-1
ΔD_x	-8.0E-5	1.41E-3	-4.28E-3	1.99E-3	D_x	2.1E-2	-
ΔD_y	1.9E-5	5.57E-5	-1.06E-4	1.04E-4	D_y	1.0E-2	-
ΔQ_1	64.3115	1.17E-2	-2.25E-2	2.77E-2	Q_1	64.338	64.285
ΔQ_2	59.3215	1.18E-2	-1.82E-2	2.99E-2	Q_2	59.350	59.302
ΔX	2.7E-8	4.73E-7	-7.60E-7	1.42E-6	X	7.0E-8	-4.2E-5
ΔY	2.6E-8	4.54E-7	-9.27E-7	1.08E-6	Y	2.6E-6	-6.1E-6
ΔpX	-5.9E-8	1.25E-6	-3.68E-6	2.22E-6	pX	7.3E-6	-1.0E-5
ΔpY	1.2E-7	7.41E-7	-1.28E-6	7.18E-5	pY	7.2E-5	-4.8E-7

To visualize the correction efficiency the actual correction $\beta_0 + \Delta\beta_a$ is plotted over the β_d value to be corrected. For errors generated in the arc quadrupoles all corrected seeds lie on the diagonal. This is shown in Fig.6.24 (Plot A). Plot B refers to errors generated in the insertion triplet. In this case if the resulting errors in $\beta^\star$ exceed a value

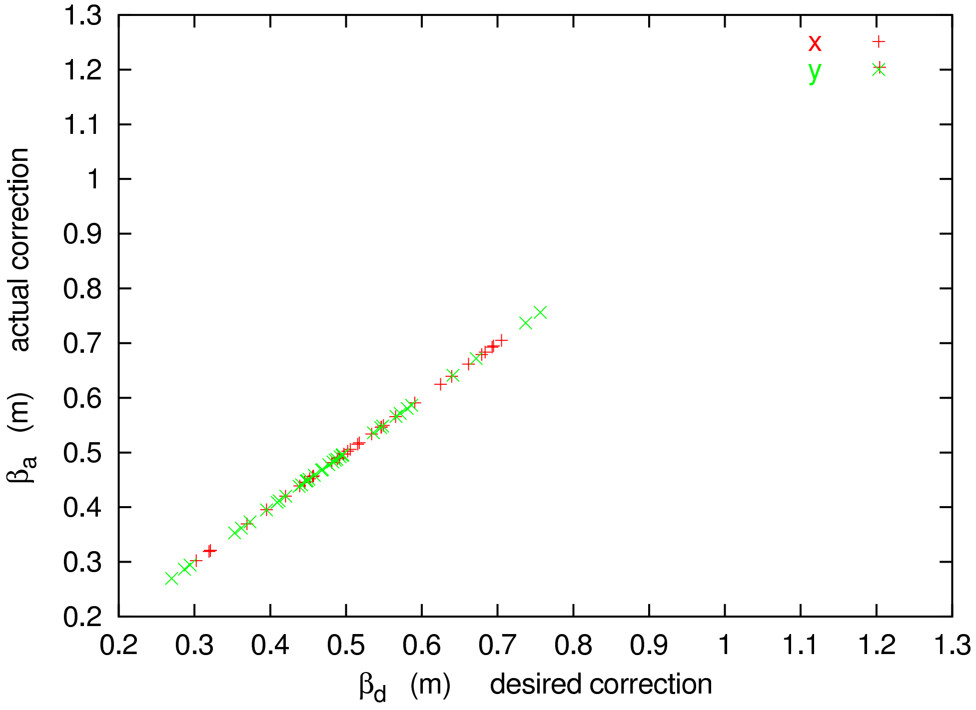

Plot A

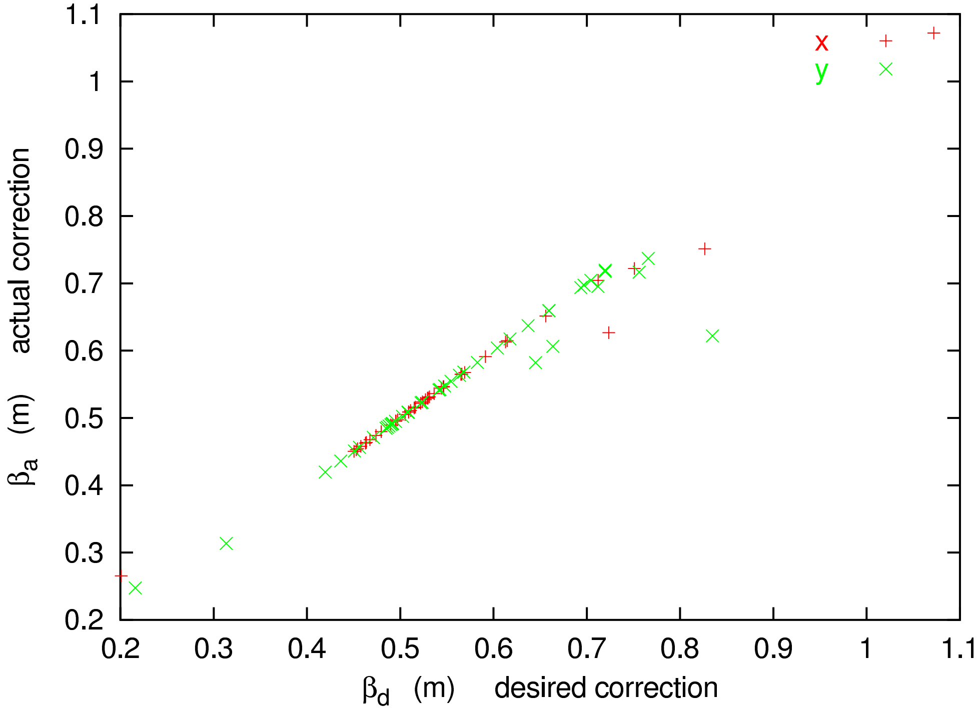

Plot B

Figure 6.24: Correction efficiency for errors generated in the arc quadrupoles (Plot A) and in the insertion triplet quadrupoles (Plot B). The corrected seeds lie on the diagonal. Imperfectly corrected seeds lie off diagonal. The field errors of the arc quadrupoles (MQ's) were enlarged compared to those expected by a factor of seven. This was done to be able to compare the results to those generated by the insertion triplets, where errors have a much larger effect.

of $\approx \pm 25\%$ the knobs fail to work especially for positive $\Delta\beta$ values.

It is demonstrated here, that with the application of tuning knobs, local triplet errors (the source of the error is located in the triplet of the insertion, where the tuning knobs are used for correction.) up to an approximate error level of $\pm 20\%$ can be corrected. For opperations it is not advisable to proceed in this manner. Triplet errors are expected to be the largest error sources. They act on both beams simultaneously. Also their number is limited and it is therefore advisable to identify the triplet magnet which is the source of the error by beam-based measurements and correct the field error locally.

Performance with Closed Orbit Errors and Crossing Angle Bumps

It was indicated by the characterization of the tuning knobs that the steering effect is small when applying the knobs. To verify this, horizontal and vertical field errors were generated by dipole gradient errors (a1 and b1) and quadrupole misalignments on top of quadrupole gradient errors. The a1 and b1 field errors created a closed orbit distortion which was corrected with the standard correction tool in MADX to an rms value of 0.5 mm. This tool will be available in reality in the control room. Hence this creates a scenario equivalent to the real storage ring. The tuning knobs were then applied to correct the IP β-functions to their nominal values.

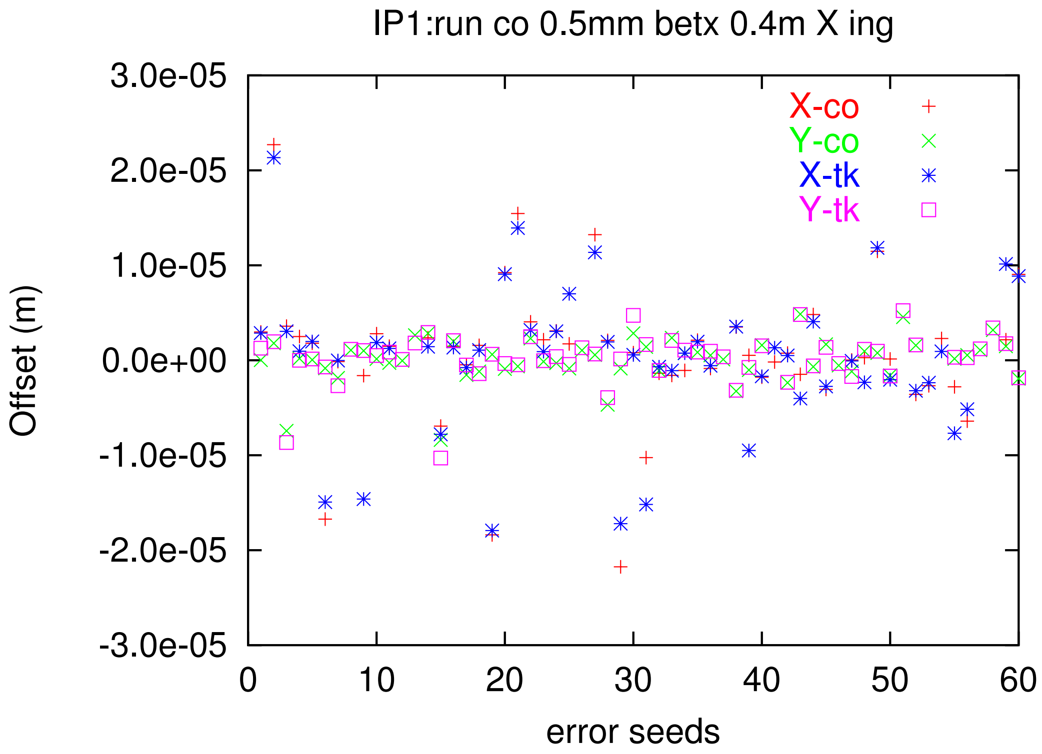

Figure 6.25: Steering effect in IP**1** of the tuning knobs applied in IP1 when changing the horizontal IP1 β-function from 0.5 m to 0.4 m in the presence of closed orbit (co) distortion, which was corrected to 0.5 mm rms. The horizontal X-co and vertical Y-co offsets correspond to the value after the closed orbit correction. The horizontal X-tk and vertical Y-tk offset correspond to the value after the horizontal IP1 β-function was reduced by the tuning knobs.

The result of these simulations was difficult to analyze as two effects, closed orbit and $\beta^{\star}$-correction, are appearing at the same time. It was not transparent how much of the steering effect was caused by the $\beta^{\star}$ correction and how much by the orbit correction. For this reason it was decided to study the steering effect in a different manner. The errors to create the closed orbit distortions were introduced as before but no quadrupole gradient errors were distributed over the lattice. Instead the knobs were used to change the IP β-function in a controlled way. This way the effect of closed orbit and $\beta^{\star}$-correction were separated as the tuning knobs were applied in a controlled manner. The $\beta^{\star}$ values were changed by $\pm 20\%$ from their nominal value.

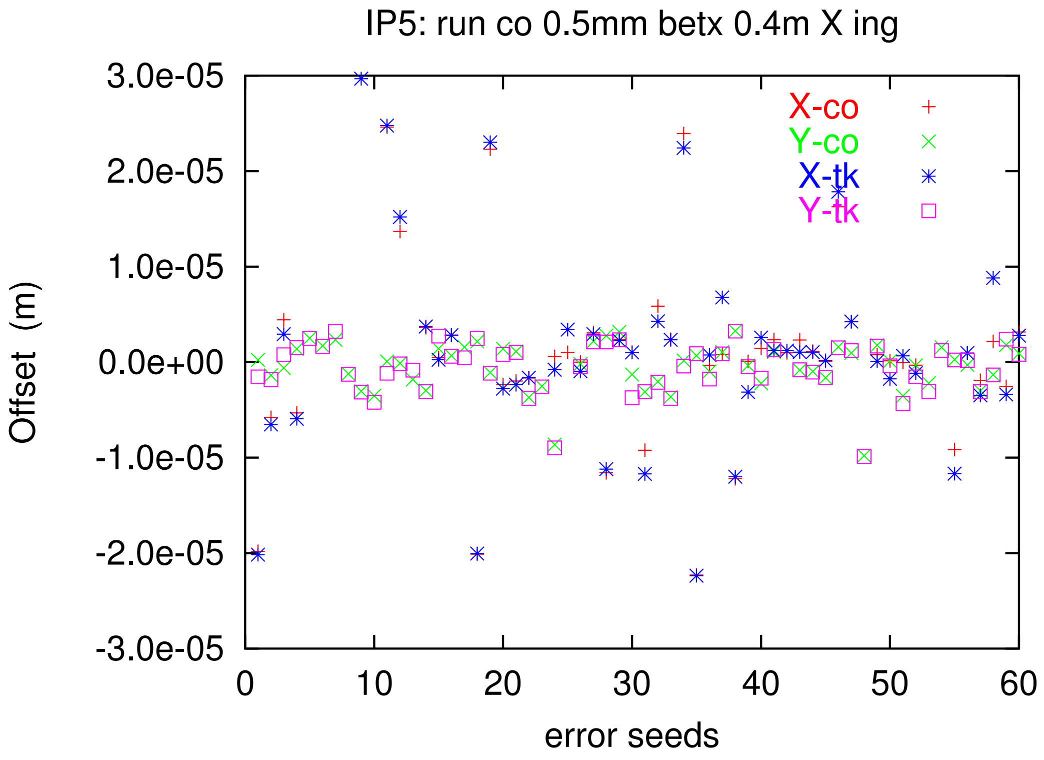

Figure 6.26: Steering effect in IP**5** of the tuning knobs applied in IP1 when changing the horizontal IP1 β-function from 0.5 m to 0.4 m in the presence of closed orbit distortion, which was corrected to 0.5 mm rms. The horizontal X-co and vertical Y-co offsets correspond to the value after the closed orbit correction. The horizontal X-tk and vertical Y-tk offset correspond to the value after the horizontal IP1 β-function was reduced by the tuning knobs.

It was important to monitor both high luminosity IPs as the steering effect is not confined to the manipulated insertion. One simulation run consisted of 60 different seeds. The resulting orbit change from the change of $\beta_x^{\star}$ from 0.5 meter to 0.4 meter is shown in Fig.6.25 for IP1 and in Fig.6.26 for IP5.

The plots depict the steering effect in IP1 and IP5 created by applying the tuning knobs applied in IP1 to change the horizontal IP1 β-function from 0.5 m to 0.4 m in the presence of closed orbit distortion. The original closed orbit distortions had been corrected to 0.5 mm rms beforehand. The curves X-co and Y-co correspond to the horizontal and vertical offset of the beam in IP1 and IP5 after the closed orbit correction tool had been applied. The curves X-tk and Y-tk correspond to the horizontal and vertical offset of the beam after the tuning knobs had been used to change the horizontal IP1 β-function. The steering effect is given by the difference between the values after closed orbit correction and after tuning knob application. The plots show only the seeds were the initial offset was smaller or equal two σ. This was done because a greater offset means the two beams had been moved out of collision. In a real machine the application of the tuning knobs in such a situation is irrelevant as there is no luminosity signal on which the $\beta^\star$ correction could be based.

All combinations of $\beta^\star$ changes for both horizontal and vertical planes were performed in a simulation series. The major result of this work was that the steering effect is in any case smaller than one σ. The magnitude of the steering effect is correlated with the beam offset after the closed orbit correction. The bigger the offset is after the closed orbit correction, the bigger the steering effect of the knobs. As the steering of the beam is always smaller than one σ and the beams therefore remain in collision an IP steering correction can be applied after the $\beta^\star$ tuning to correct this effect. Hence the steering effect bears no risk for the tuning knob application.

Beam-Beam Effects

The last series of simulations concerned beam-beam effects, especially the effect of the long-range beam-beam kicks on the performance of the tuning knobs. This was simulated by using the programs MAD and TRAIN together. MAD was used to calculate the optics functions and maps. These were passed on to TRAIN which computed the self consistent orbit of all 2808 LHC bunches for both beams in presence of long-range beam-beam kicks. For this orbit the new crossing angle and beam separation was calculated for each bunch. The nominal standard bunch train for LHC was used for these calculations.

This is done for both beams. Hence an additional set of tuning knobs for beam 2 was calculated, following the same procedure described in the previous section, with a similar characteristic behavior.

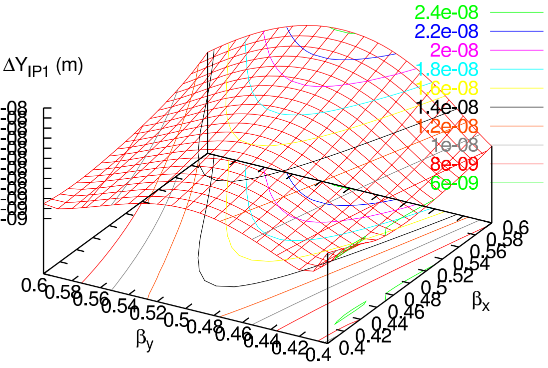

Figure 6.27: Variation of the vertical separation of the beams in IP1 when changing the IP1 β-functions simultaneously for both beams.

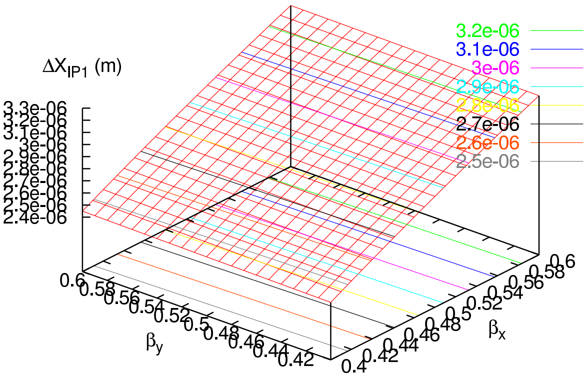

Figure 6.28: Variation of the horizontal separation of the beams in IP1 when changing the IP1 β-functions simultaneously for both beams.

The nominal lattice was set up with standard dipole errors and quadrupole misalignments for both beams. The two sets of tuning knobs were used to correct random quadrupole gradient errors. All errors were corrected and the effect of the knobs created no significant changes.

To characterize the effects of the knobs on beam separation and crossing angle in the presence of long-range kicks the tuning knobs were applied to change the horizontal and vertical β-functions. The scanning of the knob strength was done by changing the $\beta^\star$ values for both beams to the same value. This corresponds to a realistic scenario as unequal beam sizes affect the life time negatively. The resulting beam separations for the horizontal and vertical plane in IP1 and IP5 are presented in Fig.6.27, Fig.6.28, Fig.6.29 and Fig.6.30. The values in the plots represent the mean value of all 2808 bunches.

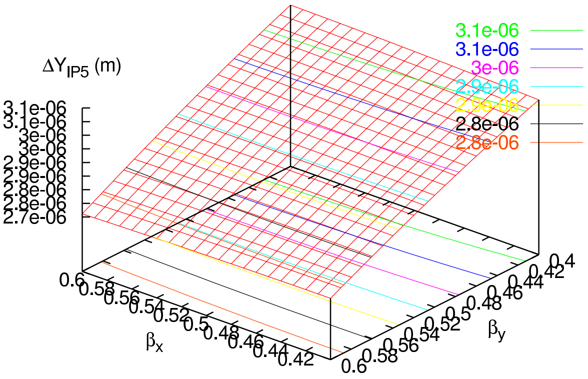

Figure 6.29: Variation of the vertical separation of the beams in IP5 when changing the IP1 β-functions simultaneously for both beams.

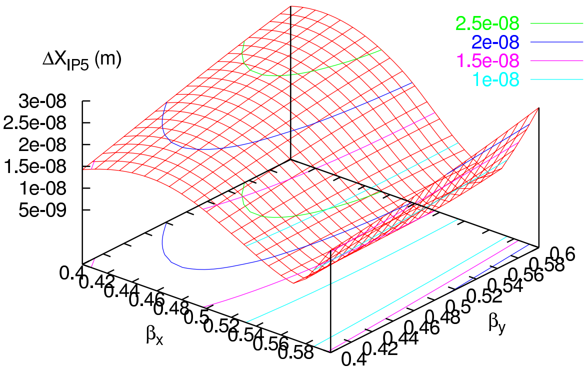

Figure 6.30: Variation of the horizontal separation of the beams in IP5 when changing the IP1 β-functions simultaneously for both beams.

From the four plots the following two points are to be mentioned. First the beam separation caused by the tuning knobs is negligible and second, the beam separation varies more strongly in the plane with no crossing angle in IP1.

The figure of merit for the influence of the long range kicks is the change of luminosity in both IPs when applying the tuning knobs. This is interesting in cases where the tuning knobs are used to increase the luminosity. The result of this simulation is shown in plot 6.31.

The long range beam-beam kicks do not prevent luminosity gains in IP1 when using tuning knobs to squeeze the β functions in IP1. The effect of long range beam-beam kicks is visible in the fact that the increase in the luminosity in IP1 is not linear. There is also a slight luminosity reduction in IP5. This effect is small and can be easily compensated by a set of tuning knobs for this IP.

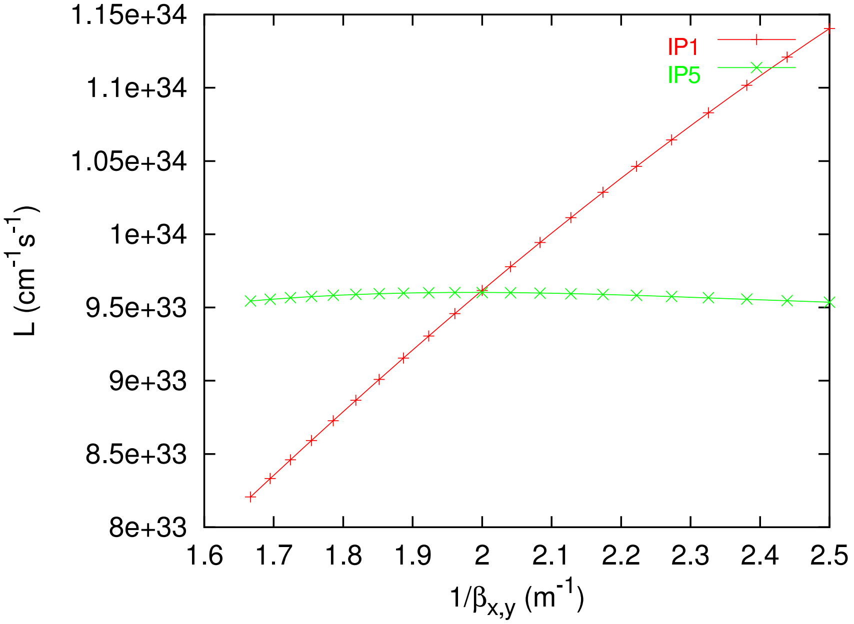

Figure 6.31: Luminosity increase in IP1 and IP5 when squeezing the IP1 β-functions.

Chapter 7

RHIC - Relativistic Heavy Ion Collider

To adjust the β-function at the IP several approaches have been discussed theoretically and simulated for the LHC. As the LHC is under construction and the functionality of the knobs is essential, the work was repeated for RHIC, since it is an excellent testbed for verification. The specific difference of the RHIC to the LHC lattice, which was investigated before, is the nested power supply system illustrated in Fig.7.1. This reduced the number of adaptable tuning quadrupoles. Also several quadrupoles which serve as tuning quads are coupled to each other. The lattice which was used for the study was converted from line to sequence format in MADX to rotate the starting point from STAR to IP4. The knobs were calculated for PHENIX, which I will refer to as IP8.

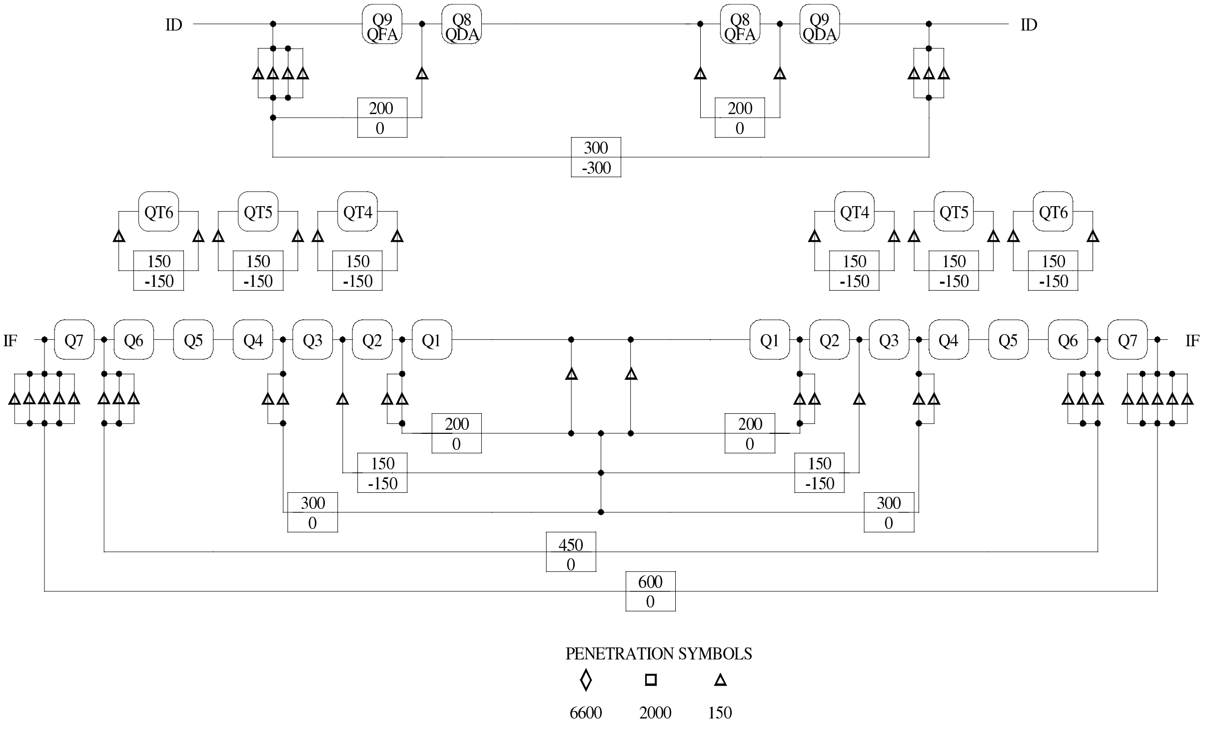

Figure 7.1: Nested power supply system as used in IR8 and IR6 in RHIC.

In addition the optics constraints were monitored in STAR, which I will refer to as IP6.

7.1 Calculating and analyzing the response Matrix.

As mentioned above, the nested power supply system makes the behavior of the coupled tuning quads not easily predictable. For this reason and because of the strongly nonlinear behavior (see Fig.7.2) of the first by MAD matching calculated knobs the response matrix for all in principle usable quadrupoles was computed with MADX as described earlier.

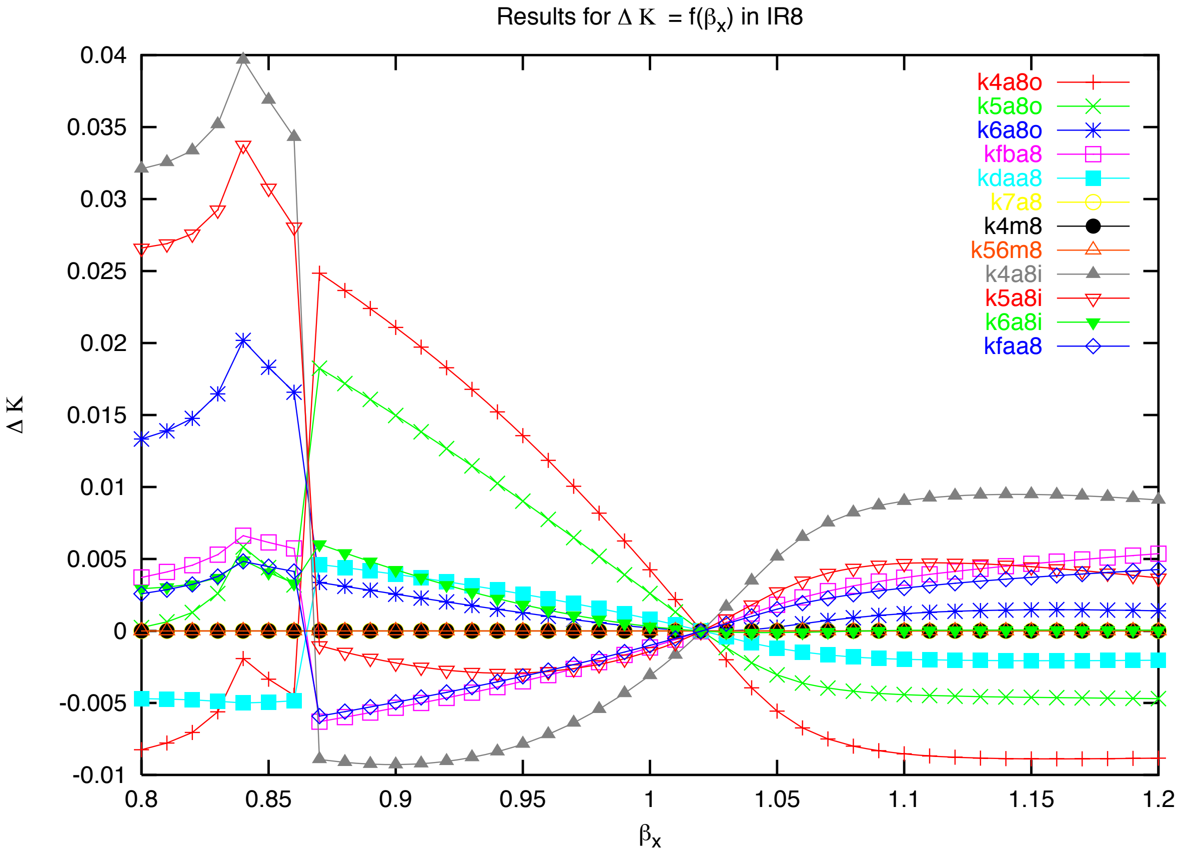

Figure 7.2: Non linear behavior when matching different values for $\beta_x^\star$. The behavior of the quadrupole change ΔK is strongly nonlinear in the range between 0.87 and 1.2 meter. In addition at 0.87 m there is a sudden change of the solution. At this point the function behaves discontinuous. This and the nonlinearity render the solution not applicable in practice.

The quadrupoles which were available in principle are listed in Table 7.1. The nominal strength (for 1m $\beta^\star$ at IP6 and IP8) of the different quadrupoles or combinations was varied over ranges of $\pm 5\%$ to $\pm 95\%$ (the maximum range for each quadrupole or combination was chosen so as to correspond to the whole stable region of the solution) of the nominal strength with 40 intermediate steps. The parameters α, β, D and Q for both planes where recorded. These were then plotted as a function of the change of the quadrupole strength. The investigation of $\beta = f(\Delta K)$ shows, that there is a strong difference in its behavior. Three different cases can be identified:

- The β-function is only enlarged, independent of the sign of the applied change, as indicated in Fig.7.3.
- The change of the β-function depends on the sign of the applied change, but $\beta = f(\Delta K)$ is strongly nonlinear (see fig.7.4).
- The β-function changes over a wide range almost linearly (see fig.7.5).

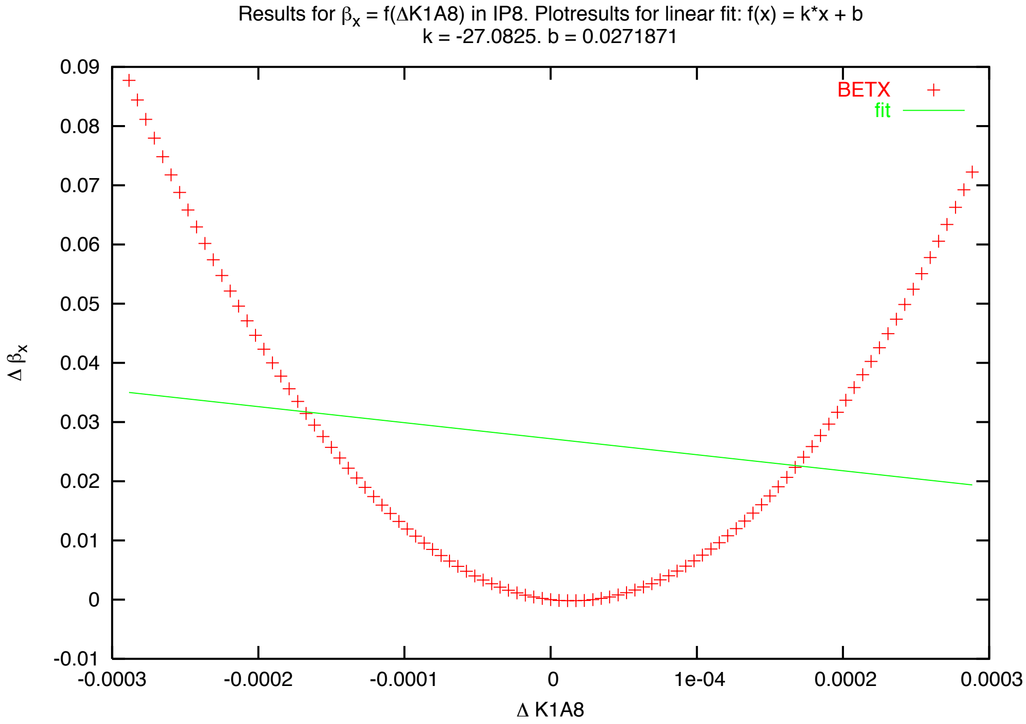

Figure 7.3: Plot A: Response of β_x at IP8 to the change of K1A8 which controls the strength K of the coupled triplet quadrupoles HQ1O8, HQ1I8 at the left and at the right of IP8. The quadrupole strengths were changed in a range of $\pm 5\%$ about the nominal strengths for 1m $\beta^\star$ at IP6 and IP8.

In addition the other parameters α, β, D and Q are categorized in the same way, but only as additional information and not as a criterion for selection. Only the third category is adaptable without any additional consideration. The variables for the control of the strengths of the quadrupoles are being classified according to this scheme as shown in Table 7.1. This table indicates, that the number of usable quadrupoles lies between six and ten on both sides. All ten were used for the construction of the knobs, except for one case (MAD match version 11) where nine were used.

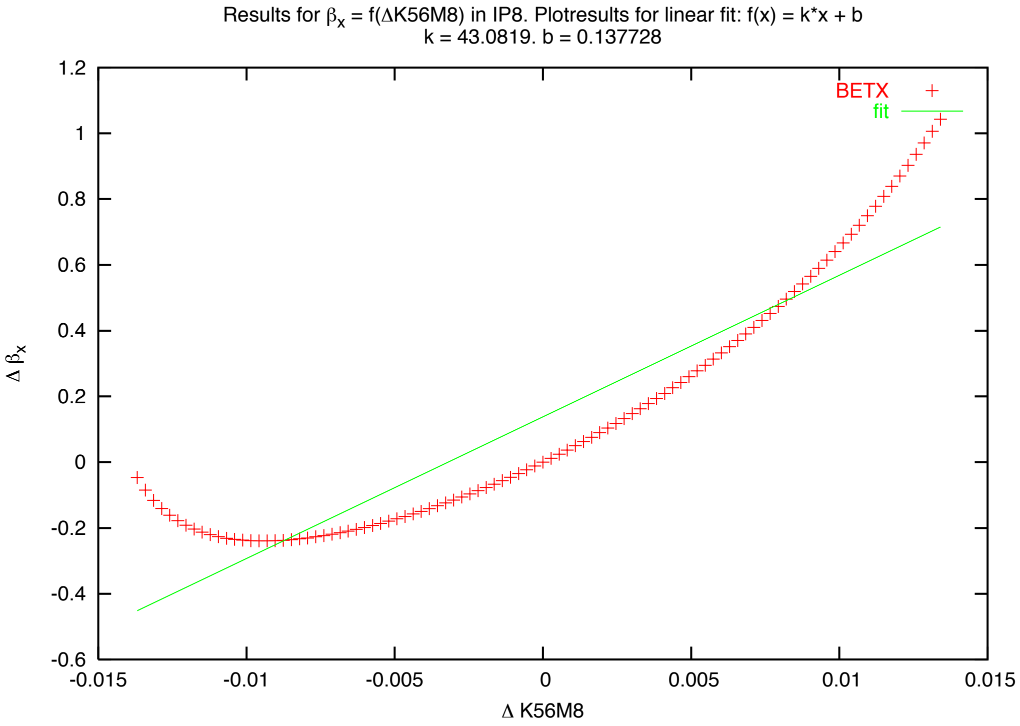

Figure 7.4: Response of β_x at IP8 to the change of K56M8 which controls the strength K of the coupled quadrupoles Q6O8, Q5O8, Q6I8, Q5I8 at the left and at the right of IP8. The quadrupole strengths were changed in a range of $\pm 15\%$ about the nominal strengths.

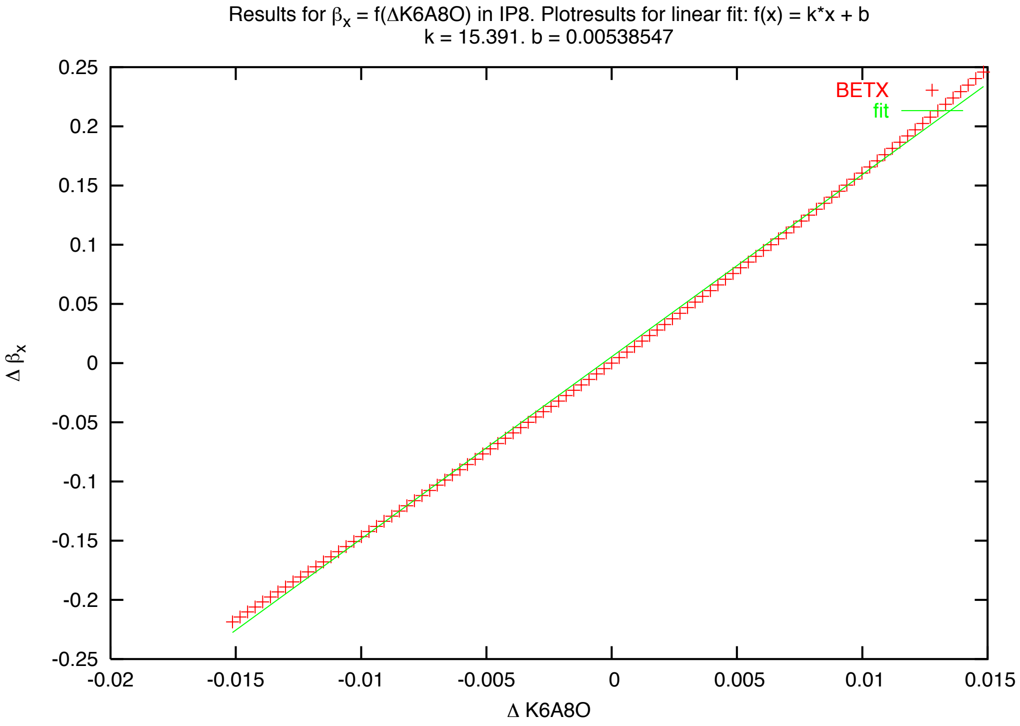

Figure 7.5: Response of β_x at IP8 to the change of K6A8O which controls the strength K of the quadrupole Q6OT8 right from IP8. The quadrupole strength was changed in a range of $\pm 95\%$ about the nominal strengths.

Table 7.1: Results of the response matrix analysis. Category 1 indicates single quadrupoles or quadrupoles on a common power supply which are not applicable as tuning quadrupoles, those in category 2 are applicable only with restrictions and those in 3 without any restrictions.

name	category	usable range	name	category	usable range
K1A8	1	-	K5A8O	3	$\pm 50\%$
K2A8	1	-	K6A8I	3	$\pm 50\%$
K3A8	1	-	K6A8O	3	$\pm 50\%$
K4A8I	3	$\pm 50\%$	K7A8	2	$\pm 5\%$
K4A8O	3	$\pm 50\%$	KDAA8	2	$\pm 5\%$
K4M8	1	-	KFAA8	2	$\pm 5\%$
K56M8	1	-	KFBA8	2	$\pm 5\%$
K5A8I	3	$\pm 50\%$			

7.2 Calculating knobs by linearly fitting MAD matching results.

According to the response matrix analysis, the number of maximum usable quadrupoles, ten in total (see Table 7.1), is smaller than the maximum number of constraints. These are α, β and dispersion functions, in IP6 and IP8, tune, tune slope and chromaticity (16 in total). Depending on the specific lattice some of these are either not constrainable or do not change or cannot be constrained in certain combinations. First simulations showed, that dispersion could not be controlled with this approach. However, the changes in dispersion do not increase the IP spot size significantly. Several combinations of different quadrupoles and constraints were simulated and the best two results are described below.

7.2.1 Knob version 10

For this version quadrupoles or combinations of them, which are controlled by the following K values, were chosen: K4A8O, K5A8O, K6A8O, KFBA8, K4A8I, K5A8I, K6A8I, KFAA8, KDAA8 and K7A8. The basis for the selection was the response matrix analysis according to the results summarized in Table 7.1. As the behavior of a lattice, when choosing different sets of constraints, is a specific feature of each individual lattice, various sets were considered and the best one was chosen for further simulations. This set is for version 10 the α and β-functions at IP8 and IP6 as well as the tune Q. These were used in MADX to match over the range of $\pm 20\%$ of the nominal $\beta^{\star}$ value. The result is shown in Fig. 7.6 for the horizontal plane.

When trying to use these results to construct the tuning knob for the vertical plane the result is not monotonic and highly nonlinear. Taking the same result in a range of $\pm 10\%$ as shown in Fig.7.7 as the basis to construct the knob (by fitting the slopes for each quadrupole) gives a very promising result. The calculated values of the knobs for the horizontal and vertical plane are shown in Table 7.2.

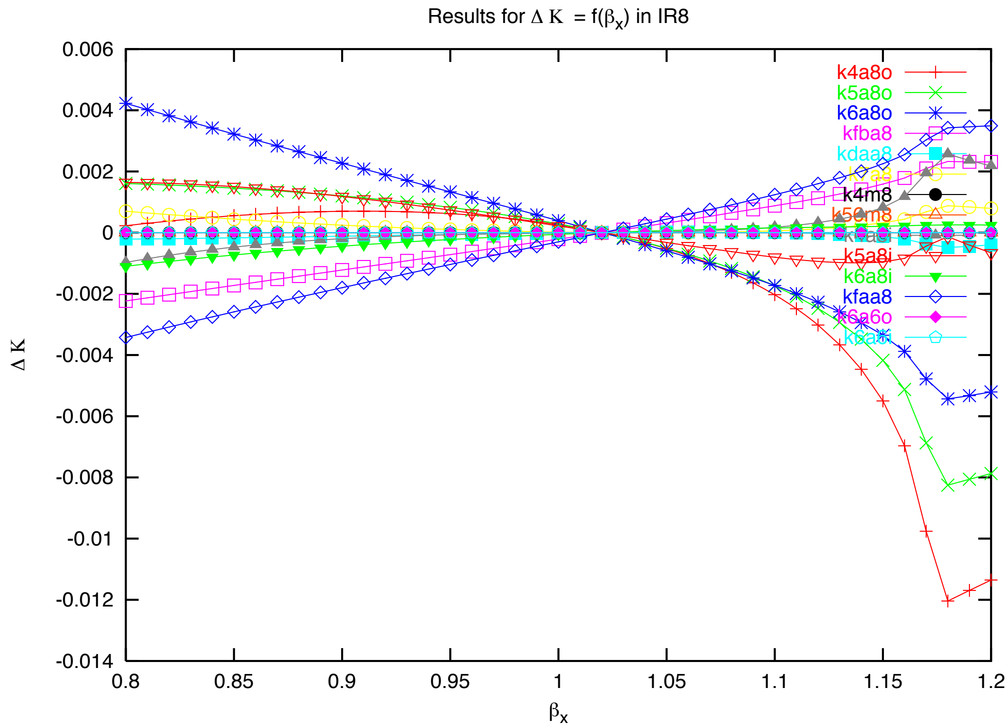

Figure 7.6: Result when matching $\beta_x^\star$ in IP8 in a range of $\pm 20\%$ around the nominal $\beta^\star$ value of one meter with K4A8O, K5A8O, K6A8O, KFBA8, K4A8I, K5A8I, K6A8I, KFAA8, KDAA8 and K7A8 and $\alpha_x^\star$, $\alpha_y^\star$, $\beta_y^\star$ in IP6 and IP8, $\beta_x^\star$ in IP6 as well as Q_1 and Q_2 as constraints.

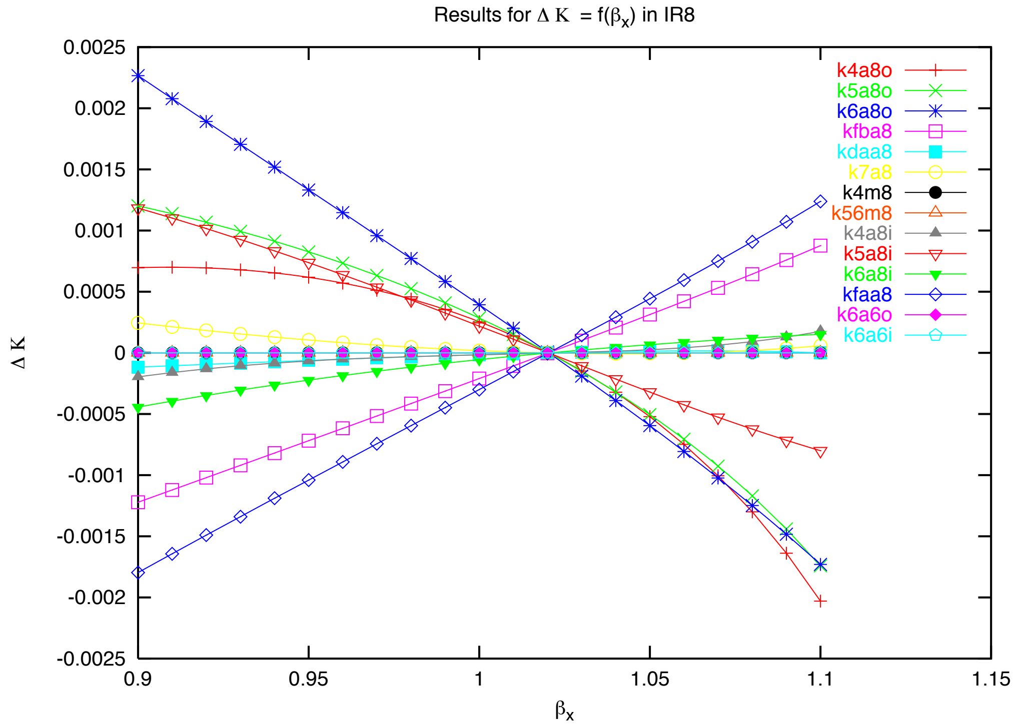

Figure 7.7: Result when matching $\beta_x^\star$ in IP8 in a range of $\pm 10\%$ around the nominal $\beta^\star$ value of one meter with K4A8O, K5A8O, K6A8O, KFBA8, K4A8I, K5A8I, K6A8I, KFAA8, KDAA8 and K7A8 and $\alpha_x^\star$, $\alpha_y^\star$, $\beta_y^\star$ in IP6 and IP8, $\beta_x^\star$ in IP6 as well as Q_1 and Q_2 as constraints.

Table 7.2: Calculated values for the horizontal and vertical knob vectors by MAD matching version 10.

match version 10					
$K[m^{-1}]$	$x - plane$	$y - plane$	$K[m^{-1}]$	$x - plane$	$y - plane$
K4A8I	-0.001430	0.027712	K6A8O	0.019648	-0.004527
K4A8O	0.012573	0.006009	K7A8	0.001013	0.000282
K5A8I	0.010229	0.022689	KDAA8	-0.000668	-0.013897
K5A8O	0.014056	0.014612	KFAA8	-0.015013	0.001780
K6A8I	-0.002940	0.019187	KFBA8	-0.010407	-0.003237

To characterize the behavior of the knobs, both knobs are applied simultaneously and scanned over the operative range, which is for both planes $\pm 20\%$. The values of the constraints on the four outermost points of the knobs range are shown in Table 7.3 for IP8 and IP6. These results are all within the given boundaries for the constraints.

Table 7.3: The changes of the constraints in IP8 and IP6 when setting the multipliers KBX and KBY to the edge points of their operative range calculated by MAD match version 10.

KBX	KBY	$\beta_x[m]$	$\beta_y[m]$	α_x	α_y	$D_x[m]$	
MAD match version 10 IP8							Q_1
-0.2	-0.2	8.35e-01	8.03e-01	-1.04e-02	-2.43e-03	4.58e-03	28.2210
0.2	-0.2	1.24e+00	8.03e-01	-6.89e-03	-1.35e-02	-1.89e-02	28.2187
0.0	0.0	1.02e+00	9.84e-01	-1.17e-02	-2.38e-03	2.44e-03	28.2200
-0.2	0.2	8.34e-01	1.19e+00	-6.13e-03	-9.20e-03	1.93e-02	28.2182
0.2	0.2	1.24e+00	1.19e+00	-1.55e-02	9.84e-04	2.51e-04	28.2202
MAD match version 10 IP6							Q_2
-0.2	-0.2	9.50e-01	1.00e+00	1.03e-02	1.05e-02	3.74e-02	29.2296
0.2	-0.2	9.52e-01	1.01e+00	2.81e-02	2.48e-02	-5.69e-03	29.2273
0.0	0.0	9.52e-01	9.97e-01	9.97e-03	-1.53e-04	2.58e-02	29.2300
-0.2	0.2	9.52e-01	1.00e+00	2.64e-02	1.64e-02	5.57e-02	29.2286
0.2	0.2	9.54e-01	9.99e-01	1.92e-02	5.17e-03	1.50e-02	29.2303

The two top pictures of Fig.7.8 on page 102, illustrate the linearity and orthogonality when varying the multipliers KBX and KBY in a range of $\pm 20\%$ with 40 intermediate steps. The other plots on page 102 and 103 show the behavior of $\alpha^{\star}$ and $D^{\star}$ at IP8 and IP6 as well as the tunes when applying the knobs.

7.2.2 Knob version 11

For version 11 quadrupoles or quadrupole combinations which are controlled by the following K values were chosen: K4A8O, K5A8O, K6A8O, KFBA8, K4A8I, K5A8I, K6A8I, KFAA8, and KDAA8 (one less than in version 10). As constraints the α_x and β-functions at IP8 and α and β-functions at IP6 as well as the tune Q were used. α_y

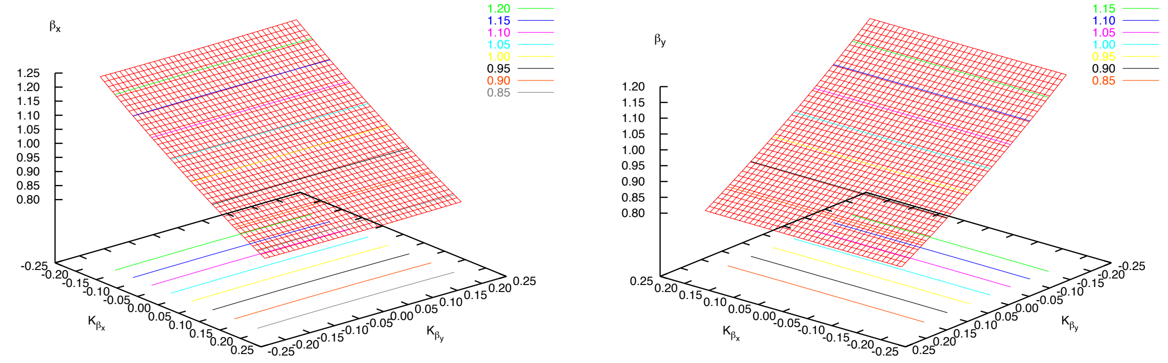

$\beta_x IP8$ $\beta_y IP8$

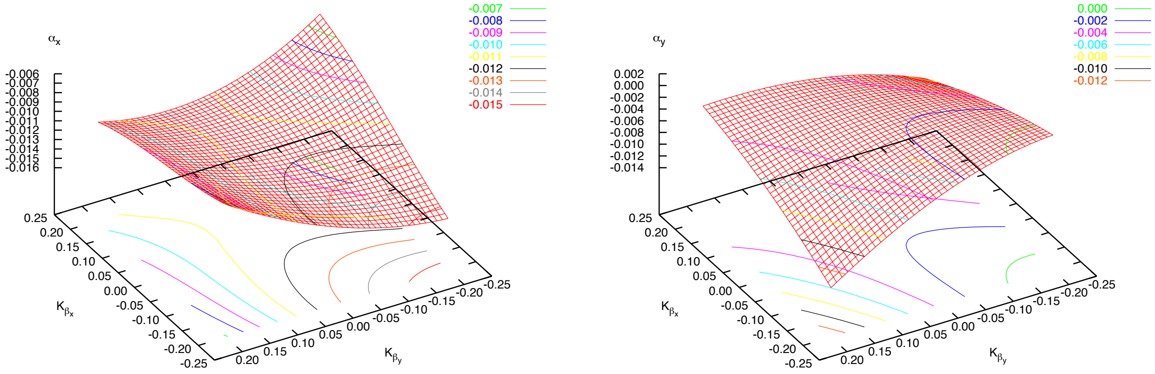

$\alpha_x IP8$ $\alpha_y IP8$

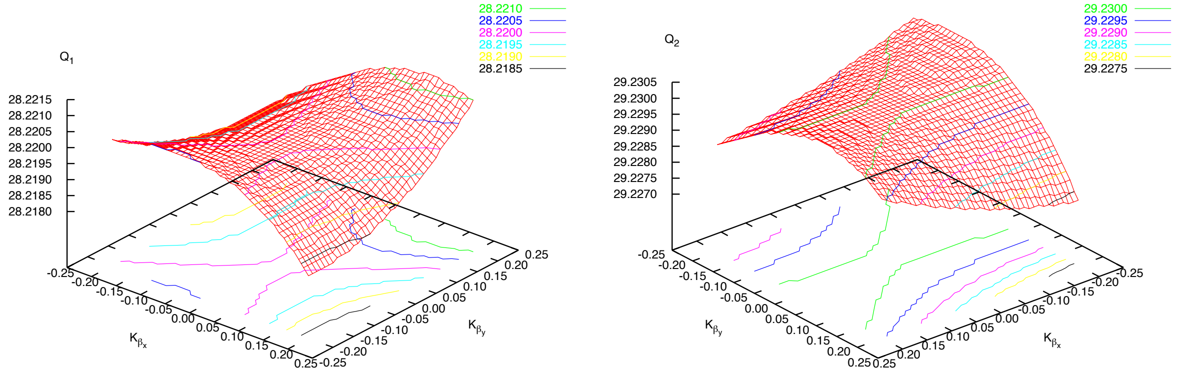

Q_1 Q_2

Figure 7.8: Change of $\alpha^\star$, $\beta^\star$ in IP8 and the tune when applying the knobs version 10 over a range of $\pm 20\%$ around the nominal value of $\beta^\star = 1m$.

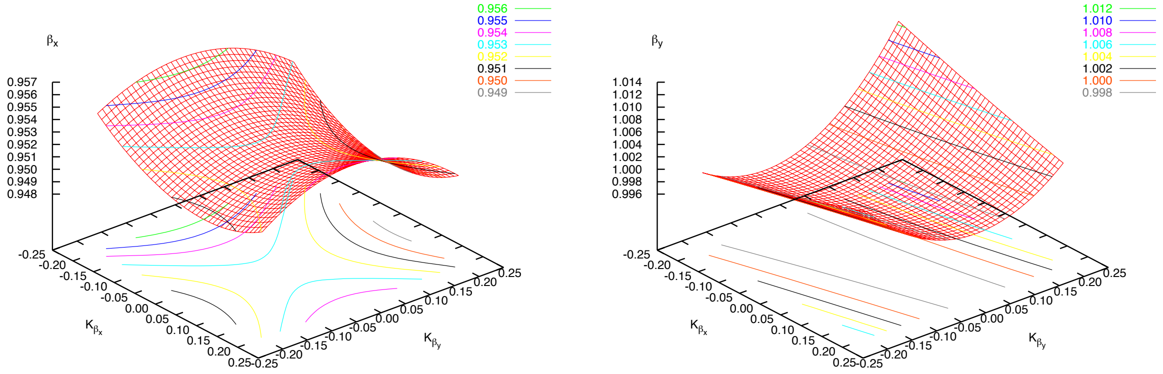

$\beta_x IP6$

$\beta_y IP6$

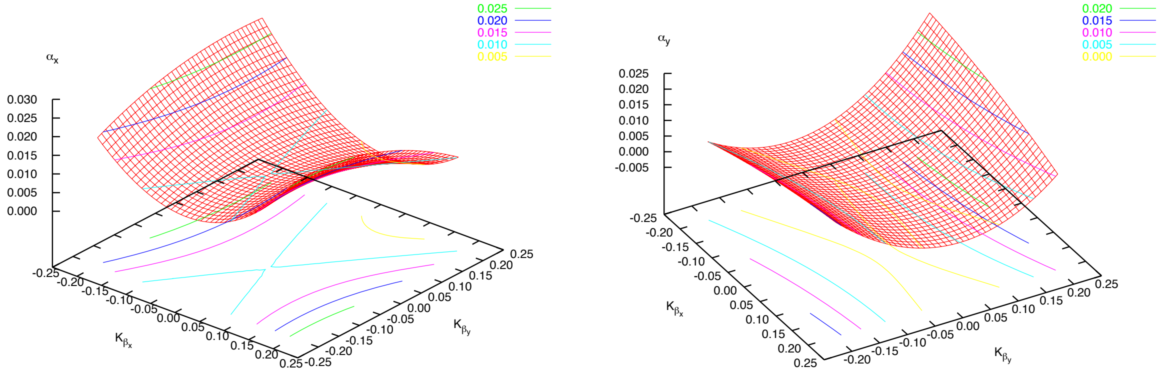

$\alpha_x IP6$

$\alpha_y IP6$

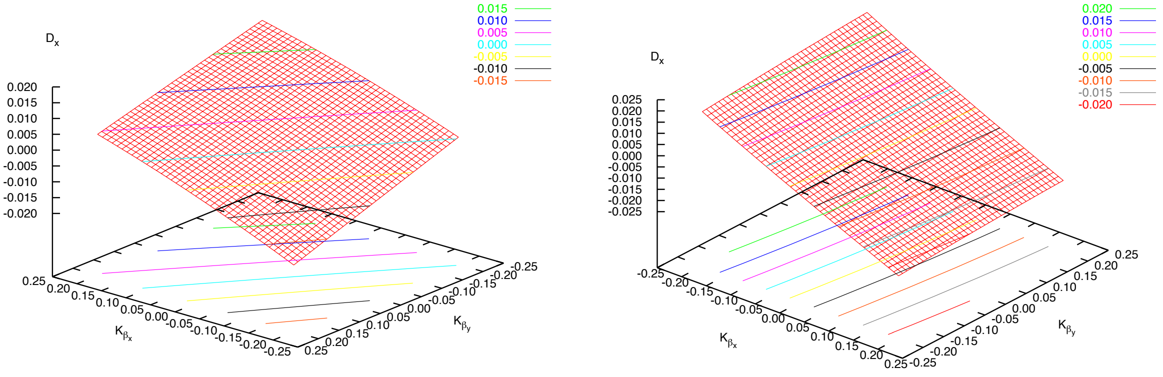

$D_x IP8$

$D_x IP6$

Figure 7.9: Change of $\alpha^{\star}$, $\beta^{\star}$, D_x in IP6 and D_x in IP8 when applying the knobs version 10 over a range of $\pm 20\%$ around the nominal value of $\beta^{\star} = 1m$.

was not constrained because simulations showed this to be best choice. One constraint of version 10 had to be given up because one quadrupole less was used. Also here a range of $\pm 10\%$ was used to calculate the knob values. The linearity of the matching is shown in Fig.7.10 and Fig.7.11. The values for the calculated horizontal and vertical knob vectors are listed in Table 7.4.

Table 7.4: Calculated values for the horizontal and vertical knob vectors by MAD matching version 11.

match version 11					
$K[m^{-1}]$	$x-plane$	$y-plane$	$K[m^{-1}]$	$x-plane$	$y-plane$
K4A8I	-0.038045	0.000898	K6A8O	-0.017309	-0.003807
K4A8O	-0.000181	-0.035329	K7A8	0	0
K5A8I	-0.036588	-0.001332	KDAA8	0.005019	0.010350
K5A8O	-0.005577	-0.031991	KFAA8	0.010940	0.010940
K6A8I	-0.004583	-0.014744	KFBA8	0.010526	0.005053

The performance of these knobs is shown in Table 7.5 on page 104. The behavior of the constraints is similar to the ones of version 10 which are shown on pages 102 and 103.

Both knob sets (Version 10 and 11) fulfill the required condition for the constraints. Compared to version 10 version 11 has the better performance for the dispersion but the confinement of the β-function change to IR8 is slightly degraded. Also the tune change is increased. The choice for either of these knob sets for operation depends on the demands on the constraints.

Table 7.5: Calculated values for the horizontal and vertical knob vectors by MAD match version 11.

KBX	KBY	$\beta_x[m]$	$\beta_y[m]$	α_x	α_y	$D_x[m]$	
MAD match version 11 IP8							Q_1
-0.2	-0.2	8.29e-01	8.09e-01	3.54e-02	-4.80e-02	5.19e-03	28.2225
0.2	-0.2	1.28e+00	8.10e-01	2.12e-02	1.89e-02	-2.84e-03	28.2235
0.0	0.0	1.02e+00	9.84e-01	-1.17e-02	-2.38e-03	2.44e-03	28.2200
-0.2	0.2	8.16e-01	1.20e+00	-5.94e-02	-1.59e-02	5.81e-03	28.2181
0.2	0.2	1.25e+00	1.20e+00	-3.37e-02	2.02e-02	-4.72e-04	28.2200
MAD match version 11 IP6							Q_2
-0.2	-0.2	9.43e-01	1.00e+00	2.58e-03	-5.59e-03	-2.29e-02	29.2322
0.2	-0.2	9.37e-01	9.96e-01	3.27e-03	-1.72e-02	6.49e-04	29.2331
0.0	0.0	9.52e-01	9.97e-01	9.97e-03	-1.53e-04	3.98e-04	29.2300
-0.2	0.2	9.60e-01	9.99e-01	1.56e-02	6.24e-03	1.01e-03	29.2289
0.2	0.2	9.58e-01	1.00e+00	3.08e-02	1.16e-02	2.37e-02	29.2300

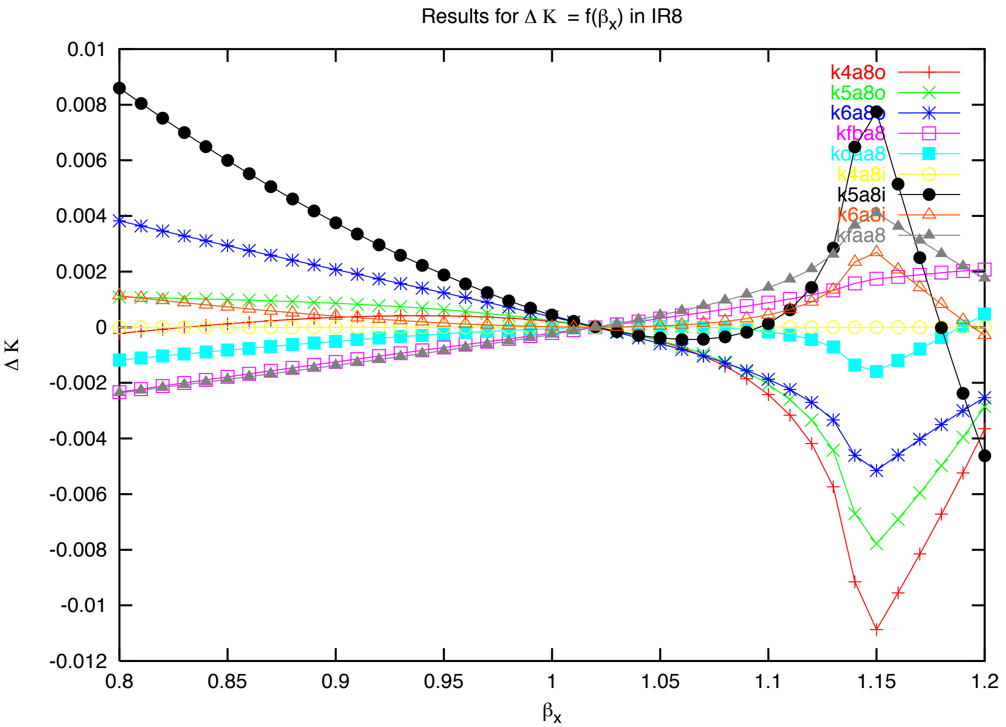

Figure 7.10: Result when matching $\beta_x^\star$ in IP8 in a range of $\pm 20\%$ around the nominal $\beta^\star$ value of one meter with K4A8O , K5A8O, K6A8O, KFBA8, K4A8I, K5A8I, K6A8I, KFAA8 and KDAA8 and $\alpha_x^\star$, $\alpha_y^\star$, $\beta_x^\star$ $\beta_y^\star$ in IP6 and $\alpha_y^\star$, $\beta_y^\star$ in IP8 as well as Q_1 and Q_2 as constraints.

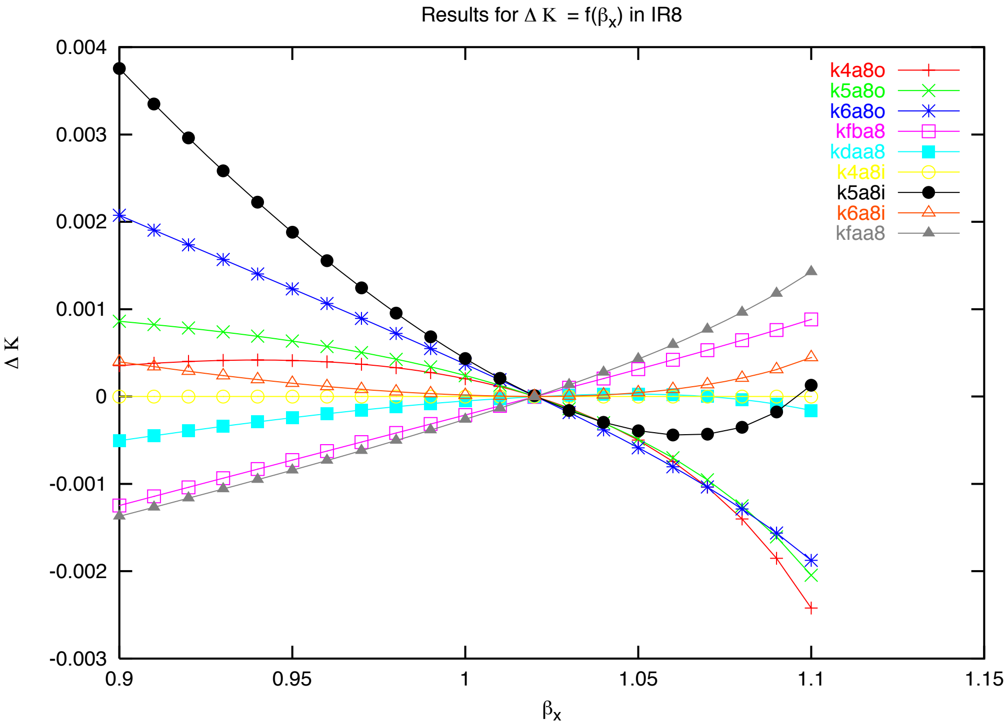

Figure 7.11: Result when matching $\beta_x^\star$ in IP8 in a range of $\pm 10\%$ around the nominal $\beta^\star$ value of one meter with K4A8O , K5A8O, K6A8O, KFBA8, K4A8I, K5A8I, K6A8I, KFAA8 and KDAA8 and $\alpha_x^\star$, $\alpha_y^\star$, $\beta_x^\star$ $\beta_y^\star$ in IP6 and $\alpha_y^\star$, $\beta_y^\star$ in IP8 as well as Q_1 and Q_2 as constraints.

7.3 Calculating knobs using the response matrix.

As noted tuning knobs can be determined by analytically inverting the response matrix. Therefore specific conditions have to be fulfilled. The response matrix must be a square matrix (number of tuning knobs is equal to number of constraints) and must not be singular or ill conditioned. For a rectangular matrix a pseudo inversion can be performed. This creates an error which can be minimized by minimizing the Norm

$$||\mathbf{I} - \mathbf{R} \cdot \mathbf{A}||, \tag{7.1}$$

where **A** is the pseudo inverted matrix. In the latter case one can try to find a solution by using singular value decomposition. The second problem can be the nonlinearity of the matrix. This means the bigger the changes of the increments to the quadrupoles are, the bigger is the deviation of the knobs' behavior between calculated prediction and actual behavior in the simulation. In this case one can try to minimize the error by compromising between minimizing the increment of the quadrupoles and allowing small changes for constraints which are supposed to be fixed. These are tune, chromaticity, α functions and dispersion.The maximum range of the allowed change depends on whether there is a possibility of correcting it, e.g., for tune and chromaticity there are special corrector magnets in the lattice. These corrections determine the acceptable range of change. For the other parameters one has to estimate the allowable range by requiring a negligible perturbation of the lattice functions.

7.3.1 Inverting the response matrix.

In the case of the RHIC lattice in the region of IR8 and IR6 the response matrix is well conditioned and the number of constraints was chosen to be equal to the number of tuning quadrupoles whereby a square response matrix is generated. The matrix is shown below.

$$R = \left[\begin{matrix}
1.71e+01 & -5.23e+00 & -2.30e+01 & 5.67e+00 & 2.41e+00 \\
-8.50e+00 & 1.83e+01 & 5.46e+00 & -3.08e+01 & 3.95e+00 \\
6.68e+00 & -6.61e+00 & -1.83e+01 & 1.25e+00 & 8.61e+00 \\
2.31e+00 & 4.80e+00 & 2.39e+00 & 1.16e+00 & -1.43e+01 \\
-1.67e+01 & -7.16e+00 & 2.21e+01 & 5.77e+00 & -1.95e+00 \\
7.04e+00 & 1.77e+01 & -5.95e+00 & -2.42e+01 & 1.63e+00 \\
-7.65e+00 & -4.86e+00 & 2.02e+01 & -7.06e-01 & -9.29e+00 \\
-5.23e+00 & -6.85e+00 & -1.87e-01 & 1.89e+01 & 1.45e+01 \\
-2.87e+00 & 1.35e+00 & 4.66e+00 & -9.08e-01 & -1.46e+00 \\
1.39e+00 & -2.99e+00 & -9.41e-01 & 4.87e+00 & 2.34e+00
\end{matrix}\right.$$

$$\left.\begin{array}{rrrrr}
-4.79e+00 & 1.27e+01 & 2.49e+00 & -2.20e+01 & -1.99e+00 \\
7.71e+00 & -1.53e+00 & -2.74e+01 & 4.42e+00 & -4.31e+00 \\
1.34e+01 & -1.67e+01 & -2.81e+00 & 1.60e+01 & -2.75e+01 \\
-5.67e+00 & 2.17e+01 & -4.28e+00 & 3.07e+00 & 6.72e-01 \\
8.26e-03 & -2.10e+01 & 8.43e+00 & 2.29e+01 & -1.11e+01 \\
2.88e+00 & 1.88e+01 & -1.27e+01 & -5.25e+00 & -3.09e+00 \\
1.53e+01 & 1.86e+01 & 1.96e+00 & -1.66e+01 & -2.71e+01 \\
-8.99e+00 & 1.91e+01 & -4.29e+01 & -1.19e+00 & 3.04e+00 \\
2.34e+00 & 3.18e+00 & -1.60e+00 & 4.35e+00 & 4.49e+00 \\
-1.51e+00 & 3.21e+00 & 8.87e+00 & -8.52e-01 & -6.91e-01
\end{array}\right]$$

The values are only spread over a range of three orders of magnitude with the exception of one element which deviates by five orders. By inverting the matrix and solving the linear system one obtains a well behaved solution for the knobs. The solution of this calculation for the knobs (Table 7.6) does not significantly differ from the one obtained by MAD matching (see in Tables 7.2 and 7.4). The behavior of the constraints when changing the knobs by ±20% in both planes is summarized in the following Table 7.7. The behavior within this range is comparable to that for the MAD matching method (in Plots on page 102 and 103).

Table 7.6: Values for the horizontal and vertical knob vectors calculated inverting the response matrix.

inverted response matrix					
$K[m^{-1}]$	$x - plane$	$y - plane$	$K[m^{-1}]$	$x - plane$	$y - plane$
K4A8I	-0.000614	0.021053	K6A8O	0.019450	-0.004733
K4A8O	0.014470	0.007187	K7A8	0.000584	0.001000
K5A8I	0.010935	0.018653	KDAA8	-0.000622	-0.013267
K5A8O	0.015107	0.015269	KFAA8	-0.014742	0.001375
K6A8I	-0.002481	0.017698	KFBA8	-0.010357	-0.003547

7.3.2 Pseudo inverting and conditioning the response matrix by Singular Value Decomposition (SVD).

Using SVD [27] to invert the matrix gives the same result within machine precision compared to direct inversion. In this case the primary goal of SVD is not to invert but to perform the following conditioning. The singular value decomposition of the matrix

Table 7.7: The changes of the constraints in IP8 and IP6 when setting the multipliers KBX and KBY to the edge points of their operative range using knobs calculated by inverting the linear matrix.

KBX	KBY	$\beta_x[m]$	$\beta_y[m]$	α_x	α_y	$D_x[m]$	
inverted response matrix IP8							Q_1
-0.2	-0.2	8.37e-01	8.02e-01	-1.51e-02	1.47e-03	4.26e-03	28.2201
0.2	-0.2	1.23e+00	8.02e-01	-5.55e-03	-6.47e-03	-1.82e-02	28.2187
0.0	0.0	1.02e+00	9.84e-01	-1.17e-02	-2.38e-03	2.44e-03	28.2200
-0.2	0.2	8.38e-01	1.20e+00	-6.31e-03	-7.41e-03	1.85e-02	28.2181
0.2	0.2	1.23e+00	1.20e+00	-1.42e-02	-1.47e-04	6.31e-04	28.2203
inverted response matrix IP6							Q_2
-0.2	-0.2	9.54e-01	9.99e-01	1.67e-02	6.78e-03	-1.91e-02	29.2299
0.2	-0.2	9.51e-01	1.00e+00	2.56e-02	2.17e-02	2.28e-02	29.2276
0.0	0.0	9.52e-01	9.97e-01	9.97e-03	-1.53e-04	3.98e-04	29.2300
-0.2	0.2	9.51e-01	1.00e+00	2.79e-02	1.74e-02	-2.02e-02	29.2286
0.2	0.2	9.53e-01	1.00e+00	1.66e-02	5.61e-03	2.01e-02	29.2303

gives three matrices of which the second s is diagonal (see below).

$$s = \begin{pmatrix} 68.17 & 0 & 0 & 0 & 0 & 0 & 0 & 0 & 0 & 0 \\ 0 & 58.44 & 0 & 0 & 0 & 0 & 0 & 0 & 0 & 0 \\ 0 & 0 & 50.02 & 0 & 0 & 0 & 0 & 0 & 0 & 0 \\ 0 & 0 & 0 & 48.29 & 0 & 0 & 0 & 0 & 0 & 0 \\ 0 & 0 & 0 & 0 & 44.07 & 0 & 0 & 0 & 0 & 0 \\ 0 & 0 & 0 & 0 & 0 & 21.74 & 0 & 0 & 0 & 0 \\ 0 & 0 & 0 & 0 & 0 & 0 & 8.62 & 0 & 0 & 0 \\ 0 & 0 & 0 & 0 & 0 & 0 & 0 & 7.86 & 0 & 0 \\ 0 & 0 & 0 & 0 & 0 & 0 & 0 & 0 & 1.65 & 0 \\ 0 & 0 & 0 & 0 & 0 & 0 & 0 & 0 & 0 & 1.10 \end{pmatrix}$$

It can be used to condition the problem. In case of big differences between the values one can set the inverse of the smaller singular values to zero and construct a conditioned inverted response matrix. This reduces the number of eigenvectors and therefore the dimension of the matrix. But the eigenvectors, which are associated with these small singular values, are not linearly independent or are similar to one or a combination of others, so that the resulting conditioned matrix and its solution are similar to the original. This method eliminates the parts of the solution which create the smallest changes by maximum effort. By doing so a small error is introduced, but the magnitude of the quadrupole strength change is greatly decreased. This way errors from the nonlinear behavior of the response matrix are reduced. A compromise between these contradicting effects is found empirically.

For the RHIC case the values of the diagonal matrix vary only by one and a half orders of magnitude as shown above. Two different cases were studied in which the smallest two (case I) and the smallest four (case II) values of the diagonal matrix s were

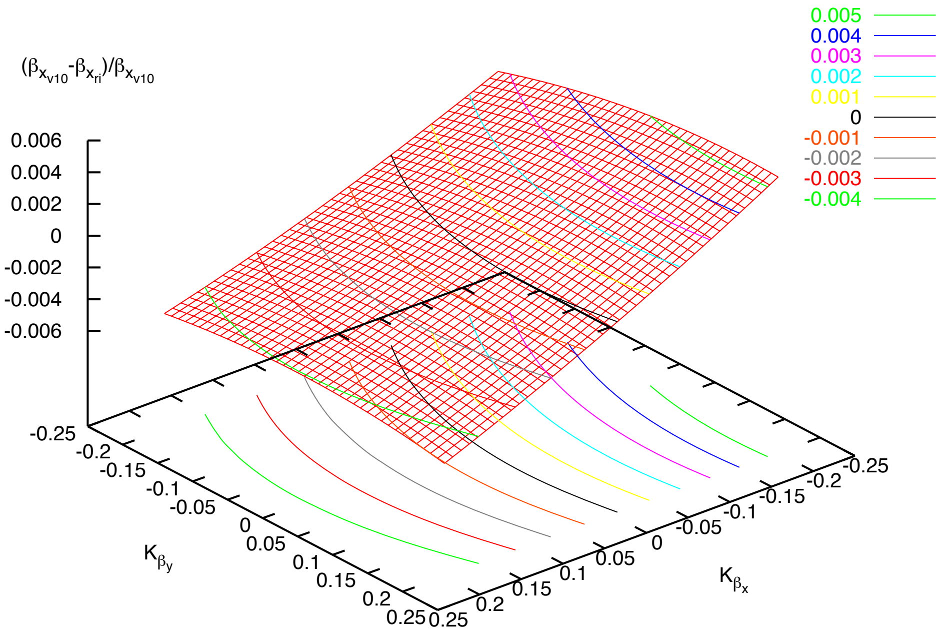

Figure 7.12: Comparing the incremented change of $\beta^{\star}$ in IP8 for the knobs computed by MAD matching version 10 and response matrix inversion.

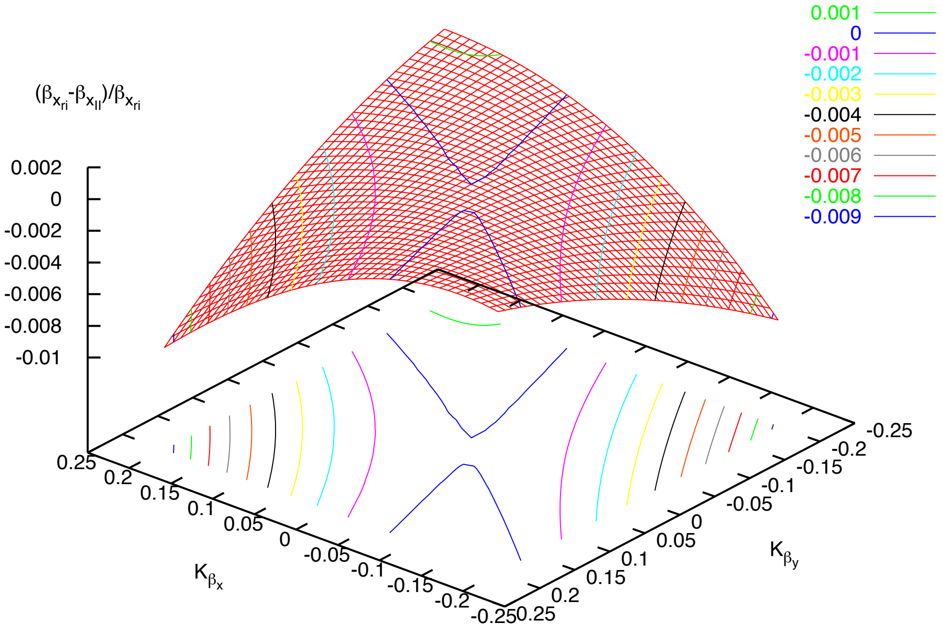

Figure 7.13: Comparing the incremented change of $\beta^{\star}$ in IP8 for the knobs computed by response matrix inversion and the response-matrix conditioning using SVD.

set to zero in the inversion. The values of the calculated knobs are shown in Table 7.8 and the behavior of the constraints is summarized in Table 7.9. Again it does not differ much from the one obtained by MAD matching which is shown on pages 102 and 103 or from the one obtained by full inversion. The conditioning brought no improvement of the behavior.

The differences of the $\beta^\star$ changes at IP8 between the two methods of MAD matching and the response matrix inversion, and between the response matrix inversion and SVD conditioned pseudo response matrix are shown in Fig. 7.12, Page 109, and Fig. 7.13, Page 109. The biggest difference between MAD matching and SVD conditioned pseudo response matrix is 1.4 % of the desired change (e.g., 0.28 % in the absolute β value).

Table 7.8: Values for the horizontal and vertical knob vectors calculated by SVD inversion and conditioning for two different cases.

$K[m^{-1}]$	case I		case II	
	$x - plane$	$y - plane$	$x - plane$	$y - plane$
K4A8I	-0.001430	0.027712	-0.038045	0.000898
K4A8O	0.012573	0.006009	-0.000181	-0.035329
K5A8I	0.010229	0.022689	-0.036588	-0.001332
K5A8O	0.014056	0.014612	-0.005577	-0.031991
K6A8I	-0.002940	0.019187	-0.004583	-0.014744
K6A8O	0.019648	-0.004527	-0.017309	-0.003807
K7A8	0.001013	0.000282	0	0
KDAA8	-0.000668	-0.013897	0.005019	0.010350
KFAA8	-0.015013	0.001780	0.010940	0.010940
KFBA8	-0.010407	-0.003237	0.010526	0.005053

7.3.3 Calculating tuning knobs using an adapted Moore Penrose method to condition the response matrix.

In case of nonlinear response of the constraints to the quadrupole increments ΔK, solving the linear system to construct the knobs creates an error which depends on the size of the change and on the response behavior. A method [28][22] to minimize the error is to compromise between the allowable quadrupole increments ΔK and the target values for the constraints. The relation of the maximum changes of different tuning quads to each other can be determined by analyzing the plots which where used to calculate the response matrix (see Fig.7.3-Fig.7.5). By using the method of the maximum likelihood [29]

$$\mathcal{L}\left(\vec{\alpha}\right) = \prod_i f\left(x_i; \vec{\alpha}\right) \tag{7.2}$$

were the x_i are the measured quantities, $\vec{\alpha}$ the set of unknown parameters, $f\left(x_i; \vec{\alpha}\right)$ the probability density function (for RHIC the proton beams have a two dimensional

Table 7.9: The changes of the constraints in IP8 and IP6 when setting the multipliers KBX and KBY to the edge points of their operative range calculated by SVD inversion and conditioning.

KBX	KBY	β_x	β_y	α_x	α_y	D_x	
SVD conditioned response matrix case I IP8							Q_1
-0.2	-0.2	8.33e-01	7.99e-01	-4.46e-02	3.72e-02	7.19e-03	28.2209
0.2	-0.2	1.23e+00	8.11e-01	3.72e-03	2.86e-02	-4.01e-03	28.2097
0.0	0.0	1.02e+00	9.84e-01	-1.17e-02	-2.38e-03	2.44e-03	28.2200
-0.2	0.2	8.43e-01	1.20e+00	-3.68e-02	-1.92e-02	7.50e-03	28.2275
0.2	0.2	1.22e+00	1.18e+00	-2.26e-02	5.11e-03	-1.95e-03	28.2179
SVD conditioned response matrix case II IP8							
-0.2	-0.2	8.29e-01	7.95e-01	-3.46e-02	2.55e-02	4.48e-03	28.2098
0.2	-0.2	1.23e+00	8.00e-01	-6.15e-03	2.67e-03	-1.82e-02	28.2200
0.0	0.0	1.02e+00	9.84e-01	-1.17e-02	-2.38e-03	2.44e-03	28.2200
-0.2	0.2	8.39e-01	1.19e+00	-9.54e-03	-4.26e-03	1.83e-02	28.2176
0.2	0.2	1.22e+00	1.18e+00	-2.52e-02	9.52e-03	1.50e-03	28.2288
SVD conditioned response matrix case I IP6							Q_2
-0.2	-0.2	9.63e-01	9.85e-01	4.34e-04	-2.47e-03	-1.74e-02	29.2317
0.2	-0.2	9.47e-01	9.91e-01	2.50e-02	-1.95e-03	2.53e-02	29.2430
0.0	0.0	9.52e-01	9.97e-01	9.97e-03	-1.53e-04	3.98e-04	29.2300
-0.2	0.2	9.59e-01	1.00e+00	1.30e-02	8.65e-03	-2.21e-02	29.2142
0.2	0.2	9.57e-01	1.00e+00	3.24e-02	2.21e-02	1.91e-02	29.2269
SVD conditioned response matrix case II IP6							
-0.2	-0.2	9.65e-01	9.93e-01	1.75e-02	1.30e-02	-1.14e-02	29.2209
0.2	-0.2	9.50e-01	1.00e+00	2.24e-02	1.54e-02	1.49e-02	29.2235
0.0	0.0	9.52e-01	9.97e-01	9.97e-03	-1.53e-04	3.98e-04	29.2300
-0.2	0.2	9.51e-01	1.00e+00	2.36e-02	1.78e-02	-1.25e-02	29.2339
0.2	0.2	9.63e-01	9.98e-01	2.91e-02	2.32e-02	1.36e-02	29.2375

Gaussian profile in good approximation), one calculates the optimized solution for a chosen set of weights for the constraints (allowed deviation from target values) and limits on the changes of quadrupole strength (minimizing the change with respect to different linear ranges calculated by response matrix analysis). The following relation holds,

$$\chi^2 = \chi^2_{min} + (\alpha - \tilde{\alpha})^T \mathbf{V}^{-1} (\alpha - \tilde{\alpha}) \tag{7.3}$$

where χ^2 is the minimum, χ^2_{min} the residual minimum, $\tilde{\alpha}$ the set of calculated parameters (constraints or quadrupole changes ΔK) and $\mathbf{V}$ the weight matrix. $\mathbf{V}$ is a diagonal matrix whose diagonal elements equal the inverted square weight variables $\frac{1}{\Delta p^2}$ for both unknown sets of parameters (constraints, ΔK). Taking the derivative one obtains a conditioned response matrix ($\mathbf{H}$) as a function of the measured response matrix ($\mathbf{R}$) and the two weight matrices ($\mathbf{\Sigma}$) and ($\mathbf{S}$)

$$\mathbf{H} = \mathbf{R}^T \mathbf{\Sigma} \mathbf{R} + \mathbf{S} \tag{7.4}$$

Table 7.10: Values of the allowable constraints variation σ and stiffness of the different tuning quads (s) vector used by the adapted Moore Penrose method to condition the response matrix.

K	stiff	K	stiff	constraints	$\frac{1}{\sigma}$	constraints	$\frac{1}{\sigma}$
K4A8I	5	K6A8O	0	α_x(IP6)	100	α_y(IP8)	100
K4A8O	5	K7A8	10	α_y(IP6)	100	β_x(IP8)	100
K5A8I	5	KDAA8	10	β_x(IP6)	100	β_y(IP8)	100
K5A8O	5	KFAA8	20	β_y(IP6)	100	Q_1	10
K6A8I	0	KFBA8	20	α_x(IP8)	100	Q_2	10

For the RHIC lattice the stiff values s_i of the quadrupole changes (with $\frac{1}{s_i^2}$ as the diagonal elements of the weight matrix $\mathbf{S}$) calculated from the results of the response matrix analysis are compiled in Table 7.10. The table also contains the σ_i of the constraints (with $\frac{1}{\sigma_i^2}$ as the diagonal elements of the weight matrix $\boldsymbol{\Sigma}$). The calculated knobs are summarized in Table 7.11 and the characterization of the constraints when the knobs are applied in Table 7.12. The application of this adapted Moore Penrose method for multidimensional optimization to the RHIC lattice brought no noticeable improvement as the nonlinear behavior for the selected set of quadrupoles is not very strong in the range of the applied changes.

Table 7.11: Calculated values for the horizontal and vertical knob vectors using the adapted Moore Penrose method to condition the response matrix.

inverted response matrix					
$K[m^{-1}]$	$x-plane$	$y-plane$	$K[m^{-1}]$	$x-plane$	$y-plane$
K4A8I	0.001245	0.018071	K6A8O	0.019781	-0.004401
K4A8O	0.007830	0.008608	K7A8	0.001632	0.001638
K5A8I	0.011726	0.016415	KDAA8	-0.001103	-0.012421
K5A8O	0.011204	0.016315	KFAA8	-0.013396	0.001580
K6A8I	-0.002723	0.016528	KFBA8	-0.008741	-0.003731

7.4 Results from Beam Experiments

To test these calculated knobs beam experiments were performed at the Relativistic Heavy Ion Collider (RHIC) at Brookhaven National Laboratory (BNL), Upton N.Y.. These had the goal to prove the validity of the developed knob theory, the range of application and search of possible error sources for malfunctioning of the knobs. As the available beam time was very limited and the knobs calculated with the different methods are very similar only one knob was tested. Due to differences in the MAD model and the Online Model, which is used to operate the collider, the knobs had to be recalculated based on this latter model with response analysis. The resulting knobs are similar to the ones above and are thus not shown here.

Table 7.12: The changes of the constraints in IP8 and IP6 when setting the multipliers KBX and KBY to the edge points of their operative range calculated by using the adapted Moore Penrose method to condition the response matrix.

KBX	KBY	$\beta_x[m]$	$\beta_y[m]$	α_x	α_y	$D_x[m]$	
IP8							Q_1
-0.2	-0.2	8.36e-01	8.04e-01	-1.62e-02	6.89e-03	3.72e-03	28.2172
0.2	-0.2	1.23e+00	8.04e-01	-8.69e-03	-3.39e-03	-1.88e-02	28.2206
0.0	0.0	1.02e+00	9.84e-01	-1.17e-02	-2.38e-03	2.44e-03	28.2200
-0.2	0.2	8.38e-01	1.19e+00	-9.83e-03	-7.42e-03	1.93e-02	28.2166
0.2	0.2	1.23e+00	1.19e+00	-1.57e-02	1.25e-03	1.52e-03	28.2230
IP6							Q_2
-0.2	-0.2	9.55e-01	9.94e-01	1.72e-02	1.27e-02	-1.61e-02	29.2288
0.2	-0.2	9.52e-01	1.00e+00	2.44e-02	2.27e-02	1.83e-02	29.2266
0.0	0.0	9.52e-01	9.97e-01	9.97e-03	-1.53e-04	3.98e-04	29.2300
-0.2	0.2	9.53e-01	1.01e+00	2.59e-02	1.23e-02	-1.58e-02	29.2301
0.2	0.2	9.55e-01	1.00e+00	1.84e-02	3.71e-03	1.74e-02	29.2307

The beam experiments were performed in two major stages. The first was to test the stability of the beam when applying the tuning knobs. For this stage there were only four bunches with low energy injected, accelerated and squeezed. This is to prevent damage to the installation in case of knob induced beam loss. At this stage the knobs were applied and the stability observed. When passing this stage a new batch of bunches (nominal number and intensity) was injected and the procedure above repeated.

The results of these experiments are shown below. All plots shown in the following were copied from the control system during the experiments automatically or manually into the automatic logbook and are taken from there. These are original data without any post-experiment data manipulation. In total four experiments were performed during four beam-experiment shifts. The results from experiment one and three are not discussed here because during these shift operational problems prevented the program to go ahead. In both cases operational errors caused the quench protection system to abort the beam and started the quench recovery procedure. This produces a large time delay and the knob related beam experiment was terminated.

7.4.1 Beam Experiment 2

The first preparative stage was passed without any problem. Six bunches for each beam with nominal bunch intensity (lower total intensity) were injected. This was followed by the ramp procedure during which the beams are accelerated and simultaneously squeezed. This is done to ramp the magnets continuously to stay on the calibration curve. After bringing the two beams into collision the knobs were applied in two steps. For the first step the nominal β-function at the IP was squeezed by 6%, for the second step by 12%. After each step tune changes for both planes, life time and

Table 7.13: Injected beam statistics automatic recorded in the log book of the RHIC control room for the beam experiment beta star squeeze during the second experiment.

Injected Beam Statistics for Fill number 4668

Injection start time: Tue Mar 2 22:31:07 2004
Injection complete time: Tue Mar 2 22:33:02 2004

Ring	Blue	Yellow
Bunches/Cycles	56/14	56/14
Avg Bunch in RHIC (10^9 Au Ions)	0.761	0.666

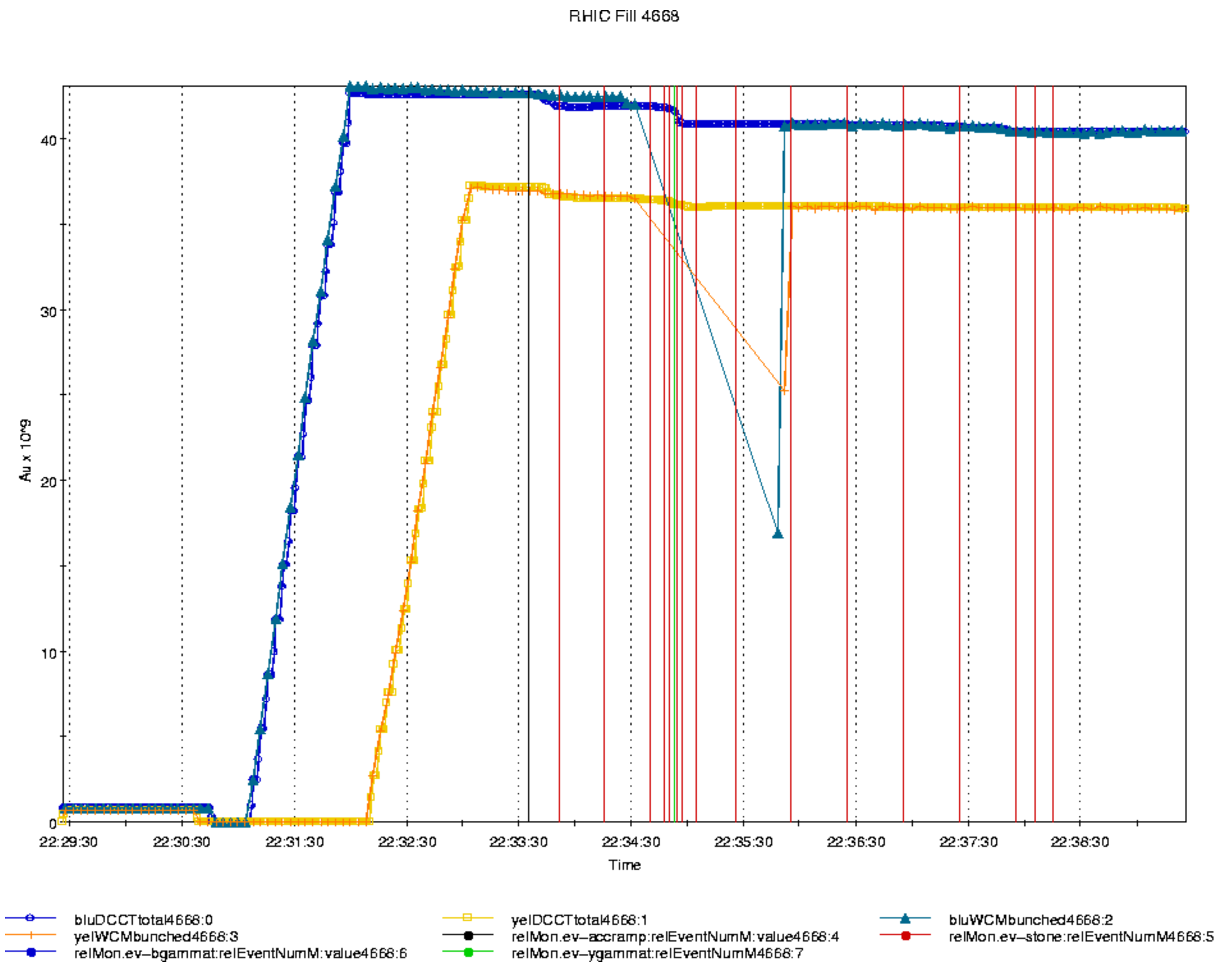

Figure 7.14: Ramp data from the beam-ions log sequencer. The plot shows the intensity of the two beams, blue and yellow. In the first part the beams are filled in batches of 4 bunches 14 times, first blue and then yellow. Then the acceleration and squeeze (from injection to collision optics) is performed. During this process a loss in intensity can be observed.

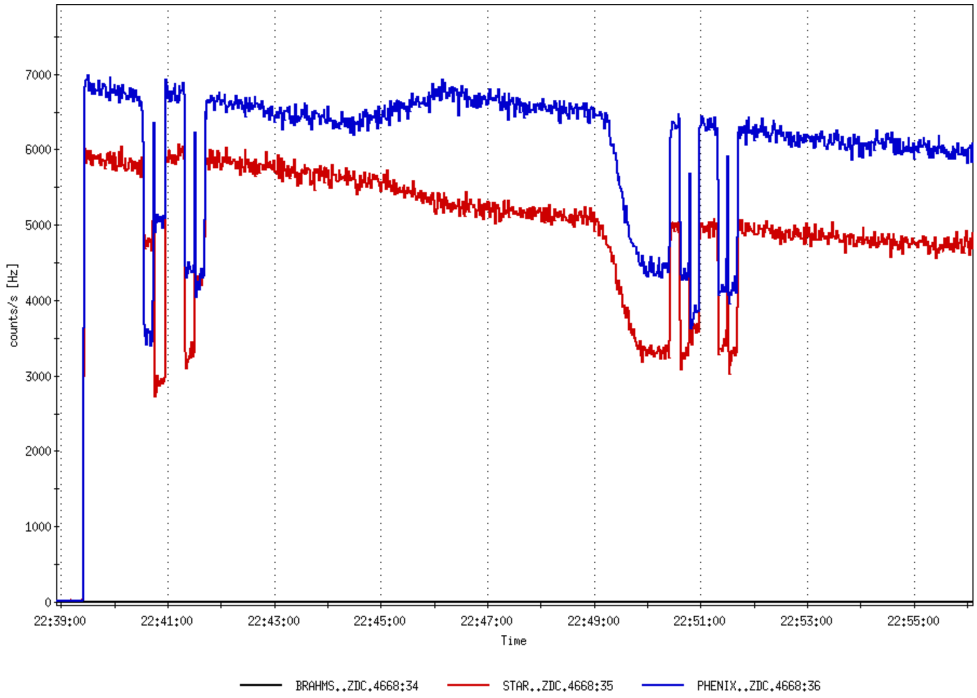

Figure 7.15: Counting rates during the offset optimization with LISA and when applying the tuning knob by decreasing the horizontal and vertical β-function at the IP for both beams in IP8. The blue graph shows the counting rate in IP8 and the red in IP6.

counting rates were observed. No problems concerning beam stability were observed. In addition the dispersion was measured. To change to a higher intensity mode to increase the statistics of the counting rate measurement by increasing the number of bunches, the beam was aborted. The same procedure as described above was repeated as shown in Fig.7.14. The injection beam statistics logged by the automatic sequencer is listed in Table 7.13.

At this point the two beams are brought into collision and the offset between the two beams is minimized. This is done by an automatic application called LISA (Long Island Steering Application). During this process one beam is moved with respect to the other in steps and the counting rate is recorded. This way the beam-beam collision is centered by maximizing the counting rate in both horizontal and vertical plane. This can be seen in plot 7.15 in the left section. The optimization is performed in IP8 (blue curve) and IP6 (red curve). Comparing the level of counting rates before and after optimization reveals, that the collision was centered prior to the correction. The original cogging process (bringing the beams into collision) had already optimized the offset.

After the application of LISA the tuning knobs introduced a reduction of the nominal horizontal and vertical β-function in IP8 of 12%. This happend about between 22:44.5 and 22:46. This can be clearly observed in Fig.7.15. The counting rates of the blue graph are increased during this process. The red graph shows a slight decrease in the counting rate. As no changes were made in this IR the first assumption was a perturbation of the β-function in IP6 by the knob due to a β wave (β beat) leaking out of IR8. This explanation is dismissed by the constant counting rate in IP10. A beta wave must effect all IPs. Later data and lattice analysis pointed out the following explanations. Dispersion created by the knobs magnified the existing dispersion in IP6 so that the beam size was increased there, resulting in a decreasing counting rate. IP10 did not show this effect because the knob induced dispersion on top of the residual one still remained below the limit increasing the beam size at the IP.

After the squeeze of the knobs LISA was applied a second time to see, if the knobs would introduce an offset at the IP. As depicted in the right section of Fig.7.15 there was no improvement in the rates and thus no steering effect of the knobs.

The most important question when planing the beam experiments was how the stability of the beam would react to the perturbation of the knob induced changes. A direct answer to this question is the beam loss. It is constantly measured during operation and therefore a direct comparison before and after applying the knob is possible. This is absolutely essential, because the beam loss is a characteristic which varies from fill to fill. Fig.7.16 shows the beam decay measured before, during and after squeezing the beam with the tuning knobs. During the squeeze there is a spike in the yellow beam. This can be explained by the fact, that the ratio of the knob for the tuning quadrupoles cannot be kept constant during the ramp of the magnets. This has various reasons like different response times for the different magnets (main magnet

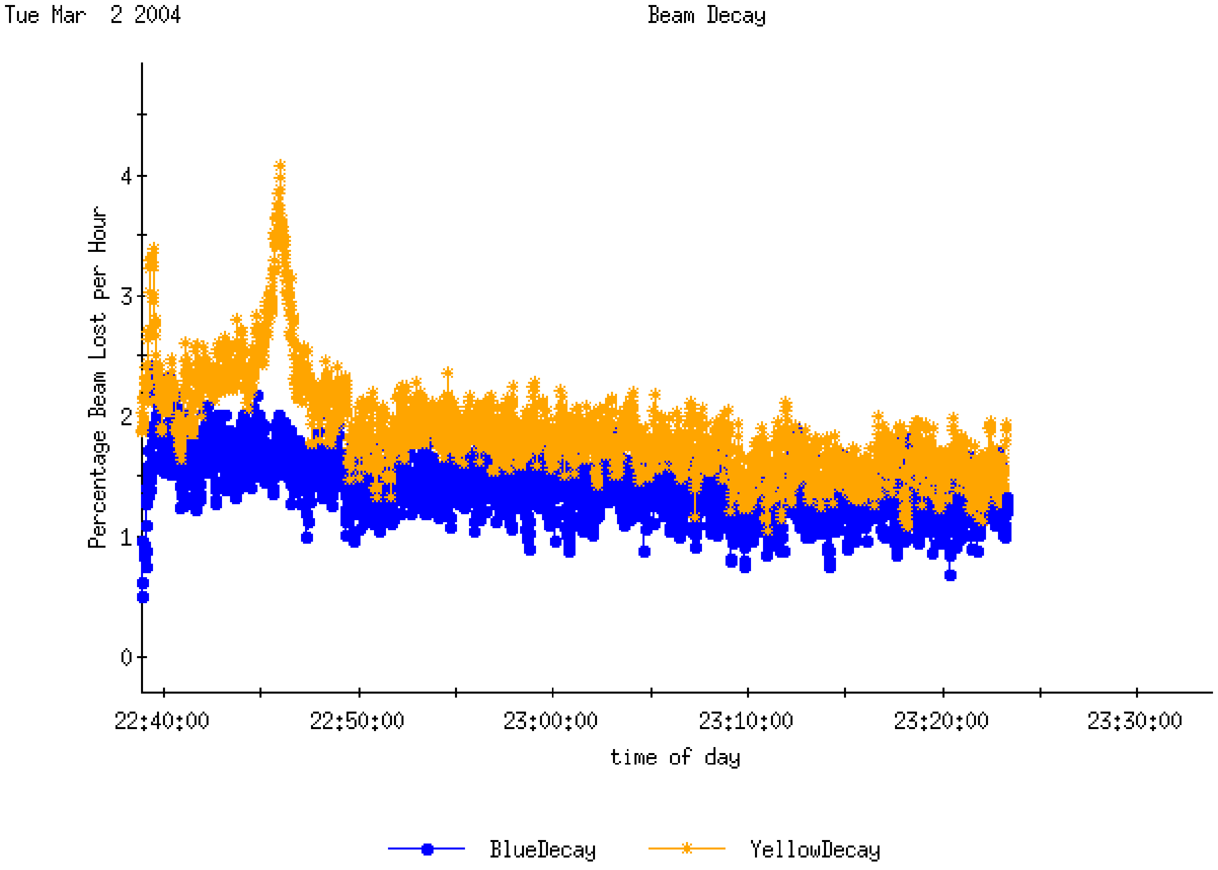

Figure 7.16: Beam loss measurement for blue and yellow ring before, during and after applying the tuning knob.

or corrector), operating system and so on. Important is that the beam is not lost and that the level of beam loss recovers to a value close to the level it had originally. For this experiment it was an unexpected surprise that the beam loss was reduced by the perturbation of the tuning knobs as shown in Fig.7.16. As a result also the background measured in the different IPs went down (see Fig.7.17).

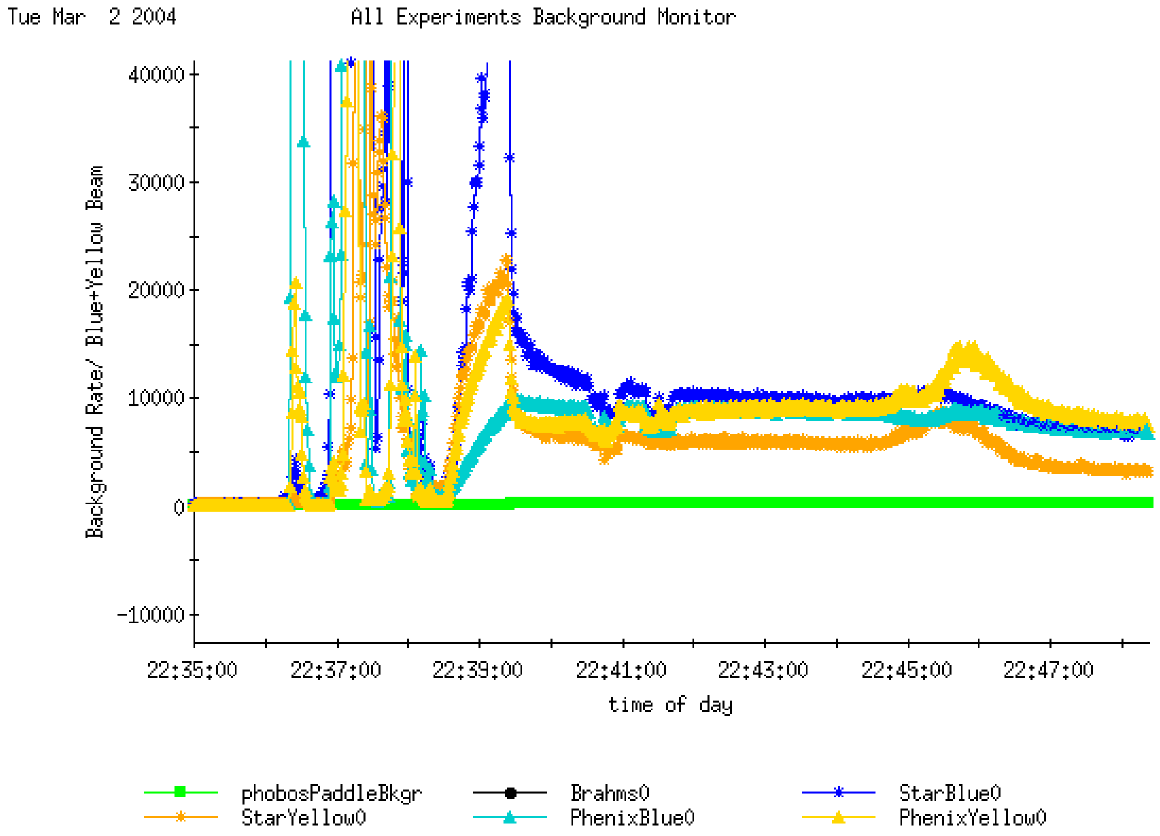

Figure 7.17: Background rates from the different IPs measured before, during and after applying the tuning knobs for $\beta^\star$ squeeze.

The IP β-functions at IP6, IP8 and IP10 with nominal optics and after applying the knob changes taken from the on-line model are shown in Table 7.14. The reduction of $\beta^\star$ in IP8 is slightly less than 12%. This is due to the perturbative approach. The changes in the other two IPs are negligible.

Table 7.14: $\beta^\star$ function in IP6, IP8 and IP10 before and after applying the tuning knob with a nominal change of -12% of the original $\beta^\star$ value in IP8 for the blue beam.

	IP6 (STAR)		IP8 (PHENIX)		IP10 (PHOBOS)	
	$\beta_x^\star[m]$	$\beta_y^\star[m]$	$\beta_x^\star[m]$	$\beta_y^\star[m]$	$\beta_x^\star[m]$	$\beta_y^\star[m]$
nominal settings	1.046	1.049	1.062	1.066	3.133	3.087
tuning knobs applied	1.046	1.053	0.947	0.951	3.125	3.096
change [%]	0	0.3	10.8	10.7	0.3	0.3

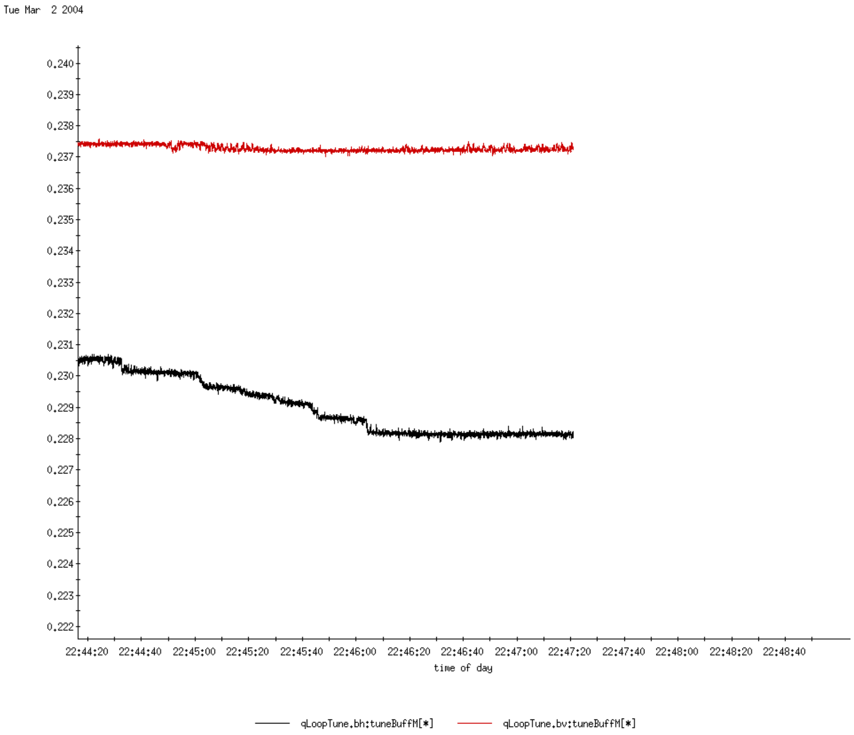

Figure 7.18: Tune change during the squeeze of the IP β-functions in the blue beam. The black curve shows the horizontal, the red the vertical tune.

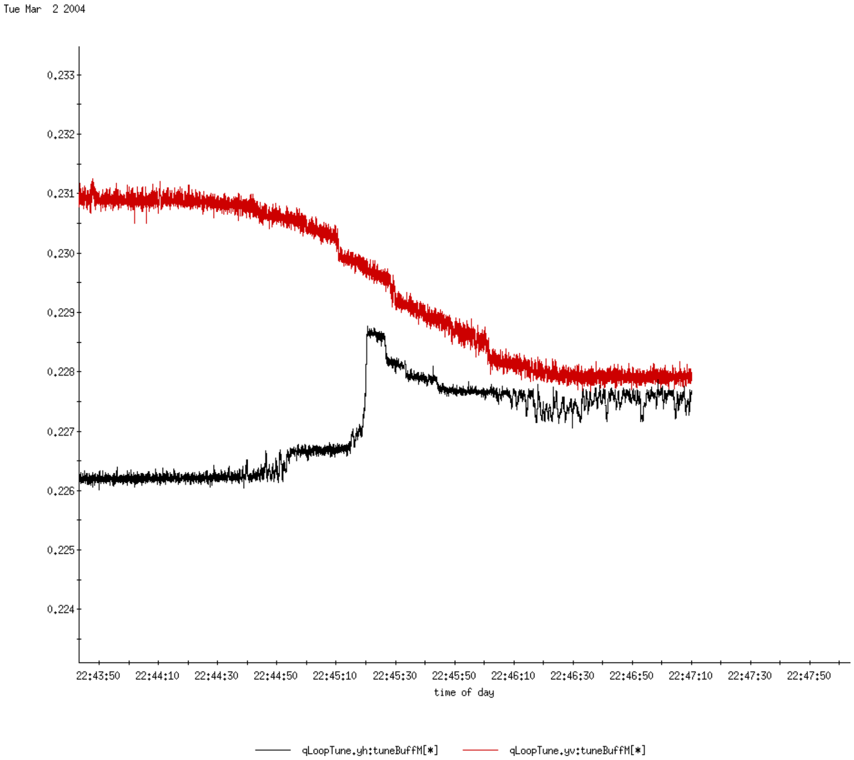

Figure 7.19: Tune change during the squeeze of the IP β-functions in the yellow beam. The black curve shows the horizontal, the red the vertical tune.

One important constraint is the tune. Figures 7.18 and 7.19 display the tune change during the β-squeeze. The tunes in the yellow beam are not changing more. This only seems so because the original tunes are closer to each other and the scale is different.

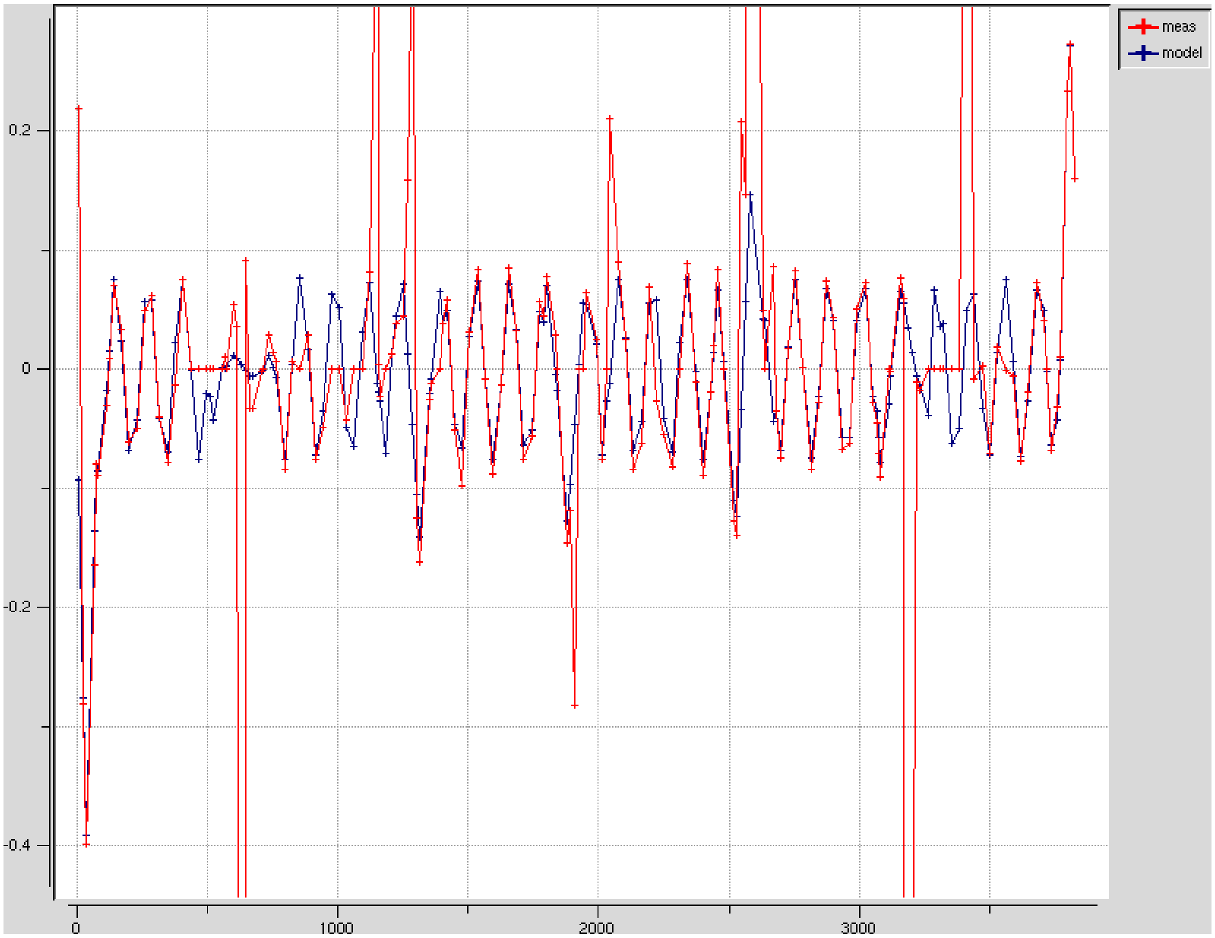

Figure 7.20: Comparison of the dispersion wave introduced by the tuning knob as predicted by the on-line model (blue curve) and measured (red curve).

All changes introduced to measurable constraints had been predicted by the simulation performed with the on-line model. The change of dispersion was very interesting from the point of testing the accuracy of the model used for the calculations. As the dispersion could not be constrained the introduced perturbation was predicted by the model. The second important point for this discussion is the fact, that by applying a “radial bump” (changing the rf frequency in the accelerating cavities and thereby changing the orbit of the beam through the introduced energy shift) and taking the difference of the orbit before and after, the dispersion can be measured at all BPMs around the entire ring. Doing this before and after applying the knob gives the dispersion wave introduced by the tuning knobs. This wave can be compared to the prediction made by the simulation as depicted in Fig.7.20. The blue curve shows the measured dispersion wave, the blue the simulated. The red curve has a couple of very high spikes. They are due to false BPM readings during the measurement. The red curve is bigger in general. This is due to the fact that the radial bump is not exactly one millimeter. The measured curve has to be corrected for this error which was not possible because of data unavailability. The phase of the waves is of greater interest in this case. If there is a significant difference between model and real machine (probed by the measurement) the phase of the two curves would separate at some point and would stay separated. This would indicate an error in the model. The phases for the two graphs in Fig.7.20 show excellent agreement for the entire ring. This indicates that the model is in very good agreement with the real machine and that all simulated changes of the constraints are correct with a small error.

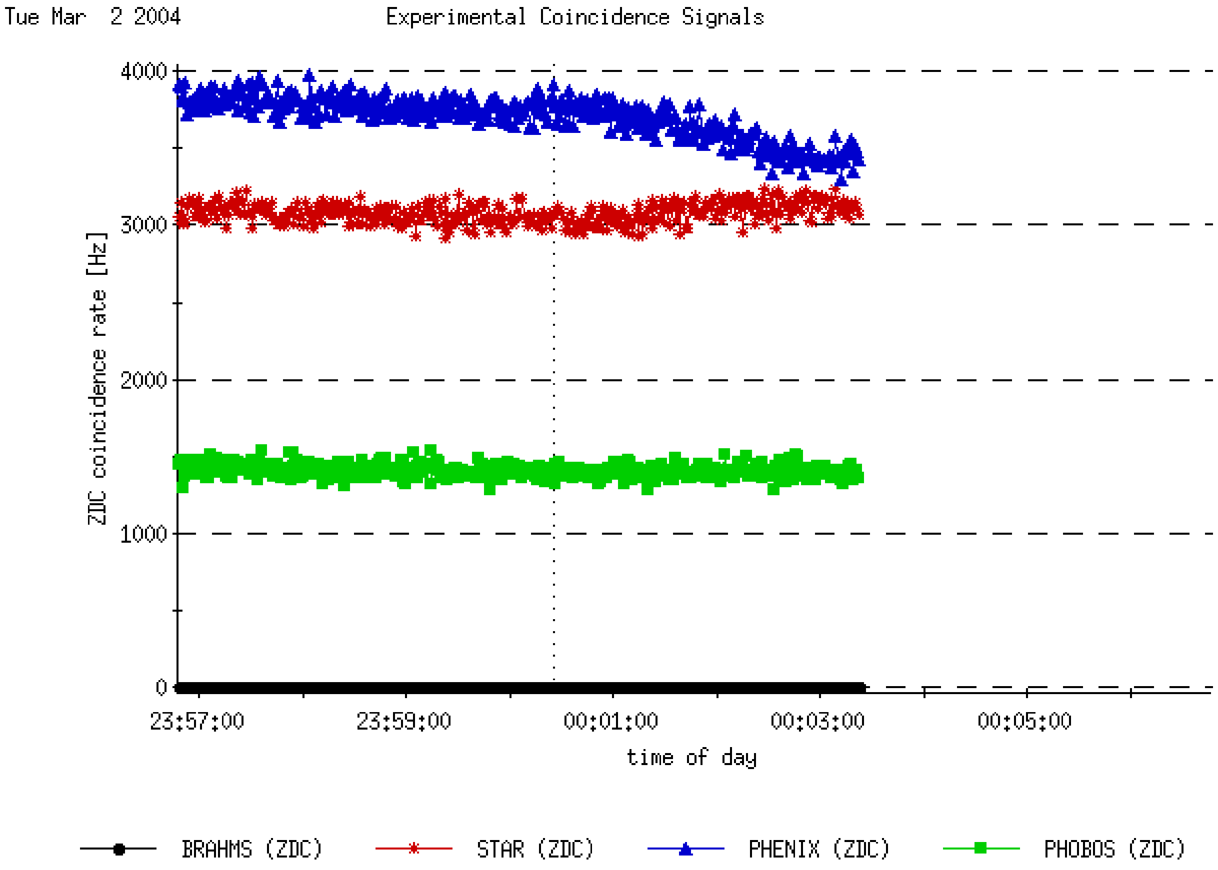

Figure 7.21: Counting rates during the reversal of the knob induced changes in IP8. The blue curve shows the counting rate in IP8, the red in IP6 and the green in IP10 (PHOBOS).

One important feature of the tuning knobs is to have the possibility to apply them repeatedly. This requires all changes to be reversible. To test this, the knob changes were reversed (between 00:01:10 and 00:02:20) and during this time, the tunes, beam loss rates, background rates and counting rates were observed. The results are shown in Figs.7.21 to 7.25 on this and the following pages.

All observed quantities showed the reversed behavior compared to the one during the knob induced squeeze. This indicates that in case of the RHIC knob the effect is reversible and thus the knobs are repeatedly applicable. For a long term statement a great number of cycles would have to be performed with the knobs and all relevant

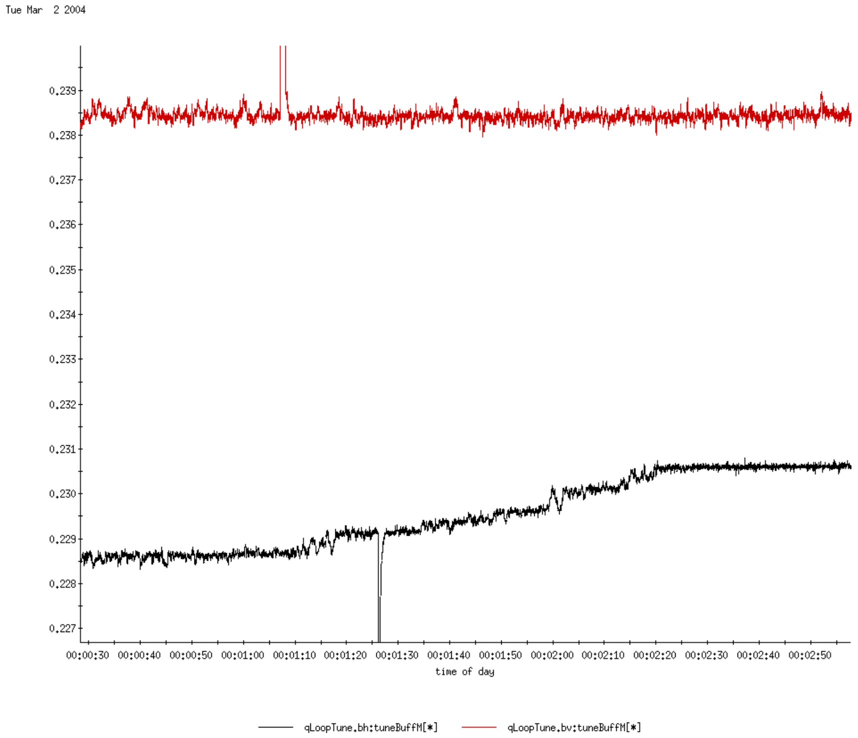

Figure 7.22: Tune change during the unsqueeze of the IP β-functions in the blue beam. The black curve shows the horizontal, the red the vertical tune.

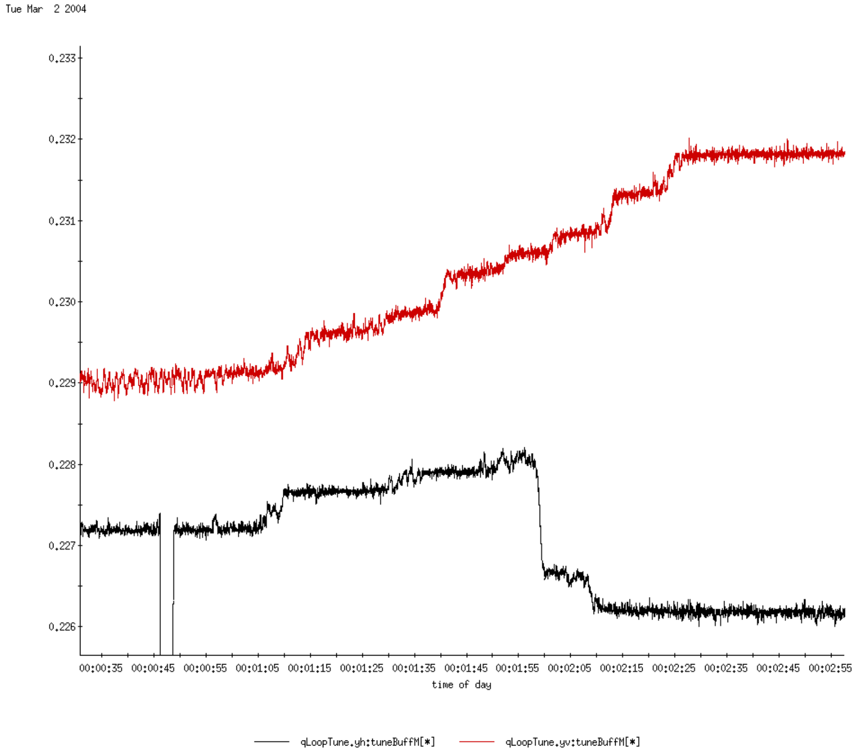

Figure 7.23: Tune change during the unsqueeze of the IP β-functions in the blue beam. The black curve shows the horizontal, the red the vertical tune.

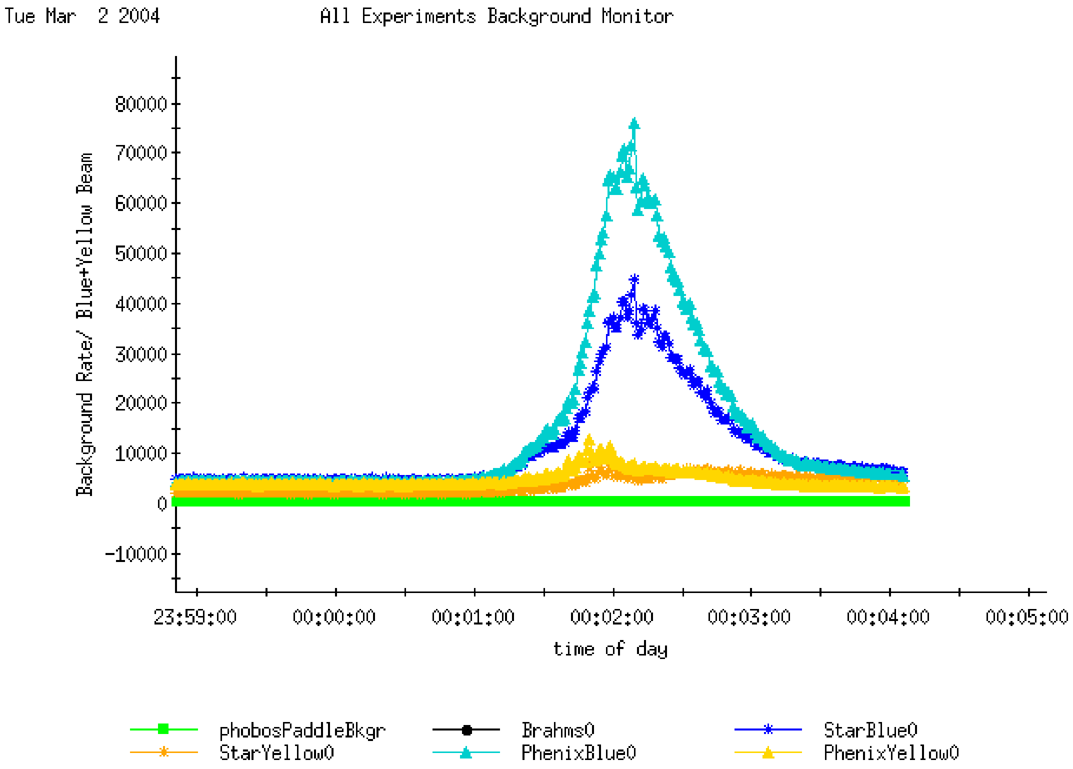

Figure 7.24: Background rates in the different IPs measured before during and after unsqueezing the IP β-functions with the tuning knob.

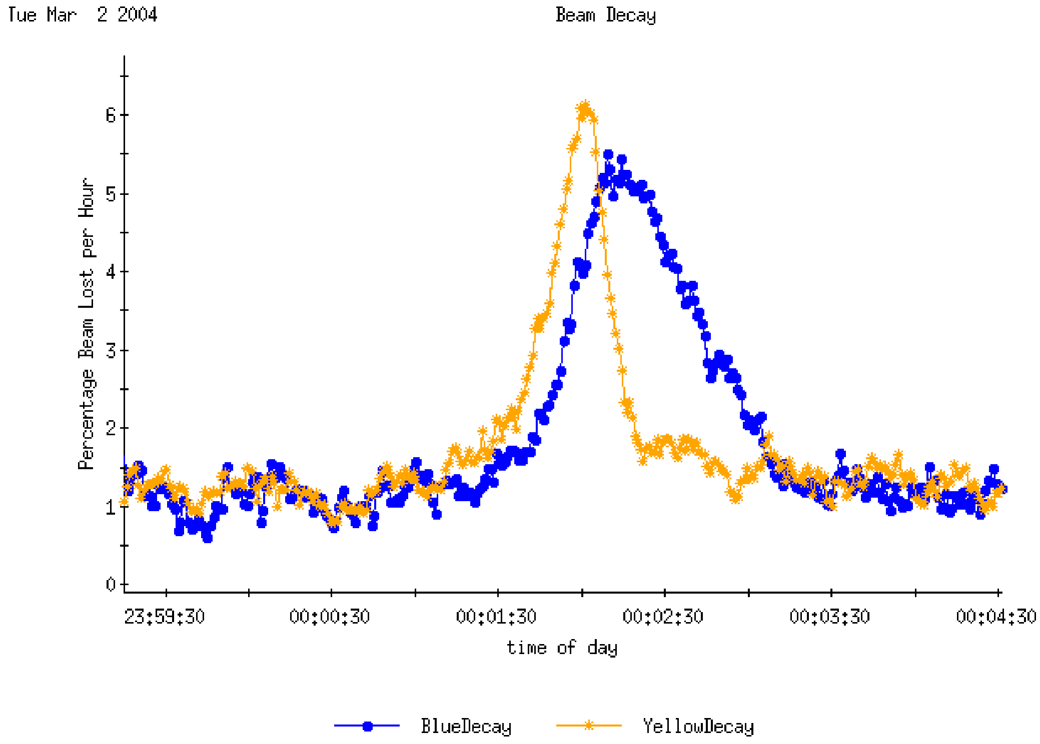

Figure 7.25: Beam loss measurement in blue and yellow ring before during and after unsqueezing the IP β-functions with the tuning knob.

quantities monitored during this period. This was not possible due to time limits.

7.4.2 Beam Experiment 4

Encouraged by the success of the second beam experiment a further experiment was planned. The goal of this was to squeeze also the second high luminosity IP to provide more luminosity. The first idea was to have an independent knob set for each experiment. The simulations performed soon showed that this is not feasible. For different reasons it was not possible to calculate a second knob set for IP6 with the same behavior of the constraints. The dispersion at the IP was increased much more strongly by any knob. A second problem was the limitation of the usable tuning quadrupoles. All calculated knobs were limited by the power supplies to about a maximum change of six percent of the nominal $\beta^\star$ value.

Earlier simulation had shown that the constraints behaved best when both IPs were manipulated simultaneously. Taking this information into account it was decided to create a knob set which squeezes both IP β-functions at the same time. This approach was fruitful and the results of the beam experiment testing this knob set is discussed in this section.

Contrary to the knob set of IP8, this solution indicated during the simulation already that the dispersion change is of a limiting magnitude. This partially results from a higher residual dispersion in IP6.

The injection beam statistics for the fill as automatically logged by the sequencer is summed up in Table 7.15. The operational mode is different from the one of the first beam experiment. This mode was chosen to give the experimental group a chance to take data with the squeezed optic.

Table 7.15: Injected beam statistics automatic recorded in the log book of the RHIC control room for the beam experiment beta star squeeze during the fourth experiment.

Injected Beam Statistics for Fill number 4794

Injection start time: Wed Mar 17 05:15:03 2004
Injection complete time: Wed Mar 17 05:16:43 2004

Ring	Blue	Yellow
Bunches/Cycles	45/12	45/12
Avg Bunch in RHIC (10^9 Au Ions)	0.802	0.815

The beam intensities are recorded in Fig.7.26 during injection and ramp. The different mode of operation results in a lower total beam intensity but the difference in intensity between the two beams (yellow and blue) is clearly smaller.

After this step and after bringing the beams into collision the anti-integer tunes were measured to check the tune separation between the horizontal and vertical plane of each beam.

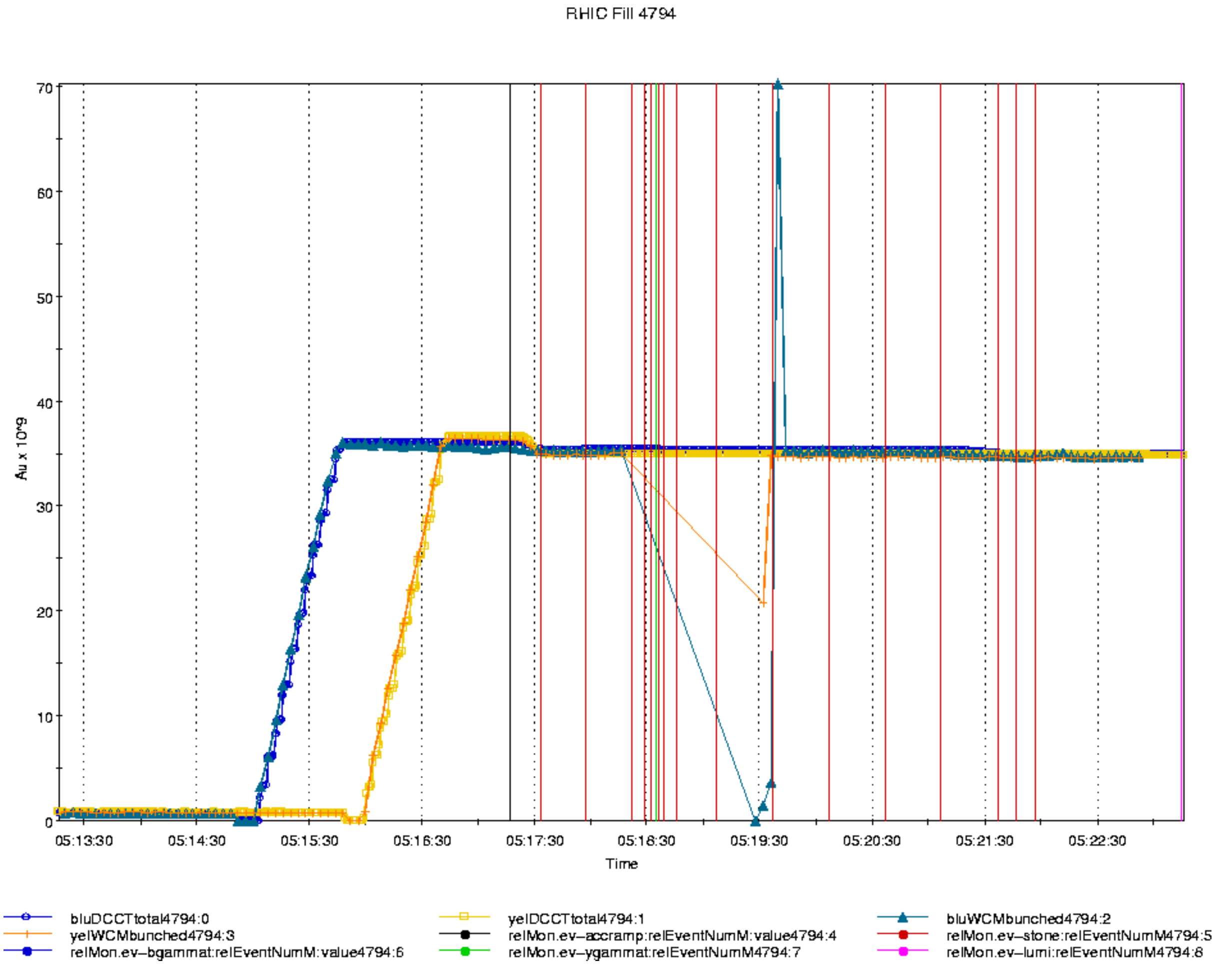

Figure 7.26: Ramp data from the beam-ions log sequencer. The plot shows the intensity of the two beams blue and yellow. In the first part the beams are filled in batches of 4 bunches 11 times and terminated by a single bunch, first blue and then yellow. Then the acceleration and squeeze (from injection to collision optics) is performed. During this process a loss in intensity can be observed.

blue	horizontal	0.219
	vertical	0.236
yellow	horizontal	0.234
	vertical	0.226

The preparations were completed by a beam offset minimization with LISA. The steering correction brought an increase in luminosity. The $\beta^{\star}$ squeeze with the tuning knobs was started at about 05:44 and lasted until 05:48. During this time the counting rates measured in IP6 and IP8 increased constantly as depicted in Fig.7.27. The rates in IP8 (blue curve) increased more than in IP6 (red curve). This was not expected from the optic data computed by the on-line model recorded in Table 7.16.

Rerunning the steering correction (LISA) brought a further increase in the counting rates at IP6 as shown in Fig.7.28. The original difference in the counting rates between IP6 and IP8 before applying the tuning knobs was approximately restored (Fig.7.28 to

Table 7.16: $\beta^\star$ function in IP6, IP8 and IP10 before and after applying the tuning knob with a nominal change of -12% of the original $\beta^\star$ value in IP6 and IP8 for the blue and yellow beam.

		IP6 (STAR)		IP8 (PHENIX)		IP10 (PHOBOS)	
		$\beta_x[m]$	$\beta_y[m]$	$\beta_x[m]$	$\beta_y[m]$	$\beta_x[m]$	$\beta_y[m]$
blue	nominal settings	1.043	1.057	1.060	1.071	3.131	3.092
	tuning knobs applied	0.931	0.937	0.947	0.952	3.128	3.078
	change [%]	10.7	11.4	10.6	11.1	0.1	0.5
yellow	nominal settings	1.092	1.056	1.078	1.050	3.015	3.056
	tuning knobs applied	0.974	0.944	0.961	0.939	3.026	3.072
	change [%]	10.8	10.6	10.9	10.6	0.4	0.5

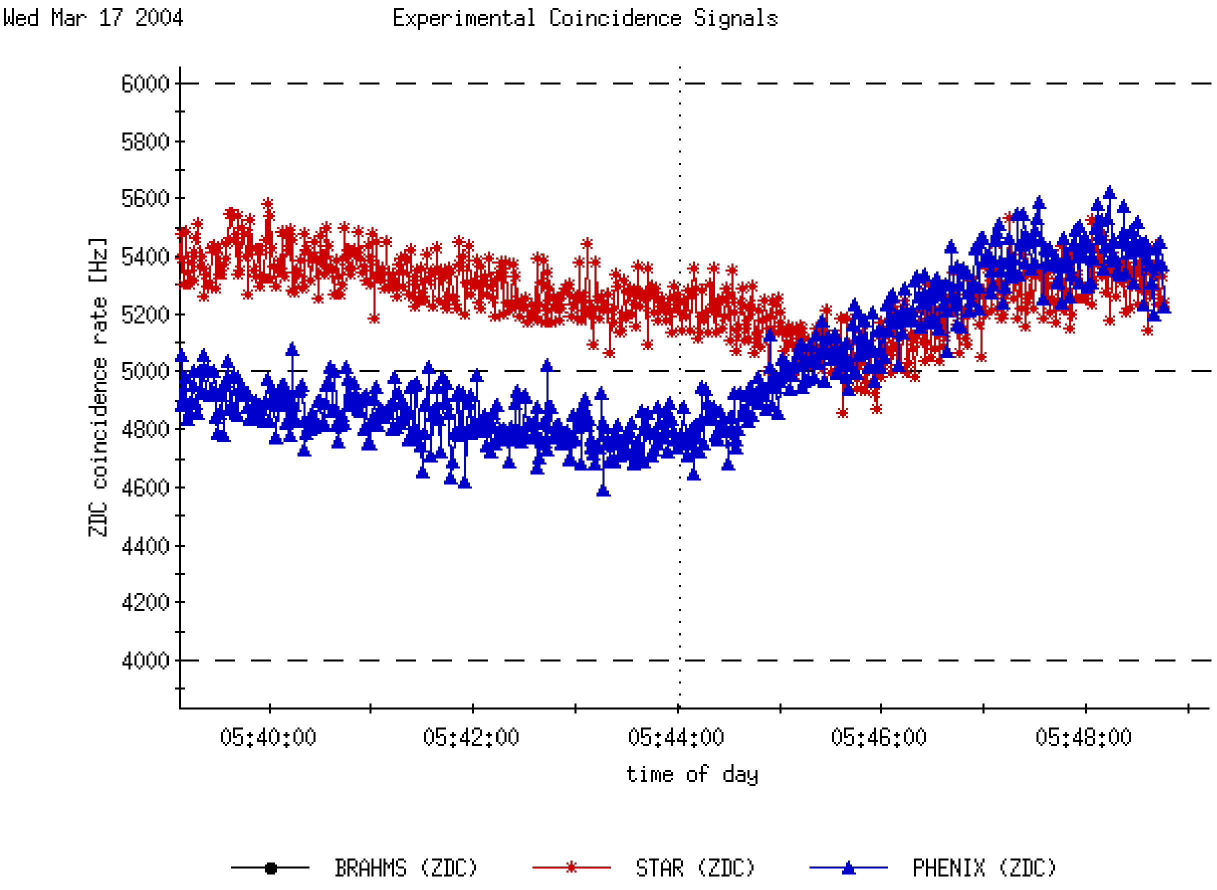

Figure 7.27: Counting rates during the application of the tuning knobs by decreasing the horizontal and vertical β-function at the IP for both beams in IP6 and IP8. The blue curve shows the counting rate in IP8 and the red in IP6.

Fig.7.26). A possible explanation is a bigger offset in the closed orbit from the design orbit in the tuning quadrupoles in IP6 . Due to the dipole kick to a beam which passes through a quadrupole off center, the knobs have a parasitic dipole component. This can cause a serious problem if the dipole kick is so strong that it drives the two beams out of collision. For this experiment it caused no further problems as its effect could be corrected by LISA.

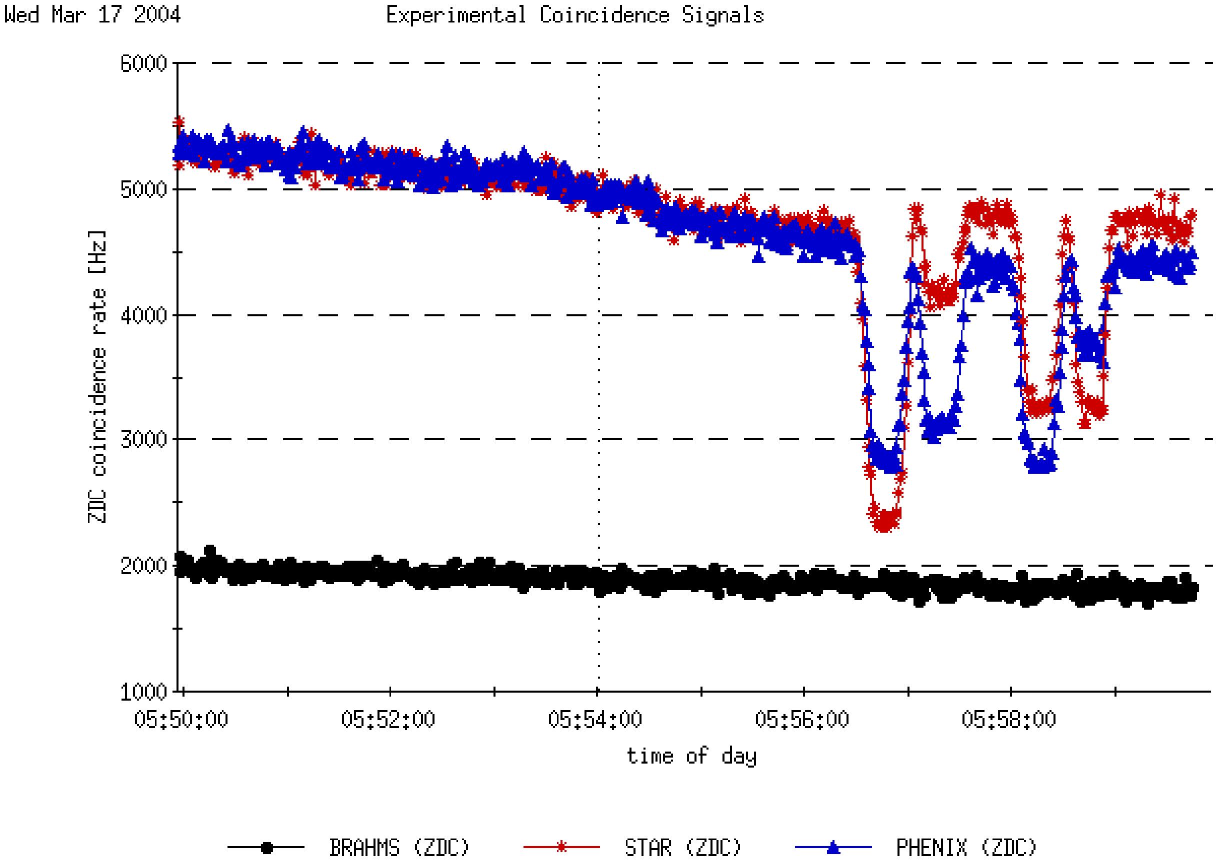

Figure 7.28: Counting rates during the offset optimization with LISA. The blue curve shows the counting rate in IP8 (PHENIX) and the red curve the counting rate in IP6 (STAR).

A more serious problem was caused by the increase in loss rates (see Fig.7.29) and backgrounds (see Fig.7.30). The loss rates in the yellow beam could be recovered quickly. This was done by retuning the vertical plane to increase the tune separation of the horizontal and the vertical plane. The tune separation had been too small and it seems that a resonance had been excited. The loss rates in the blue ring could also be recovered by decoupling the horizontal from the vertical plane. This allowed the tunes to be closer to a resonance without affecting the beam life time. The effect of both of these measures can be seen in plots7.29 and 7.30. The negative effects on loss rates and background appearing during the application of the tuning knobs were the result of the condition of the machine at this time and could be completely compensated.

Due to the corrections the experimental groups were able to take data with the knob squeezed-optics. The results of these measurements are not available at this time. So

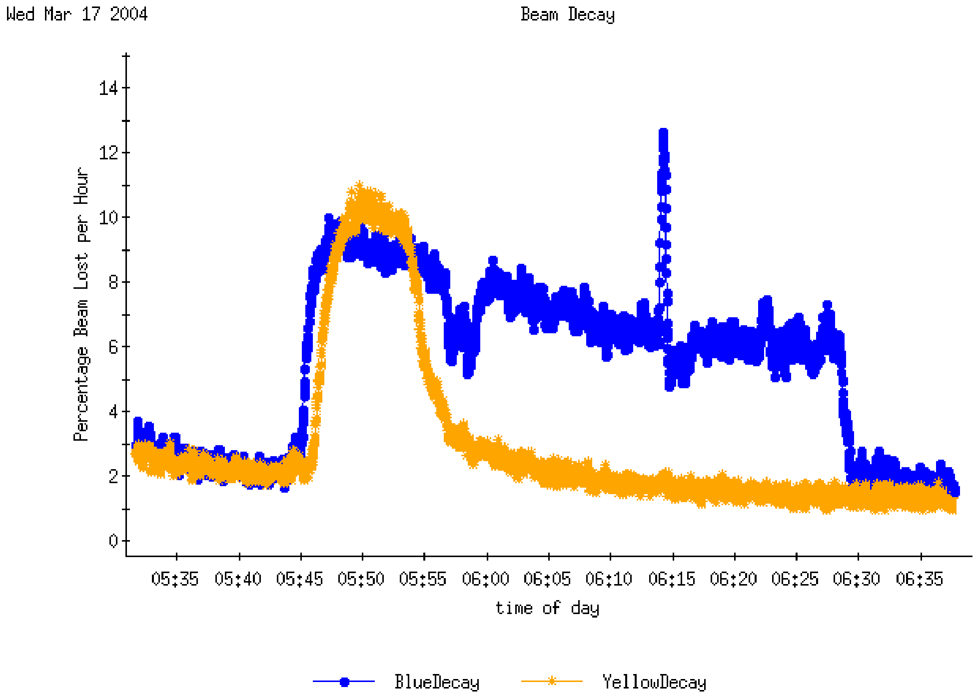

Figure 7.29: Beam loss measurement in blue and yellow before during and after squeezing the β-functions in IP6 and IP8 with the tuning knobs.

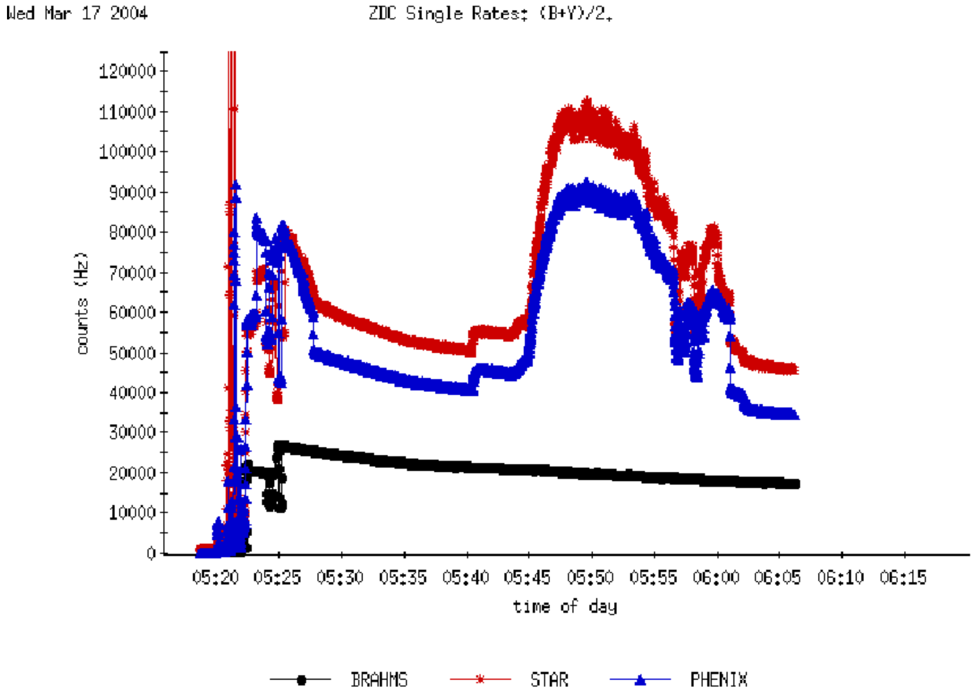

Figure 7.30: Background rates from the different IPs measured before, during and after applying the tuning knobs for $\beta^\star$ squeeze.

no results are presented.

The main result of the fourth experiment is, that a simultaneous correction of β-functions in IP6 and IP8 is possible by the computed tuning knobs.

Chapter 8

Results, Conclusion and Outlook

The proof of principle was given that under certain conditions a set of quadrupoles can be found to construct a tuning knob which modifies the IP β-function. This knob introduces well defined changes in the lattice functions and obeys a number of constraints.

8.1 LHC $\beta^\star$ Tuning Knobs

For the LHC the changes to the lattice functions introduced by the calculated tuning knobs are all within the specified limits. Normal and skew quadrupole gradient errors randomly introduced in the arc quadrupoles can be corrected with these knobs.

The same optics errors generated in the final focus triplet quadrupoles, which are located in the same interaction region as the manipulated IP cannot be corrected if the $\beta^\star$ change is larger than $\approx 20\%$. This is not too surprising, since triplet errors change the transfer matrices between the knob quadrupoles on either side of the IP and the effort to correct these errors is larger than for errors generated outside the same interaction region. It is favorable to correct these errors locally by correcting the field at the error source.

The functionality of the tuning knobs in presence of crossing angle, closed orbit distortions and parasitic long range beam-beam kicks has been simulated. These effects influence the performance of the knobs, but the result still meet all demands.

The possibility of squeezing the IP β-function to increase the luminosity has been probed in simulations and was shown to be feasible. The limit for this squeeze is determined by the limits of the tuning quadrupoles (maximum field strength) as well as by aperture requirements in the final focus triplet magnets.

8.2 RHIC $\beta^\star$ Tuning Knobs

Optics tuning knobs were calculated for IP8 of RHIC, using four different approaches: (1) MAD matching, (2) response matrix inversion, (3) pseudo response matrix inversion and conditioning using singular value decomposition (SVD) and (4) response matrix inversion and conditioning using an adapted Moore Penrose method to perform multidimensional minimization. These knobs change either the horizontal or the vertical β-function in a specific interaction point (IP8) by perturbing other optics functions (α, orthogonal β, D and Q in both planes) at the IP which is tuned or in any other part of the lattice within specified boundaries. Six different knobs were calculated for RHIC of which five can be directly compared. All calculated knobs work well in simulations over a range of $\pm 20\%$ (operative range) and the performance of the different knobs is similar in the simulation for all four methods.

The practicality of this type of tuning-knob scheme was explored in experimental studies at RHIC. For these experiments two different knob sets were computed with the on-line model, which controls the collider: one set acting on IP8 and a second acting on IP6 and IP8 simultaneously. Both knobs were applied successfully squeezing the IP β-functions $\approx 12\%$ in both cases. This increased the luminosity counting rate by $\approx 10\%$.

8.3 $\beta^\star$ Measurement

Based on the possibility to change the IP β-functions with the tuning knobs a new $\beta^\star$ measurement method has been developed. With this method the folded beam size, namely the quadratic sum of the beam sizes in the same plane of two colliding beams ($\Sigma^2 = \sigma_1^2 + \sigma_2^2$), as measured in a "Van der Meer" or "Vernier" scan can be decomposed and the individual beam sizes be determined. Due to technical problems with the application controlling the "Vernier Scan", the experimental proof of principle of the newly developed $\beta^\star$ measurement method was not possible at RHIC.

The standard method to measure the IP β-function was adapted to the asymmetric lattice of LHC. This method was advanced by analytically linking the measured tune changes induced by a set of quadrupole gradient variations to the IP β-functions.

8.4 Outlook

One major conclusion of this thesis is the fact that there is no obvious general condition which explicitly qualifies if for a given lattice the desired tuning knobs can be constructed. Every lattice has to be analyzed separately. A possible continuation would be to more precisely analyze the constraints based on the response matrix and its nonlinear expansion to derive such a condition, which should imply the possibility of computing $\beta^\star$ tuning knobs for a set of constraints and operating range.

In the recent past a new method to find the global minimum has been introduced in the matching routine of MAD. This genetic code still works with static matching constraints. In this thesis attempts were made and shown to be successful to use dynamic matching constraints. A future combination of both these methods might bring a great advance in lattice design.

A new $\beta^\star$ measurement method has been developed and a standard method has been advanced. The result of the simulation will need to be verified on a real machine.

Bibliography

[1] E. D. Courant and H. S. Snyder, "Theory Of The Alternating-Gradient Synchrotron," Annals Phys. **3**, 1-48 (1958) [Annals Phys. **281**, 360-408 (2000)].

[2] D. A. Edwards and M. J. Syphers, "An Introduction To The Physics Of High-Energy Accelerators," New York, USA: Wiley (1993) 292 p (Wiley series in beam physics and accelerator technology)

[3] H. Wiedemann, "Particle Accelerator Physics: Basic Principles And Linear Beam Dynamics," Berlin, Germany: Springer (1993) 445 p

[4] H. Wiedemann, "Particle Accelerator Physics: 2: Nonlinear And Higher Order Beam Dynamics," Berlin, Germany: Springer (1995) 464 p.

[5] S. Y. Lee, "Accelerator Physics," Singapore, Singapore: World Scientific (1999) 491 p

[6] M. Conte and W. W. MacKay, "An Introduction To The Physics Of Particle Accelerators," Singapore, Singapore: World Scientific (1991) 250 p

[7] E. Forest, "Beam Dynamics: A New Attitude And Framework," Amsterdam, Netherlands: Harwood (1998) 463 p

[8] P. J. Bryant and K. Johnsen, "The Principles Of Circular Accelerators And Storage Rings," Cambridge, UK: Univ. Pr. (1993) 357 p

[9] A. W. . Chao, (ed.) and M. Tigner, (ed.), "Handbook Of Accelerator Physics And Engineering," Singapore, Singapore: World Scientific (1999) 650 p

[10] S. Turner, "Advanced Accelerator Physics. Proceedings, 5th Course Of The Cern Accelerator School, Rhodos, Greece, September 20-October 1, 1993. Vol. 1, 2," Geneva, Switzerland: CERN Geneva - CERN-95-06 1098 p

[11] S. Turner, "General Accelerator Physics. Proceedings, Cas Cern Accelerator School, 5th Course, Jyvaeskylae, Finland, September 7-18, 1992. Vol. 1, 2," Geneva, Switzerland: CERN Geneva - CERN-94-01 1024 p

[12] W. Herr and B. Muratori, "Concept Of Luminosity," to be published

[13] W. Herr, "Beam-Beam Interactions," to be published

[14] K. Yokoya et al., “Tune shift of coherent beam-beam oscillations,” Part.Acc.27, 181 (1990).

[15] H. Grote and F. C. Iselin, ‘The MAD program version 8.4: User’s reference manual,’ CERN-SL-90-13-AP-REV.2.

[16] H. Grote and F. C. Iselin, ‘The MAD program version 8.13: Physical Methods Manual,’ CERN-SL-92-AP

[17] H. Grote and F. C. Iselin, ‘The MAD program version 8.10: Programmers Reference Manual,’ CERN-SL-92-AP

[18] F. Schmidt, et al., MAD X homepage: http://frs.home.cern.ch/frs/Xdoc/mad-X.html

[19] J. Safranek, “Experimental determination of storage ring optics using orbit response measurements”, Nucl. Ins. And Meth. A388, **27** (1997)

[20] J. Safranek, G. Portmann, A. Terebilo and C. Steier, “MATLAB-based LOCO,” SLAC-PUB-9464 *Presented at 8th European Particle Accelerator Conference (EPAC 2002), Paris, France, 3-7 Jun 2002*

[21] . Robin, J. Safranek and W. Decking, “Realizing the benefits of restored periodicity in a particle storage ring,” Phys. Rev. ST Accel. Beams **2** (1999) 044001.

[22] D. Schulte, private communication

[23] W. Venturini Delsolaro (AT/MTM), private communication

[24] R. Wolf, private communication

[25] W.Wittmer ‘Luminosity Optimization by Adjusting LHC $\beta^\star$ at Collision.’ CERN Proceedings Nanobeam 2002 Lausanne, Switzerland, 2-6 September 2002,p 199-205, see also the nanobeam web page: http://icfa-nanobeam.web.cern.ch/icfa-nanobeam/paper/wittmer.pdf

[26] W. Wittmer, A. Verdier, F. Zimmermann ‘Correcting the LHC $\beta^\star$ at Collision’ CERN-LHC-Project-Report-647, see also http://warrior.lbl.gov:7778/pacfiles/papers/WEDNESDAY/AM_POSTER/WPAB083/WPAB083.PDF

[27] W. Press, S. Teukolsky, W. Vetterling, B. Flannery, ‘Numerical Recipes in C The Art of Scientific Computing Second Edition’, CAMBRIDGE UNIVERSITY PRESS Cambridge New York Port Chester Melbourne Sydney

[28] M. Galassi, J. Davies, J. Theiler, B. Gough, G. Jungman, M. Booth, F. Rossi, ‘GNU Scientific Library Reference Manual’ Edition 1.3,for GSL Version 1.3 9 February 2003, see also http://www.network-theory.co.uk/gsl/manual/gsl-ref.pdf

[29] R. M. Barnett et al.,'Review of Particle Properties', Physical Review D54, 1 (1996) http://pdg.lbl.gov/

[30] F. James and M. Roos, 'Minuit' A System For Function Minimization And Analysis Of The Parameter Errors And Correlations,' Comput. Phys. Commun. **10** (1975) 343.

[31] E. Keil, "Truly selfconsistent treatment of the side effects with bunch trains," CERN-SL-95-75-AP

[32] H. Grote and W. Herr, "Self-consistent orbits with beam-beam effect in the LHC," CERN-LHC-PROJECT-REPORT-502B *Prepared for Beam-beam Workshop at Fermilab, Batavia, Illinois, 25-27 Jun 2001*

[33] N. J. Walker, J. Irwin and M. Woodley, SLAC-PUB-6207 *Presented at 1993 Particle Accelerator Conference (PAC 93), Washington, DC, 17-20 May 1993*

[34] M. G. Minty and F. Zimmermann, "Measurement And Control Of Charged Particle Beams," Berlin, Germany: Springer (2003) 364 p.